DIAGENESIS OF C, N AND Si IN MARINE SEDIMENTS FROM THE WESTERN TROPICAL NORTH ATLANTIC AND EASTERN SUBTROPICAL NORTH PACIFIC: PORE WATER MODELS AND SEDIMENTARY STUDIES

by

Lauren Stephanie Chong

A Dissertation Presented to the
FACULTY OF THE USC GRADUATE SCHOOL
UNIVERSITY OF SOUTHERN CALIFORNIA
In Partial Fulfillment of the
Requirements for the Degree
DOCTOR OF PHILOSOPHY
(GEOLOGICAL SCIENCES)

AUGUST 2013

This work is dedicated to my grandfather, Peter Chong, who has inspired me throughout my entire life and taught me to never give up.

ACKNOWLEDGMENTS

It is amazing how quickly five years can pass, and the number of amazing people you meet in that time who have a role in shaping your life. Primarily, I thank Dr. Will Berelson, who has supported me throughout this process and has guided me towards becoming a careful and competent marine geochemist; it's certainly been an interesting ride. He taught me how to tease out information from even the most spaghetti-like pore water profiles, and that successfully recovering sediment cores from over 5 km deep in the ocean is an act of badassery. I thank Dr. Doug Hammond for sharing his knowledge of sedimentary geochemical modeling with me; he was the first person in all my years of schooling to make me realize that I, in fact, do understand differential equations, and was always willing to check the math from my model. I also thank Dr. Doug Capone, for his insights on the nitrogen cycle and helpful suggestions. I would also like to acknowledge the other members of my qualifying exam committee, Dr. Sergio Sañudo-Wilhelmy and Dr. Sarah Feakins, for their comments and contributions as I developed my proposals. I am also deeply thankful to the Chief Scientist of the ANACONDAS project, Dr. Patricia Yager for making it possible for us to collect such an extensive set of samples. Thanks are also due to the scientists involved in the LONO cruise.

In my lab, first and foremost, Dr. Masha Prokopenko played an important role in teaching me everything she knows about mud, including how to become covered in it during sampling. From my very first cruise at USC to Santa Barbara Basin, subsequent cruises to SPOT, and our cruise to the Gulf of California, she was a constant source of positive energy on the ship and especially in the cold room. My

early interests in the nitrogen cycle were easily burgeoned by her passion and extensive knowledge on the subject, as we bonded over the long hours babysitting the MIMS. I would also like to thank my former lab mates, Dr. Lisa Collins and Dr. Tim Riedel, for seeing me through my first few years of grad school, and even after their graduation, being available to go to for support. My current lab mates, John Fleming and Caty Tems, have been great to work with both in and out of the lab, and I hope the insights and knowledge I've passed on to you are useful. I am also thankful to the Berelson Lab tech, Nick Rollins, who participated in the collection of every sediment core analyzed in this dissertation. His relaxed, good nature and sense of humor lightened our long hours in the cold van, and we shared in many shenanigans in Barbados. The undergraduate students who assisted with my work, Cara Fassino, Jake Porter, and especially Alice Bitzer, made my life infinitely easier by grinding my sediment samples and acid cleaning a mountain of sample bottles.

I have made many friends at USC and beyond who have made these years enjoyable and to whom thanks are due, but my biggest thank you goes to my dear friend, Dr. Esther Singer. It is a certainty to me that I would not have completed graduate school without her support, friendship, love, and sheer moxie. She was my peer role model whom I strived to emulate, she gave me strength and courage through the tough times, and it was with her that I learned that I should probably refrain from consuming half a fifth in the future. Kelp forest, my dear.

I thank my family for their support and unwavering belief in me: Mom, Dad, Scott, Anna, Kristi, and even little Jocey and Talia. They were a constant source of strength, red wine, and love, not necessarily in that order. Finally, I thank Charlie,

whose faith in me belies our relative short time together thus far, and who has helped me over this final hurdle. He inspires me to reach for even greater heights in everything I am yet to do. MFAS.

TABLE OF CONTENTS

Chapter 1: Introduction

COUPLING BETWEEN THE OCEAN CARBON AND NITROGEN CYCLE AND THE DEGRADATION OF ORGANIC MATTER IN MARINE SEDIMENTS:

The biogeochemical processes occurring in the upper meters of marine sediments have a profound impact on the cycling of many elements in the ocean, both on a local and global scale. Many of these processes can be linked either directly or indirectly to the degradation of organic matter. Microbially driven reactions influence the chemistry of nutrients (Anderson and Sarmiento, 1994; Bender et al., 1977; Froelich et al., 1979), trace metals (de Baar and de Jong, 2001; Boyd and Ellwood, 2010; McManus et al., 2006; Rauch and Pacyna, 2009), major ions (Berner and Berner, 2012; Broecker and Peng, 1982; James and Palmer, 2000; Sayles, 1979), and carbonates (Archer, 1996; Emerson et al., 1980; Jahnke and Jahnke, 2004). Microbial influence on bSi remineralization is also likely, although less understood (Holstein and Hensen, 2010; McManus et al., 1995; Van Cappellen and Qiu, 1997). Additionally, the diagenesis of organic matter in the sediments affects the flux of organic carbon to the deep biosphere as well as the eventual burial of organic carbon in the rock record (Middelburg and Meysman, 2007), and thus the global oxygen budget on geologic time scales.

The oceanic carbon cycle is a dynamic system where combined physical, chemical, and biological processes affect the size and distribution of the oceanic carbon pool. In the surface ocean, atmospheric CO_2 is 'fixed' by photosynthetic marine plankton into organic material, and while much of this new carbon is quickly recycled (Middelburg et al., 1993), a fraction of it is exported to the deep ocean via

the biological pump. The biological pump is the series of biologically mediated processes responsible for transporting organic carbon from the surface ocean to the deep sea, providing a pathway for CO_2 removal from the atmosphere (Passow and Carlson, 2012; Volk and Hoffert, 1984) over potentially long time scales (Falkowski et al., 2000). The efficiency with which these export and remineralization processes occur affects the magnitude of the removal of carbon and nutrients from the ocean, and ultimately, the air-sea balance of CO_2 (Falkowski et al., 1998).

The carbon and nitrogen cycles are tightly linked, as N limitation hinders primary production in large areas of the worlds oceans, particularly in oligotrophic subtropical/tropical gyres (Davey et al., 2008; Falkowski et al., 1998; Zehr and Ward, 2002). Early studies of N as a limiting nutrient in the marine environment led to the determination of the 'Redfield Ratio', which posits that the material in marine organic matter will have a fixed C:N:P of 106:16:1 (Redfield, 1934; Redfield et al., 1963), though there have been subsequent revisions to this ratio (Anderson and Sarmiento, 1994). The nitrogen cycle is driven by a combination of assimilatory and dissimilatory biological transformations (Brandes et al., 2007; Thamdrup, 2012). Diazotrophs fix N_2 gas from the atmosphere into a biologically usable form, adding 'new' nitrogen to the euphotic zone of the ocean (Capone et al., 2005; Carpenter and Romans, 1991; Carpenter et al., 1999; Falkowski et al., 1998). Fixed N is removed by a variety of nitrogen removal pathways in the water column and sediments (Burgin and Hamilton, 2007), with new processes being uncovered as researchers try to understand the complexities of the nitrogen cycle (Thamdrup, 2012). In spite of the body of work on oceanic nitrogen cycles and budgets, a large uncertainty exists in

both inputs and outputs, for example, the global magnitude of N losses in part due to insufficient knowledge of the biogeochemical pathways involved in the sedimentary N cycle (Codispoti, 2007).

MOTIVATION FOR THIS STUDY

Sedimenting particles provide a link between the surface ocean, the deep sea, and the sediments below. The flux of material to the deep ocean can vary on every imaginable time scale (Deuser et al., 1983; Deuser and Ross, 1980). However, there is a generally accepted paradigm that only a small fraction of surface ocean primary production settles on the sea floor, approximately 1-1.5% in the open ocean and up to 17% on the upper slopes (Wollast, 1998). When organic matter reaches the sea floor, it is subjected to a variety of biologically-driven mineralization processes, and the sediments and pore waters record the sequence and rate of organic matter degradation in the shape and positioning of the profiles of oxidants and metabolites (Froelich et al., 1979; Goloway and Bender, 1982; Heggie et al., 1987). There is another generally accepted paradigm that only a small fraction of the organic carbon that reaches the sea floor survives remineralization, but degradation efficiency and burial rates can vary significantly throughout the globe (Blair and Aller, 2012; Canfield, 1994; Canfield et al., 2005; Henrichs and Reeburgh, 1987; Middelburg and Meysman, 2007). Burial is a key process in the biological pump that links the 'fast' cycles occurring in the ocean-atmosphere system with the 'slow' cycles in the sediments that operate on geological time scales.

Studies of the strength and efficiency of the biological pump have generally used a 'top down' approach, making estimates of production and export with

various methods employed within the euphotic zone. However, surface methods of quantifying export are complicated by spatial and temporal variability of the surface ocean, and do not necessarily provide an accurate assessment of the amount of organic material reaching the deep ocean. The sediments can be considered the 'ultimate sediment trap', integrating surface export over longer timescales than the surface ocean (Herman et al., 2001; Jahnke, 1990; Reimers et al., 1992), but using them as a reliable means of analyzing carbon and nitrogen cycling on a global scale requires an improvement in the sparse spatial coverage of field measurements and in our knowledge of the biogeochemical pathways involved in sedimentary cycling.

This study addresses C and N cycling in sediments at two locations from two perspectives, based on the sensitivity of the biological pump to the input of nutrients from upwelling and from rivers (de la Rocha, 2003). The bulk of this dissertation involves research that looks at the impact of the Amazon River on the export of organic matter in the Western Tropical North Atlantic. This work involves extensive spatial coverage of sediment core collection, carbon oxidation rates derived from pore water nitrate models, Si remineralization rates, an analysis of nutrient fluxes, and an assessment of biogenic sedimentation. The secondary part of this dissertation is a study that examines the nitrogen cycle in the upwelling region of the Eastern Tropical North Pacific, looking at how biological nitrate transport affects losses from the biologically available pool of nitrogen, and characterizing the environmental factors that promote this process through thorough study of pore water N species, including N_2 and N_2O.

STRUCTURE OF THE DISSERTATION

Chapter 2 examines the spatial patterns of carbon and biogenic silica remineralization in the surface sediments underlying the Amazon River Plume from an extensive set of sediment cores and analysis of pore water profiles. One specific goal is to assess the importance of diatom-diazotroph associations to the export of material reaching the deep-sea floor. Pore water profiles of NO_3^- are modeled using a multi-G, diffusion-reaction model to estimate the amount of carbon oxidized from oxic diagenesis and denitrification. The model is fit to pore water data collected on mm- and cm-scales to a depth of ~40 cm, though pore waters were collected from depths of >400 cm. Assuming that nearly all of the organic carbon reaching the sea floor is oxidized, remineralization rates should be nearly equivalent to the deposition rates. Profiles of dissolved Mn are used to determine the depth where oxygen concentrations go to zero. Pore water silica is modeled to calculate the bSi remineralization flux. The distinct pattern of benthic fluxes is discussed in relation to the location of the river plume and an integral of the total amount of C and Si recycled is presented.

Chapter 3 takes a look at biogenic sedimentation beneath the Amazon River Plume from a solid phase perspective. It provides a somewhat geologic view on the early diagenetic picture developed in Chapter 2. Downcore profiles of biogenic components are presented along with $\Delta^{14}C$ calendar ages, sedimentation rates, and ^{210}Pb inventories and mixing coefficients. The sedimentation rates and sediment organic carbon and biogenic silica concentrations are used to calculate the burial flux of each component, and these rates are compared to remineralization rates

from Chapter 2. The sum of remineralization and burial provides a value of biogenic matter rain to the sea floor. The rain rates to the sea floor are extrapolated to the surface ocean using the canonical Martin Curve, and the resulting export fluxes are compared to measurements from surface tethered sediment traps.

Chapter 4 examines the suboxic diagenetic processes affecting organic carbon burial in the sediments underlying the Amazon River Plume. Pore water profiles from gravity cores are analyzed to determine the zonation of the terminal electron acceptors and to estimate the flux of carbon consumed by anaerobic processes. The concentration gradients of manganese, iron, nitrate and ammonium suggest the involvement of several less-studied processes of nitrogen diagenesis. Flux determinations help define various reaction stoichiometries and authigenic mineral accumulation rate estimates.

Chapter 5 reports the rates of benthic nitrogen cycling and assesses the controls on biological nitrate sequestration and transport in sediments underlying oxygen deficient areas of the Eastern North Pacific along the western coast of North America. A nitrogen mass balance is constructed based on benthic fluxes of N_2, NH_4^+ and NO_3^- as well as pore water profiles of N_2, NO_3^-, NO_2^-, N_2O, Fe^{2+} and HS^-. Pore water profiles reveal that at both sulfidic and iron-rich sites, there are subsurface maxima in NO_3^-, NO_2^- and N_2O that are likely caused by the sequestration of NO_3^- by infaunal microbiota. Biological nitrate transport appears to be a ubiquitous process in suboxic and anoxic sediments, but the magnitude of its importance to nitrogen

removal is related to whether the sediments are sulfidic or iron-rich. This chapter has been published in Marine Chemistry (Chong et al., 2012).

A summary of this dissertation appears as Chapter 6.

REFERENCES

Anderson, L.A., and Sarmiento, J.L., 1994, Redfield ratios of remineralization determined by nutrient data analysis: Global Biogeochemical Cycles.

Archer, D.E., 1996, An atlas of the distribution of calcium carbonate in sediments of the deep sea: Global Biogeochemical Cycles, v. 10, no. 1, p. 159–174.

Bender, M.L., Fanning, K., Froelich, P.N., Heath, G.R., and Maynard, V., 1977, Interstitial nitrate profiles and oxidation of sedimentary organic matter in the eastern equatorial Atlantic: Science, v. 198, no. 4317, p. 605–609.

Berner, E.K., and Berner, R.A., 2012, Global environment: water, air and geochemical cycles: Princeton University Press, Princeton, NJ.

Blair, N.E., and Aller, R.C., 2012, The fate of terrestrial organic carbon in the marine environment: Annual Review of Marine Science, v. 4, p. 401–423.

Boyd, P.W., and Ellwood, M.J., 2010, The biogeochemical cycle of iron in the ocean: Nature Geoscience, v. 3, no. 10, p. 675–682, doi: 10.1038/ngeo964.

Brandes, J.A., Devol, A.H., and Deutsch, C., 2007, New developments in the marine nitrogen cycle: Chemical Reviews, v. 107, p. 577–589.

Broecker, W.S., and Peng, T.-H., 1982, Tracers in the sea:, p. 690.

Burgin, A., and Hamilton, S.K., 2007, Have we overemphasized the role of denitrification in aquatic ecosystems? A review of nitrate removal pathways: Frontiers in Ecology and the Environment, v. 5, no. 2, p. 89–96.

Canfield, D.E., 1994, Factors influencing organic carbon preservation in marine sediments: Chemical Geology, v. 114, no. 3, p. 315–329.

Canfield, D.E., Kristensen, E., and Thamdrup, B., 2005, Aquatic Geomicrobiology: Academic Press.

Capone, D.G., Burns, J.A., Montoya, J.P., Subramaniam, A., Mahaffey, C., Gunderson, T., Michaels, A.F., and Carpenter, E.J., 2005, Nitrogen fixation by Trichodesmium spp.: An important source of new nitrogen to the tropical and subtropical North Atlantic Ocean: Global Biogeochemical Cycles, v. 19, no. 2, p. GB2024, doi: doi:10.1029/2004GB002331.

Carpenter, E.J., and Romans, K., 1991, Major role of the cyanobacterium Trichodesmium in nutrient cycling in the North Atlantic Ocean.: Science, v. 254, no. 5036, p. 1356.

Carpenter, E.J., Montoya, J.P., Burns, J.A., Mulholland, M., Subramaniam, A., and Capone, D.G., 1999, Extensive bloom of a N2 fixing symbiotic association in the tropical Atlantic Ocean: Marine Ecology Progress Series, v. 188, p. 273–283.

Chong, L.S., Prokopenko, M.G., Berelson, W.M., Townsend-Small, A., and McManus, J., 2012, Nitrogen cycling within suboxic and anoxic sediments from the continental margin of Western North America: Marine Chemistry, v. 128-129, p. 13–25, doi: 10.1016/j.marchem.2011.10.007.

Codispoti, L.A., 2007, An oceanic fixed nitrogen sink exceeding 400 Tg N/a vs the concept of homeostasis in the fixed-nitrogen inventory: Biogeosciences, v. 4, p. 233–253.

Davey, M., Tarran, G.A., Mills, M.M., Ridame, C., Geider, R.J., and LaRoche, J., 2008, Nutrient limitation of picophytoplankton photosynthesis and growth in the tropical North Atlantic: Limnology and Oceanography,, p. 1722–1733.

de Baar, H.J.W., and de Jong, J.T.M., 2001, Distributions, sources, and sinks of iron in seawater, *in* IUPAC series on analytical and physical chemistry of environmental systems, p. 123–254.

Deuser, W.G., and Ross, E.H., 1980, Seasonal change in the flux of organic carbon to the deep Sargasso Sea: Nature, v. 283, p. 364–365.

Deuser, W.G., Brewer, P.G., Jickells, T.D., and Commeau, R., 1983, Biological control of the removal of abiogenic particles from the surface ocean: Science, v. 219, no. 4583, p. 388.

Emerson, S.R., Jahnke, R.A., Bender, M.L., Froelich, P.N., Klinkhammer, G.P., Bowser, C., and Setlock, G., 1980, Early diagenesis in sediments from the eastern equatorial Pacific, I. Pore water nutrient and carbonate results: Earth and Planetary Science Letters, v. 49, no. 1, p. 57–80.

Falkowski, P.G., Barber, R.T., and Smetacek, V., 1998, Biogeochemical controls and feedbacks on ocean primary production: Science, v. 281, p. 200–206.

Falkowski, P.G., Scholes, R.J., Boyle, E.A., Canadell, J.G., Canfield, D., Elser, J., Gruber,

N., Hibbard, K., Hogberg, P., and Linder, S., 2000, The global carbon cycle: a test of our knowledge of earth as a system: Science, v. 290, no. 5490, p. 291–296.

Froelich, P.N., Klinkhammer, G.P., Bender, M.L., Luedtke, N.A., Heath, G.R., Cullen, D., Dauphin, P., Hammond, D.E., Hartman, B., and Maynard, V., 1979, Early oxidation of organic matter in pelagic sediments of the eastern equatorial Atlantic: suboxic diagenesis: Geochimica et Cosmochimica Acta, v. 43, no. 7, p. 1075–1090.

Goloway, F., and Bender, M.L., 1982, Diagenetic models of interstitial nitrate profiles in deep sea suboxic sediments: Limnology and Oceanography,, p. 624–638.

Heggie, D.T., Maris, C., Hudson, A., Dymond, J., Beach, R., and Cullen, J.L., 1987, Organic carbon oxidation and preservation in NW Atlantic continental margin sediments: Geological Society, London, Special Publications, v. 31, no. 1, p. 215–236.

Henrichs, S., and Reeburgh, W.S., 1987, Anaerobic mineralization of marine sediment organic matter: Rates and the role of anaerobic processes in the oceanic carbon economy: Geomicrobiology Journal, v. 5, no. 3-4, p. 191–237.

Herman, P.M., Soetaert, K., Middelburg, J.J., Heip, C.H.R., Lohse, L., Epping, E., Helder, W., Antia, A.N., and Peinert, R., 2001, The seafloor as the ultimate sediment trap—using sediment properties to constrain benthic–pelagic exchange processes at the Goban Spur: Deep Sea Research Part II: Topical Studies in Oceanography, v. 48, no. 14, p. 3245–3264.

Holstein, J.M., and Hensen, C., 2010, Microbial mediation of benthic biogenic silica dissolution: Geo-Marine Letters, v. 30, no. 5, p. 477–492.

Jahnke, R.A., 1990, Early diagenesis and recycling of biogenic debris at the seafloor, Santa Monica Basin, California: Journal of Marine Research, v. 48, no. 2, p. 413–436.

Jahnke, R.A., and Jahnke, D., 2004, Calcium carbonate dissolution in deep sea sediments: reconciling microelectrode, pore water and benthic flux chamber results: Geochimica et Cosmochimica Acta, v. 68, no. 1, p. 47–59.

James, R.H., and Palmer, M.R., 2000, Marine geochemical cycles of the alkali elements and boron: the role of sediments: Geochimica et Cosmochimica Acta, v. 64, no. 18, p. 3111–3122.

la Rocha, de, C., 2003, The Biological Pump, *in* Holland, H.D. and Turekian, K.K. eds., Treatise on Geochemistry, Elsevier, p. 84–107.

McManus, J., Berelson, W.M., Severmann, S., Poulson, R.L., Hammond, D.E., Klinkhammer, G.P., and Holm, C., 2006, Molybdenum and uranium geochemistry in continental margin sediments: Paleoproxy potential: Geochimica et

Cosmochimica Acta, v. 70, no. 18, p. 4643–4662.

McManus, J., Hammond, D.E., Berelson, W.M., Kilgore, T.E., DeMaster, D.J., Ragueneau, O.G., and Collier, R.W., 1995, Early diagenesis of biogenic opal: Dissolution rates, kinetics, and paleoceanographic implications: Deep Sea Research II, v. 42, no. 2-3, p. 871–903.

Middelburg, J.J., and Meysman, F.J., 2007, Burial at sea: Science (Washington), v. 316, no. 5829.

Middelburg, J.J., Vlug, T., Jaco, F., and Van Der Nat, W.A., 1993, Organic matter mineralization in marine systems: Global and Planetary Change, v. 8, no. 1, p. 47–58.

Passow, U., and Carlson, C.A., 2012, The biological pump in a high CO 2 world: Marine Ecology Progress Series, v. 470, p. 249–271.

Rauch, J.N., and Pacyna, J.M., 2009, Earth's global Ag, Al, Cr, Cu, Fe, Ni, Pb, and Zn cycles: Global Biogeochemical Cycles, v. 23, no. 2.

Redfield, A., 1934, On the proportions of organic derivatives in sea water and their relation to the composition of plankton: University Press of Liverpool, Liverpool, UK.

Redfield, A., Ketchum, B., and Richards, F.A., 1963, The influence of organisms on the composition of sea water, *in* The Sea, Ideas and Observations on the Progress in the Study of the Seas, Interscience, p. 26–77.

Reimers, C.E., Jahnke, R.A., and McCorkle, D.C., 1992, Carbon fluxes and burial rates over the continental slope and rise off central California with implications for the global carbon cycle: Global Biogeochemical Cycles, v. 6, no. 2, p. 199–224.

Sayles, F.L., 1979, The composition and diagenesis of interstitial solutions--I. Fluxes across the seawater-sediment interface in the Atlantic Ocean: Geochimica et Cosmochimica Acta, v. 43, no. 4, p. 527–545.

Thamdrup, B., 2012, New Pathways and Processes in the Global Nitrogen Cycle: Annual Review of Ecology, Evolution, and Systematics, v. 43, no. 1, p. 407–428, doi: 10.1146/annurev-ecolsys-102710-145048.

Van Cappellen, P., and Qiu, L., 1997, Biogenic silica dissolution in sediments of the Southern Ocean. I. Solubility: Deep Sea Research Part II: Topical Studies in Oceanography, v. 44, no. 5, p. 1109–1128.

Volk, T., and Hoffert, M.L., 1984, Ocean carbon pumps - Analysis of relative strengths and efficiencies in ocean-driven atmospheric CO2 changes, *in* Tarpon Springs, FL, p. 99–110.

Wollast, R., 1998, Evaluation and comparison of the global carbon cycle in the coastal zone and in the open ocean: The sea, v. 10, p. 213–252–252.

Zehr, J.P., and Ward, B.B., 2002, Nitrogen Cycling in the Ocean: New Perspectives on Processes and Paradigms: Applied and Environmental Microbiology, v. 68, no. 3, p. 1015–1024, doi: 10.1128/AEM.68.3.1015-1024.2002.

Chapter 2: Biogenic matter export influenced by the Amazon River plume: Patterns of remineralization in deep-sea sediments.

(submitted to Deep Sea Research)

L.S. Chong, W.M. Berelson, J. McManus, D.E. Hammond, N.E. Rollins, P.L. Yager

ABSTRACT

The path of the Amazon Plume as it mixes into the Western Tropical North Atlantic (WTNA) has been characterized and mapped by satellite imagery and cruise surveys. It has been suggested that plume waters create ecological niches favorable for N_2 fixation, where blooms of diatoms and their diazotrophic cyanobacterial symbionts have been implicated in increasing carbon export. However, the track of the plume is subject to temporal and spatial variability, making it difficult to assess if there is a particular region of the plume that favors enhanced export, and it is unclear how much of the surface production reaches the deep ocean. Here, we used multi-cores collected throughout the Demerara Slope and Abyssal Plain at depths ranging from 1800-5000 m to document benthic diagenetic processes. Pore waters were extracted from sediments using both millimeter and cm-scale resolution extraction techniques. Profiles of NO_3 and $Si(OH)_4$ were modeled with a diffusion-reaction equation to define POC degradation and bSi remineralization rates. Pore water Mn^{+2} helped constrain the model by indicating the depth where oxygen

concentrations went to zero. The model output was used to define the spatial patterns of POC and bSi arrival at the sea floor. Benthic carbon oxidation fluxes ranged from 0.16 – 1.92 mmol m^{-2} d^{-1}, and Si fluxes ranged from 0.14 – 1.35 mmol m^{-2} d^{-1}. There is a distinct axis of POC and bSi deposition on the deep sea floor aligned NW with the axis of river plume water. POC shows a distinct gradient along this axis with highest fluxes closest to the river mouth. bSi has a more diffuse zone of deposition and remineralization. The impact of the Amazon plume on benthic fluxes can be detected northward to 10°N and eastward to 47°W.

INTRODUCTION

Rivers impact the cycling of carbon in the ocean by providing a source of nutrients as well as trace elements that can enhance primary production, resulting in net carbon transport to the deep sea (Eppley and Peterson, 1979; Raymond and Cole, 2003; Smith and Hitchcock, 1994). The Amazon River is responsible for one fifth of the total riverine discharge to the world oceans (Gibbs, 1972), delivering freshwater at a rate of 1.93 ± 0.13 x 10^5 m^3sec^{-1} onto the Brazilian shelf (Perry et al., 1996). Plume waters can be traced northwest to the Caribbean in the late spring during periods of maximum discharge as well as eastward into the North Atlantic due to the seasonal retroflection of the North Brazil Current (NBC) in the fall (Froelich et al., 1978; Johns et al., 1998; Muller-Karger et al., 1988; Muller-Karger et al., 1995). It delivers high concentrations of both nutrients (annual means: $Si(OH)_4$ = 141-149 µmol kg^{-1}, PO_4^{-3}= 0.6-0.8 µmol kg^{-1}, NO_3^-= 12-23 µmol kg^{-1}, NH_4^+= 0.4-0.5

μmol kg^{-1}, and urea = 0.4-1.2 μmol kg^{-1}) and large amounts of organic carbon (POC: 1.4 x 10^{13} g yr^{-1}, DOC: 2.2 x 10^{13} g yr^{-1} at Obidos; POC: 3.5 x 10^{12} g yr^{-1}, DOC: 2.95 x 10^{13} g yr^{-1} at Macapá) to the Western Tropical North Atlantic (WTNA) (DeMaster and Pope, 1996; DeMaster et al., 1996; Aller et al., 1996; Richey et al., 1990; Ward et al., 2013 in press). The Amazon also discharges approximately 1.2 x 10^{9} metric tons (1.2x10^{15} g) per year of sediment (Meade et al., 1985; Milliman and Meade, 1983), of which, ~20% moves northwestward in the form of suspended sediments and as migrating mudbanks (Kineke et al., 1996; Nittrouer et al., 1995; Wells and Coleman, 1981).

The tropical North Atlantic is generally considered to be a net source of CO_2 to the atmosphere (Deuser et al., 1988; Mikaloff Fletcher et al., 2007; Takahashi et al., 2002), however, CO_2 uptake has been observed in the region, particularly in waters influenced by the Amazon River Plume (Cooley et al., 2007; Cooley and Yager, 2006; Ternon et al., 2000). Subramaniam et al., (2008) hypothesized that the Amazon Plume supports ecological niches in the outer plume (30 < Sea Surface Salinity (SSS) < 35) where surface waters are depleted in N but contain a relative excess of dissolved Si and P (Shipe et al., 2006; Subramaniam et al., 2008). This creates optimal conditions for diatom-diazotroph associations (DDAs), which have been suggested to be an important vector for carbon sequestration and export in this region (Carpenter et al., 1999; Foster et al., 2007; Subramaniam et al., 2008). Recently, Yeung et al., (2012) confirmed that DDA blooms increase carbon export efficiency, however, it is unclear if the blooms also result in an increase in the material reaching the deep ocean. Sediment traps deployed at 150 m by

Subramaniam et al., (2008) showed a correlation between the presence of DDAs in the water column and trap mass flux, but this does not tell us how much carbon reaches the sea floor. A trap deployed at 3200m at 13.22 ˚N, 41.68˚E (Deuser et al., 1988), showed a relationship between higher primary productivity and higher particle flux, but it is unknown if DDAs were responsible for the blooms. We have adopted the approach of using the sediments as 'the ultimate sediment trap' (Herman et al., 2001; Jahnke et al., 1990; Reimers et al., 1992) to map and quantify the export of carbon and biogenic Si to the deep sea in the area of the WTNA influenced by the Amazon Plume.

The majority of work on marine sediments in the area of the Amazon Plume has been limited to the river mouth and the adjacent continental shelf. Within surface sediments of the Amazon delta, both terrestrial and marine organic matter contribute to early diagenetic remineralization processes, but the marine fraction dominates (60-70%) (Aller and Blair, 2006; Aller et al., 2004). The river dispenses a terrestrial C_{org} load of 0.6-0.7 mg C m^{-2} with a bulk isotopic value of -27.7 to -28.1 ‰ (Hedges et al., 1986; Keil et al., 1997). The total C_{org} carrying capacity declines to 0.2-0.3 mg C m^{-2} <100 km from the river mouth (Blair et al., 2004; Keil et al., 1997). As the material moves northwest along the continental shelf, carried along by the North Brazil Current, rapid sediment mixing and suboxic diagenesis in fluidized mud beds progressively depletes the supply of terrestrial organic matter (Aller, 1998; Aller and Blair, 2006; Kineke et al., 1996; Kuehl et al., 1986; Kuehl et al., 1996). By the time sediment reaches the shelf off French Guiana, the total sediment C_{org} carrying capacity is 0.12-0.14 mg C m^{-2} with a bulk isotopic value of -24.7‰,

thus only ~10% of the original terrestrial C_{org} load remains 600 km from the Amazon River mouth (Aller and Blair, 2006). Radiocarbon analyses confirmed that the POC suspended in the plume near the river mouth and within the waters above the continental shelf contains a significant terrestrial component, while in the open ocean it is mainly of marine origin (Druffel, 2005). Our work includes sites 500-1200 km from the Amazon River mouth in the open ocean.

In deeper waters in this region, pore water studies have been completed on cores from the Amazon Fan (Schulz et al., 1994; Kasten et al., 2003; Kasten et al., 1998; Schlünz et al., 1999) and the Ceara Rise (Martin and Sayles, 1996; Martin and Sayles, 2006; Wenzhöfer and Glud, 2002). These studies serve as an excellent reference to our study, insofar as today, these areas are subject to little direct influence from the river plume.

For many open ocean environments, it has been shown that the organic matter reaching the sea floor in the deep ocean is nearly completely remineralized during early diagenesis (Bender and Heggie, 1984; Burdige, 2007; Canfield, 1994; Hedges and Keil, 1995; Premuzic et al., 1982), hence the oxidation flux should closely approximate the deposition flux. We measured and modeled pore water NO_3^- profiles and interpreted their shape as a proxy for carbon oxidation (Goloway and Bender, 1982; Martin et al., 1991; Martin and Sayles, 1996; Martin and Sayles, 2006). This approach has a benefit over measurements of oxygen gradients, which for cores recovered from great depths are subject to artifacts (Wenzhöfer et al., 2001). With sufficient benthic coverage, we can identify where deposition is

occurring and compare this 'footprint' to productivity in the surface ocean. We also calculate the flux of dissolved Si to provide an indication of the importance of biogenic silica (e.g., diatoms) export throughout the region.

STUDY AREA AND METHODS

We present data from the ANACONDAS (Amazon iNfluence on the Atlantic: CarbOn export from Nitrogen fixation by DiAtom Symbioses) project, which consisted of three cruises throughout the WTNA aboard the *R/V Knorr* (May-June 2010), the *R/V Melville* (September-October 2011), and the *R/V Atlantis* (July 2012). We collected sediment cores from 32 sites throughout the Demerara Slope/Abyssal Plain (Fig. 1), using a multi-corer with 9.8 cm (ID) diameter core tubes (Barnett et al., 1984) from depths of 1800-5044 m (Table 1). Immediately after recovery, cores were transferred to a temperature-controlled cold van (~2 ˚C) where the sediment-water interface (SWI) was inspected. At least two cores were selected for pore water extraction that had a visibly undisturbed SWI and clear overlying water (OLW); they were processed for pore waters as described below. An additional core from each station was sectioned in 1 cm intervals from the SWI to 5 cm, and in 2 cm intervals thereafter. An aliquot of mud from each interval was collected in a pre-weighed glass container and used to determine the porosity by weight loss after drying. Dried sediment was subsequently ground to a fine powder with an agate mortar and pestle and used for solid phase analyses.

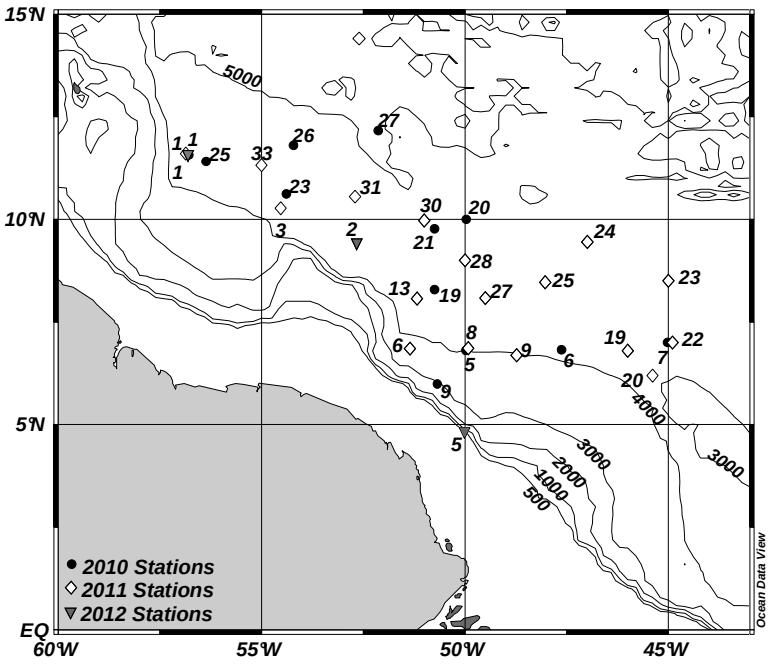

Figure 1. Map of study area. Circles represent stations from the 2010 cruise. Diamonds represent stations from the 2011 cruise. Triangles represent stations from the 2012 cruise. Depth contours are given in m. The Amazon River mouth is at 0˚N 50˚W.

Table 1. Site locations and descriptions.

Station	Latitude (˚N)	Longitude (˚W)	Water Depth (m)	BW Si (μM)	BW NO_3 (μM)
2010					
1	11.57	56.79	4373	39.4	21.3
5	6.81	49.98	3975	32.0	20.4
6	6.82	47.63	4088	34.6	22.0
7	7.00	45.02	4394	48.7	21.2
9	5.92	50.73	3014	26.6	19.0
19	8.29	50.75	4854	47.0	21.2
20	10.00	49.97	4854	59.8	21.1
21	9.77	50.75	4863	58.1	23.4
23	10.62	54.39	4486	55.1	21.2
25	11.41	56.36	4465	74.9	23.9
26	11.80	54.21	4777	57.6	24.2
27	12.16	52.13	5044	58.5	24.9
2011					
1	11.60	56.86	4362	40.4	22.7
3	10.27	54.53	4393	49.1	20.0
6	6.85	51.35	3760	35.9	19.8
8	6.86	49.92	3997	34.2	20.0
9	6.69	48.73	4030	31.7	19.3
13	8.07	51.18	4450	39.6	19.4
19	6.78	45.96	4205	48.6	20.0
20	6.19	45.43	4197	41.4	20.1
22	7.00	44.90	4435	59.8	22.9
23	8.50	45.00	4709	76.0	24.1
24	9.45	46.99	4784	55.8	22.5
25	8.47	48.03	4526	45.0	22.1
27	8.08	49.53	4415	48.0	21.8
28	9.00	50.00	4672	60.5	24.5
30	10.00	50.99	4910	69.3	25.2
31	10.55	52.70	4889	77.0	27.7
33	11.32	55.00	4650	58.9	23.7
2012					
1	11.57	56.81	4390	35.9	23.8
2	9.42	52.66	4764	65.6	20.9
5	4.82	50.01	1770	18.8	18.9

Pore Water Collection

Pore water was extracted from multi-cores in two ways. In one method, pore water was expressed at mm-scale resolution directly into 20 mL sample syringes by whole core squeezing (WCS) (Bender et al., 1987; Berelson et al., 2005) using a hydraulic jack-based apparatus described in Chong et al., (2012). Sample depths from the WCS were determined from the cumulative volume of water expressed and are dependent on having an accurate representation of the sediment porosity profile as well as the assignment of the SWI when the piston reached the sediment surface (z=0). Overall uncertainty in WCS depth assignments was ± 0.2 cm. Pore water collected by WCS was filtered through a 0.8/0.2 μm Acrodisk syringe filter directly into sample bottles for subsequent NO_3^- and Si analyses. NO_3^- samples were treated with sulfamic acid and NaOH to remove NO_2^- prior to freezing (Granger and Sigman, 2009).

Pore water was also collected at cm-scale resolution throughout the full length of each core (ranging from 25-60 cm) using Rhizon soil samplers (Rhizosphere Research Products) inserted through pre-drilled holes in the core tube. Plastic syringes with polyethylene plungers (Norm-ject) were attached to the Rhizons to draw and hold vacuum to extract pore waters. Overall sample volumes were approximately 12 mL, which were split into separate sample bottles for subsequent analysis of dissolved metals, NO_3^-, and Si.

Sample Analyses

Dissolved Si was analyzed shipboard using the acid-molybdate colorimetric method (Strickland and Parsons, 1972) with a flow-through spectrophotometer. Analytical uncertainty for Si standard replicates was < ± 6%. The cores were subject to significant warming during retrieval since they are collected from depths where *in situ* bottom water temperatures are approximately 1.5-2 ºC (WOCE Data Products Committee, 2002). Previous work has shown that there is a reversible temperature desorption effect for silicate, resulting in a 2.5% increase in the silicic acid concentration per ºC above *in situ* temperatures (McManus et al., 1995). We applied this correction to the 2010 samples assuming that the pore water temperatures warmed approximately half as much as the OLW. We base this approximation on the temperature measured in sediment cores from different stations measured by inserting a temperature probe into the center of the core after measuring the temperature of, and draining the OLW. In 2011 and 2012, a temperature probe was added to the WCS outlet, allowing for the pore water temperature to be measured directly during the extraction procedure. An average of the first three sample temperatures was used to calculate the overall correction factor. For all stations, it was assumed that the Rhizon cores warmed to the same extent as the WCS cores. The uncertainty in temperature correction may add up to a 10% increase in the uncertainty of pore water dissolved Si concentrations.

NO_3^- was analyzed on 100 µL samples using a Teledyne NO_x box with a chemiluminescence detector (Braman and Hendrix, 1989). Uncertainty in replicate samples was < ±3%.

Analyses for Mn were performed on Rhizon samples; they were analyzed on a Thermo Elemental X-Series II ICP-MS or a Leeman Labs Prodigy ICP-OES at Oregon State University. For the 2010 samples, the detection limit for Mn was ~0.01 μM for all runs, in 2011 the detection limit ranged from 0.19 – 3.6 μM over the different runs, and in 2012 the detection limit was between 0.015 - 2.0 μM for different runs. For 2010 samples above the detection limit, average uncertainties for Mn were 11% (average for all samples); in 2011, 5%; and in 2012, 0.7%.

Porosity

Porosity data were fit two ways. First, data from the upper 6 cm were fit with either equation 1 or 2, aiming to minimize the χ^2 of the fit:

$$\phi = a + be^{c*z} \quad (1)$$

$$\phi = a + bz^{c} \quad (2)$$

where ϕ is porosity, z is depth, and a, b and c are fitting parameters. Using the best fitting equation, the porosity was extrapolated back to the SWI for each station, and this SWI porosity was used in the calculation of diffusive fluxes of Si and NO_3^-. The full porosity profile for each station (to depths of 20-45 cm) was fit with Eq. (1) for use in the modeling NO_3^- profiles.

PORE WATERS MODELS

Dissolved Si

Since it has been shown that deeper pore waters are subject to squeezing artifacts (Berelson et al., 1990; Sayles et al., 1996), and the coarser resolution of Rhizon sampling does not define the curvature in dissolved Si as well as the WCS (McManus et al., 1995), only the top 1cm of WCS silica profiles was used to determine the flux across the SWI. The data was fit with either a simple polynomial:

$$C = C_0 + m_1 x + m_2 x^2 \qquad (3)$$

or an exponential solution to the diagenetic equation determined by McManus et al., (1995):

$$C = C_d - (C_d - C_0)\exp(-\beta x) \qquad (4)$$

where m_1, m_2, C_d, and ß are fitting parameters (C_d is generally the concentration as x approaches infinite depth), and C_0 is the concentration of $Si(OH)_4$ at the SWI (Fig 2). The equation yielding the best fit, determined by minimizing χ^2, was used to calculate the diffusive flux of dissolved Si across the SWI using Fick's first law applied to Eq. (3) or (4) where $J = -\phi^3 D_{sw}(dC/dx)$. The D_{sw} value used was 5.5×10^{-6} $cm^2 s^{-1}$ (McManus et al., 1995).

Nitrate

Goloway and Bender (1982) observed that deep sea nitrate (N) profiles had three characteristic profile shapes (Fig. 3): nitrification only (Type 1), nitrification

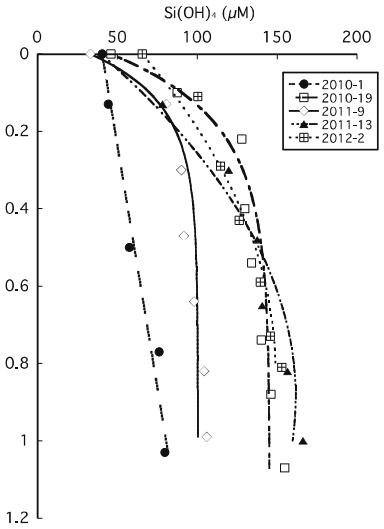

Figure 2. Best model fits of $Si(OH)_4$ using the top 1 cm of WCS data, showing stations with the highest and lowest fluxes.

overlying a zone of denitrification (Type 2), and a nitrification zone that is separated from the denitrification zone by a zone of diffusion (Type 3). They defined the nitrification zone extending to a depth $\hat{x}$, where $\partial^2 N/\partial x^2 = 0$. Our model follows their general formulation with a few exceptions and differences. We calculated the value of $\hat{x}$ by taking the second derivative of a third order polynomial fit to the data below N_{max}, thereby solving for x when the second derivative=0. As discussed below, this depth is close to the depth where measurable Mn^{2+} appears in pore waters, due to the depletion of O_2. For stations where no dissolved Mn was detected in the pore waters, $\hat{x}$ was ascribed to be equal to the depth of the deepest point in the profile, though this will yield a lower limit to the true nitrification flux. In a Type 3 profile, a zone with no net reaction lies below the zone of production, so the profile appears to be linear through this zone. A deeper zone of consumption, which begins at the depth x_m, drives this linearity. For profiles that follow this pattern, x_m was assigned after visual analysis of the NO_3^- profile. It is possible, but not necessary, for x_m to equal the depth at which NO_3^- goes to zero.

While our profile designations followed those of Goloway and Bender (1982), our model utilizes the diagenetic equation of Martin and Sayles (2006). In this formulation, we used a double exponential function to represent the oxidation of organic matter by oxygen, assuming that the C_{org} pool consists of a faster and a slower reacting component. While sedimentary organic matter likely contains a continuum of reactivities (Boudreau and Ruddick, 1991), the spatial resolution of our data precludes the inclusion of more than two depth-dependent functions (Hammond et al., 1996). Thus, following prior work (Hales et al., 1994; Hammond et

al., 1996; Martin and Sayles, 1996; Martin and Sayles, 2004; Martin and Sayles, 2006), nitrate vs. depth (x) is described such that:

$$0 = \frac{d}{dx}\left\{\phi^3 D_{sw} \frac{dN}{dx}\right\} + \phi P(x) \qquad (5)$$

where:

$$P(x) = [A]\gamma\left\{\kappa_f e^{-\alpha_f x} + \kappa_s e^{-\alpha_s x}\right\} - [1 - A]\kappa_d e^{-\alpha_d x} N \qquad (6)$$

and ϕ is the depth-dependent porosity (Eq. 1), D_{sw} is the diffusivity in seawater (cm^2/sec). P(x) is the depth-dependent reaction rate ($\mu mol/cm^3 sec$) of either nitrate production or consumption in bulk sediment. Following Martin and Sayles (2006), when $x < \hat{x}$, A=1, and $x \geq \hat{x}$, A=0, such that the first term on the right-hand side of Eq. 6 expresses nitrate production as a function of oxygen consumption. The second term in Eq. 6 expresses denitrification as an exponentially decreasing process. For production, κ_f and κ_s are the reaction rates at x=0 for oxygen consumption ($\mu mol\ O_2\ cm^{-3} sec^{-1}$) and α_f and α_s (cm^{-1}) are the depth attenuation coefficients for fast and slow reacting pools of organic carbon, respectively. For consumption, κ_d is the reaction rate at the top of the denitrification zone ($\mu mol\ N\ cm^{-3} sec^{-1}$), and α_d is the depth attenuation coefficient (cm^{-1}) for denitrification.

We assume that the reaction for oxic organic matter degradation results in the production of NO_3^- via nitrification, and that it follows the stoichiometry determined by Anderson and Sarmiento (Anderson and Sarmiento, 1994) where $C:O_2 = 120/170$. This is consistent with the ratio determined by Hammond et al., (1996) in equatorial Pacific sediments. NO_3^- production is stoichiometrically related

to the consumption of oxygen, where $C:O_2/C:N = NO_3^-/O_2 = \gamma$. Surface sediment C:N ratios were measured at USC on an Elantech 1110 Elemental Analyzer to determine the value of γ to be used in the model (Table 2).

At sites with NO_3^- consumption, we assume that denitrification is coupled to carbon oxidation such that

$$(CH_2O)_{106}(NH_3)_{16} + 94.4\ HNO_3 \rightarrow 55.2\ N_2 + 106\ CO_2 + 177.2\ H_2O \quad (7)$$

The boundary conditions in the Martin and Sayles model are structured to allow the model to handle both the Type 1 and 2 profiles, but do not address Type 3 as the few Type 2 profiles in their dataset showed very little linearity. Our data shows several profiles that could be either Type 2 or Type 3. While it is possible that all of the profiles could be fit with the Type 1 or 2 models, it is also possible that including a zone of no reaction may produce a better fit. Thus, we have rewritten Eq. (5) such that no reaction occurs between $\hat{x}$ and x_m:

$$0 = \frac{d}{dx}\{\phi^3 D_{sw}\frac{dN}{dx}\} + B\phi P(x) \quad (8)$$

when $x < \hat{x}$, B=1, $\hat{x} < x < x_m$, B=0, and for $x \geq x_m$, B=1. Eq. (8) coupled with Eq. (6) allows for nitrification to drive the reaction term above $\hat{x}$, for denitrification to be dominant below x_m, and for there to be no net reaction between $\hat{x}$ and x_m.

Prior models of deep-sea NO_3^- profiles generally assumed a constant porosity or used a single equation to describe the change in porosity with depth across multiple stations; here, we applied Eq (1) to the porosity profile for each station and

Table 2. Surface sediment C:N.

Station	Depth (cm)	C/N (molar)
2010		
20	0.5	7.52
21	2.5	6.89
26	0.5	7.23
2011		
6	0.5	6.56
8	0.5	7.36
13	0.5	7.42
25	0.5	6.86
31	0.5	5.48
2012		
2	0.5	7.2
	Average	6.95
	sample stdev	0.63
	γ	0.10
	±	0.01

incorporated it into the model, thus allowing for changes in porosity with depth specific to each station.

We generated a model fit from data obtained using two pore water extraction methods. WCS NO_3^- data was binned into 0.5 cm intervals to reduce the impact of potentially anomalous data points on the curve fit, and these data were combined with Rhizon data. While this approach merges data from separate cores, we get good agreement between WCS and Rhizon data (Fig. 3A) at depths where these two methods overlap; the WCS provides better definition of the shape of the nitrate profile curvature near the SWI, the rhizon data provide insights into the depth of the nitrate max and denitrification.

The diagenetic equation (Eq. 5 or 8) was solved in Matlab® using a differential equation solver (bvp4c), and the adjustable parameters were determined by coupling the solution to a least squares fitting algorithm (lsqcurvefit) and a global optimization solver (multistart). Parameter optimization used the trust-region-reflective (Moré and Sorensen, 1983) approach that is built into the lsqcurvefit algorithm. The model parameters are summarized in Table 3, and sensitivity tests were run to examine the relative impact of several of the fixed parameters. The high degree of freedom in the model creates the potential for multiple solutions to the differential equation. To address this issue, the multistart solver was implemented to run multiple iterations (30-50) of the model using a range of randomly generated starting points for the adjustable parameters. Upon completion, the solution with the best fit, the 'global' solution to Eq. (5) or (8), was

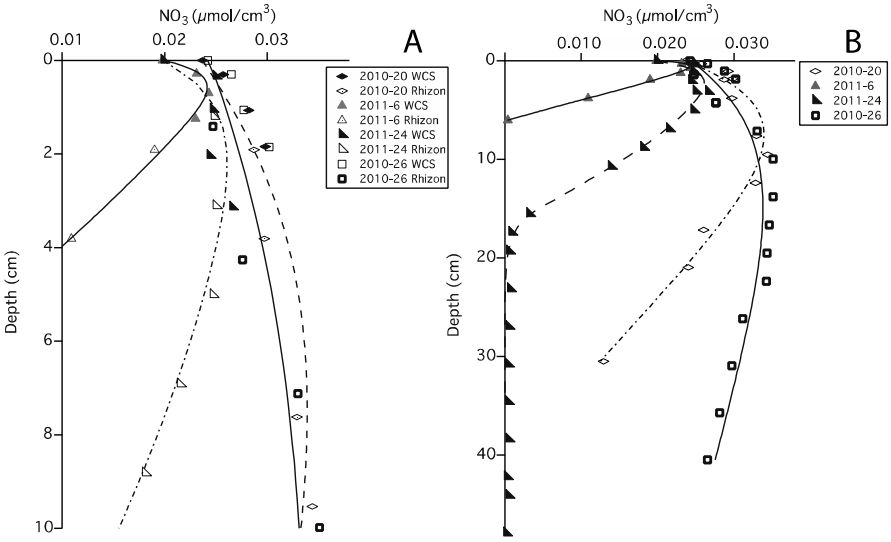

Figure 3. Examples of NO_3- model fit to data showing solutions to Type 1 (2010-27), Type 2 (2011-6, 2011-24), and Type 3 (2010-20). A) The upper 10 cm of the pore water profiles. Filled symbols indicate WCS data, open symbols indicate Rhizon data. B) The full pore water profiles.

Table 3. Descriptions of parameters used in the NO_3^- model and how they were determined. S/A indicates whether the parameter is static or adjustable in the model.

Parameter	Units	S/A	Determination	Description	Comments
$\hat{x}$	cm	S	calculated	boundary between NO_3^- production and consumption	Second derivative of a third order polynomial fit to the data below the $[NO_3^-]$ max
N_0	μmol cm^{-3}	S	measured	OLW $[NO_3^-]$	From Multi-core OLW
γ		S	ascribed	$[NO_3^-]/[O_2]$	Assumed a constant C/O_2 of 0.71 divided by the average measured C/N
D_{sw}	μmol cm^{-2} sec^{-1}	S	ascribed	diffusivity of NO_3^- in seawater	Value from Hammond et al., (1996)
f		A	measured	porosity	f modeled as exponential fit to data (Eq. 1)
f_0		S	calculated	porosity at the SWI	Extrapolation of Eqs. (1) and (2) to the SWI
x_m	cm	S	ascribed	boundary below the zone of no reaction	Value chosen by visual analysis of pore water profile
k_f	μmol cm^{-3}	A	model determined	reaction rate constant for nitrification of 'fast' reacting carbon	Solved by model given an initial guess
a_f	cm^{-1}	A	model determined	attenuation coefficient for nitrification of 'fast' reacting carbon	Solved by model given an initial guess
k_s	μmol cm^{-3}	A	model determined	reaction rate constant for nitrification of 'slow' reacting carbon	Solved by model given an initial guess
a_s	cm^{-1}	A	model determined	attenuation coefficient for nitrification of 'slow' reacting carbon	Solved by model given an initial guess
k_d	μmol cm^{-3}	A	model determined	reaction rate constant for denitrification	Solved by model given an initial guess
a_d	cm^{-1}	A	model determined	attenuation coefficient for denitrification	Solved by model given an initial guess

identified as having the lowest objective function value (fval) by the lsqcurvefit solver and the fitting parameters from the best solution were used to generate a model profile of $[NO_3]^-$ (Fig. 3). All of the stations resembling Type 2 or Type 3 profiles were run through both the 2- and 3-layer models, and the reported results exhibited the lowest reduced χ^2 value.

Nitrate production (R_n) and consumption (R_d) were converted to fluxes by integrating the reaction rate (Eq. 6) over the depth ranges of x=0 → $\hat{x}$ and x=$\hat{x}$ → x_{max}, respectively. To check the model flux accuracy, nitrification and denitrification fluxes were also calculated from model profile gradients at the SWI and at $\hat{x}$ using Fick's first law ($J = \phi_0^3 D_{sw}\, dN/dx$). Agreement between model integration and diffusive gradient fluxes were within ± 25%. The carbon oxidation fluxes in the production zone (C_n) were calculated by multiplying the R_n flux by the average C:N ratio of organic matter (Table 2), and in the consumption zone, we used a CO_2 production:nitrate consumption ratio of 1.12 (Eq. 7) to calculate the carbon oxidation flux (C_d) from R_d. The total amount of organic carbon oxidized through NO_3^- production and consumption (C_{tot}) is the sum of C_n and C_d.

RESULTS

Porosity and solid phase analyses

Porosity profiles generally showed a steady decline with depth. The porosity at the SWI ranged from 0.90 - 0.97 (Table 4) and declined to values less than 0.75.

Table 4. Summary of flux results.

Station	SWI □	Si Flux (mmol/m²d)	x̂ (cm)	x_m (cm)	Mn Appear (cm)	C_n (mmol/m²d)	C_{tot} (mmol/m²d)	Red-χ^2
2010 (May-June)								
1	0.91	0.14	23.0	-	> 23	0.17 (0.46)	0.18 (0.47)	5.5
5	0.94	0.67	12.4	15.0	10	0.53	0.53	9.7
6	0.93	0.18	10.9	13.0	14	0.32	0.35	16
7	0.92	0.19	27.1	-	28	0.40 (1.21)	0.40 (1.21)	1.6
9	0.95	0.89	12.2	-	10	1.13	1.13	32
19	0.90	1.35	6.8	-	7	0.43 (1.16)	0.45 (1.18)	3.7
20	0.93	0.28	37.0	-	37	0.41	0.41	72
21	0.94	0.34	14.9	-	18	0.45	0.47	175
23	0.91	0.45	19.0	-	19	0.61	0.61	7.1
25	0.95	0.30	38.0	-	> 38	0.23	0.23	27
26	0.92	0.26	45.0	-	> 45	0.16	0.16	106
27	0.92	0.27	49.0	-	> 49	0.16	0.16	46
2011 (Sept-Oct)								
1	0.93	0.48	30.0	-	> 30	0.29	0.29	3.8
3	0.95	0.94	18.4	22.0	15	0.62	0.64	15
6	0.93	0.95	3.9	-	5	1.38	1.38	23
8	0.94	0.49	7.4	-	8	0.56	0.59	38
9	0.91	0.56	7.9	-	8	0.43	0.47	6.0
13	0.91	0.99	7.9	-	8	0.72	0.75	64
19	0.92	0.34	22.4	27.5	30	0.17 (0.84)	0.21 (0.85)	6.9
20	0.91	0.40	28.0	-	> 28	0.23	0.23	24
22	0.92	0.23	25.0	35.0	38	0.46	0.46	4.1
23	0.94	0.36	24.4	31.0	35	0.32	0.32	28
24	0.92	0.25	11.0	15.0	14	0.63	0.65	13
25	0.91	0.51	14.6	18.0	20	0.32	0.34	55
27	0.92	0.55	11.2	-	10	0.50	0.53	25
28	0.98	0.35	7.9	10.0	10	0.31	0.33	2.2
30	0.92	0.26	15.2	-	16	0.52	0.54	7.7
31	0.96	0.36	24.8	33.0	29	0.39	0.39	1.3
33	0.90	0.32	34.1	37.0	36	0.44	0.44	8.5
2012 (July)								
1	0.93	0.29	34.0	-	> 34	0.21	0.22	38
2	0.93	0.71	7.8	-	8	0.99 (1.92)	1.04 (1.96)	7.5
5	0.94	0.76	3.0	-	4	1.86	1.92	2.0

Parameters generated from the porosity fitting equations are listed in Appendix A.

The average surface sediment C:N ratio from 9 stations throughout the study region was 6.9 ± 0.6 (Table 2). This value, combined with the Anderson and Sarmiento (1994) C:O_2 ratio, yielded a γ of 0.10 (Eq. 6).

Pore water Si profiles and fluxes

Bottom water Si values (measured from core OLW) ranged from 24 – 77 μM, reflecting a steep gradient in deep water $Si(OH)_4$ in this region (WOCE Data Products Committee, 2002). Pore water profiles showed an increase in concentration with depth below the SWI, with most profiles reaching an asymptotic maximum value. A few profiles decrease after reaching a maximum (Fig. 4D-F), and these are discussed further in Chapter 4. The dissolved Si maximum ranged from ~150 μM at station 2010-7, one of the easternmost stations, to 400 μM at station 2012-5, both the shallowest coring site and closest to the Amazon River mouth.

Data from the top 1 cm of the WCS were used to calculate the diffusive flux of $Si(OH)_4$ across the SWI (Fig. 2). Dissolved Si fluxes ranged from 0.14 – 1.35 mmol m^{-2} d^{-1} (Table 3). The highest flux was observed at station 2010-19 (1.35 mmol $m^{-2}d^{-1}$), and the lowest fluxes (0.14 – 0.3 mmol $m^{-2}d^{-1}$) were observed throughout the northern and eastern edges of the study region.

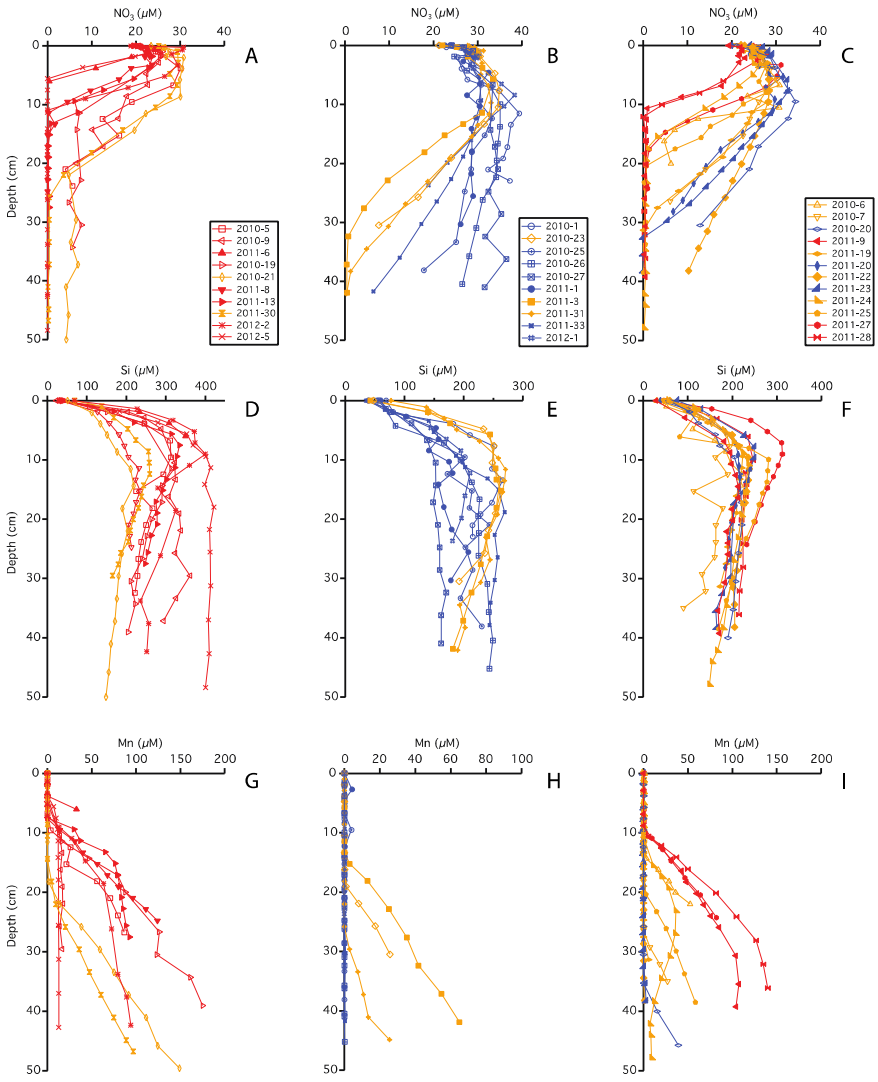

Figure 4. Pore water profiles of NO_3-, $Si(OH)_4$, and dissolved Mn. Profile color indicates Mn appearance depth: <10 cm (red), 10 – 30 cm (orange), >30 cm (blue). The left column represents all stations from zone A, center column from zone B, and right column from zone C (see Discussion)

Pore water Mn and NO_3^- profiles

Dissolved Mn was detectable in the pore waters at 25 of the 32 stations in the study region (Table 4). The 'Mn appearance depth' is the approximate depth where Mn was measured to be over the detection limit for that at two consecutive depths. This depth ranged from as shallow as 4 cm (2011-6) to deeper than 50 cm (Fig. 4G-I). The Mn appearance depth is also the approximate depth where oxygen is depleted from the pore waters (Froelich et al., 1979), and should be approximately equal to the value of $\hat{x}$. The steepest gradients in Mn with depth are at sites where Mn appears at shallow depths in the core.

OLW nitrate values ranged between 19.8 – 25.2 μM, which are similar to values reported by WOCE for sites at comparable depths (WOCE Data Products Committee, 2002). Pore water NO_3^- profiles all showed an increase with depth below the SWI followed by a decrease below a NO_3^- maximum at all but a few stations (Fig. 4A-C). Stations in the northern portion of the study area (2010-1, 2011-1, 2012-1, and 2010-27) display the most clearly defined Type 1 profiles, while all of the others were either Type 2 or Type 3.

Decompression and warming can create artifacts in surficial pore water NO_3^- concentrations due to the oxidation of ammonium released from the bursting of cells containing NO_3^--rich vacuoles near the SWI (Berelson et al., 1990; Cai et al., 1995), however, the agreement between the OLW NO_3^- concentration and near-interface WCS data indicates that this artifact may not have a significant influence on these profiles.

NO_3^- model results

Nitrification and denitrification together contribute to the total organic carbon oxidized fluxes (Table 4, Fig. 5A). The highest carbon oxidation fluxes in the region are closest to the shelf edge and closest to the Amazon River mouth (near 5°N 50°W), with a sharp gradient further to the north and east. The largest benthic flux was 1.92 mmol C $m^{-2}d^{-1}$ at station 2012-5. To the north (12-13°N), the flux decreased to ~ 0.23 mmol $m^{-2}d^{-1}$ at station 1, and 0.16 mmol $m^{-2}d^{-1}$ at station 2010-27. As far east as 45°W, the flux ranged from 0.46 mmol $m^{-2}d^{-1}$ at station 2011-22 and 0.32 mmol $m^{-2}d^{-1}$ at station 2011-23.

The reduced χ^2 value helps define the quality of model fit to the observed data (Hammond et al., 1996). However, for five stations (2010-1, 2010-7, 2010-19, 2011-19 2012-2), the calculated fluxes were deemed to be 'suspect' even with a low reduced χ^2 value. At these stations, it appeared that even after binning, the WCS data caused the model fit to be overly steep in the nitrification zone, resulting in an artificially high flux. Removing the WCS data from the model fits yielded a lower flux (2-3x), while removing WCS data from other stations produced very little change in the results. When the WCS data was excluded, the stations in question had fluxes that were in much better agreement with their geographic counterparts, as well as with sites that had similar Mn appearance depths. As a result of this analysis, we believe that these five stations are best represented by flux values that do not use

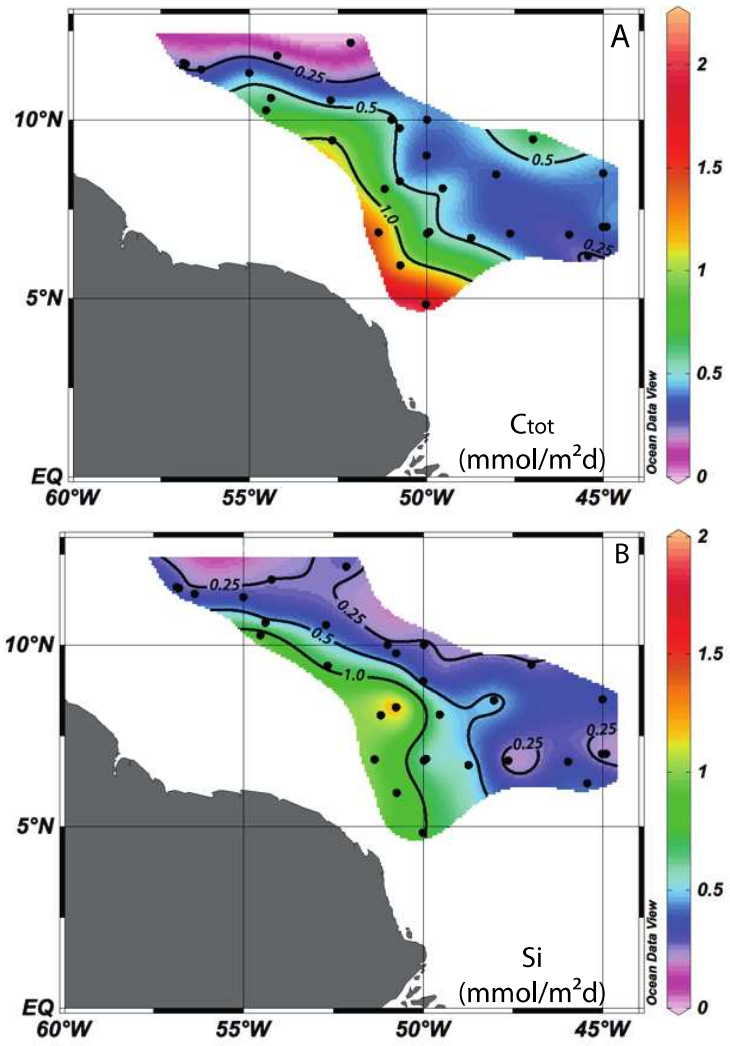

Figure 5. Benthic flux model results in map view. Units are in mmol m^{-2} d^{-1}
A) Benthic carbon oxidation fluxes. B) Benthic $Si(OH)_4$ fluxes.

the WCS data in the model, however, the value of the flux when the data are included are included in Table 4.

We also compared the multi-G model used here to a single-G model, and determined that in nearly every case, the multi-G model produced a better fit to the data as shown by the reduced χ^2 value. The results from this test are available in Appendix A.

Discussion

Model Reproducibility and Uncertainties

Over the three years of sample collection, it is possible that variability in the amount of sedimentary disturbance (bioturbation) or carbon rain might affect our flux results. Seasonal variability in the delivery of organic matter from the surface ocean to the sea floor can occur over short time scales (weeks to months), likely a reflection of changes in surface primary production (Deuser and Ross, 1980; Deuser et al., 1981; Deuser, 1986). However, while benthic oxygen consumption has been shown to vary seasonally by a factor of 2-3 times in the deep Pacific and north Atlantic (Smith and Baldwin, 1984; Pfannkuche, 1993), little change in the benthic response to changing POC flux was observed in the western Atlantic at BATS (Sayles et al., 1994). In our dataset, three sets of stations were repeats, allowing us to examine the potential temporal variability. The cores: 2010-1, 2011-1, and 2012-1 were all from the same coordinates, as were 2010-5 and 2011-8, and also 2010-7

and 2011-22. The standard deviation of the average dissolved Si flux from these sets was 55%, 22%, and 14% respectively. For the NO_3^- model fluxes, the spread in C_{tot} was 24%, 7%, and 10%. The agreement in flux estimates between these repeat stations indicates that the sediment reactivity remained relatively constant over the three years of sample collection despite collection during different seasons. At 5 sites, we also analyzed more than two cores from a single multi-corer deployment and on these replicates we found the sample standard deviation for fluxes of Si was 22% and for NO_3^- was 5%. This points to a meter-scale consistency in benthic conditions, indicates that the application of the steady state assumption is appropriate, and gives us confidence that our sample collection procedure was reproducibly consistent.

Model sensitivity analysis was performed to better understand the influence that input parameters have on the flux results, as well as on the quality of the model fit to the data (Table 3). The values of D_{sw}, N_0, and $\hat{x}$ were changed one at a time by ± 5%, and the value of γ was changed by ± 50%. These values reflect the uncertainty in the value, measurement, or depth assignment in the case of D_{sw}, N_0, and $\hat{x}$. The range of γ reflects the influence of the very wide range of C:N observed in floating surface traps from this region (Chapter 3) and from deep traps moored in the same region (Honjo, 1980). This sensitivity analysis was run on five stations that are representative of a wide range of carbon oxidation rates (2010-27, 2011-3, 2011-6, 2011-20, 2011-24). The effect of each variable was assessed by calculating the amount of change observed in the flux relative to the baseline (Figure 6), where the

baseline is the flux determined from the original values chosen for these static parameters (Table 3).

Both the integrated nitrification rates and the total carbon fluxes were found to be most sensitive to large changes in γ. As expected, a change in γ greatly affects the carbon flux because it changes the C:N ratio used in the stoichiometric calculation of C_{tot} from R_n. Thus, having good constraints on the C:N ratio is important for model accuracy. We used values of C:N measured from the uppermost surface sediments to define the best value for γ, and these measurements show that the actual uncertainty in γ is ± 10% (Table 2). It is possible that the measured values are representative of the more refractory component of organic matter rather than that which is rapidly degraded; however, relatively high concentrations (0.63-0.96 μg Chl-a g-sediment^{-1}) of chlorophyll-a were measured in the surface sediments, indicating that labile carbon was still present (Appendix A). Uncertainty in γ is likely the largest contributor to uncertainty in our model flux estimates and we believe that this contributes 10-30% uncertainty to the overall estimate of C_{tot}.

The value of N_0 also has the potential to significantly change the estimated fluxes, as it is highly influential in dictating the slope of the concentration gradient below the SWI. This influence is evident in the test results as lowering this parameter by 5% resulted in a ~50% difference in the carbon flux while an increase resulted in a ~30% change (Figure 6). We constrained N_0 by taking an average OLW value from both the Rhizon and WCS cores (~3 samples), and found that our measurements agreed well with WOCE data for nearby stations at the same depth

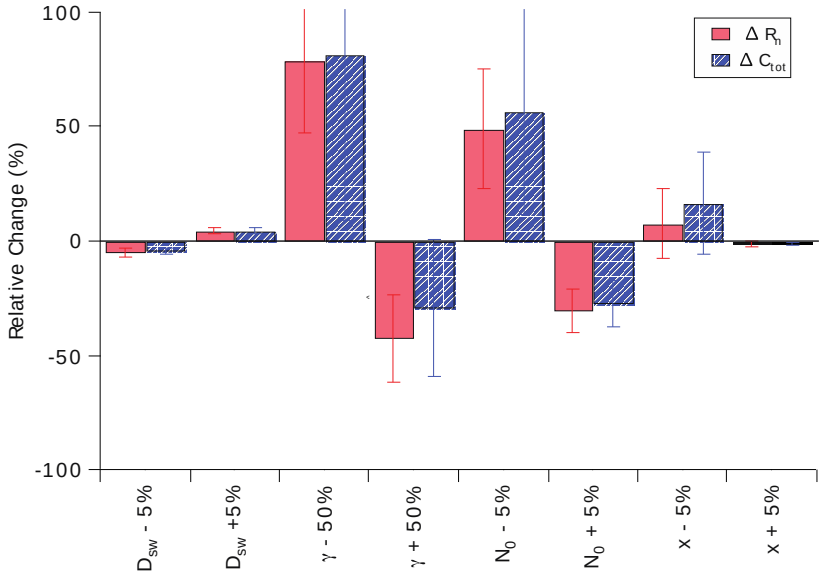

Figure 6. Results from sensitivity analyses of the static parameters in the NO□ model. The relative % change was chosen as described in Methods.

(WOCE Data Products Committee, 2002). We believe the overall uncertainty in fluxes resulting from uncertainty in N_0 is <30%.

The values of $\hat{x}$ and D_{sw} have a minor effect on the flux results. Martin and Sayles (2006) identified $\hat{x}$ as the depth of oxygen disappearance from the pore waters. We chose to use the inflection point in the NO_3^- profile where production changes to consumption. The appropriateness of this strategy was confirmed by the good agreement between the values of $\hat{x}$ (or x_m in the case of Type 3 profiles) and the depth at which Mn appears in the pore waters (generally agreed to ± 5 cm; Fig. 7). At seven stations, Mn did not appear in the pore waters, but the NO_3^- profile showed signs of NO_3^- consumption. At these stations, $\hat{x}$ was assigned to be equal to the depth of the last data point, and thus fluxes at these sites (2010-1, 2010-25, 2010-26, 2010-27, 2011-1, 2011-20, 2012-1) may carry greater uncertainty than the rest. We chose to use a value for nitrate diffusivity (1.05×10^{-5} cm^2 sec^{-1}) based on previous studies (Martin and Sayles, 1996), and found a 5% change in D_{sw} produced a change of ~5% in both the carbon flux and the integrated nitrification rate. These results agree with Martin et al (1991), who reported that using a constant value for D_{sw} results in an uncertainty in the nitrogen flux of 3-14%.

Since the uncertainties in the static parameters are linked, we have followed the procedure of Hammond et al., (1996) where the fractional flux uncertainty is equal to the largest fractional uncertainty in the fitting parameters. We acknowledge that other uncertainties (i.e. porosity) may influence the overall uncertainty in flux in addition to these parameters discussed. Given the constraints and uncertainties

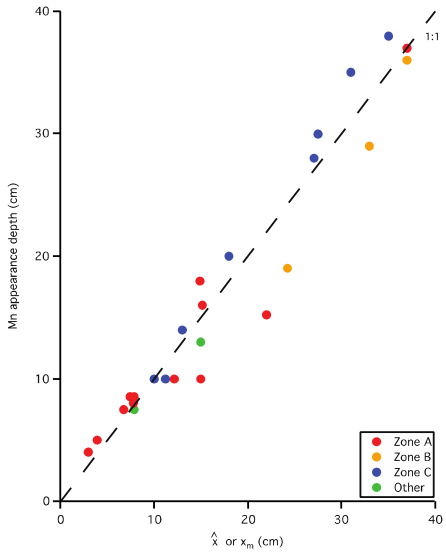

Figure 7. Mn appearance depth vs. $\hat{x}$ or x_m. Excludes stations where Mn did not appear in the pore waters.

associated with the input parameters, and potential additional uncertainties, we believe the fluxes generated from the NO_3^- model to be accurate to < ± 40%.

Spatial patterns of benthic fluxes

The benthic carbon oxidation fluxes form a pattern in the shape of a 'tongue' extending to the northwest (Fig. 5A, Fig. 8), generally following the trajectory of the average position of the spring plume. The sediments reveal very steep flux gradients over a much narrower area than the freshwater plume. The flux attenuation across this feature is striking, decreasing to the east by 1.5 mmol $m^{-2}d^{-1}$ (nearly a factor of 10) and by a similar magnitude to the N and NW between 11-13°N. Off the axis of the high flux 'tongue', fluxes are fairly low and are generally consistent with values from the equatorial and low latitude central Pacific (Hammond et al., 1996).

Benthic $Si(OH)_4$ fluxes follow a similar pattern to the carbon fluxes, but cover a slightly larger longitudinal space and the tongue also extends further to the northwest (Fig. 5B). Biogenic silica deposition appears to also follow the trajectory of the spring plume, but shows some influence of the fall retroflection as well (Fig. 8). The highest dissolved Si fluxes, unlike carbon fluxes, do not appear closest to the river mouth, but further north. These differences suggest that the deposition of C_{org} and bSi is somewhat decoupled, and perhaps indicating that biogenic Si ballast is not the only factor responsible for the deposition of organic carbon.

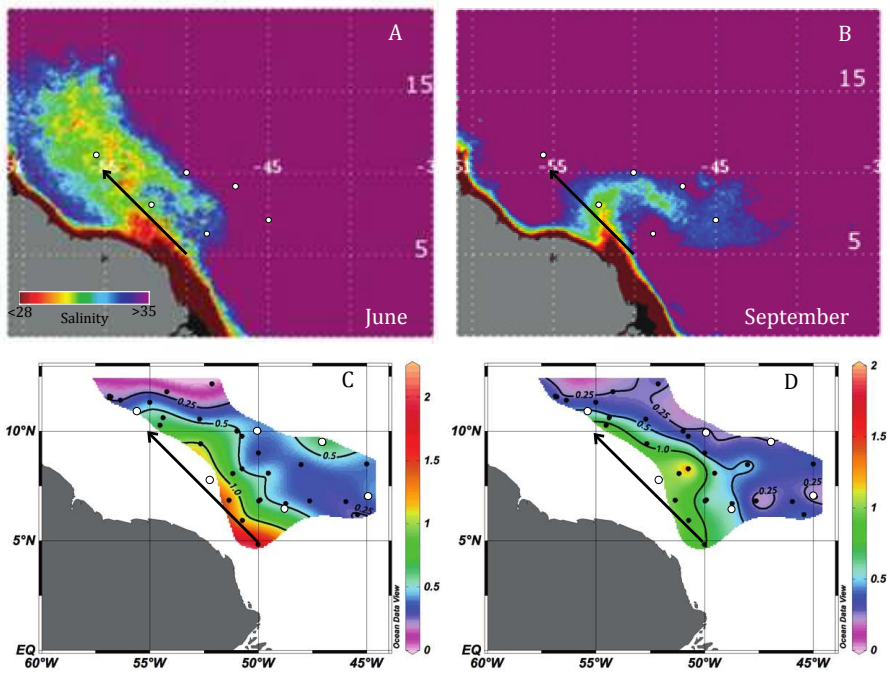

Figure 8. Model results compared to sea surface salinity (A. Subramaniam). The black arrow indicates the approximate trajectory of the spring plume, and the white circles provide reference points of comparison. A) 10-year average SSS from the month of June, when the spring plume is fully developed. B) 10-year average SSS from September showing the full extent of the NBC retroflection. C) Map of benthic carbon fluxes with reference points. D) Map of benthic Si fluxes with reference points.

It has been shown that the majority (>90%) of organic carbon reaching the sea floor in the deep ocean is remineralized (Bender and Heggie, 1984; Burdige, 2007; Canfield, 1994; Hedges and Keil, 1995; Premuzic et al., 1982). To verify this, we assumed an average sedimentation rate of 3 cm kyr^{-1} (Damuth, 1977), took an average porosity for each station, and used the wt% C_{org} from the C:N measurments to estimate a burial flux. The average burial flux comprised 9% of the total C_{org} rain arriving at the sea floor. Thus, we can assume that the remineralization fluxes of C_{tot} are nearly equivalent to the deposition fluxes of C_{org}, though they are clearly a lower estimate.

Using a ten-year, monthly average salinity of the plume generated from satellite data (A. Subramanian, unpublished K490 data following Del Vecchio and Subramaniam (2004)), we examined how closely the surface freshwater plume is reflected on the deep sea floor pattern of C_{org} remineralization. Focusing on the months that exhibit the full extension of the northwest plume and the retroflection period (June and September), we observed a distinct similarity between the pattern and axis of benthic carbon fluxes, and the trajectory of the spring plume (Figure 8A,C). Stations with the highest carbon fluxes are located closest to the continental shelf and to the river mouth. The concentration 'contours' in the pattern of benthic carbon fluxes appear to mirror the salinity gradient of the northwest plume suggesting highest export of C_{org} in the lower salinity waters.

There is very little signal in benthic carbon deposition related to the eastward extension of the Amazon plume (Fig. 8B,C) with the exception of one,

isolated hotspot of carbon flux. It is unlikely that we missed the pattern of the seasonal fall retroflection because coring covered the areal extent of the average retroflection plume position. Another possibility is that the retroflection has much greater spatial variability than the spring plume. Annual changes in the surface plume over several hundred years would reduce the intensity of the sediment signal. It is also possible that flow and chemical conditions in plume waters during the retroflection are not conducive to C_{org} production and export, however we note that the plume is only in the retroflection position a few months per year, while at least some part of the plume travels to the NW all year-round. The flux patterns suggest the influence of the retroflection impacts bSi more than C_{org} export.

From satellite images (Fig. 8A-B) we defined three distinct zones (Fig. 9): a zone where the plume is present both in the spring and fall (zone A), a zone that contains only the spring plume waters (zone B), and a zone influenced only by the fall retroflection (zone C). Three stations (2010-27, 2011-9, 2011-24) fall in regions deemed to be 'uninfluenced' by any plume water based on the overall 10-year average climatology. Dividing the region into zones helps in the budget and spatial summary presented below.

To better examine the relationship between the deposition of organic carbon and biogenic silica throughout this region, benthic fluxes were plotted against each other (Fig. 10). The majority of stations fall into a broad cloud relatively centered around a 1:1 flux ratio when the fluxes are < 0.8 mmol m^{-2} d^{-1}. All of the zone C stations fall into this category, as do the majority of the zone B stations. Stations in

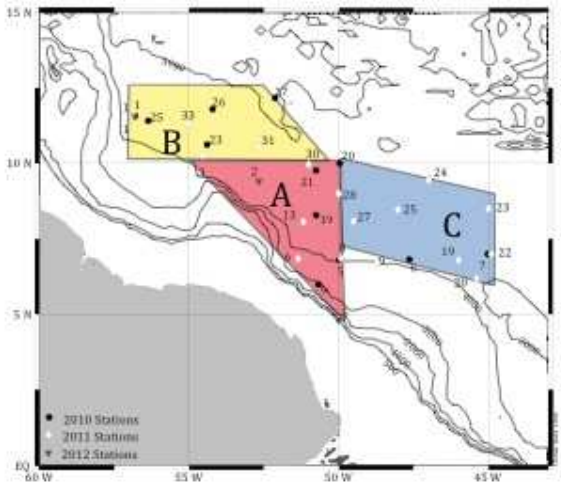

Figure 9. Division of the study area into three zones. Zone A reflects the area of overlap between the NW plume and retroflection. Zone B shows stations influenced by the NW spring plume only, and Zone C reflects the area covered by the retroflection only.

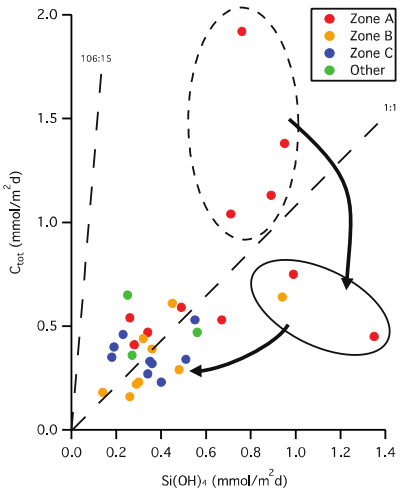

Figure 10. Carbon fluxes vs dissolved Si fluxes. Units are in mmol m-2 d-1. The dashed line surrounds stations 2012-5, 2011-6, and 2010-9. The solid circle surrounds stations 2011-13, 2010-19, and 2011-3. The arrows depict the direction of dispersion of plume waters from the core axis of the plume (the dashed line) outwards.

zones A and B have somewhat higher C_{tot} and $Si(OH)_4$ fluxes than zone C, but there is not a consistent difference between zones B and C with respect to biogenic material deposition. The six stations with a highest fluxes reveal an interesting pattern: stations with high-C/med-Si fluxes are the four stations directly in line with the plume axis, and the stations with high-Si/lower-C are the next closest. It appears that water exiting the river first fuels an area of high carbon deposition, followed by high silica deposition, and then modest amounts of C_{org} and bSi. This pattern is confirmed through latitudinal and longitudinal comparison of C_{tot} and $Si(OH)_4$ fluxes (Fig. 11). The fluxes are generally uniform throughout the entire area decreasing away from the axis of the NW plume. Stations with highest C_{org} and bSi deposition occur at different latitudes. The zone of highest carbon deposition does not exactly coincide with the zone of highest bSi deposition, demonstrating our point that the processes responsible for C_{org} and bSi export are somewhat decoupled from one another.

It is possible that this pattern of fluxes is simply an effect of water depth, so we compared C_{tot} and $Si(OH)_4$ vs. water depth. For C_{tot}, three stations, 2012-5, 2010-9, and 2011-6 show a trend of increasing fluxes with decreasing depth, but the rest of the Zone A stations, as well as all of the other stations, show no correlation to water depth. $Si(OH)_4$ shows no correlation with water depth in any zone. Thus, water depth is unlikely to have a significant influence on our observations of latitudinal and longitudinal patterns.

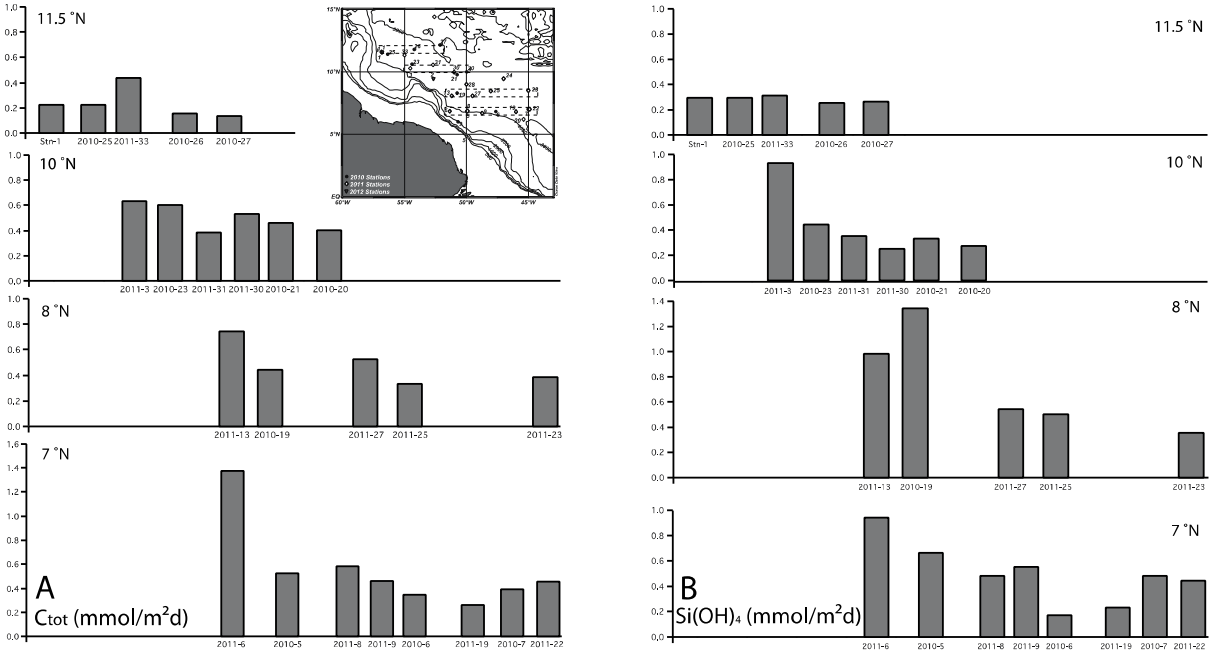

Figure 11. Latitudinal transects of benthic fluxes. Units are in mmol m^{-2} d^{-1}. Bar location on the x-axis reflects relative longitude. A) C_{tot} fluxes. B) $Si(OH)_4$ fluxes.

To quantify the total amount of C_{org} reaching the sea floor in this region, we averaged the fluxes of the stations contained within each of the three zones, where each covers an area of ~ 150,000 km^2. The average benthic carbon oxidation flux was 0.85, 0.35, and 0.37 mmol m^{-2} d^{-1} in zones A, B, C respectively, confirming that the highest flux is closest to the most proximal portion of the river plume axis and that zones B and C are virtually identical in terms of flux. This pattern is somewhat unexpected given that for the most of the year, water flows northwest to zone B while zone C only sees the influence of the plume for a few months each fall. Integrating over the area of each zone results in oxidized C_{org} fluxes of 0.047, 0.019, and 0.020 Tmol C y^{-1}, and thus there is 0.087 Tmol C y^{-1} oxidized throughout the area covered by the three zones (450,000 km^2).

We further extrapolated to the total area of the deep sea that is influenced by the plume by estimating the total coverage of the fully developed plume and retroflection where the water depth is >3000 m using the average salinity data from Fig. 8, expanding zones B and C and including the three stations that fell outside of the zone boundaries. Thus, given an area of ~900,000 km^2 influenced by the Amazon River Plume, ~0.15 Tmol C y^{-1} has been reaching the deep sea floor. For this same region, Subramanian et al., (2008) estimate C export of 2.3 Tmol C y^{-1} from the surface ocean at 150 m. This result suggests that ~7% of organic carbon export reaches the deep ocean; in comparison, a Martin Function parameterization predicts ~5%. Little of this C is expected to be of terrestrial origin since it has been shown

that minimal terrestrial POC reaches the open ocean (Aller and Blair, 2006; Druffel, 2005). Our sediment C:N data also indicates that the C_{org} reaching the deep sea is likely of marine origin.

Regional and global comparisons

Martin and Sayles (2006) used a model of pore water NO_3^- profiles to estimate the benthic carbon fluxes from a wide range of deep-sea sediments throughout the global ocean (Table 5). In particular, they analyzed many profiles from the Ceara Rise, just southeast of our study area, resulting in fluxes ranging from 0.17 – 0.51 mmol C m^{-2} d^{-1}. These values are in good agreement with the fluxes we calculated for nearby stations. Wenzhöfer and Glud (2002) presented an extensive synthesis of rates of benthic dissolved oxygen uptake (DOU) from both sides of the Atlantic basin between 35 ºN and 50 ºS. We took the *in situ* measurements from their dataset, extracted all stations from depths > 3000m, and used the Anderson and Sarmiento C:O_2 to derive carbon oxidation fluxes. In the WTNA, their results yielded fluxes ranging from 0.21 – 0.63 mmol m^{-2} d^{-1}. While the majority of their stations were also from the Ceara rise, one station fell directly within our study region between stations 2011-3 and 2012-2 and had a flux of 0.51 mmol m^{-2} d^{-1}, consistent with our results (0.64 and 1.04 mmol m^{-2} d^{-1}, respectively).

Across the Atlantic basin, stations at comparable latitudes yielded a similar range of fluxes (Table 5): 0.14 – 0.61 mmol m^{-2} d^{-1} at Sierra Leone Rise, and 0.56 –

Table 5. Comparison of benthic carbon fluxes from around the glove. The number in parenthesis indicates the number of stations from each site.

Study Region	**Latitude**	**Longitude**	**C_{tot} Range** (mmol $m^{-2}d^{-1}$)
ANACONDAS (this study)	4-12˚N	45-57 ˚W	0.16-1.92 (32)
BATS[d]	31˚N	64 ˚W	0.16-0.24 (9)
Western Tropical North Atlantic[a]	4-9˚N	42-54 ˚W	0.21-0.63 (11)
Ceara Rise[c]	5-6˚N	42-44 ˚W	0.17-0.51 (11)
Southwest Atlantic[a]	35-37˚S	47-52 ˚W	0.54-1.02 (3)
Cape Verde Plateau[c]	12-18˚N	21-23 ˚W	0.30-1.10 (11)
Eastern Tropical North Atlantic[a]	8-19˚N	17-21 ˚W	0.56-1.8 (2)
Sierra Leone Rise[c]	5-10˚N	21-24 ˚W	0.14-0.61 (11)
Eastern Equatorial North Atlantic[a]	1˚N-6˚S	3-10 ˚E	1.20-2.54 (2)
Southeast Atlantic[a]	28-29˚S	8-13 ˚E	0.35-2.22 (3)
Equatorial Pacific[b]	9˚N-12˚S	140 ˚W	0.10-0.55 (16)
Equatorial Pacific[c]	11˚N-6˚S	132-137 ˚W	0.19-1.00 (18)
South Pacific Gyre[e]	24-46˚S	117-165 ˚W	0.09-1.03 (11)
Southern Ocean Pacific Sector[c]	56-66˚S	169-170 ˚W	0.08-1.36 (12)

[a] Wenzhöfer and Glud (2002) and references therin

[b] Hammond et al., (1996)

[c] Martin and Sayles (2006) and references therin

[d] Sayles et al (1994)

[e] Fischer et al (2009)

1.80 mmol m^{-2} d^{-1} in the Eastern Tropical North Atlantic (Martin and Sayles 2006 and references therein; Wenzhöfer and Glud 2002 and references therein). Eastern margins of ocean basins generally have higher productivity than western margins, thus the similarity between benthic fluxes across the Atlantic, at comparable latitudes, indicates that the Amazon Plume is likely responsible for enhancing the overall productivity of the WTNA. Carbon oxidation fluxes from this study are comparable to many other deep-sea sites throughout the global ocean, including the Cape Verde Plateau, the Sierra Leone Rise, the South Pacific Gyre, and the Southern Ocean, but are higher than fluxes observed at BATS (Table 5).

The reactivity of organic matter

Following other diagenetic models, our nitrate model assumes that the degrading pool of organic material in the sediments contains a faster and a slower reacting component (Hammond et al., 1996; Martin and Bender, 1988; Martin and Sayles, 1996; Martin and Sayles, 2004; Martin and Sayles, 2006). A best-fit model solution yields the values of oxygen consumption rate (κ) of the 'fast' and 'slow' components that decline exponentially with depth as dictated by the attenuation coefficients (α, Eq. 5). The value of $\kappa\alpha^{-1}$, adjusted by $C:O_2$ (Anderson and Sarmiento, 1994), is another measure of carbon oxidation fluxes partitioned into fast and slow components, J_f and J_s (values provided in Appendix A).

The use of a fast and slow pool of C_{org} to generate oxygen consumption results in a strong control on C_{tot} by the fast reacting pool. In the equatorial Pacific, Hammond et al., (1996) found that 70-90% of the total C_{org} flux was driven by the

'fast' reacting pool. A plot of J_f/C_{tot} for the ANACONDAS region shows how much of the C flux is attributable to the faster reacting C (Fig. 12). The fast component appears to dominate the total carbon flux throughout most of the region, and in the region of highest C_{org} deposition, the fast reacting fraction consistently constitutes >90% of the flux. However, in the region of the study area following the pattern of the retroflection, there is an area where the fast component only comprises 40-50% of the flux. This result indicates that there is a large zone underlying the retroflection plume that receives less reactive organic material than the rest of the area. One explanation of this pattern is that reactive carbon is sinking more quickly within Zone A due to the abundance of lithogenic ballast from the river. As the plume loses its influence on ocean productivity, less reactive and possibly terrestrial C_{org} constitutes a larger fraction of the export. Farthest from plume influence, marine-derived organic matter dominates and this generates the moderately high fraction of 'fast' reactive C, 60-80%, at the northern and eastern edges of the study area.

Martin and Sayles (2006) utilized a similar nitrate model to examine pore water profiles from the Ceara Rise and also determined κ_f, from which we calculated J_f (Supplemental Table ST-2). The Ceara Rise sites closest to our study sites were at ~45°W and 5°N at depths between 3200-4700 m and had an average J_f of 0.25 ± 0.15 mmol C m^{-2} d^{-1}, comprising 72 ± 12% (SE of the mean) of the total C flux. Thus, the Ceara Rise, which currently receives very little influence from the Amazon Plume, has approximately the same proportion of reactive carbon as Zone B and Zone C (72 ± 11% and 68 ± 8.7%, respectively). Sites within Zone A have a higher

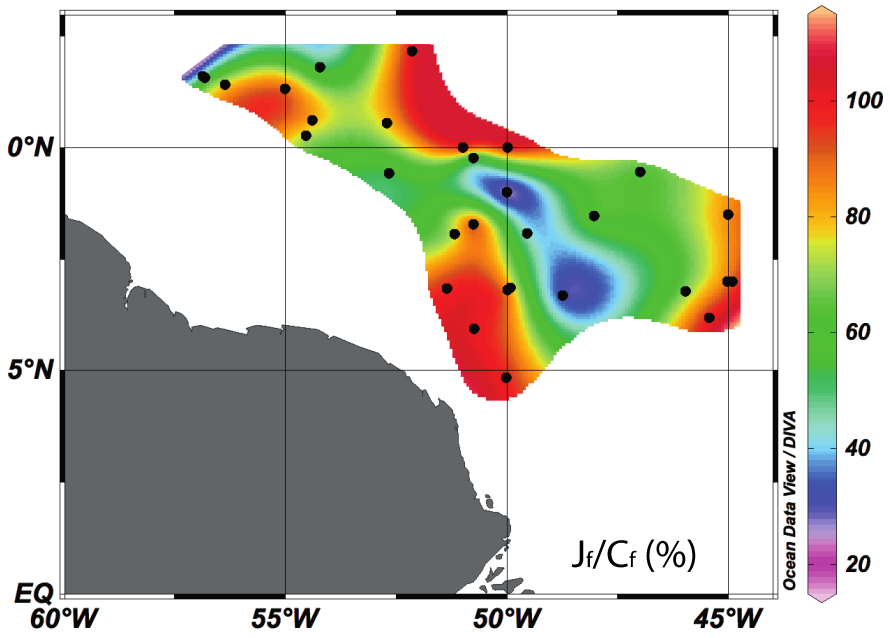

Figure 12. Map of Jf/Ctot for sediment at the SWI. Jf is the oxidation flux of the fast-reacting component of the total C flux.

fraction of reactive carbon making up the total C flux (83 ± 7.3%). Zone A also has a higher average flux of J_f (0.75± 0.52 mmol m^{-2} d^{-1}) as compared to the other two zones (0.35±0.26 and 0.27±0.14 mmol m^{-2} d^{-1}, respectively). Zone A not only receives more reactive carbon than the rest of the region, but the fast-reacting component generally contributes more to the total C flux.

The benthic patterns and DDAs

Previous work has indicated that DDA blooms tend to appear in 'mesohaline' waters (28-32) and increase surface export of C_{org} (Carpenter et al., 1999; Foster et al., 2007; Subramaniam et al., 2008; Yeung et al., 2012). However, the pattern of carbon oxidation in sediments does not show significantly higher fluxes in the region where the salinity is historically ~30, but rather it shows the highest fluxes associated with the core of the low salinity plume waters. Yeung et al. (2012) showed evidence of DDA activity and C_{org} export centered in waters with SSS=32. While our results indicate that the plume leaves a definitive pattern on the deep sea floor, the zone of observed DDA production does not appear to be a zone of high C_{org} deposition. We do see a broad zone of high bSi deposition, and this may relate to DDA activity, however it would appear that the organic carbon content of these blooms is rapidly attenuated in the water column.

CONCLUSIONS

The Amazon River Plume leaves a distinct footprint of C_{org} and bSi deposition and remineralization in the underlying deep sea sediments as far as 1200 km from the river mouth. There is an axis of C_{org} and bSi deposition that mirrors the axis of the freshwater plume as it travels NW from 5°N and 50°W. Both C_{org} and bSi remineralization rates are attenuated to the NW and E with a much steeper gradient than would be expected from analysis of surface plume salinity alone. Benthic carbon oxidation fluxes ranged from 0.16 – 1.92 mmol m^{-2} d^{-1} throughout the study region, with the highest fluxes localized in the core axis of the Amazon River Plume extending to the northwest. Benthic $Si(OH)_4$ fluxes ranged from 0.14 – 1.35 mmol m^{-2} d^{-1}, and covered a wider latitudinal expanse towards the northwest while to the east fluxes were consistently low.

Deposition follows a pattern of high-C/high-Si near the axis of the plume, low-C/high-Si as plume waters move away from the central axis, and low-C/low-Si throughout the rest of the area. The region underlying the fall retroflection plume appears to be of minor importance to C_{org} and bSi export compared to the spring plume. The disconnect between the patterns of C_{org} and bSi deposition indicates that their export is somewhat decoupled from one another. There may be a role of DDA's (Yeung et al., 2012) in exporting bSi from the surface ocean to depth, but it does not appear that mesohaline waters, especially around 30 ± 2, provide a zone of enhanced C_{org} export to the deep sea.

The fluxes of the fast-reacting pool of organic material is highest within the plume axis and is also attenuated to the NW and E. This component accounts for >90% of the total C_{org} oxidized on the sea floor underlying the proximal plume. Sites quite distal from plume influence also receive a greater fraction of fast-reacting C_{org}. However, there is a zone, primarily in the area of the retroflection, where fast C_{org} contributes only 40-50% of the total C flux. This may indicate the deposition of more refractory, possibly terrestrially-derived C_{org}.

Overall, 0.15 Tmol C y^{-1} is remineralized in abyssal sediments in the 900,000 km^2 region influenced by the Amazon River Plume, constituting ~10% of the estimated C export flux for the region. The plume has a direct impact on increasing C_{org} export in the Western Atlantic, as C oxidation fluxes in this region are demonstrably greater than those at similar latitudes in the Eastern Atlantic. Globally, the highest benthic C oxidation fluxes measured below the Amazon River Plume are of similar magnitude to those observed in the Eastern Equatorial Atlantic, the Southeastern Atlantic, and the Southern Ocean.

ACKNOWLEDGEMENTS

NSF grant #OCE-0934073 supported the contributions of WB, LC and NR, and #0929339 and #1029889 supported the contributions of JM. We are thankful to the captains and crews of the R/V Knorr, R/V Melville, and R/V Atlantis. We would also like to acknowledge the members of the at-sea and shore-based science party and all contributors to the ANACONDAS project especially Chief Scientist Patricia

Yager. We thank John Fleming, Emily Mortazavi, Jesse Muratli, Alice Bitzer, Cara Fassino, Neha Ahmed, and Jake Porter for their contributions to this work.

REFERENCES

Aller, R.C., 1998, Mobile deltaic and continental shelf muds as suboxic, fluidized bed reactors: Marine Chemistry, v. 61, no. 3-4, p. 143–155, doi: 10.1016/S0304-4203(98)00024-3.

Aller, R.C., and Blair, N.E., 2006, Carbon remineralization in the Amazon-Guianas tropical mobile mudbelt: A sedimentary incinerator: Continental Shelf Research, v. 26, no. 17-18, p. 2241–2259.

Aller, R.C., Blair, N.E., Xia, Q., and Rude, P., 1996, Remineralization rates, recycling, and storage of carbon in Amazon shelf sediments: Continental Shelf Research, v. 16, no. 5-6, p. 753–786.

Aller, R.C., Heilbrun, C., Panzeca, C., Zhu, Z., and Baltzer, F., 2004, Coupling between sedimentary dynamics, early diagenetic processes, and biogeochemical cycling in the Amazon–Guianas mobile mud belt: coastal French Guiana: Marine Geology, v. 208, no. 2-4, p. 331–360.

Anderson, L.A., and Sarmiento, J.L., 1994, Redfield ratios of remineralization determined by nutrient data analysis: Global Biogeochemical Cycles.

Barnett, P., Watson, J., and Connelly, D., 1984, A multiple corer for taking virtually undisturbed samples from shelf, bathyal and abyssal sediments.: Oceanologica Acta, v. 7, p. 399–408.

Bender, M.L., and Heggie, D.T., 1984, Fate of organic carbon reaching the deep sea floor: a status report: Geochimica et Cosmochimica Acta, v. 48, no. 5, p. 977–986.

Bender, M.L., Martin, W.R., Hess, J., Sayles, F.L., Ball, L., and Lambert, C.E., 1987, A whole-core squeezer for interfacial pore-water sampling: Limnology and Oceanography,, p. 1214–1225.

Berelson, W.M., Hammond, D.E., Xu, X., O'Neill, D., Chin, C., and Zukin, J., 1990, Benthic fluxes and pore water studies from sediments of the central equatorial north Pacific: Nutrient diagenesis: Geochimica et Cosmochimica Acta, v. 54, p. 3001–3012.

Berelson, W.M., Prokopenko, M.G., Sansone, F.J., Graham, A.W., McManus, J., and Bernhard, J.M., 2005, Anaerobic diagenesis of silica and carbon in continental margin sediments: discrete zones of TCO2 production: Geochimica et Cosmochimica Acta, v. 69, no. 19, p. 4611–4629, doi: 10.1016/j.gca.2005.05.011.

Blair, N.E., Leithold, E., and Aller, R.C., 2004, From bedrock to burial: the evolution of particulate organic carbon across coupled watershed-continental margin systems: Marine Chemistry, v. 91, p. 141–156.

Boudreau, B.P., and Ruddick, B.R., 1991, On a reactive continuum representation of organic matter diagenesis: American Journal of Science, v. 291, no. 5, p. 507–538.

Braman, R., and Hendrix, S., 1989, Nanogram nitrite and nitrate determination in environmental and biological materials by vanadium (III) reduction with chemiluminescence detection: Analytical Chemistry, v. 61, no. 24, p. 2715–2718.

Burdige, D.J., 2007, Preservation of organic matter in marine sediments: controls, mechanisms, and an imbalance in sediment organic carbon budgets?: Chemical Reviews-Columbus, v. 107, no. 2, p. 467–485.

Cai, W.-J., Reimers, C.E., and Shaw, T., 1995, Microelectrode studies of organic carbon degradation and calcite dissolution at a California continental rise site: Geochimica et Cosmochimica Acta, v. 59, no. 3, p. 497–511.

Canfield, D.E., 1994, Factors influencing organic carbon preservation in marine sediments: Chemical Geology, v. 114, no. 3, p. 315–329.

Carpenter, E.J., Montoya, J.P., Burns, J.A., Mulholland, M., Subramaniam, A., and Capone, D.G., 1999, Extensive bloom of a N2 fixing symbiotic association in the tropical Atlantic Ocean: Marine Ecology Progress Series, v. 188, p. 273–283.

Chong, L.S., Prokopenko, M.G., Berelson, W.M., Townsend-Small, A., and McManus, J., 2012, Nitrogen cycling within suboxic and anoxic sediments from the continental margin of Western North America: Marine Chemistry, v. 128-129, p. 13–25, doi: 10.1016/j.marchem.2011.10.007.

Cooley, S.R., and Yager, P.L., 2006, Physical and biological contributions to the western tropical North Atlantic Ocean carbon sink formed by the Amazon River plume: Journal of Geophysical Research, v. 111, no. C8, p. 1–14, doi: 10.1029/2005JC002954.

Cooley, S.R., Coles, V.J., Subramaniam, A., and Yager, P.L., 2007, Seasonal variations in the Amazon plume-related atmospheric carbon sink: Global Biogeochemical Cycles, v. 21, no. 3, p. GB3014, doi: 10.1029/2006GB002831.

Damuth, J.E., 1977, Late Quaternary sedimentation in the western equatorial

Atlantic: GSA Bulletin, v. 88, no. 5, p. 695, doi: 10.1130/0016-7606(1977)88<695:LQSITW>2.0.CO;2.

Del Vecchio, R., and Subramaniam, A., 2004, Influence of the Amazon River on the surface optical properties of the western tropical North Atlantic Ocean: Journal of Geophysical Research, v. 109, no. C11, p. C11001, doi: doi:10.1029/2004JC002503.

DeMaster, D.J., and Pope, R.H., 1996, Nutrient dynamics in Amazon shelf waters: results from AMASSEDS: Continental Shelf Research, v. 16, no. 3, p. 263–289.

DeMaster, D.J., Smith, W.O., Jr, Nelson, D.M., and Aller, J.Y., 1996, Biogeochemical processes in Amazon shelf waters: chemical distributions and uptake rates of silicon, carbon and nitrogen: Continental Shelf Research, v. 16, no. 5, p. 617–643.

Deuser, W.G., 1986, Seasonal and interannual variations in deep-water particle fluxes in the Sargasso Sea and their relation to surface hydrography: Deep Sea Research Part A. Oceanographic Research Papers, v. 33, no. 2, p. 225–246.

Deuser, W.G., and Ross, E.H., 1980, Seasonal change in the flux of organic carbon to the deep Sargasso Sea: Nature, v. 283, p. 364–365.

Deuser, W.G., Muller-Karger, F.E., and Hemleben, C., 1988, Temporal variations of particle fluxes in the deep subtropical and tropical North Atlantic: Eulerian versus Lagrangian effects: Journal of Geophysical Research, v. 93, no. C6, p. 6857–6862.

Deuser, W.G., Ross, E.H., and Anderson, R.F., 1981, Seasonality in the supply of sediment to the deep Sargasso Sea and implications for the rapid transfer of matter to the deep ocean: Deep Sea Research Part A. Oceanographic Research Papers, v. 28, no. 5, p. 495–505.

Druffel, E.R.M., 2005, Input of particulate organic and dissolved inorganic carbon from the Amazon to the Atlantic Ocean: Geochemistry Geophysics Geosystems, v. 6, no. 3, p. Q03009, doi: 10.1029/2004GC000842.

Eppley, R., and Peterson, B., 1979, Particulate organic matter flux and planktonic new production in the deep ocean: Nature, v. 282, no. 5740, p. 677–680.

Foster, R.A., Subramaniam, A., Mahaffey, C., Carpenter, E.J., Capone, D.G., and Zehr, J.P., 2007, Influence of the Amazon River plume on distributions of free-living and symbiotic cyanobacteria in the western tropical north Atlantic Ocean: Limnology and Oceanography,, p. 517–532.

Froelich, P.N., Atwood, D., and Giese, G., 1978, Influence of Amazon River discharge on surface salinity and dissolved silicate concentration in the Caribbean Sea: Deep Sea Research, v. 25, no. 8, p. 735–744.

Froelich, P.N., Klinkhammer, G.P., Bender, M.L., Luedtke, N.A., Heath, G.R., Cullen, D., Dauphin, P., Hammond, D.E., Hartman, B., and Maynard, V., 1979, Early oxidation of organic matter in pelagic sediments of the eastern equatorial Atlantic: suboxic diagenesis: Geochimica et Cosmochimica Acta, v. 43, no. 7, p. 1075–1090.

Gibbs, R., 1972, Water chemistry of the Amazon River: Geochimica et Cosmochimica Acta, v. 36, no. 9, p. 1061–1066.

Goloway, F., and Bender, M.L., 1982, Diagenetic models of interstitial nitrate profiles in deep sea suboxic sediments: Limnology and Oceanography,, p. 624–638.

Granger, J., and Sigman, D.M., 2009, Removal of nitrite with sulfamic acid for nitrate N and O isotope analysis with the denitrifier method: Rapid Communications in Mass Spectrometry, v. 23, p. 3753–3762.

Hales, B., Emerson, S.R., and Archer, D.E., 1994, Respiration and dissolution in the sediments of the western North Atlantic: estimates from models of in situ microelectrode measurements of porewater oxygen and pH: Deep Sea Research I, v. 41, no. 4, p. 695–719.

Hammond, D.E., McManus, J., Berelson, W.M., Kilgore, T.E., and Pope, R.H., 1996, Early diagenesis of organic material in equatorial Pacific sediments: stoichiometry and kinetics: Deep Sea Research Part II: Topical Studies in Oceanography, v. 43, no. 4-6, p. 1365–1412.

Hedges, J.I., and Keil, R.G., 1995, Sedimentary organic matter preservation: an assessment and speculative synthesis: Marine Chemistry, v. 49, p. 81–115.

Hedges, J.I., Clark, W.A., Quay, P.D., Richey, J.E., Devol, A.H., and Santos, U. de M., 1986, Compositions and fluxes of particulate organic material in the Amazon River: Limnology and Oceanography,, p. 717–738.

Herman, P.M., Soetaert, K., Middelburg, J.J., Heip, C.H.R., Lohse, L., Epping, E., Helder, W., Antia, A.N., and Peinert, R., 2001, The seafloor as the ultimate sediment trap—using sediment properties to constrain benthic–pelagic exchange processes at the Goban Spur: Deep Sea Research Part II: Topical Studies in Oceanography, v. 48, no. 14, p. 3245–3264.

Honjo, S., 1980, Material fluxes and modes of sedimentation in the mesopelagic and bathypelagic zones: Journal of Marine Research, v. 38, p. 53–97.

Jahnke, R.A., Reimers, C.E., and Craven, D.B., 1990, Intensification of recycling of organic matter at the sea floor near ocean margins: Nature, v. 348, no. 6296, p. 50–54.

Johns, W.E., Lee, T.N., Beardsley, R.C., Candela, J., Limeburner, R., and Castro, B., 1998, Annual cycle and variability of the North Brazil Current: Journal of

physical Oceanography, v. 28, no. 1, p. 103–128.

Kasten, S., Freudenthal, T., Gingele, F.X., and Schulz, H.D., 1998, Simultaneous formation of iron-rich layers at different redox boundaries in sediments of the Amazon deep-sea fan: Geochimica et Cosmochimica Acta, v. 62, no. 13, p. 2253–2264.

Kasten, S., Zabel, M., Heuer, V., and Hensen, C., 2003, Processes and signals of nonsteady-state diagenesis in deep-sea sediments and their pore waters: The South Atlantic in the Late Quaternary: Reconstruction of material budget and current systems,, p. 431–459.

Keil, R.G., Mayer, L., Quay, P.D., Richey, J.E., and Hedges, J.I., 1997, Loss of organic matter from riverine particles in deltas: Geochimica et Cosmochimica Acta, v. 61, no. 7, p. 1507–1511.

Kineke, G.C., Sternberg, R.W., Trowbridge, J.H., and Geyer, W.R., 1996, Fluid-mud processes on the Amazon continental shelf: Continental Shelf Research, v. 16, no. 5, p. 667–696.

Kuehl, S.A., DeMaster, D.J., and Nittrouer, C.A., 1986, Nature of sediment accumulation on the Amazon continental shelf: Continental Shelf Research, v. 6, no. 1, p. 209–225.

Kuehl, S.A., Nittrouer, C.A., Allison, M.A., Faria, L.E.C., Dukat, D.A., Jaeger, J.M., Pacioni, T.D., Figueiredo, A.G., and Underkoffler, E.C., 1996, Sediment deposition, accumulation, and seabed dynamics in an energetic fine-grained coastal environment: Continental Shelf Research, v. 16, no. 5, p. 787–815.

Martin, W.R., and Bender, M.L., 1988, The variability of benthic fluxes and sedimentary remineralization rates in response to seasonally variable organic carbon rain rates in the deep sea: A modeling study.: American Journal of Science, v. 288, no. 6, p. 561–574.

Martin, W.R., and Sayles, F.L., 1996, CaCO3 dissolution in sediments of the Ceara Rise, western equatorial Atlantic: Geochimica et Cosmochimica Acta, v. 60, no. 2, p. 243–263.

Martin, W.R., and Sayles, F.L., 2004, Organic matter cycling in sediments of the continental margin in the northwest Atlantic Ocean: Deep Sea Research Part I, v. 51, no. 3, p. 457–489.

Martin, W.R., and Sayles, F.L., 2006, Organic matter oxidation in deep-sea sediments: distribution in the sediment column and implications for calcite dissolution: Deep Sea Research Part II, v. 53, p. 771–792.

Martin, W.R., Bender, M.L., Leinen, M., and Orchardo, J., 1991, Benthic organic carbon

degradation and biogenic silica dissolution in the central equatorial Pacific: Deep Sea Research Part A. Oceanographic Research Papers, v. 38, no. 12, p. 1481–1516.

McManus, J., Hammond, D.E., Berelson, W.M., Kilgore, T.E., DeMaster, D.J., Ragueneau, O.G., and Collier, R.W., 1995, Early diagenesis of biogenic opal: Dissolution rates, kinetics, and paleoceanographic implications: Deep Sea Research II, v. 42, no. 2-3, p. 871–903.

Meade, R.H., Dunne, T., Richey, J.E., Santos, U. de M., and Salati, E., 1985, Storage and remobilization of suspended sediment in the lower Amazon River of Brazil: Science, v. 228, no. 4698, p. 488–490.

Mikaloff Fletcher, S.E., Gruber, N., Jacobson, A.R., Gloor, M., Doney, S.C., Dutkiewicz, S., Gerber, M., Follows, M.J., Joos, F., Lindsay, K., Menemenlis, D., Mouchet, A., Müller, S.A., and Sarmiento, J.L., 2007, Inverse estimates of the oceanic sources and sinks of natural CO 2and the implied oceanic carbon transport: Global Biogeochemical Cycles, v. 21, no. 1, p. GB1010–19, doi: 10.1029/2006GB002751.

Milliman, J.D., and Meade, R.H., 1983, World-wide delivery of river sediment to the oceans: The Journal of Geology,, p. 1–21.

Moré, J.J., and Sorensen, D.C., 1983, Computing a trust region step: SIAM Journal on Scientific and Statistical Computing, v. 4, no. 3, p. 553–572.

Muller-Karger, F.E., Mcclain, C., and Richardson, P.L., 1988, The dispersal of the Amazon's water: Nature, v. 333, p. 56–59, doi: doi:10.1038/333056a0.

Muller-Karger, F.E., Richardson, P.L., and McGillicuddy, D., 1995, On the offshore dispersal of the Amazon's Plume in the North Atlantic: Comments on the paper by A. Longhurst,'Seasonal cooling and blooming in tropical oceans': Deep Sea Research Part I: Oceanographic Research Papers, v. 42, no. 11, p. 2127–2137.

Nittrouer, C.A., Kuehl, S.A., Sternberg, R.W., and Figueiredo, A.G., 1995, An introduction to the geological significance of sediment transport and accumulation on the Amazon continental shelf: Marine Geology, v. 125, no. 3-4, p. 177–192.

Perry, G.D., Duffy, P.B., and Miller, N.L., 1996, An extended data set of river discharges for validation of general circulation models: Journal of Geophysical Research: Oceans (1978–2012), v. 101, no. D16, p. 21339–21349.

Pfannkuche, O., 1993, Benthic response to the sedimentation of particulate organic matter at the BIOTRANS station, 47ºN, 20ºW: Deep Sea Research II, v. 40, no. 1-2, p. 135–149.

Premuzic, E.T., Benkovitz, C.M., Gaffney, J.S., and Walsh, J.J., 1982, The nature and

distribution of organic matter in the surface sediments of world oceans and seas: Organic Geochemistry, v. 4, no. 2, p. 63–77.

Raymond, P.A., and Cole, J.J., 2003, Increase in the export of alkalinity from North America's largest river: Science, v. 301, no. 5629, p. 88–91.

Reimers, C.E., Jahnke, R.A., and McCorkle, D.C., 1992, Carbon fluxes and burial rates over the continental slope and rise off central California with implications for the global carbon cycle: Global Biogeochemical Cycles, v. 6, no. 2, p. 199–224.

Richey, J.E., Hedges, J.I., Devol, A.H., and Quay, P.D., 1990, Biogeochemistry of carbon in the Amazon River: Limnology and Oceanography, v. 35, no. 2, p. 352–371.

Sayles, F.L., Deuser, W.G., Goudreau, J.E., DIckinson, W.H., Jickells, T.D., and King, P., 1996, The benthic cycle of biogenic opal at the Bermuda Atlantic Time Series site: Deep Sea Research Part I: Oceanographic Research Papers, v. 43, no. 4, p. 383–409.

Sayles, F.L., Martin, W.R., and Deuser, W.G., 1994, Response of benthic oxygen demand to particulate organic carbon supply in the deep sea near Bermuda:.

Schlünz, B., Schneider, R.R., Müller, P.J., and Showers, W.J., 1999, Terrestrial organic carbon accumulation on the Amazon deep sea fan during the last glacial sea level low stand: Chemical Geology, v. 159, p. 263–281.

Schulz, H.D., Dahmke, A., Schinzel, U., Wallmann, K., and Zabel, M., 1994, Early diagenetic processes, fluxes, and reaction rates in sediments of the South Atlantic: Geochimica et Cosmochimica Acta, v. 58, no. 9, p. 2041–2060.

Shipe, R.F., Curtaz, J., Subramaniam, A., Carpenter, E.J., and Capone, D.G., 2006, Diatom biomass and productivity in oceanic and plume-influenced waters of the western tropical Atlantic ocean: Deep Sea Research Part I: Oceanographic Research Papers, v. 53, no. 8, p. 1320–1334.

Smith, K.L., Jr, and Baldwin, R.J., 1984, Seasonal fluctuations in deep-sea sediment community oxygen consumption: central and eastern North Pacific: Nature, v. 307, no. 2, p. 624–626.

Smith, S.M., and Hitchcock, G.L., 1994, Nutrient enrichments and phytoplankton growth in the surface waters of the Louisiana Bight: Estuaries, v. 17, no. 4, p. 740–753.

Strickland, J.D.H., and Parsons, T.R., 1972, A Practical Handbook of Seawater Analysis: Fisheries Research Board of Canada, Ottowa, Canada.

Subramaniam, A., Yager, P.L., Carpenter, E.J., Mahaffey, C., Björkman, K.M., Cooley, S.R., Kustka, A., Montoya, J.P., Sañudo-Wilhelmy, S.A., Shipe, R.F., and Capone,

D.G., 2008, Amazon River enhances diazotrophy and carbon sequestration in the tropical North Atlantic Ocean: Proceedings of the National Academy of Sciences of the United States of America, v. 105, no. 30, p. 10460–10465.

Takahashi, T., Sutherland, S.C., Sweeney, C., Poisson, A., Metzl, N., Tilbrook, B., Bates, N.R., Wanninkhof, R., Feely, R.A., and Sabine, C., 2002, Global sea-air CO2 flux based on climatological surface ocean pCO2, and seasonal biological and temperature effects: Deep Sea Research Part II: Topical Studies in Oceanography, v. 49, no. 9-10, p. 1601–1622.

Ternon, J., Oudot, C., Dessier, A., and Diverres, D., 2000, A seasonal tropical sink for atmospheric CO2 in the Atlantic Ocean: the role of the Amazon River discharge: Marine Chemistry, v. 68, no. 3, p. 183–201.

Ward, N.D., Keil, R.G., Medeiros, P.M., Brito, D.C., Cunha, A.C., Dittmar, T., Yager, P.L., Krusche, A.V., and Richey, J.E., 2013, Degradation of terrestrially-derived lignin macromolecules in the Amazon River: Nature Geoscience,, doi: 10.1038/ngeo1817.

Wells, J., and Coleman, J., 1981, Periodic mudflat progradation, northeastern coast of South America; a hypothesis: Journal of Sedimentary Research, v. 51, no. 4, p. 1069.

Wenzhöfer, F., and Glud, R.N., 2002, Benthic carbon mineralization in the Atlantic: a synthesis based on in situ data from the last decade: Deep Sea Research Part I, v. 49, p. 1255–1279.

Wenzhöfer, F., Holby, O., and Kohls, O., 2001, Deep penetrating benthic oxygen profiles measured in situ by oxygen optodes: Deep Sea Research I, v. 48, p. 1741–1755.

WOCE Data Products Committee, 2002, WOCE Global Data, Version 3.0: WOCE International Project Office.

Yeung, L.Y., Berelson, W.M., Young, E.D., Prokopenko, M.G., Rollins, N., Coles, V.J., Montoya, J.P., Carpenter, E.J., Steinberg, D.K., Foster, R.A., Capone, D.G., and Yager, P.L., 2012, Impact of diatom-diazotroph associations on carbon export in the Amazon River plume: Geophysical Research Letters, v. 39, no. 18, p. L18609, doi: 10.1029/2012GL053356.

Chapter 3: Biogenic sedimentation and geochemical properties of deep-sea sediments of the Demerara Slope/Abyssal Plain: Influence of the Amazon River Plume

ABSTRACT

As the Amazon River plume mixes into the North Atlantic Ocean, it may support ecological niches favorable for the N_2 fixation driven by the symbiosis between diatoms and their diazotrophic cyanobacterial symbionts. This proposed diatom-diazotroph association (DDA) should result in increased carbon export from a limited region of plume influence. However, it is unclear whether or not these diatom assemblages are the primary drivers of export in the river plume and the amount and composition of surface export that actually reaches the deep sea floor is not well defined. Here we used floating sediment traps deployed at 150 and 250 m and multicores collected throughout the Demerara Abyssal Slope and Plain at depths ranging from 3000-5000 m to assess the export of biogenic materials. Sediment accumulation rates were determined from ^{14}C ages of foraminifera obtained at 2-5 depths from 7 cores. The sedimentation rate (1-4 cm/ky) represents the average accumulation over the past 8000 years, though model simulations indicate that sedimentation rates have increased by 2-4 times in the last few thousand years. Sparse evidence suggests that glacial accumulation rates were

2-10 times greater. The C_{org} and bSi composition of the sediments was combined with sedimentation rate to determine the burial flux. C_{org} burial represented 4-16 % of the C_{org} raining to the deep sea floor, and bSi burial represented 1-9% of the bSi rain. Sediment mixing (bioturbation) was studied in 11 cores using ^{210}Pb as a tracer and sediment focusing was studied in 7 cores using ^{230}Th as a tracer.

INTRODUCTION

The outflow of the Amazon River forms a plume of low salinity (<36 ppt) water that extends offshore and northwest over the north Brazilian continental shelf (Smith and DeMaster, 1996; Lentz and Limeburner, 1995; Neumann, 1969). These waters can be traced northwest to the Caribbean (Froelich et al., 1978), as well as eastward into the eastern North Atlantic due to the seasonal retroflection of the North Brazil Current (Muller-Karger et al., 1988). The plume is responsible for the delivery of both nutrients and organic matter to the western tropical North Atlantic (WTNA) (Aller et al., 1996; DeMaster and Pope, 1996; DeMaster et al., 1996; Richey et al., 1990; Smith and DeMaster, 1996), as well as dispensing 1.2×10^9 tons yr^{-1} of suspended sediment (Meade et al., 1985).

CO_2 uptake has been observed in the WTNA, particularly in the vicinity of the Amazon River plume, in an area of the Atlantic generally considered to be a net source of CO_2 to the atmosphere (Cooley et al., 2007; Cooley and Yager, 2006; Mikaloff Fletcher et al., 2007; Takahashi et al., 2002; Ternon et al., 2000). The areal extent of this uptake and its impact on the sediment column has not been previously

studied. It has been suggested that the plume contains waters that are depleted in N but contain a relative excess of P, Fe and dissolved Si, creating ideal conditions for the proliferation of diatom-diazotroph associations (DDAs), which have been suggested to be a factor in increasing carbon export (Carpenter et al., 1999; Foster et al., 2007; Shipe et al., 2006; Subramaniam et al., 2008). Yeung, et al., (2012) showed that DDA blooms do increase carbon export efficiency, but it is unknown how much of this material reaches the deep ocean.

A past study in the WTNA utilizing a moored sediment trap at 13.5˚N 54.0˚W (the northern limit of our study region; Fig. 1) showed that the mass flux between 3755 m and 5068 m was nearly identical (46.4 and 47.0 mg $m^{-2}d^{-1}$, respectively) between Nov-1977 and Feb-1978 (Honjo, 1980). A later study found that the mass flux of sinking material at 3200 m at 13.22˚N 57.68˚W displayed a high amount of inter-annual variability (42 ± 24 mg m^{-2} d^{-1} Jun 1981-Apr 1982; 115 ± 47 mg m^{-2} d^{-1} Apr 1982-Jul 1983) and suggested that the variability was derived from variability in surface blooms in Amazon plume waters (Deuser et al., 1988). Floating sediment traps deployed by Subramaniam et al. (2008) showed a correlation between the presence of DDAs and the overall mass flux at 150 m in waters of salinity ~32 (152 ± 26 mg m^{-2} d^{-1} at stations with salinity 30-34 versus 42 ± 8 mg m^{-2} d^{-1} at stations with salinity >35), but this is not entirely diagnostic for quantifying the amount of biogenic material that reaches the sea floor, nor for identifying DDAs as the primary vector of that export.

Here, we describe patterns of biogenic sedimentation throughout the Demerara Rise/Abyssal Plain and compare the accumulation of biogenic material to export fluxes derived from floating sediment traps deployed in 2010 and 2011. We have already discussed patterns of remineralization (Chapter 2), hence we also construct a budget of total C_{org} rain (remineralization + accumulation). We further assess the correlation between the surface ocean and the deep sea by looking at the distribution of C_{org}, N_{org}, and bSi, as well as the isotopic composition of the material caught by traps versus that found in the sediments. We also examine the pattern of sediment mixing and sediment focusing (using Th-234 data provided by R.F. Anderson and M. Fleisher at LDEO).

STUDY AREA

This study presents results from the ANACONDAS (Amazon iNfluence on the Atlantic: CarbOn export from Nitrogen fixation by Diatom Symbioses) project. Three cruises took place throughout the WTNA aboard the *R/V Knorr* (May-June 2010), the *R/V Melville* (September-October 2011), and the *R/V Atlantis* (July 2012). Most of the study sites are quite far from the river mouth but still clearly under river plume influence, covering an approximate area of 450,000 km^2 (Fig. 1).

The mean flow of the Amazon River is 1.8×10^5 m^3 s^{-1}, discharging 1.2×10^9 tons y^{-1} of sediment, most of which moves northwest in the form of suspensions and coastal mudbanks (Kineke et al., 1996; Meade et al., 1985; Nittrouer et al., 1995; Wells and Coleman, 1981). Within the surface sediments of the Amazon delta, both

Figure 1. Map of study sites. (*) indicate sediment trap deployments. ■ is a deep trap array deployed by Honjo (1980). ♦ is a deep trap array deployed by Deuser et al., 1988.

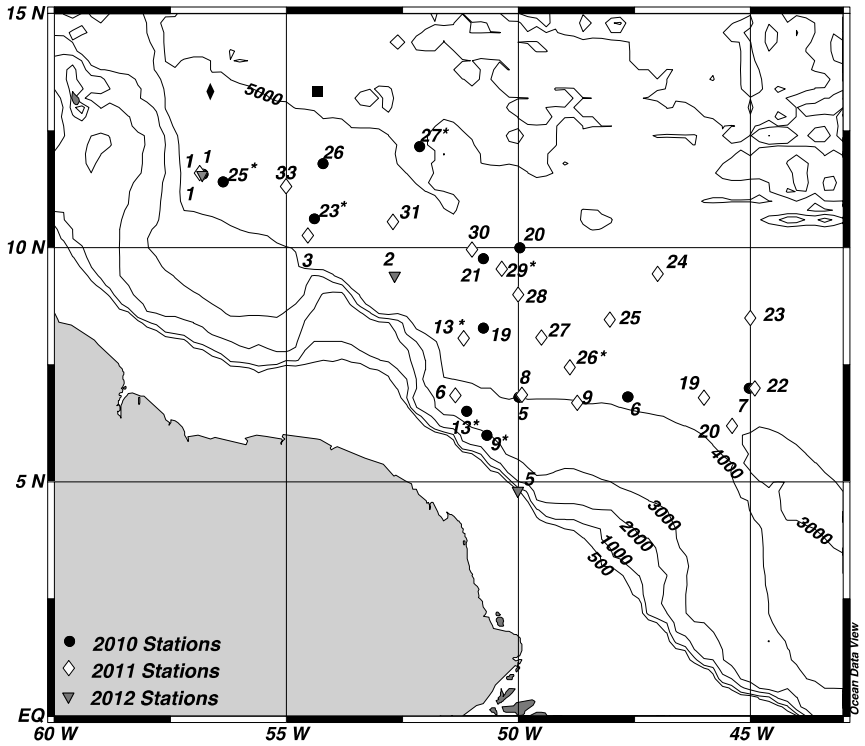

terrestrial and marine organic matter, dominated by the marine fraction (60-70%), contribute to early diagenetic reactions (Aller et al., 2004; Aller and Blair, 2006). Rapid sediment mixing and suboxic diagenesis depletes the supply of terrestrial organic material (Aller and Blair, 2006). It is thought that most Amazon River sediments are trapped on the continental shelf (Damuth and Embley, 1981; Damuth and Kumar, 1975; Milliman et al., 1975), however the plume extending to 12°N may carry a significant load of fine, suspended material.

The sediments of the continental rise and abyssal plain adjacent to the Amazon mobile mud belt consist predominantly of brown pelagic and grey hemipelagic sediments with sedimentation rates ranging from 4 to 7 cm kyr^{-1} on the lower continental rise to 2 to 4 cm kyr^{-1} on the abyssal plain (Damuth, 1977).

METHODS

Sediment Cores

We collected sediment cores at 32 sites (Fig. 1, Table 1) throughout the Demerara Slope/Rise and Abyssal Plain using a multi-corer with 9.8 cm diameter (I.D) core tubes (Barnett et al., 1984). Upon recovery on deck, cores were immediately transferred to a temperature-controlled van (~2˚C). One core from each station was sectioned in 1 cm intervals from the sediment-water interface (SWI) to 5 cm, and in 2 cm intervals thereafter. Two aliquots of mud were collected from each interval. The first aliquot was collected into a pre-weighed glass

Table 1. Site descriptions and data available from each station.

Station	Latitude (°N)	Longitude (°W)	Depth (m)	Traps	TC	TIC	$\delta^{13}C$	$\delta^{15}N$	bSi	^{210}Pb	^{14}C
2010											
1	11.57	56.79	4373		x	x	x	x			
5	6.81	49.98	3975		x	x	x	x	x	x	
6	6.82	47.63	4088		x	x	x	x	x		
7	7.00	45.02	4394		x	x	x	x			
9	5.92	50.73	3014	x				x			
13	6.50	51.11	3500*	x							
19	8.29	50.75	4854		x	x	x	x		x	x
20	10.00	49.97	4854		x	x	x	x		x	
21	9.77	50.75	4863		x	x	x	x	x	x	x
23	10.62	54.39	4486	x	x	x	x	x	x	x	
25	11.41	56.36	4465	x	x	x	x	x	x	x	
26	11.80	54.21	4777		x	x	x	x	x	x	
27	12.16	52.13	5044	x	x	x	x	x	x	x	x
2011											
1	11.60	56.86	4362		x	x	x	x	x		x
3	10.27	54.53	4393		x	x	x	x			
6	6.85	51.35	3760		x	x	x	x	x		
8	6.86	49.92	3997		x	x	x	x		x	
9	6.69	48.73	4030		x	x	x	x	x		x
13	8.07	51.18	4450	x	x	x	x	x	x		
19	6.78	45.96	4205		x	x	x	x			
20	6.19	45.43	4197		x	x	x	x	x		x
22	7.00	44.90	4435		x	x	x	x			
23	8.50	45.00	4709		x	x	x	x	x	x	x
24	9.45	46.99	4784		x	x	x	x	x		
25	8.47	48.03	4526		x	x	x	x	x	x	x
26	7.45	48.89	4200*	x							
27	8.08	49.53	4415		x	x	x	x			
29	9.55	50.36	4784	x							
31	10.55	52.70	4889		x	x	x	x	x	x	x
33	11.32	55.00	4650		x	x	x	x			
2012											
2	9.42	52.66	4764		x	x	x		x		

* Depth estimated from nearby stations

container, which was used to determine the sediment porosity by weight loss after drying. Dried sediment was ground to a fine powder using an agate mortar and pestle. The second aliquot was sieved through 200-μm mesh and the material remaining on the mesh was rinsed with de-ionized water and dried.

Total Carbon, Organic Carbon, Carbonate, $\delta^{13}C_{TIC}$, $\delta^{13}C_{org}$, and $\delta^{15}N$

Wt% total carbon (TC), as well as the wt% and $\delta^{13}C$ of inorganic carbon (TIC) were measured on aliquots of ground sediment. TC was analyzed using an Elantech 1110 Elemental Analyzer (EA) connected to a Picarro G2121-i isotopic CO_2 analyzer. The standard used for TC analysis was an AR-15 calcite standard (9.65± 0.01 %C, -9.9 ± 0.1‰ $\delta^{13}C$). The carbon content was determined through measuring numerous replicates on the EA. The isotopic standard is in the process of intercalibration with UC Davis stable isotope lab and with the Adkins lab at the California Institute of Technology. We used 15-50 mg of ground sediment weighed into 9 mm tin cups for sample analysis. The relative uncertainty of the TC measurements, based on the uncertainty of the standards from every run, was <1.5% of the wt%.

The wt% and $\delta^{13}C$ of TIC was measured on a Picarro CRDS analyzer using 15-50 mg of ground sediment weighed into quartz tubes. The tubes were capped and evacuated for 30 seconds. Each tube was then injected with 3 mL of 10% H_3PO_4 and vortexed for 1 minute to homogenize the mixture. Samples sat for a minimum of 30 minutes prior to analysis. The standard used for TIC analysis was an optical calcite

(OPT) standard (12.002 %C, +2.47 ± 0.01 $\delta^{13}C$). The relative uncertainty in wt% and $\delta^{13}C$ of TIC were determined from the average uncertainty of the standards from every run, and was 2.5% of the wt% and 2.5‰, respectively. Wt% organic carbon (C_{org}) was determined as the difference between wt% TC and wt% TIC, and $\delta^{13}C_{org}$ was calculated by isotopic mass balance using wt% Corg, wt% TIC, and $\delta^{13}C_{TIC.}$ The uncertainty in $\delta^{13}C_{org}$ was 6.5% due to the cumulative uncertainties in the other values of the mass balance.

$\delta^{15}N$ was measured on bulk sediments from the two uppermost depth intervals from the 2010 and 2011 stations. Samples were sent to the UC Davis stable isotope lab for analysis.

Biogenic Silica

Solid biogenic silica was measured using an alkaline leaching method (DeMaster, 1981; Strickland, 1968). From selected cores, ~50 mg of ground sediment was placed in a 50 mL plastic centrifuge tube along with 50 mL of 5% (wt/vol) of a sodium carbonate solution. The samples were incubated in an 80˚C water bath for 5 hours, with periodic mixing. 0.5 mL aliquots were removed at hours 3, 4, and 5 into pre-weighed plastic test tubes. The samples were re-weighed, neutralized with dilute hydrochloric acid, and then analyzed colorimetrically. Blanks were also analyzed to correct for colorimetric variations from using different batches of Na_2CO_3. Dissolved Si concentrations were plotted versus time, and a linear fit to the data was extrapolated back to the y-axis, where the intercept was

assumed to be the amount of Si released from $bSiO_2$. The molar concentration of Si was then used to calculate the wt% $bSiO_2$ in a sample, assuming a molecular weight of 60.0 g mol^{-1}. For the sediment trap samples, between 0.3 – 12 mg of trap material was leached for $bSiO_2$.

^{210}Pb

^{210}Pb activity was measured at 11 sites using an intrinsic germanium gamma counter in the radioisotope lab at USC. The standard used was IAEA-315. Measurements were made at 7 depths from each of the chosen cores between the SWI and 20 cm. Approximately 1.5 g of ground sediment was used for each analysis. Corrections for sample geometry were made based on the sample height. Samples were counted for 23-140 hours and the gamma spectra (keV) were analyzed for the nuclides ^{210}Pb (46), ^{234}Th (63), ^{224}Ra (241), ^{214}Pb (296, 352), ^{214}Bi (609), ^{137}Cs (662), ^{228}Ac (338, 911), and ^{40}K (1461). Supported ^{210}Pb activity was found by calculating a weighted average for ^{214}Pb and ^{214}Bi, and assuming a 9% loss of ^{222}Rn, based on measurements of loss from powders that were prepared similarly. Excess ^{210}Pb activity was calculated as the difference of total and supported ^{210}Pb. The analytical uncertainty in excess ^{210}Pb was typically 35 Bq kg^{-1} ranging from about 10 to 150% of the excess ^{210}Pb. There may be additional uncertainty in the excess ^{210}Pb profiles due to the uncertainty in the value of supported ^{210}Pb stemming from the assumed loss of ^{222}Rn.

^{14}C

Eight sites were selected for radiocarbon analysis. Sieved material from 2-5 depths from each site was examined under a microscope to determine the type and quality of material present. The visual examination of the sieved material used for ^{14}C dating showed that it was primarily comprised of benthic foraminifera. Material was hand selected to exclude miscellaneous grains, and aliquots of ~40 mg of material were sent to the UC Irvine Keck AMS facility for radiocarbon analysis. The ^{14}C ages were converted to calendar age using the Calib 6.0 conversion program and the Marine09 calibration curve (Stuiver and Reimer, 1993; Reimer et al., 2009). The uncertainty after calibration was ± <150 yr. The marine calibration includes a reservoir age correction of 400 years, and which was adjusted for local effects following Stuiver and Braziunas (1993) using ΔR values from the Marine Reservoir Correction Database (http://www.calib.qub.ac.uk/marine/marexpl.html).

Sediment Traps

Material sinking out of the surface ocean was collected using free-floating, surface-tethered particle interceptor traps (Knauer et al., 1979). In 2010, the traps were deployed at 150 m with a single trap array on each string, two strings at each station. In 2011 there was a trap at 150 m and at 250 m on each string, two strings per station. There were 5 locations at which traps were deployed during the 2010 cruise, and 3 during 2011. The traps drifted with the surface currents, and their

location was monitored using RDF beacons and satellite-tracking buoys attached to each array.

Each trap array held 12 polycarbonate tubes; each tube had a diameter of 9.8 cm (ID). The material that fell into a tube was funneled to a 50 ml Falcon tube that was pre-filled with 0.2 μm-filtered seawater that had its salinity increased by 10 ppt, was borate buffered, and poisoned with $HgCl_2$. Upon recovery, samples were kept at 4˚C until processing, generally within 1-2 days. Material from each array was blended into 3 splits, and samples were examined under a binocular microscope to remove 'swimmers'. Splits were filtered either onto a 25mm 0.2 μm GF/F filter or onto a 25 mm nitrocellulose filter. Filters were dried at 25˚C and stored until returned to the lab post-cruise. On land, filters were weighed, and splits of filtered material were used to determine total carbon, total nitrogen, organic carbon, carbonate, $\delta^{13}C_{TIC}$, $\delta^{13}C_{TC}$, $\delta^{15}N$, and biogenic silica content.

RESULTS

Organic Carbon and Total Carbonate in Sediments

Twenty-eight stations were analyzed downcore for TC and TIC (Fig. 2). At all of these stations, the resultant C_{org} content calculated by difference was generally < 1 wt%. A separate analysis of C_{org} done by pre-acidification of sediments and analysis on an elemental analyzer showed agreement with the difference method to within <3% (relative to each other). It is apparent that stations closest to the river

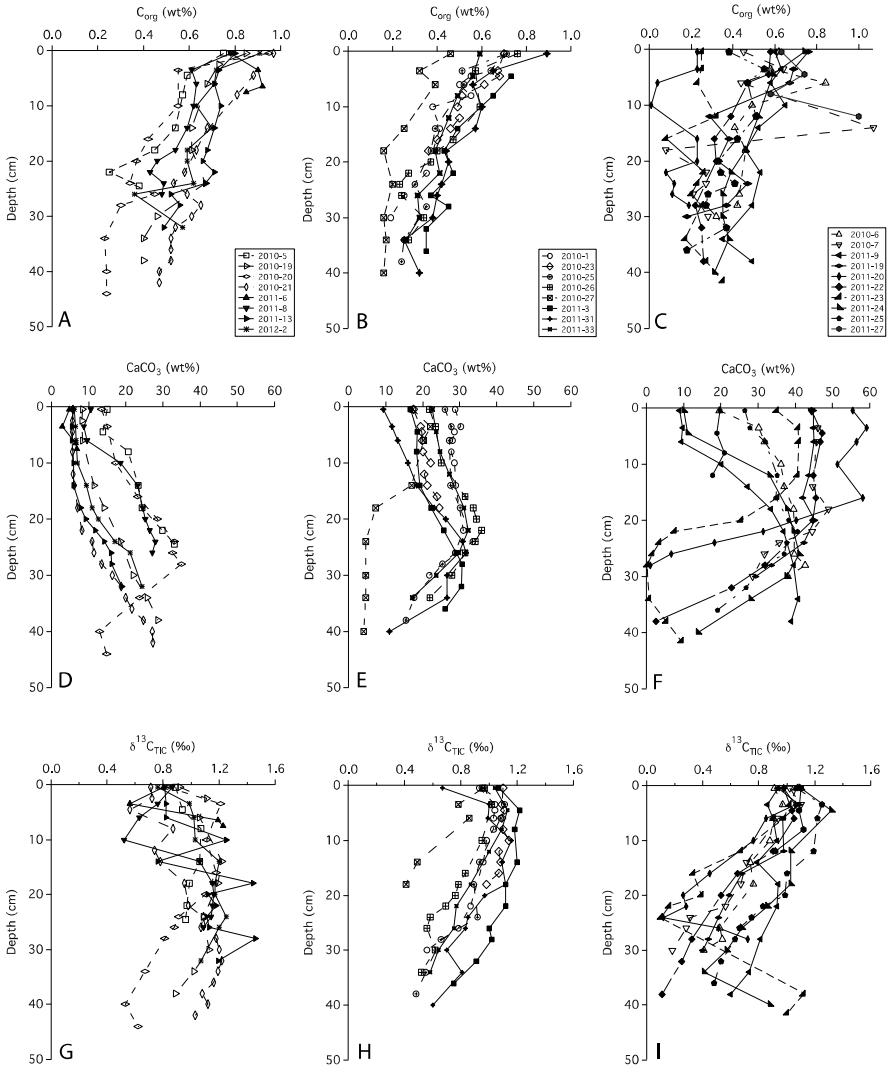

Figure 2. Sediment C_{org}, $CaCO_3$, and $\delta^{13}C_{(TIC)}$. The left column represents stations from the central plume (south of 10°N and west of 50°W), the center column represents the northern stations, the right column represents the eastern stations. Uncertainty in C_{org} was <1.5%, uncertainty in wt% $CaCO_3$ was 2.5%, and uncertainty in $\delta^{13}C_{(TIC)}$ was 2.5%.

mouth (Fig. 2A-C) have the highest surface C_{org} content (0.75-0.97 wt%) compared to those in the north (0.46-0.89 wt%) and the east (0.23-0.76 wt%). Overall, the C_{org} profiles decreased with depth in a somewhat exponential fashion, yet it is not clear that the profiles reached an asymptotic value over the depths sampled. Only core 2010-7 had a layer of abnormally high C_{org} (1 wt% Corg) lying between sediments that had 0.4-0.3 wt % C_{org}.

TIC wt% was converted to $CaCO_3$ wt% and surface sediment values ranged considerably, from 4.7 wt% (2011-6) to 55.4 wt% (2011-20) (Fig. 2D-F). Stations closest to the river mouth and within the main axis of the NW plume (Hu et al., 2004) were generally low in surface $CaCO_3$, ranging from 4.7 – 15.0 wt%. Downcore, these stations increased in wt% with depth, except 2010-20 which increased to ~30 cm and then decreased below this depth. To the north, surface $CaCO_3$ ranged from 9.3 – 28.6 wt%. Downcore, the sediment profiles remained fairly consistent or increased slightly to ~20 cm, below which $CaCO_3$ wt% decreased. The eastern stations showed greater variability in surface $CaCO_3$, ranging from 8.8 – 55.4 wt%. Downcore, nearly all of the stations in this region showed a precipitous decrease below 20 cm with the exception of station 2011-9 that increases with depth. All downcore data is available in tabular form in Appendix B and on the ANACONDAS data repository web site (http://data.bco-dmo.org/jg/dir/BCO/ANACONDAS/).

Sediment Stable Isotopes: $\delta^{13}C_{TIC}$, $\delta^{13}C_{org}$, and $\delta^{15}N$

Measurements of $\delta^{13}C_{TIC}$ were generally between 0-1.3‰ throughout the study region and downcore (Fig. 2G-I, Appendix B). At sites closest to the river mouth, surficial values ranged from 0.83 – 0.92 ‰, with downcore values being relatively consistent at each station. In the northern section of the study area, the surface values were between 0.67 – 1.10 ‰ and downcore the isotopes became slightly lighter with depth (by ~ 0.4‰ change). In the eastern region, the surface values ranged from 0.91 – 1.10 ‰ and downcore, all of the isotope profiles became lighter with depth (< 0.8‰ change) though a few stations (2011-23, 2011-20, 2011-24) became heavier below 25 cm. There does not appear to be a consistent relationship between wt % $CaCO_3$ and $\delta^{13}C_{TIC}$.

The surface sediment $\delta^{13}C_{org}$ ranged from -17.58 to -21.09‰, generally reflecting a marine signal, though a few stations (2010-7, 2011-25) had a lighter isotopic value, -23.96 to -31.07‰, potentially indicating a significant contribution from terrestrial material (Fig. 3). Downcore isotope profiles varied from site to site; some stations (i.e. 2010-23) were fairly consistent with depth, some became heavier with depth (i.e. 2010-21), and some became lighter with depth (i.e. 2010-1).

Surface sediment $\delta^{15}N$ isotopes (PON from bulk sediments) were generally uniform throughout the study region, ranging between 4.50-5.16‰ (Fig. 3). The majority of stations had a $\delta^{15}N$ of around 5‰.

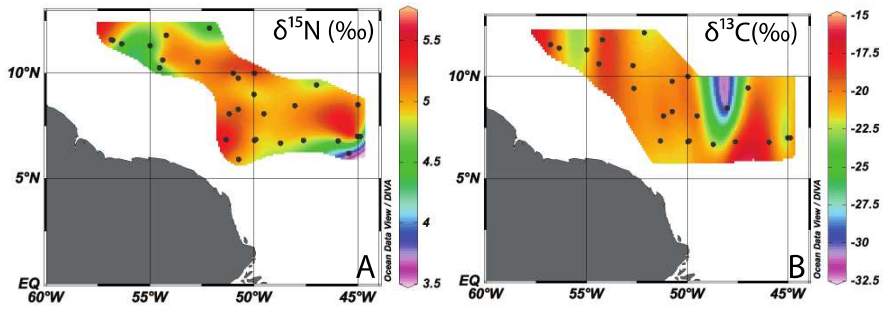

Figure 3. A) $\delta^{15}N$ of surface sediments. B) $\delta^{13}C$ of surface sediments.

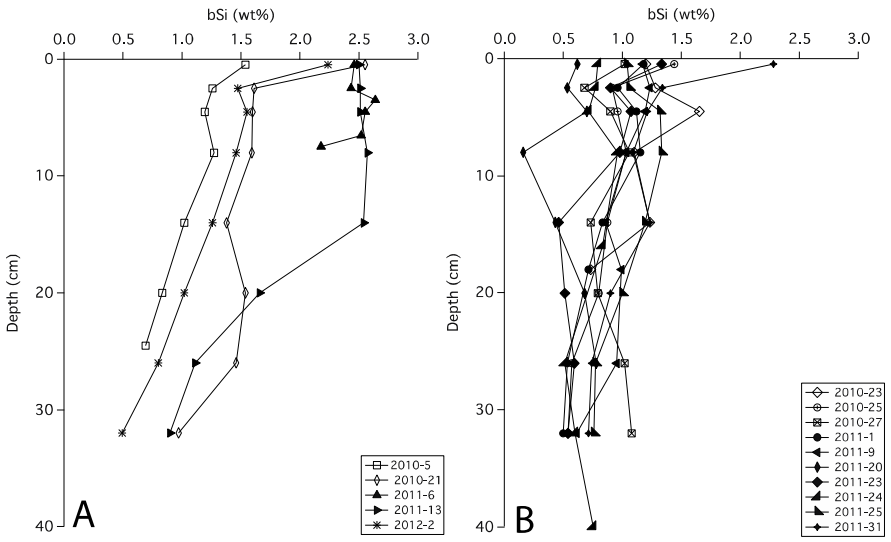

Figure 4. Downcore profiles of bSi. A) Stations from the zone south of 10°N and west of 50°W. B) All other stations.

Biogenic Silica

Biogenic SiO_2 in the sediment was measured at 10 stations throughout the study region (Fig. 4). Surface values ranged from 0.62 wt% at 2011-20 to 2.55 wt% at 2010-21. Downcore, most stations showed a decrease with depth. Station 2011-13 was consistent at 2.5 wt% before decreasing below 15 cm. In contrast, at 2011-20, the $bSiO_2$ composition was low (< 0.7 wt%) throughout the entire sediment profile.

^{210}Pb

The excess ^{210}Pb in surface sediments varied from 73 – 1155 Bq kg^{-1}, and all profiles showed a generally exponential decrease with depth (Fig. 5). Most of the profiles establish the background value of ^{210}Pb by 10 cm, though stations 2010-5, 2010-21, 2011-8, and 2011-31 show measurable excess ^{210}Pb to a depth of about 12 cm, and at station 2010-19 excess ^{210}Pb persists to 16 cm (Table 2).

^{14}C Calendar Ages

The overall ages of the sediments in the study area ranged from 614 ybp to 28069 ybp (Table 3). The age of sediments from 4.5 cm were youngest at stations 2011-9 and 2010-19 (663 ybp and 1407 ybp, respectively). The surface age increased to the northwest at stations 2011-1 and 2011-31 (2284 ybp and 3573 ybp), and was the oldest at station 2011-23 (4985 ybp) in the east.

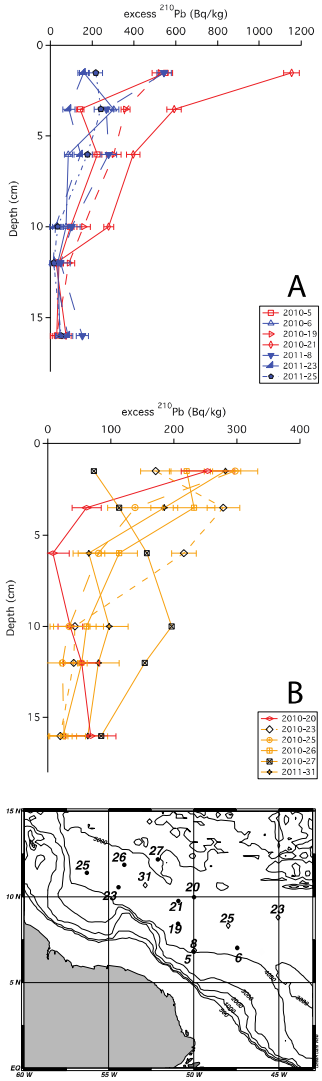

Figure 5. Downcore profiles of excess ^{210}Pb. A) Stations south of 10°N. B)Stations north of 10°N. Red: stations south of 10°N and west of 50°W. Yellow: stations north of 10°N. Blue: stations east of 50°W.

Table 2. Excess ^{210}Pb Inventory, mixing coefficient, and sediment mixed layer depth.
(*) Data did not fit an exponential, and so D_b was not determined

Station	Depth (m)	Inventory (dpm cm^{-2})	D_b (cm^2 yr^{-1})	D_b Error[b] %	Mixing Depth (cm)
2010					
5	3975	77	0.4	32	12
6	4088	56	3.1	71	12
19	4854	115	1.3	12	16
20	4854	33	0.06	67	6
21	4863	133	0.6	20	12
23	4486	60	1.1	62	10
25	4465	42	0.3	15	10
26	4777	61	1.6	22	12
27*	5044	68			10
2011					
8	3997	97	1.2	24	12
23	4709	50	2.8	66	10
25	4526	56	1.3	35	10
31	4889	51	1.4	36	12
Water Column[a]					
	3800	54			
	4950	82			

[a] Total water column inventory (in situ production plus atmospheric input) from the central tropical North Atlantic (Cochran et al., 1990)

[b] Error was determined through propagation of the error of the fitting parameters

Table 3. Calendar ages calculated from the $\Delta^{14}C$ measurements.

Station	UCIAMS #	Depth cm	Calendar Age Range ybp		Average
2011-1	117880	4.5	2360	2208	2284
	107608	16	4633	4482	4558
	117881	22	6627	6467	6547
	117882	28	7707	7589	7648
	107609*	34	5872	5709	5791
2011-9	117883	4.5	711	614	663
	107610	16	2820	2750	2785
	107611	38	8458	8359	8409
2010-19	117876	4.5	1459	1355	1407
	107612	18	2741	2540	2641
	107614	38	7234	7063	7149
2011-23	117885	4.5	5061	4908	4985
	107615	16	10600	10441	10521
	107616	41.5	20289	19827	20058
2011-31	117884	4.5	3642	3503	3573
	107617	16	5665	5547	5606
	107618	38	10541	10334	10438
2010-21	117877	24	3453	3314	3384
	107620	30	5300	5085	5193
	107621	42	7428	7289	7359
2010-27	117878	16	9134	8980	9057
	117879	38	28069	27003	27536
2011-20	117887	16	10240	10058	10149
	117888	24	11100	10753	10927
2011-25	117889	16	8047	7923	7985
	117890	36	10279	10133	10206

* Calendar age is significantly different from the other samples and was not used in the calculation of the sedimentation rate.

Sediment Traps

The mass flux at 150 m ranged from 50 ± 8 mg m^{-2} d^{-1} at station 2010-25 to 1149 ± 1 mg m^{-2} d^{-1} at station 2011-13 (Table 4). The mass flux at 250 m, ranged from 67 ± 11 mg m^{-2} $^{-1}$ at station 2011-29 to 809 ± 272 mg m^{-2} d^{-1} at station 2011-13. At stations where traps were at both depths, one station showed a decline in flux with depth (2011-13), one was relatively constant with depth (2011-29) and one showed an increase in mass flux with depth (2011-26). The station with the highest flux in 2011 (2011-13) was ~ 4X larger than the highest flux observed in 2010 (2010-9). Both of these deployments occurred along the core axis of the plume, however the traps at 2011-13 were carried to the SE by the retroflecting plume. The other stations from each year were otherwise comparable to one another.

The POC flux at 150 m was highest at station 2011-13 (4.2 ±0.3 mmol $^{-2}$ d^{-1}) and lowest at stations 2010-25 and 2011-29 (0.5 ± 0.1 mmol m^{-2} d^{-1}). Biogenic silica was also highest at station 2011-13 and was lowest at station 2010-27 (2.41 ± 0.03 mmol $m^{-2}d^{-1}$ and 0.04 ± 0.01 mmol m^{-2} d^{-1}, respectively). The C:N ratios in the 150 m traps ranged from 5.70 to 10.2. The stations closest and furthest from the river mouth had a C:N of ~ 6, while the others were around 8-10.

The $\delta^{15}N$ isotopes from the 150 m traps ranged from 2.68 ± 0.98‰ to 4.83 ± 0.89 ‰, and did not reveal any distinct spatial patterns. The lightest values (≤ 3‰) were observed at station 2010-25, 2010-27, 2010-13, and 2011-29. Stations 2010-9, 2010-13, 2010-23 and 2011-26 had heavier values 4.3-4.8‰.

Table 4. Sediment trap fluxes and isotopic measurements.

Station	Depl. Time	Trap Depth	Mass Flux	POC	PN	CaCO3	bSi	$d^{13}C(C_{org})$	$d^{15}N$	C:N	Si:C
	(hrs)	(m)	(mg/m^2d)	($mmol/m^2d$)				(‰)	(‰)		
2010											
9	27	150	319 ±19	1.7 ±0.1	0.29 ±0.1	1.4 ±0.1	1.1 ±0.2	-21.5	4.32 ±0.25	5.86	0.65
13	44	150	117 ±20	1.0 ±0.2	0.18 ±0.02	0.3 ±0.1	0.37 ±0.07	-22.1 ±0.9	3.54 ±0.78	5.70	0.37
23	48	150	87 ±12	1.0 ±0.2	0.10 ±0.03	-	0.26 ±0.05	-22.4 ±1.7	4.83 ±0.89	10.2	0.26
25	44	150	50 ±8	0.5 ±0.1	0.08 ±0.02	0.3 ±0.1	0.10 ±0.02	-20.4 ±0.6	2.87 ±0.91	5.93	0.20
27	30	150	52 ±7	0.7 ±0.1	0.04 ±0.01	0.3 ±0.02	0.04 ±0.01	-21.7	2.68 ±0.98	6.05	0.06
2011											
13	63	150	1149 ±1	4.2 ±0.3	0.51 ±0.02	0.5 ±0.1	2.41 ±0.03	-21.6 ±0.6	4.73 ±0.57	8.31	0.57
13	63	250	809 ±272	2.8 ±0.9	0.38 ±0.1	0.8 ±0.3	0.67 ±0.09	-20.5 ±0.2	4.72 ±0.24	7.48	0.24
26	32	150	73 ±14	0.8 ±0.1	0.09 ±0.01	0.2 ±0.2	0.03 ±0.02	-23.6 ±0.4	4.26 ±0.16	8.22	0.04
26	32	250	114 ±1	0.8 ±0.1	0.09 ±0.01	0.1 ±0.1	0.14 ±0.07	-24.1 ±0.1	3.68 ±0.37	8.94	0.18
29	44	150	52 ±19	0.5 ±0.1	0.05 ±0.01	0.1 ±0.1	0.10 ±-0.04	-27.6 ±0.4	2.87 ±0.53	8.68	0.20
29	44	250	67 ±11	0.9 ±0.3	0.08 ±0.05	0.2 ±0.3	0.08 ±0.04	-25.3 ±1.6	1.43 ±0.42	13.6	0.09

The average $\delta^{13}C$ (C_{org}) of the 150 m trap material was generally consistent, approximately -22 ± 1.5 ‰ (Table 4). However, station 2011-29 was significantly lighter than the others at -27.6 ± 0.4 ‰. The average $\delta^{13}C$ (C_{org}) of the 250 m trap material was slightly heavier than that shallow trap at stations 2011-26 and 2011-29, but was slightly lighter at station 2011-13.

DISCUSSION

Sediment Mixing

Bioturbation of sediments influences early diagenesis, affects the physical structure of the sediments, and can impact the burial efficiency (Green et al., 2002; Sun et al., 1993). We assessed the amount of sediment reworking throughout our study area using measurements of the radionuclide ^{210}Pb. Excess ^{210}Pb in the sediments is derived from sinking particles scavenging ^{210}Pb from the water column. In the absence of sediment mixing, excess ^{210}Pb should only be found in the uppermost millimeters given the low sedimentation rates in this area. Any excess ^{210}Pb in the sediments at depth will have been introduced, presumably, by macrofaunal mixing (Rhoads, 1974; Aller, 1982). Measurements of excess ^{210}Pb in a sediment profile allows an estimate of the bioturbation diffusion coefficient, the inventory of excess ^{210}Pb in the sediments, and provides a measure of the sediment mixed layer (SML) depth.

To determine the bioturbation coefficient (D_b), we assumed that bioturbation is a diffusion-like process (Berner, 1980; Guinasso and Schink, 1975) and fit the excess ^{210}Pb data with the solution to the steady-state diagenetic equation solved by Stephens et al., (1997):

$$A = A_0 \exp(-\alpha z) \quad (1)$$

where A is the activity concentration of ^{210}Pb in Bq kg^{-1}, A_0 is the activity concentration at z=0, and α is the attenuation coefficient (yr^{-1}). A_0 was allowed to be a free parameter in the model fit to the data. Activity is related to D_b by the following:

$$\alpha = (\lambda / D_B)^{1/2} \quad (2)$$

where λ is the radioactive decay constant for ^{210}Pb (yr^{-1}).

The values of D_b derived from fits to the data ranged from 0.06 to 3.1 cm^2 yr^{-1} (Table 2) These are within the range of the mixing rates observed in the Equatorial Pacific (<0.1-16.9 cm^2 yr^{-1}) (Stephens et al., 1997) and are similar to other estimates from the deep ocean (Barsanti et al., 2011; Basso et al., 2004; DeMaster et al., 1985; Kuehl et al., 1993; Teal et al., 2008; Thomson et al., 1993). We did not observe any significant spatial patterns of D_b throughout the study area. However, there did appear to be an inverse relationship between D_b and surface wt% C_{org}; in areas of high C_{org}, the D_b was quite low (i.e. stations 2010-20, 2010-21), while where C_{org} was low, the D_b was high (i.e. stations 2010-26, 2011-23). This is curious, because it is generally believed that higher rates of mixing are correlated to higher macrofaunal

abundance, and thus higher availability of C_{org}. The high amount of macrofaunal activity in an area of low C_{org} concentrations is perhaps caused by macrofauna having to 'work harder' to find sufficient C_{org} to survive.

Alternatively, the mixing of sediments due to bioturbation may reduce surface sediment C_{org} concentrations. We examined this possibility mathematically by first assuming that the concentration of C_{org} in the sediments can be described by an exponential equation:

$$C = C_0 \exp(-ßz) \qquad (3)$$

where C_0 is the concentration of C_{org} at the SWI, $ß = \sqrt{(k/D_b)}$, and k is the rate constant of C_{org} degradation. If we use Fick's first law to describe the C_{org} flux into the sediments, we obtain

$$C_{org} \text{ flux} = -D_b \frac{dC}{dz} \qquad (4)$$

Applying Eq. 3, differentiated at z = 0, Eq. 4 becomes

$$C_{org} \text{ flux} = C_0 \sqrt{kD_b} \qquad (5)$$

If the flux and k are constant, there should be an inverse relationship between C_0 and $\sqrt{D_b}^{-1}$. Comparing C_0 and $\sqrt{D_b}$, we found that while the bioturbation rate has some influence, it does not control the surface C_{org} concentration. Variations in the delivery or reactivity of C_{org} are likely to be more important (Appendix B).

If scavenged ^{210}Pb is carried by sinking particles to the deep ocean, the total inventory of water column ^{210}Pb should be equal to the inventory of excess ^{210}Pb

found in the sediments. To calculate the sediment inventory, we first calculated the integrated sediment density based on the porosity profile over the upper 17 cm. We then used these intervals of sediment density to graphically integrate the amount of excess ^{210}Pb in each layer, obtaining the sediment inventory of excess ^{210}Pb, which ranged from 42 to 133 dpm cm^{-2}. Stations with a higher ^{210}Pb inventory appeared to correlate to the stations with elevated C_{org} wt% south of 10˚N and west of 50˚W. This indicates that the high amount of C_{org} observed on the sea floor from this area may be linked to the source of excess ^{210}Pb.

Cochran et al., (1990) estimated the total water column supply of ^{210}Pb at various stations throughout the North Atlantic. At stations in the tropical north Atlantic closest to our study area, the total inventory of the water column was estimated to be 54 dpm cm^{-2} at a 3800 m site, and 82 dpm cm^{-2} at 4900 m. Many of our stations fall within this range, though 2010-19, 2010-21, and 2011-8 were all much higher. These three stations stations have a larger than expected inventory of ^{210}Pb given what is expected in the water column from *in situ* production and atmospheric deposition (constituting 25-40% of the total water column supply) and scavenging in a purely 1-D scenario.

Stations with high inventories of excess ^{210}Pb may have experienced a large amount of sediment focusing by deep ocean currents. We examined this possibility by using ^{230}Th-normalized fluxes measured by colleagues at LDEO to calculate sediment focusing factors (Ψ) following Francois et al., (2004). ^{230}Th activity was measured from surface sediments (1-3 cm), and focusing factors were evaluated as

the accumulation rate of unsupported ^{230}Th in the sediment divided by the production rate of ^{230}Th in the overlying water column. Because ^{230}Th needs to be age-corrected, the cores in which ^{230}Th was measured are sites where ^{14}C was measured (Table 5). Stations 2010-19 and 2010-21 showed very little focusing, while stations 2011-1, 2011-23, and 2011-31 show net gain of thorium with focusing factors ranging from 1.4-1.6. Stations 2010-27 and 2011-9 show some winnowing of the sediments with focusing factors of 0.5-0.6. We compared these focusing factors with the inventories of excess ^{210}Pb normalized to a water column inventory of 68 dpm cm^{-2} (Fig. 6). Stations in the region south of 10˚N and west of 50˚W showed relatively high values for the inventories of excess ^{210}Pb, while the ^{230}Th-derived focusing factors were close to 1; stations 2010-19 and 2010-21 showed little focusing based on ^{230}Th (1.05-1.07) while the excess ^{210}Pb inventories were greater than the water column supply by ~2X at these stations. Stations 2010-5 and 2011-8 also had somewhat elevated inventories.

A large inventory of excess ^{210}Pb does not necessarily mean that there is additional sediment being delivered to a particular site since ^{210}Pb is not completely scavenged from the water column; this was confirmed by our analysis of sediment focusing. In areas with a high sedimentation rate, the amount of ^{210}Pb scavenged from the water column will be high, and can be further inflated by the addition of ^{210}Pb advected into the area from nearby waters with a lower sedimentation rate. The additional ^{210}Pb could also be brought in from outside the study area, perhaps from the continental shelf and/or from particles carried by the river plume. Suspended riverine material has an excess ^{210}Pb activity ranging from 10-34.5 ± 6.5

Table 5. Excess ^{210}Pb inventories normalized to the water column and sediment focusing factors derived from ^{230}Th

Station	^{210}Pb-Norm. Inventory[a]	Focusing Factor Ψ
2010		
5	1.1	
6	0.8	
19	1.7	1.05
20	0.5	
21	2.0	1.07
23	0.9	
25	0.6	
26	0.9	
27	1.0	0.60
2011		
1		1.41
8	1.4	
9		0.50
23	0.7	1.60
25	0.8	
31	0.8	1.51

[a] Excess ^{210}Pb inventories were normalized to a water column average of 68 dpm cm^{-2}

[b] Focusing factors derived from ^{230}Th-normalized fluxes

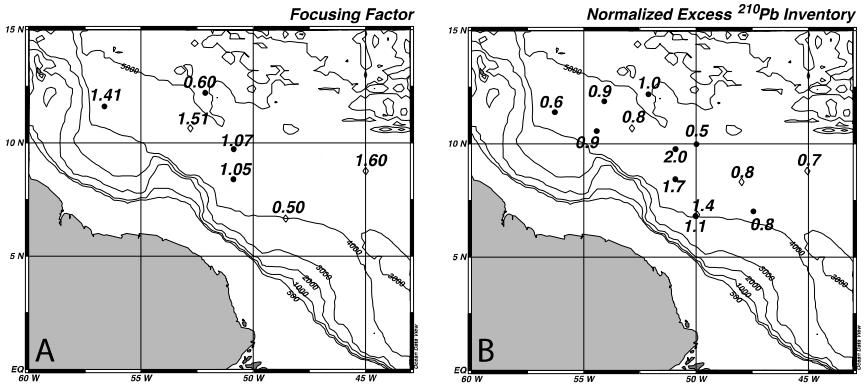

Figure 6. A) ^{230}Th-normalized sediment focusing factors. B) Excess ^{210}Pb inventories normalized to an average water column inventory.

Bq kg^{-1}, and inventories of excess ^{210}Pb from the seabed of the Amazon shelf range from 667-2000 Bq kg^{-1} (DeMaster et al., 1986; Smoak et al., 1996). Since much of the suspended sediment (85-95%) dispensed from the Amazon River is fine-grained silts and clays (Gibbs, 1976), and the shelf experiences intense reworking of the seabed through mobile mud belts (Kineke et al., 1996; Nittrouer et al., 1995; Wells and Coleman, 1981), it is quite likely that some of this material is advected seaward. It is also possible that additional ^{210}Pb is carried to the region by Antarctic Bottom Water, which spreads through the western basins of the West Atlantic as it moves northward (Stramma and England, 1999).

The depth of the mixed layer was determined by examining where the sediment profiles became depleted in excess ^{210}Pb (Fig. 5). Generally, this depth was ~10-12 cm below the SWI, though it was as shallow as 6 cm at station 2010-20 and as deep as 16 cm at station 2010-19. However, this only defines the depth of sediment mixing on the time scale of ^{210}Pb. With a half-life of 22.3 years, mixing determined by this tracer is only applicable to sedimentary processes that occur on the order of 30-100 years (Cochran et al., 1990; Craig et al., 1973; Rama and Goldberg, 1961). The sediment profiles of C_{org}, $CaCO_3$, and bSi indicated which sites and sedimentary constituents are affected on this time scale (Figs. 2, 3). We would expect constituents with longer residence times than ^{210}Pb to have a near-constant concentration in the upper 10 cm of the profile. The profiles of C_{org} do not show this consistency, rather, many profiles decrease exponentially with depth. In contrast, the upper 5-15 cm of the $CaCO_3$ profiles appeared to be well mixed for nearly all of the stations. Most of the profiles of bSi showed little evidence of mixing, with the

exception of stations 2011-6 and 2011-13, which appeared to be mixed down to ~ 8 cm and16 cm, respectively.

This comparison of ^{210}Pb mixing depths and the profiles of the biogenic components provides an indication of the reactivity of each biogenic constituent. Because the profiles of C_{org} showed little evidence of mixing predicted from the excess ^{210}Pb profiles, we can infer that reactions involving the degradation of C_{org} occur on a timescale of <100 years. At most stations, the dissolution of bSi also appeared to occur on a relatively fast time scale based on the downcore profiles, though at stations 2011-6 and 2011-13, which are our closest sites to the river mouth, bSi was well mixed to 8-16 cm (Fig. 4). The profiles of $CaCO_3$ indicate that reactions involving the dissolution or precipitation of $CaCO_3$ are fairly slow relative to the other biogenic materials, and are generally mixed on a similar time scale as ^{210}Pb.

Sedimentation Rates

We plotted the calendar age vs. depth for each station to determine the linear sedimentation rates below the ML (Table 6, Fig. 7). At most stations, the age was measured at 4.5 cm and for these cores, two sedimentation rates were calculated. We first assumed that the depth of the ML extended to 4.5 cm and included this data point in the linear fit. We alternately extrapolated the age of the ML to a depth of 10 cm, and used the age of sediment at 4.5 cm as a 'hypothetical' point in the linear fit. A previous study on the Iberian Abyssal plain found that the ML from excess ^{210}Pb

Table 6. Sedimentation rates and burial fluxes at stations where $\Delta^{14}C$ was measured. Sed. rates assuming a ML of 10 cm were used to calculate the burial fluxes. MAR and burial fluxes were determined below 16 cm.

Station	ML Sed Rate (cm kyr^{-1})	Sed. Rate[b] (cm kyr^{-1})	Sed. Rate[c] (cm kyr^{-1})	Average φ	MAR (g cm^{-2} kyr^{-1})	C_{org} Burial (mmol $m^{-2}d^{-1}$)	bSi Burial (mmol $m^{-2}d^{-1}$)	C_{org} Remin.[d] (mmol $m^{-2}d^{-1}$)	bSi Remin.[d] (mmol $m^{-2}d^{-1}$)	C_{org} f_{buried} (%)	bSi f_{buried} (%)
2010-19	25.4	3.99	5.45	0.75	5.01	0.07	0.04	0.45	1.35	13.4	-
2010-21	3.9	4.55	-	0.77	5.53	0.08	0.04	0.47	0.34	15.5	9.2
2010-27*	2.6	1.19	-	0.74	1.62	0.01	0.01	0.16	0.27	5.5	2.0
2011-1	6.2	3.24	4.22	0.69	4.55	0.04	0.01	0.29	0.48	11.4	3.5
2011-9		3.46	4.24	0.67	4.35	0.06	0.02	0.47	0.56	10.0	3.0
2011-23	1.8	2.15	2.48	0.71	2.95	0.02	0.01	0.32	0.36	6.3	1.7
2011-31	3.2	3.92	4.82	0.77	5.04	0.05	0.02	0.39	0.36	16.5	7.3

C_{org} wt% from below the depth of ^{210}Pb mixing (~14cm)

[a] Station only had calendar ages from two depths

[b] Sed. Rate assuming a ML of 10 cm

[c] Sed. Rate assuming a ML of 4.5 cm

[d] Remineralization fluxes from Chapter 2

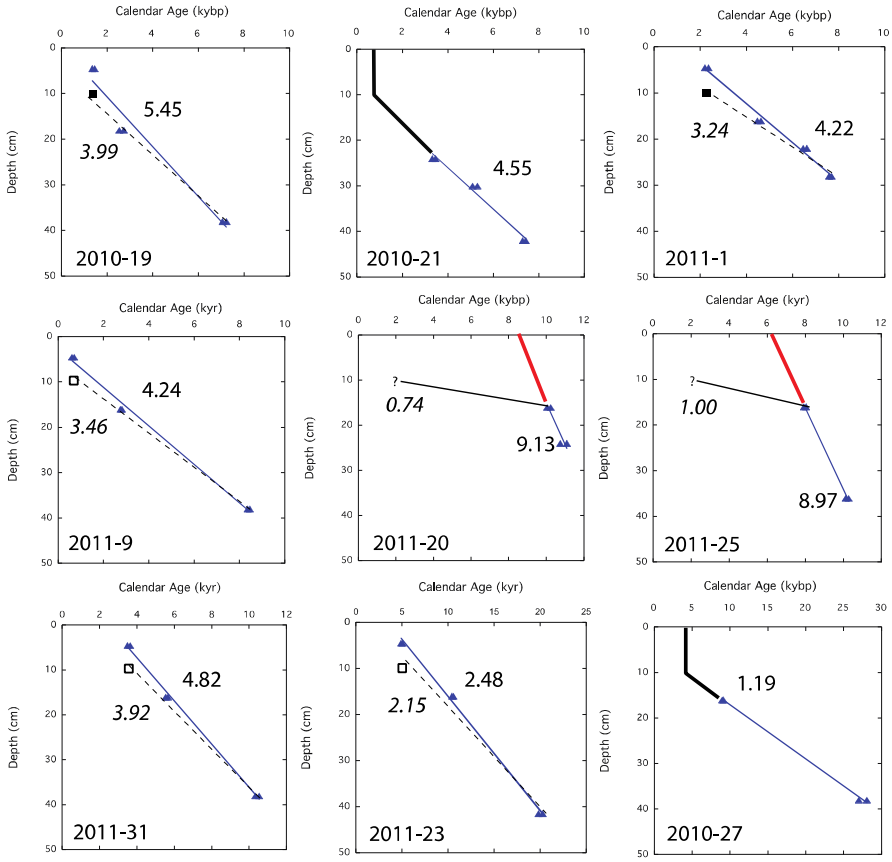

Figure 7. Linear fits to the calendar ages. Units of sedimentation are cm/kyr. Sedimentation rates calculated assuming a mixed layer (ML) depth of 4.5 cm. ▫ represent the age of mixed zone extended to 10 cm. Dashed lines show the fit if the ML was extended to 10 cm, and the sedimenation rate from this fit is italicized. At stations without an age from the ML, fits have been extrapolated back to the surface. Solid black lines assume the depth of the mixed zone extends to 10 cm. Red lines reflect sedimentation rates that are inconsistent with a ML with an average age of 2 kyr. Dotted lines are an extrapolation to an assumed ML of 2kyr extending to 10 cm depth.

profiles and a high-resolution profile of ^{14}C ages was ~ 5 cm for both tracers (Carvalho et al., 2011). Based on our ^{210}Pb ML data, we believe that a ML of 10 cm is more realistic for estimating the sedimentation rate, hence our subsequent calculations assume a deeper mixed layer. A shallower ML would result in an increase in the sedimentation rate of 15-25%.

Three stations only had 2 depths from which to calculate the sedimentation rate and are therefore more sensitive to potential errors in the ^{14}C age estimates. At these stations, the trend from two data points was extrapolated to 10 cm. At stations 2010-21 and 2010-27, this extrapolation yielded an age of the ML that is within the range of the other stations, and so we believe these rates to be reasonable. In contrast, stations 2011-20 and 2011-25 extrapolated to ages that are not consistent with an average ML age of ~2000 ybp, and these stations would require a significant decrease in the sedimentation rate in the upper 20 cm in order to agree with our estimations of the ML depth and age. The age of the sediments from these cores correlate to the earliest Holocene, and so it is possible that the sedimentation rates were higher at that time due to lower sea levels. From the same area, previous estimates of the sedimentation rates during the last glacial period ranged from 5-30 cm kyr^{-1} (Damuth, 1977). However, at station 2011-23 and 2010-27, the sediment age reached back to the last glacial maximum and the data fit indicated that sedimentation has been relatively consistent throughout the Holocene. Since we do not have a good constraint on the Holocene sedimentation rate at stations 2011-20 and 2011-25 due to the limited sampling resolution, we have chosen to omit them from the subsequent discussion of burial fluxes below.

Since the age of the mixed layer is a function of the sedimentation rate and the ML depth, we employed a simple box model to assess potential changes in the sedimentation rate during the last few thousand years (Appendix B). Assuming steady state, the ^{14}C activity of incoming material to the ML will be equal to the loss due to burial and decay. Using the depth of the ML derived from the excess ^{210}Pb profiles, and assuming the age of new material is equal to the deep water reservoir age of 800 years for this region (Broecker et al., 1999), we can calculate the sedimentation rate of the ML and compare it to the sedimentation rate at depth. Results from this simulation show that the sedimentation rates within the ML are generally slower than or the same as the rates below, though a few stations had rates that were faster. Station 2010-19 had an ML sedimentation rate that was 4X larger than the rate at depth, however, this is largely a function of the depth of the ML, as a fast rate would be required to turn over 16 cm of sediment. Given the uncertainties in the ML depth, it is likely that sedimentation rates have either remained constant or decreased since the beginning of the Holocene and calculations using the sedimentation rates at depth should provide a good estimate of the burial flux (Table 6).

Our estimates of the sedimentation rate below the ML in this area ranged from 1.19 – 4.55 cm kyr^{-1}, which are in good agreement with previously reported rates for the Demerara Abyssal Plain (2-4 cm kyr^{-1}) (Damuth, 1977). Higher sedimentation rates occur in the area south of 10 °N and west of 50°W (Fig. 8). Within this area, the average sedimentation rate is 4.3 ± 0.4 cm kyr^{-1}. North and east of this area, sedimentation rates are lower and generally similar, 2.8 ±1.4 and 3.0 ±

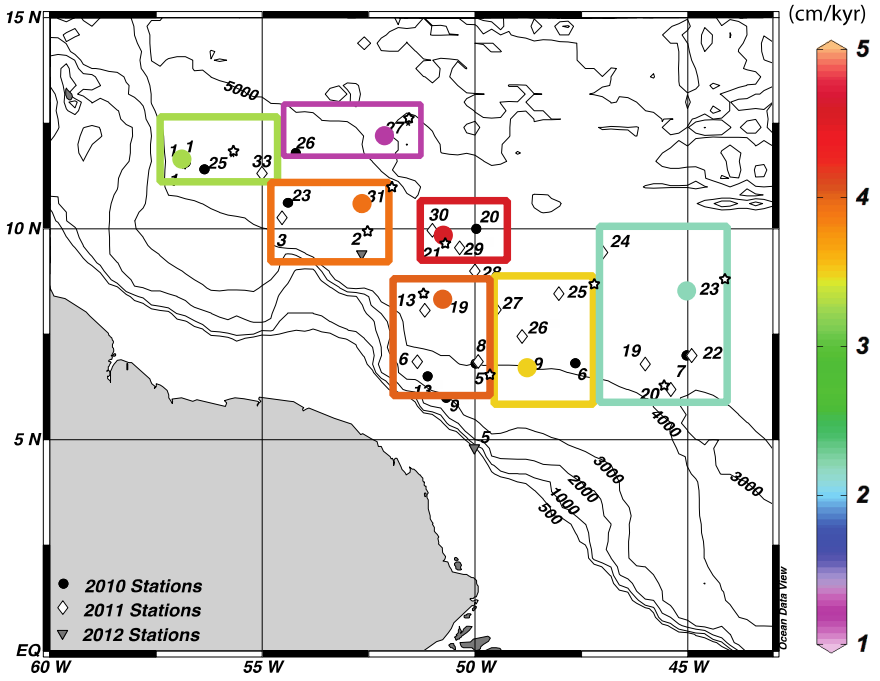

Figure 8. Extrapolation of sedimentation rates to surrounding stations. Colored circles indicate the stations where ^{14}C ages were measured and the color represents the sedimentation rate. The colored box around each group of stations shows where this sedimentation rate was applied to other stations. Starred stations are where bSi was measured. All stations shown had Corg measured.

1.2 cm kyr^{-1}, respectively. Thus, the early-Holocene sedimentation rates from the eastern portion of the study area are comparable to the northern area, despite only being affected by the Amazon Plume for a few months out of the year.

Surface Patterns and Deposition of Biogenic Materials

The overall composition of C_{org} in the sediments was <1 wt% throughout the study area, however, there was still a distinct pattern in the distribution of C_{org} in surface sediments (Fig. 9A). The zone of the highest sediment C_{org} content is centered near 10˚N 50˚W, covering much of the central part of our study area. North of 11˚N and east of 50˚W, the C_{org} wt% decreased from ~0.9 wt% by nearly a factor of 2.

Biogenic silica followed a similar distribution pattern to C_{org} (Fig. 9C), with the highest surface sediment values appearing south of 11 ˚N and west of 50˚W. The bSi content of the sediments dropped off sharply further north and east decreasing from ~2.5% in the center to <1% in the north and east.

The carbonate content of the sediments displayed a pattern opposite to C_{org} and bSi (Fig. 9B). The stations south of 10˚N and west of 50˚W had low carbonate concentrations (<10%), while the stations to the north and east were generally higher (~30 wt%), reaching ~55 wt% in the stations near 45 ˚W.

Seiter et al., (2004) regionalized the global ocean with respect to benthic biogeochemical provinces. Our data fall near the border of the GUBRACO and

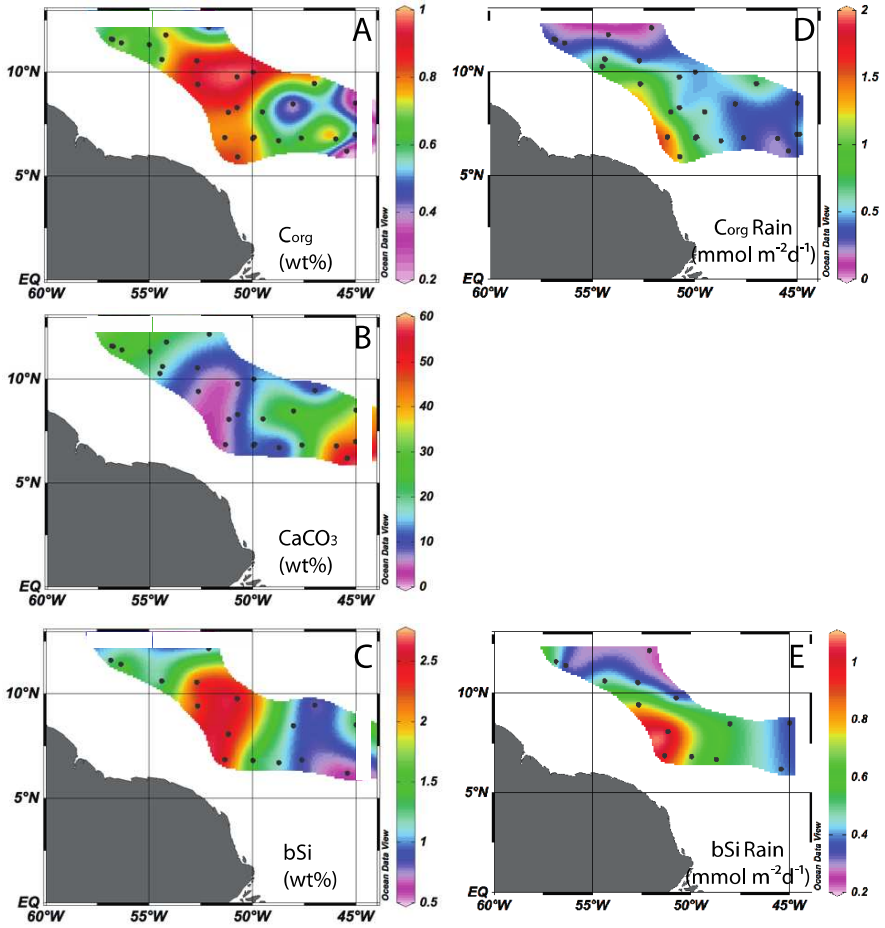

Figure 9. Spatial patterns in surface sediment biogenic composition and total rain (remineralization + burial) to the sea floor.

NOATL regions, defined as the continental margin of SE-America (Guyana) and the Northern Atlantic deep sea, respectively. For these regions, the mean Opal %, Calcite % and TOC % were 2.4%, 46.5%, 0.4% (GUBRACO) and 3.5%, 44.3%, 0.4% (NOATL) respectively. For our study, the mean surface sediment composition was 1.5% 21.0% and 0.67%, respectively, indicating that the deep-sea sediments influenced by the Amazon River plume have a greater C_{org} content and less carbonate and biogenic opal than other deep North Atlantic sites.

We divided our study area into three specific zones to better assess the influence of the NW plume vs. the eastern retroflection on sediment composition. One caveat of this survey is that bioturbation will mix recently deposited sediment with deeper, older sediments; however, the D_b is fairly similar across the study region, and so changes to the sediment composition due to bioturbation should be somewhat uniform. For this discussion, we acknowledge this caveat and treat the surface sediment as some reflection of recent sedimentation processes.

We defined Zone A as the area south of 10˚N and west of 50˚W, zone B contains the stations north of 10˚N, and zone C is east of 50˚W. Three stations (2010-27, 2011-9, 2011-24) fell outside of the area of plume influence based on 10-year average salinity (Chapter 2). Comparing the composition of biogenic materials (Fig. 10), we see that stations with the highest C_{org} wt% also have the highest bSi wt%, and that these stations tend to be in zones A and B. The zone C stations have the least C_{org} and bSi, and the highest carbonate content of these sediments. The wt % of a biogenic constituent will be a function of both its input and preservation but

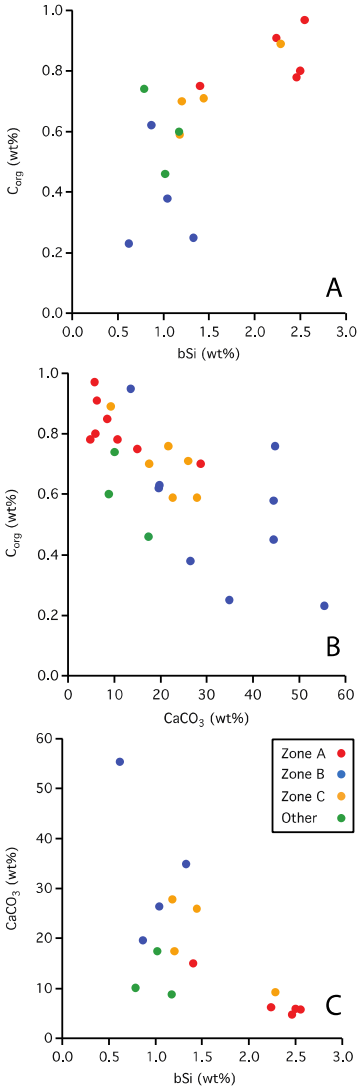

Figure 10. Comparisons of the concentration of biogenic components in the surface sediments across the study area. Zonations are described in the discussion.

also dilution with other constituents. For example, both C_{org} and bSi appear to be anti-correlated with $CaCO_3$. This could represent differences in ocean ecological structure or carbonate could be a 'dilutant' to C_{org} and bSi in this system. Most C_{org} and bSi-rich surface sediments occur closer to the Amazon River mouth, while the most $CaCO_3$ is found to the east in the area of the retroflection.

The best way to extract information about the role of oceanic ecology and sediment dilution is to calculate biogenic mass accumulation rates. Using the sedimentation rates from this study, we determined sediment mass accumulation rates, and burial fluxes of C_{org} and bSi. We calculated an average porosity from the profile at each site (Appendix B) and assumed a dry sediment density of 2.5 g cm^{-3} to calculate the bulk density of the sediments. The burial rates were calculated as:

$$\rho_b = (1 * \bar{\phi}) + \left(2.5 * (1 - \bar{\phi})\right) \qquad (6)$$

$$MAR = (C/100) * \rho_b * \omega * 1000 \qquad (7)$$

where ρ_b is the bulk density, $\bar{\phi}$ is the average porosity, MAR is the mass accumulation rate of a particular component, C is the wt% of C_{org} or bSi from a depth of 14-16 cm, and ω is the sedimentation rate. The average porosity was determined from the depths between calendar age measurements. The wt% was chosen from a depth presumed to be just below the ML. MARs were subsequently converted to flux units (mmol m^{-2} d^{-1}).

Burial fluxes were quite low, ranging from 0.01 – 0.08 mmol C m^{-2} d^{-1} and 0.01-0.04 mmol Si m^{-2} d^{-1} (Table 6). We extrapolated the sedimentation rates from

the seven stations to nearby regions (Fig. 8) to calculate burial fluxes for C_{org} and bSi at every site where biogenic components were measured downcore. C_{org} burial fluxes from our sites are similar to values that have been measured throughout the global ocean at similar water depths: Peru Rise 0.04-0.13 mmol C m^{-2} d^{-1}, Bermuda Rise 0.004 mmol C m^{-2} d^{-1}, Hatteras Rise 0.04-0.05 mmol C m^{-2} d^{-1}, and NW Africa Rise 0.01-0.27 mmol C m^{-2} d^{-1} (Reimers et al., 1992 and references therein).

To assess deep sea rain rates, we added the burial fluxes to the remineralization fluxes reported in Chapter 2. Together, burial plus remineralization will yield a value for the total rain of biogenic material to the sea floor. As remineralization dominates this equation, the spatial patterns of C_{org} and bSi rain (Fig. 9) closely mirror the remineralization patterns observed in Chapter 2. The C_{org} rain was highest near the river mouth, where a 'tongue' of elevated C_{org} rain trends to the northwest, following the path of the spring river plume (Fig. 9D). Somewhat elevated C_{org} rain rates were also observed to the east, extending approximately along 10°N. This latitude is at the northern edge of the fall retroflection plume, when the majority of the Amazon plume waters are carried eastward by the North Equatorial Counter Current (Hu et al., 2004; Muller-Karger et al., 1988; Salisbury et al., 2011). Though limited core data limits the precision of defining the bSi pattern, bSi rain also had a locus of the highest deposition occurring in Zone A, but the attenuation gradient covered a much larger longitudinal space than with C_{org} (Fig. 9E). Thus, while it appears that the retroflection plume is important for C_{org} export, it may play a greater role in enhancing the deposition of

bSi in the deep ocean even though it only affects those waters for a few months out of the year.

A large quantity of previous work has shown that nearly all of the C_{org} that reaches the sea floor in the deep ocean is remineralized (Bender and Heggie, 1984; Burdige, 2007; Canfield, 1994; Hedges and Keil, 1995; Premuzic et al., 1982), thus the burial fluxes should be small relative to remineralization fluxes. In the ANACONDAS study area, the C_{org} burial fluxes comprised 4-16% of the total carbon rain (rain = burial + remineralization). Burial constituted ~4-7% of the total C_{org} rain along the NW axis of the plume, and at the eastern edge of the study area (Fig. 11). In the center and, in particular, the northern section of the study area, burial constituted 10-16% of the total rain. This is a surprisingly large fraction of total rain. Chong et al., (submitted) determined that approximately half of the remineralized C_{org} in the center of the study area is 'slower' reacting carbon, possibly of terrestrial origin, which may contribute to enhanced burial.

Assessment of Trap Collection

The floating sediment traps from this study yielded export fluxes of POC and bSi that were internally consistent between replicate traps (± 18% and 29%, respectively)(Fig. 12). However, flux values of rain at 150 m were of a similar magnitude as the C_{org} rain fluxes we determined at depths of 4500 m (Table 7). This is curious as the flux of sinking particles is expected to significantly attenuate with

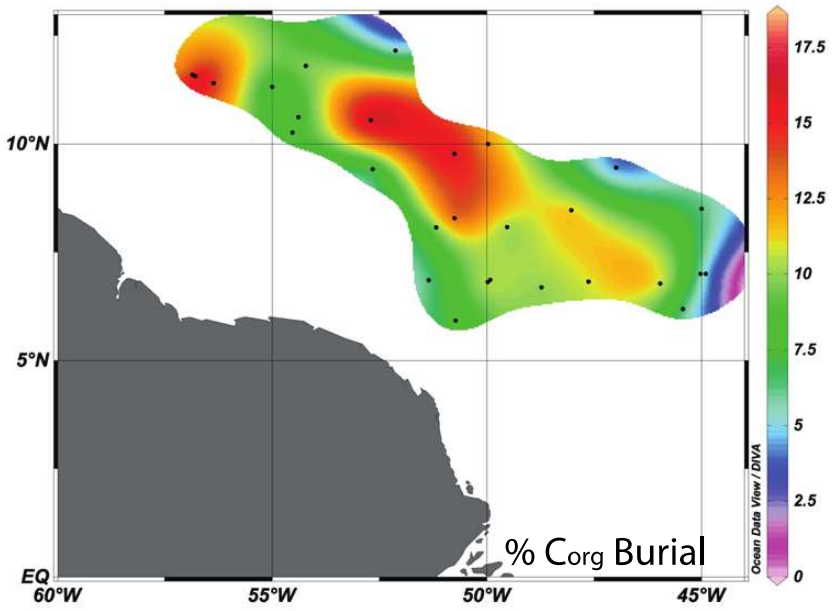

Figure 11. Spatial map of the percent of the total C_{org} rain buried in the sediments.

Table 7. Extrapolation of C_{rain} back to 100 m using the Martin curve.

Station	Water Depth (m)	C_{rain}[a] (mmol $m^{-2}d^{-1}$)	bSi_{rain}[a] (mmol $m^{-2}d^{-1}$)	C_{extrap} b=0.86[b] (mmol $m^{-2}d^{-1}$)	C_{extrap} b=0.57[c] (mmol $m^{-2}d^{-1}$)	Trap 150m POC (mmol $m^{-2}d^{-1}$)
Central Zone						
2010-5	3975	0.60	0.69	14.17	4.36	
2010-9	3014	1.22		22.89	7.88	1.7
2010-13	3500					1.0
2010-19	4854	0.52		14.65	4.11	
2010-20	4854	0.46		13.06	3.71	
2010-21	4863	0.55	0.38	15.61	4.28	
2011-6	3760	1.48	0.99	33.42	10.94	
2011-13	4450	0.83	1.04	21.81	6.57	2.8
2011-19	4205	0.24		5.87	1.77	
2011-29	4784					0.5
2011-2	4764	1.12	0.74	31.11	9.41	
Northern Zone						
2010-1	4373	0.22		5.71	1.55	
2010-23	4486	0.66	0.48	17.51	5.34	1.0
2010-25	4465	0.27	0.32	7.15	2.04	0.5
2010-26	4777	0.18		4.96	1.46	
2010-27	5044	0.17	0.28	4.93	1.50	0.7
2011-1	4362	0.33	0.49	8.44	2.50	
2011-3	4393	0.69		17.94	5.49	
2011-31	4889	0.40	0.39	11.29	3.62	
2011-33	4650	0.48		12.99	3.93	
Eastern Zone						
2010-6	4088	0.39		9.52	2.89	
2010-7	4394	0.43		11.04	3.46	
2011-8	3997	0.66		15.69	4.84	
2011-9	4030	0.52	0.58	12.43	3.83	
2011-20	4197	0.25	0.40	6.18	1.96	
2011-22	4435	0.49		12.68	4.04	
2011-23	4709	0.34	0.36	9.38	2.88	
2011-24	4784	0.68		18.87	5.89	
2011-25	4526	0.38	0.54	10.13	2.97	
2011-26	4200					0.8
2011-27	4415	0.59		15.21	4.56	

[a] Rain = remineralization+burial. Remineralization data from Chong et al., submitted

[b] C_{remin} was extrapolated to 150m using the Martin function with a b value of 0.86 (Martin et al., 1987)

[c] C_{remin} was extrapolated to 150m using the Martin function with a b value of 0.57 (based on data from Honjo 1980)

increasing depth (Martin et al., 1987; Silver and Gowing, 1991). The attenuation of the downward flux of particles sinking out of the surface ocean has been commonly parameterized as a power function known as the Martin curve: $F = F_{100}(z/100)^{-b}$, where F_{100} is the POC flux at 100 m and b is a unitless parameter describing the attenuation with depth (Martin et al., 1987). While concerns have been raised over the applicability of the Martin curve to all areas of the ocean (Buesseler et al., 2007b; Buesseler and Boyd, 2009; François et al., 2002; Howard et al., 2006; Martin et al., 2011; Schlitzer, 2002), we employed it here to obtain a qualitative estimate of the amount of surface export required to sustain the rain rates observed in the deep ocean, and thus assess the efficacy of our surface traps.

Using the 'open ocean composite' b value of 0.86, we extrapolated the deep-sea C_{org} rain rates to the surface ocean, z=100 m (Table 7). The extrapolated fluxes ranged from 4.5 -28.8 mmol m^{-2} d^{-1}, 7-17X larger than the POC fluxes established by the sediment traps. While sediment trap fluxes are subject to temporal and spatial variability in the collection of sinking particles, the systematic offset is curious. One possibility is that the Martin b-value does not accurately describe the flux attenuation at these sites. Buesseler and Boyd (2009) reported a wide range of b-values (0.27 -1.29) from locations with varying productivity throughout the global ocean; our sites may fall toward the lower range of values.

As mentioned earlier, Honjo (1980) reported flux results from a deep trap array moored at 13.5˚N 54.0˚W. We applied the power law curve fit to his POC fluxes and obtained a b value of 0.57 ± 0.02 (Appendix B), which we also applied in our

extrapolation of deep-sea rain to z=100m. That extrapolation yielded export values ranging from 1.5 – 10.9 mmol C m^{-2} d^{-1}. If our traps were capturing an accurate representation of sinking C_{org} flux, then the attenuation of flux with depth would have to be even lower than 0.57 for the trap fluxes to be coherent with the benthic fluxes. Very little attenuation in the flux with depth over 4000 m may arise if particles are sinking extremely quickly and/or if the C_{org} is rather refractory.

Another possible explanation of the trap and deep-sea rain 'imbalance' may involve uncertainties in the trap data. Hydrodynamic biases may influence trap fluxes. One of the concerns with surface tethered sediment traps is that the lateral movement of the water will affect the collection efficiency of the traps by altering the motion of sinking particles (Buesseler et al., 2007a; Gardner et al., 1997; Gust et al., 1992; Haskell et al., manuscript submitted to Deep Sea Research). Lateral advection can not only influence the trap collection efficiency (where traps can both over-collect and under-collect), but also impact the horizontal 'spread' of sinking particles throughout the water column (Deuser et al., 1990; Siegel et al., 1990; Siegel and Deuser, 1997).

Under low-flow conditions (<10 cm sec^{-1}), it has been shown that bulk fluxes of mass, POC and PON are similar between PITs style traps and neutrally buoyant traps, but there were significant differences in ^{234}Th, Si, and fecal pellet fluxes (Buesseler et al., 2000; Stanley et al., 2004). There is not yet a clear consensus of the effect of higher flow speeds. Hu et al., (2004) estimated a surface advection speed of 35 cm sec^{-1} within the plume in July based on the movement of a peak in colored

dissolved organic matter (CDOM), and a speed of 8-20 cm sec^{-1} for anti-cyclonic eddies forming in the plume. These elevated speeds could impact our traps, though not all the traps were deployed in plume waters. Additionally, Coles et al., (manuscript submitted to J. Geophys. Res.) show that the plume introduces vertical and lateral density gradients that alter the geostrophic flow, creating vertical shear in the upper 20 m of the water column (10-50 cm sec^{-1}) that can influence and intensify the surface flow. The complex physical dynamics of the Amazon Plume almost certainly have an impact on the efficacy of floating sediment traps and it is possible that our results are a lower estimate of the surface export flux.

To ascertain approximately how much POC is exported from the surface ocean in the Amazon Plume region, we compared the values of total surface C_{org} export from previous work with our extrapolated fluxes and trap. Subramaniam et al., (2008) calculated a total surface export flux of 2.3 Tmol C yr^{-1}, based on N_2 fixation rates of DDAs plus the amount of C_{org} that could be produced from the riverine supply of nitrate. Yeung et al., (2012) estimated surface export based on biological DIC uptake and total oxygen productivity, and their fluxes averaged over the total plume area yielded export rates of 3.4 and 3.3 Tmol C yr^{-1}, respectively. Benthic extrapolations of total C_{org} rain over the total plume area yield a rate of 3.9 Tmol C yr^{-1} when using a b-value of 0.86, and a rate of 1.7 Tmol C yr^{-1} if we use a b-value of 0.57. Averaging the sediment trap fluxes over the plume area produces a total export flux of 0.28 Tmol C yr^{-1}. The coherence between the Yeung et al., estimates and the benthic extrapolations when b = 0.86, is impressive. Model predictions showed that the tropical North Atlantic should be a source of 2.5 Tmol C

yr^{-1} to the atmosphere (Mikaloff Fletcher et al., 2007). However, these results indicate that the Amazon Plume is a significant sink for carbon, as previously suggested by Subramaniam et al., (2008).

Composition of Sinking POM vs. Seafloor Values

The composition of sinking material may provide some insights about the material that is sinking that that aren't evident from the fluxes alone. Most of the stations had a $\delta^{13}C(C_{org})$ at 150 m between -20.4 ‰ and -21.7 ‰ (Fig. 12), indicating that the material is likely of marine origin. At stations 2011-26 and 2011-29, the isotopic ratio was much lighter (-23.6 and -27.6 ‰, respectively), indicating a significant contribution of isotopically light material; one possibility is that this material is of terrestrial origin. We do not believe that the data are an artifact of sampling from different years, as the $\delta^{13}C(C_{org})$ value at station 2011-13 showed mostly marine character.

Previous measurements showed that the POC in the Amazon River mouth contains a large fraction of terrestrial material, with $\delta^{13}C$ values from -25.6 to -27.3 ‰ (Druffel, 2005; Showers and Angle, 1986). However, very little of this material has been measured in suspended POC pool in the open ocean (Aller and Blair, 2006; Druffel, 2005). Any terrestrial material that survives the remineralization processes on the continental shelf are likely to be refractory lignins or cellulose that resist degradation (Gough et al., 1993; Hedges et al., 1988; Opsahl and Benner, 1997). The

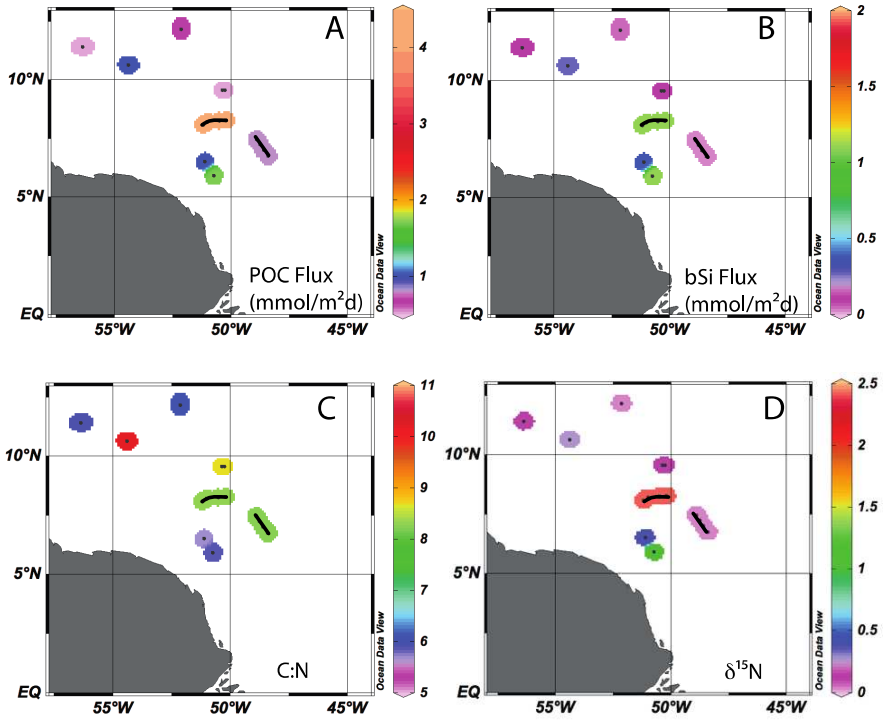

Figure 12. Spatial plots of sediment trap results. A) POC flux B)bSi flux C) C:N ratio of POM D) $\delta^{15}N$ of PON

average $\delta^{13}C$ of suspended POC in the river itself (-28.3 to -28.5 ‰) compares quite well to the isotopic composition measured directly from C3 plants in the Amazon Basin (-27.6 to -30.1 ‰) (Hedges et al., 1986). Because two of our 2011 traps captured POC with $\delta^{13}C$ values that were similarly light, we infer that there can be a significant fraction of terrestrial material exported to the sea floor far from the Amazon River. Both of these stations (2011-26 and 2011-29) are in the area of the retroflection plume, and the influx of terrestrial material is likely related to presence of this plume, as none of the 2010 traps showed much terrestrial influence. The $\delta^{13}C$ of POC at the river mouth shows some seasonal difference between May (-27.3‰) and November (-25.6‰) between times of highest and lowest river flow, respectively (Druffel, 2005; Showers and Angle, 1986).

The surface sediments generally had $\delta^{13}C_{org}$ values that reflected a marine signal, ranging from 17.58 to -21.09‰ (Fig. 3). The few stations with lighter isotopic values reside in the eastern region of the study area (2010-7, 2011-25) and isotopic values of -23.96 and -31.07‰. These data show that the lighter material captured in the sediment traps does reach the deep ocean floor, and supports the hypothesis that the retroflection plume may carry a significant amount of terrestrial material offshore.

With regards to $\delta^{15}N$, four of the traps deployed at 150 m had a $\delta^{15}N$(PON) of 4.3-4.8‰, while stations 2010-25, 2010-27, and 2011-29 had lighter values, ranging from 2.7-2.9‰ (Fig. 12). We surmised that the lighter values indicated a contribution of PON from N_2-fixation (Montoya et al., 2002). Given the lack of plume

influence at station 2010-27 (SSS = 35), the isotopically light PON was likely produced by *Trichodesmium* sp., (Carpenter and Capone, 1992; Carpenter and Romans, 1991). While stations 2010-25 and 2011-29, within the plume, also captured isotopically light PON, our data do not allow for the identification of what group of diazotrophs was responsible for this signal (none of our trap measurements identified prokaryotic information). The Si:C of the trap material did not vary systematically with $\delta^{15}N$ compositions.

At stations with traps at two depths, the isotopic composition was nearly identical between 150 m and 250 m at station 2011-13, but at stations 2011-26 and 2011-29, the $\delta^{15}N$(PON) value was lighter at 250 m (by 1-2 ‰). These stations also had a higher mass flux at 250 m, and so it is possible that the change in isotopic composition was simply an effect of collecting more isotopically light material at that depth. There was generally an increase (<2 ‰) in the $\delta^{15}N$ value between sinking POM and surface sediment values. One explanation of this offset is diagenetic alteration within the sediments (Altabet and François, 1994; François et al., 1997; Gaye et al., 2009; Nakatsuka et al., 1997). However, there is some uncertainty as to the size of the diagenetic offset: values around 4-5‰ have been reported from the open ocean, but measurements of <1‰ were made near the Canary Islands (Altabet and François, 1994; François et al., 1997; Freudenthal et al., 2001).

$\delta^{15}N$ values from the sediments of the ANACONDAS region showed that stations 2010-25 and 2010-27 had values of 4.6 ‰ and 4.5‰, and the coring

stations near the trap deployed at 2011-29 (no cores were collected at 2011-29) had surface sediment values averaging to 4.9‰ (Fig. 3). Comparing the surface sediments to the trap PON, we observed an offset of 0.17-2.0 ‰, with sediments being heavier than traps. Overall there does not appear to be a strong spatial pattern in this offset $\delta^{15}N$. The smaller degree of offset, if due to diagenetic alteration, may be an indicator that certain diagenetic reactions involved in the degradation of sedimentary organic matter impact N isotopes differently. Another hypothesis is that trap $\delta^{15}N$ reflects modern exported materials and the heavier $\delta^{15}N$ found in the sediments is an integral of the value exported for the previous 100's to 1000's of years.

On a global basis, there is a systematic increase in C:N ratios with depth for material caught in sediment traps; the average change is 0.2 ± 0.1 units per 1000 m (Schneider et al., 2003). Chong et al., (submitted) reported relatively uniform surface sediment C:N ratios from 9 sites throughout the study area, ranging from 5.5 to 7.5. Comparing these sedimentary values to the material captured by the 150 m sediment traps, the stations from 2010 generally showed an increase in the sediments, with stations 2010-9 and 2010-13 following the relationship determined by Schneider et al., (2003) very well. Stations 2010-23, and all of the 2011 stations all had C:N ratios of the sinking POM that was greater than that found in the surface sediments. These four stations all had trap C:N ratios that were above the Redfield value, ranging from 8.2 to 10.2, but otherwise had no spatial correlation between them.

Downcore Patterns

The downcore profiles of the biogenic constituents reveal how patterns of deposition have changed throughout the Holocene. However, making a generalized comparison across the region is complicated by the fact that sedimentation rates are higher to the southwest than in the east or north, and a higher sedimentation rate will typically result in a higher concentration of biogenic material in the sediments. By examining sediments of similar age, we were able to identify areas that receive more or less biogenic material compared to the rest of the region (Figs. 13-16).

The sediments in the south and west generally receive higher amounts of both C_{org} and bSi as compared to the east across several latitudes, though at 10˚N the composition was fairly uniform between the west and east. $CaCO_3$ followed a similar, but inverse pattern, where a higher amount of $CaCO_3$ reaches the seafloor at the eastern stations, except along 10˚N where deposition appeared to be relatively even.

Examining the history of biogenic material preservation on a north-south basis, following the NW plume, we observed that this axis is clearly a key area for the deposition of C_{org} and bSi in this region (Fig. 16). Both sedimentation rates are greater in the south (as evidenced by the depressed 5000 year isochron) and the biogenic content is greater in these sediments. The amount of C_{org} and bSi in the sediments is fairly high to depths of 20+ cm at stations that are in the south, and they remained this way to ~10˚N, 53˚W where there is a fairly abrupt change in biogenic content and sedimentation rate.

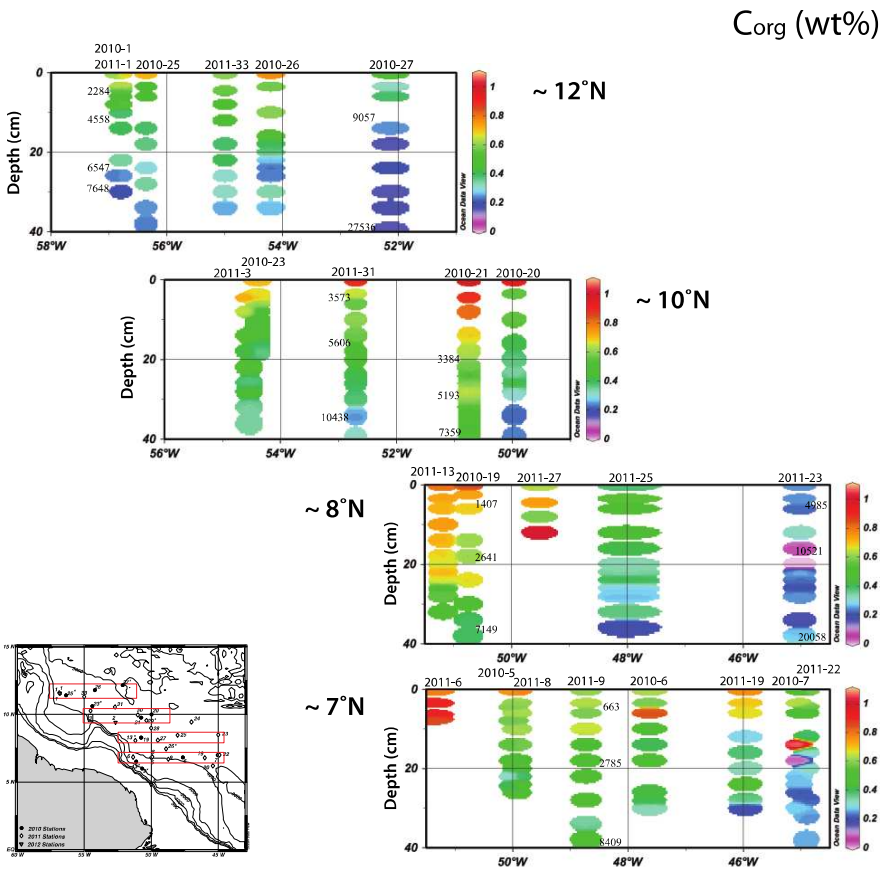

Figure 13. Downcore profiles of wt% C_{org}. Calendar ages are listed on the profile where available.

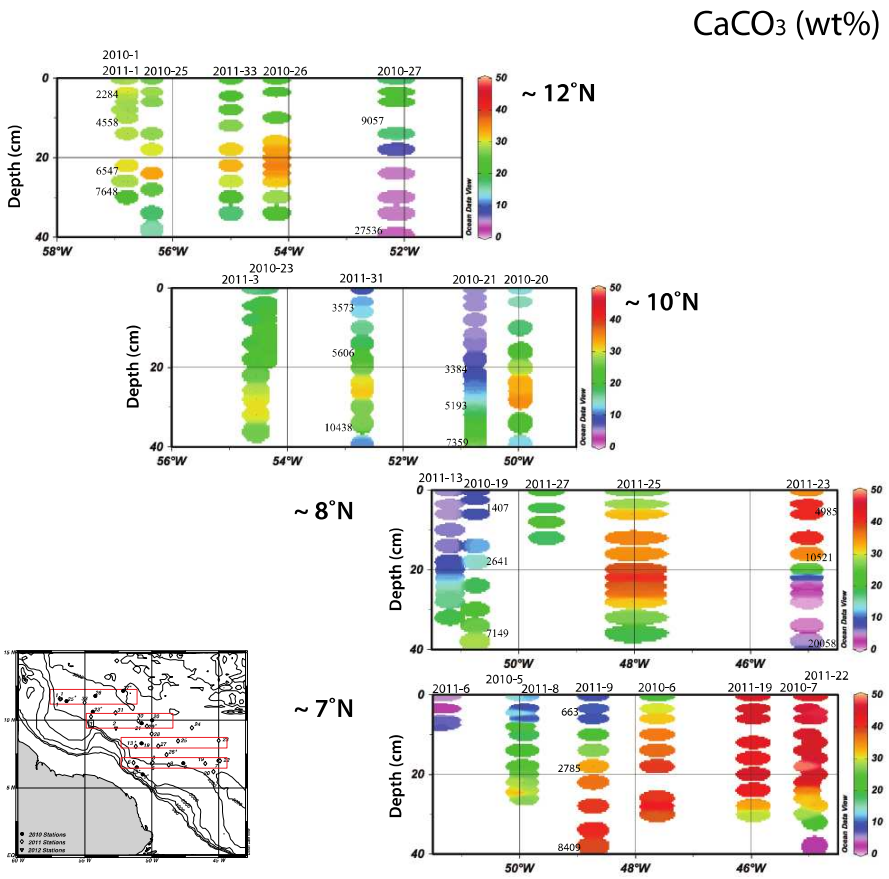

Figure 14. Downcore profiles of wt% $CaCO_3$. Calendar ages are listed on the profile where available.

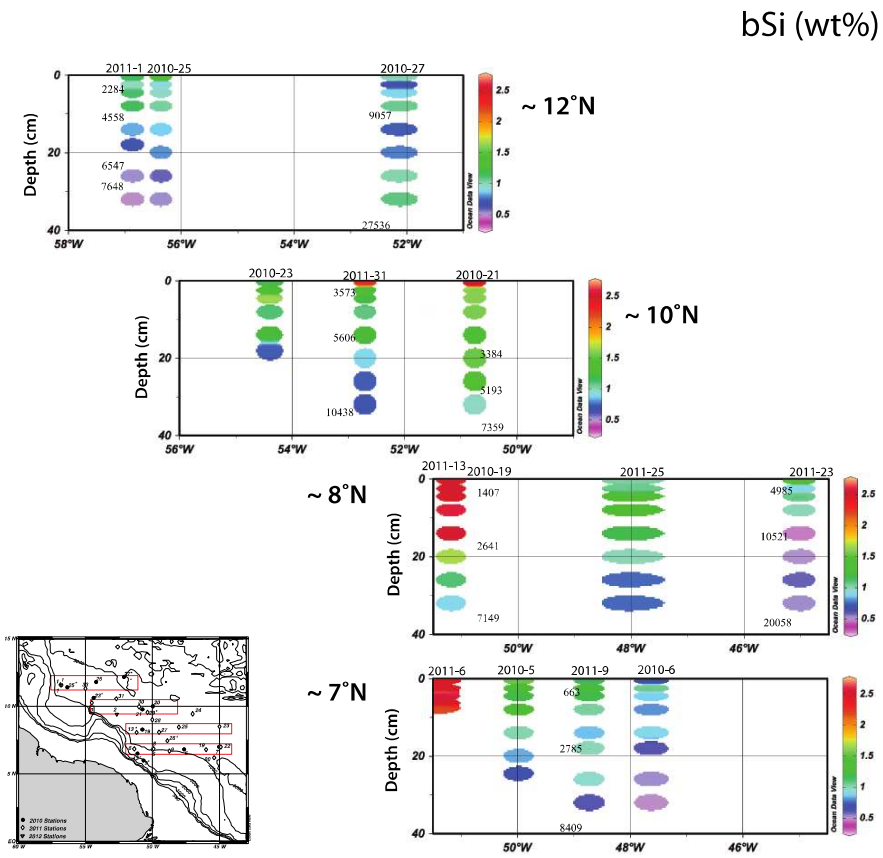

Figure 15. Downcore profiles of wt% bSi. Calendar ages are listed on the profile where available.

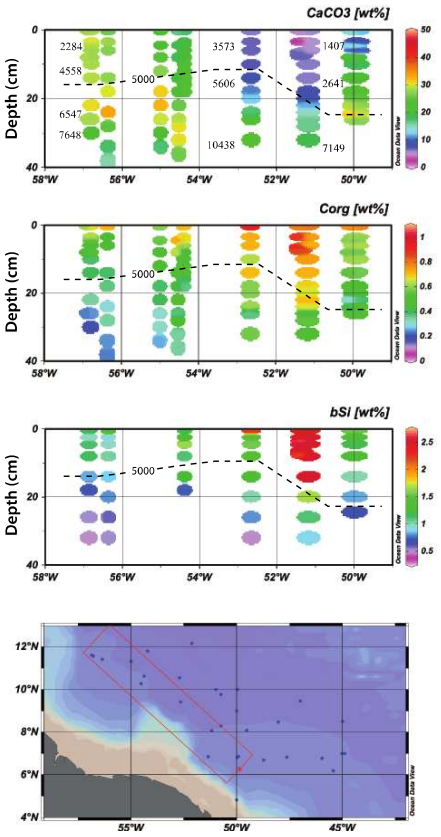

Figure 16. Downcore profiles along the NW axis of the river plume. Dashed line indicates sediments of similar age.

Our measurements of each component may be affected by the extent to which it is diluted by other constituents like carbonate or detrital material (Seiter, 2005). Thus we calculated the percent of detrital material reaching the seafloor and downcore to assess where burial of this constituent occurs and how it has changed through time. The amount of detrital material was calculated using the following relationship:

$$\%D = 100 - (\%CaCO_3 + \%bSi + 2.5*\%C_{org}) \quad (8)$$

The pattern of detrital deposition in surface sediments provided us with a footprint for the river plume integrated over several hundred years (Fig. 17). The surface sediments were comprised nearly entirely (~90%) of detrital material in the central zone of the plume - extending far to the east relative to the plume axis. Stations to the far north and particularly to the east contain a larger biogenic component, highlighting once again the importance of the retroflection plume to biogenic sedimentation and/or the lessor quantity of detrital sedimentation. Downcore, there is little variation in detrital content for the majority of the sediment profiles (Fig. 17B, C), however there was a substantial increase in the fraction of detrital material at depth at the eastern stations 2011-20 and 2011-23. This likely represents the boundary between glacial and interglacial sediments. In general, clay deposition in the Atlantic was higher during glacial times as opposed to interglacial times, resulting in lower $CaCO_3$ concentrations in glacial sediments (Bacon, 1984; Balsam and McCoy, 1987; Thomson et al., 1990). Based on the ^{14}C calendar ages, we know

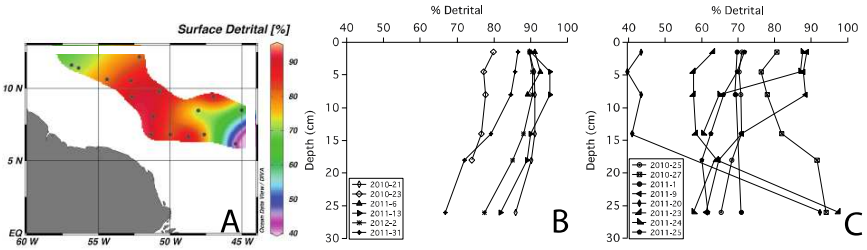

Figure 17. Estimations of the fraction of sediments composed of detrital material. A) Surface sediments. B,C) Downcore profiles of % detrital material.

that station 2011-23 reaches glacial ages at ~16 cm (Table 3), and at the horizon of detrital increase, the $CaCO_3$ composition declines rapidly to values < 5 wt%.

CONCLUSIONS

The sediments underlying the Amazon River plume have a central zone near 10˚N 50˚W that contains elevated amounts of C_{org} and bSi compared to the surrounding area. Surface sediment concentrations decrease by a factor of 2 to the north and east. The zone of high concentration of C_{org} and bSi is much more expansive than the zone of modern plume extent. $CaCO_3$ concentration in the sediment has the mirror opposite pattern, with the highest values appearing in the north and east. Mean surface C_{org}, $CaCO_3$, and bSi % in the study area was 0.67% 21.0% and 1.5%, respectively, where the $CaCO_3$ and bSi content of the plume region was lower than the regional averages, and C_{org} content was higher.

The sediment mixed layer depth determined by ^{210}Pb was generally ~10-12 cm. The sediment mixing coefficients ranged from 0.06 – 3.1 $cm^2\ yr^{-1}$, agreeing with other values from the deep ocean, but no spatial patterns were evident. The normalized excess ^{210}Pb inventory in the sediments was higher than that of the water column by ~2X at sites south of 10˚N 50˚W, but outside this zone, the stations were generally deficient in excess ^{210}Pb. ^{230}Th-derived focusing factors (from the similar stations) revealed a pattern of sediment focusing and winnowing throughout the region that was not geographically systematic. Sites with high values of normalized excess ^{210}Pb inventories in absence of high focusing derived from ^{230}Th

indicate that there is a significant amount of ^{210}Pb moved to these areas through lateral transport.

Model simulations show that the sedimentation rate has generally remained the same or decreased since the early Holocene. Sedimentation rates below the sediment ML ranged from 1.19 – 4.55 cm kyr^{-1}, agreeing with previous measurements for the Demerara Abyssal Plain. The average sedimentation rate was highest in the central zone, while rates to the north and east were comparable to each other. Thus, the retroflection plume is highly important to sedimentation. Sediment accumulation rates were used to estimate burial fluxes of C_{org} and bSi, which ranged from 0.01-0.08 mmol C $m^{-2}d^{-1}$ and 0.01-0.04 mmol SiO_2 $m^{-2}d^{-1}$, respectively. The burial fluxes comprised 4-16% of the total C_{org} rain arriving on the sea floor.

The deep-sea rain rate extrapolated to the surface using the Martin curve with a b-value of 0.86 yielded export (from 150 m) fluxes that were 7-17X greater than those recorded by floating sediment traps at the same site. Using a smaller attenuation coefficient (b=0.57) increased coherence between these values. The floating sediment traps are either under-collecting due to the complex physical dynamics of the river plume or there is very little attenuation in the POC flux with depth in this region. It is also possible that even though sediment traps are subject to temporal and spatial variability in collection our traps coincidentally recorded fluxes from the low end of the flux spectrum during each deployment.

The $\delta^{13}C(C_{org})$ of the trap material indicated that the sinking POC is primarily of marine origin at most sites, however sites that are in the zone of the retroflection plume appear to have a contribution from terrestrial material, likely derived from C3 plants. The surface sediments reflected a similar pattern in $\delta^{13}C$, with a predominantly marine signal throughout the region, though lighter values were observed in the area of the retroflection. The $\delta^{15}N$ of trap material was generally around ~4.5‰ but lighter values (~2‰) at select stations point to a contribution from N_2-fixation. There was ~ 0.2 to 2.0 ‰ offset between the sediment trap material and the bulk sediment isotopic composition, likely due to diagenetic alteration. The C:N ratios from the sediment traps were quite variable – while some of them increased with depth as expected, at four stations, the sediment trap C:N was higher than that of the sediments below.

Downcore profiles revealed that more C_{org} and bSi accumulates in the west than in the east, and more in the south than in the north of the NW plume axis. $CaCO_3$ deposition followed a very similar, but inverse pattern. Detrital material makes up the majority of the material arriving at the sea floor throughout most of the region except in the far north and the easternmost stations in the zone of the retroflection. Detrital deposition has remained fairly constant throughout the Holocene, except at easternmost stations. These stations revealed the boundary between glacial and interglacial sediments, where there was a rapid increase in the fraction of detrital material and a rapid decrease in the concentration of $CaCO_3$ at a depth of ~20 cm.

ACKNOWLEDGEMENTS

This work was supported by NSF grant #OCE-0934073 awarded to WB. We are grateful to the captains and crews of the R/V Knorr, R/V Melville, and R/V Atlantis. We would also like to acknowledge the members of the at-sea and shore-based science party and all contributors to the ANACONDAS project especially Chief Scientist Patricia Yager. We thank Troy Gunderson, John Fleming, Emily Mortazavi, Christa Wolfe, Willie Haskell, Alice Bitzer, Cara Fassino, Neha Ahmed, and Jake Porter for their assistance and contributions to this work.

REFERENCES

Aller, R.C., 1982, The effects of macrobenthos on chemical properties of marine sediment and overlying water, *in* McCall, P.L. and Tevesz, M. eds., Animal-Sediment Relations, Plenum, NY, p. 53–102.

Aller, R.C., and Blair, N.E., 2006, Carbon remineralization in the Amazon-Guianas tropical mobile mudbelt: A sedimentary incinerator: Continental Shelf Research, v. 26, no. 17-18, p. 2241–2259.

Aller, R.C., Blair, N.E., Xia, Q., and Rude, P., 1996, Remineralization rates, recycling, and storage of carbon in Amazon shelf sediments: Continental Shelf Research, v. 16, no. 5-6, p. 753–786.

Aller, R.C., Heilbrun, C., Panzeca, C., Zhu, Z., and Baltzer, F., 2004, Coupling between sedimentary dynamics, early diagenetic processes, and biogeochemical cycling in the Amazon–Guianas mobile mud belt: coastal French Guiana: Marine Geology, v. 208, no. 2-4, p. 331–360.

Altabet, M.A., and François, R., 1994, Sedimentary nitrogen isotopic ratio as a recorder for surface ocean nitrate utilization: Global Biogeochemical Cycles, v. 8, no. 1, p. 103–116.

Bacon, M.P., 1984, Glacial to interglacial changes in carbonate and clay sedimentation in the Atlantic Ocean estimated from 230 Th measurements: Chemical Geology, v. 46, no. 2, p. 97–111.

Balsam, W.L., and McCoy, F.W., 1987, Atlantic sediments: Glacial/interglacial comparisons: Paleoceanography, v. 2, no. 5, p. 531–542.

Barnett, P., Watson, J., and Connelly, D., 1984, A multiple corer for taking virtually undisturbed samples from shelf, bathyal and abyssal sediments.: Oceanologica Acta, v. 7, p. 399–408.

Barsanti, M., Delbono, I., Schirone, A., Langone, L., Miserocchi, S., Salvi, S., and Delfanti, R., 2011, Sediment reworking rates in deep sediments of the Mediterranean Sea: Science of The Total Environment, v. 409, no. 15, p. 2959–2970.

Basso, D., Thomson, J., and Corselli, C., 2004, Indications of low macrobenthic activity in the deep sediments of the eastern Mediterranean Sea: Scientia Marina, v. 68, no. S3, p. 53–62, doi: 10.3989/scimar.2004.68s353.

Bender, M.L., and Heggie, D.T., 1984, Fate of organic carbon reaching the deep sea floor: a status report: Geochimica et Cosmochimica Acta, v. 48, no. 5, p. 977–986.

Berner, R.A., 1980, Early Diagenesis: A Theoretical Approach: Princeton University Press, Princeton, NJ.

Broecker, W.S., Matsumoto, K., Clark, E., Hajdas, I., and Bonani, G., 1999, Radiocarbon age differences between coexisting foraminiferal species: Paleoceanography, v. 14, no. 4, p. 431–436.

Buesseler, K.O., and Boyd, P.W., 2009, Shedding light on processes that control particle export and flux attenuation in the twilight zone of the open ocean: Limnology and Oceanography, v. 54, no. 4, p. 1210.

Buesseler, K.O., Antia, A.N., Chen, M., Fowler, S.W., Gardner, W.D., Gustafsson, O., Harada, K., Michaels, A.F., van der Loeff, M.M., and Sarin, M., 2007a, An assessment of the use of sediment traps for estimating upper ocean particle fuxes: Journal of Marine Research, v. 65, p. 345–416.

Buesseler, K.O., Lamborg, C.H., Boyd, P.W., Lam, P.J., Trull, T.W., Bidigare, R.R., Bishop, J.K., Casciotti, K.L., DeHairs, F., Elskens, M., Honda, M.C., Karl, D.M., Siegel, D.A., Silver, M.W., et al., 2007b, Revisiting Carbon Flux Through the Ocean's Twilight Zone: Science, v. 316, no. 5824, p. 567–570, doi: 10.1126/science.1137959.

Buesseler, K.O., Steinberg, D.K., Michaels, A.F., Johnson, R.J., Andrews, J.E., Valdes, J.R., and Price, J.F., 2000, A comparison of the quantity and composition of material

caught in a neutrally buoyant versus surface-tethered sediment trap: Deep Sea Research Part I: Oceanographic Research Papers, v. 47, no. 2, p. 277–294.

Burdige, D.J., 2007, Preservation of organic matter in marine sediments: controls, mechanisms, and an imbalance in sediment organic carbon budgets?: Chemical Reviews-Columbus, v. 107, no. 2, p. 467–485.

Canfield, D.E., 1994, Factors influencing organic carbon preservation in marine sediments: Chemical Geology, v. 114, no. 3, p. 315–329.

Carpenter, E.J., and Capone, D.G., 1992, Nitrogen fixation in Trichodesmium blooms, *in* Carpenter, E.J. and Capone, D.G. eds., Marine pelagic cyanobacteria, Kluwer Academic Publishers, p. 211–218.

Carpenter, E.J., and Romans, K., 1991, Major role of the cyanobacterium Trichodesmium in nutrient cycling in the North Atlantic Ocean.: Science, v. 254, no. 5036, p. 1356.

Carpenter, E.J., Montoya, J.P., Burns, J.A., Mulholland, M., Subramaniam, A., and Capone, D.G., 1999, Extensive bloom of a N2 fixing symbiotic association in the tropical Atlantic Ocean: Marine Ecology Progress Series, v. 188, p. 273–283.

Carvalho, F.P., Oliveira, J.M., and Soares, A.M.M., 2011, Sediment accumulation and bioturbation rates in the deep Northeast Atlantic determined by radiometric techniques: ICES Journal of Marine Science, v. 68, no. 3, p. 427–435, doi: 10.1093/icesjms/fsr005.

Cochran, J.K., McKibbin-Vaughan, T., Dornblaser, M.M., Hirschberg, D., Livingston, H.D., and Buesseler, K.O., 1990, 210 Pb scavenging in the North Atlantic and North Pacific Oceans: Earth and Planetary Science Letters, v. 97, no. 3, p. 332–352.

Cooley, S.R., and Yager, P.L., 2006, Physical and biological contributions to the western tropical North Atlantic Ocean carbon sink formed by the Amazon River plume: Journal of Geophysical Research, v. 111, no. C8, p. 1–14, doi: 10.1029/2005JC002954.

Cooley, S.R., Coles, V.J., Subramaniam, A., and Yager, P.L., 2007, Seasonal variations in the Amazon plume-related atmospheric carbon sink: Global Biogeochemical Cycles, v. 21, no. 3, p. GB3014, doi: 10.1029/2006GB002831.

Craig, H., Krishnaswami, S., and Somayajulu, B., 1973, 210 Pb 226 Ra: Radioactive disequilibrium in the deep sea: Earth and Planetary Science Letters, v. 17, no. 2, p. 295–305.

Damuth, J.E., 1977, Late Quaternary sedimentation in the western equatorial Atlantic: GSA Bulletin, v. 88, no. 5, p. 695, doi: 10.1130/0016-

7606(1977)88<695:LQSITW>2.0.CO;2.

Damuth, J.E., and Embley, R., 1981, Mass-transport processes on Amazon Cone: western equatorial Atlantic: AAPG Bulletin, v. 65, no. 4, p. 629.

Damuth, J.E., and Kumar, N., 1975, Late Quaternary depositional processes on the continental rise of the western equatorial Atlantic: Comparison with the western North Atlantic and implications for reservoir-rock distribution: AAPG Bulletin, v. 59, no. 11, p. 2172–2181.

DeMaster, D.J., 1981, The supply and accumulation of silica in the marine environment: Geochimica et Cosmochimica Acta, v. 45, no. 10, p. 1715–1732.

DeMaster, D.J., and Pope, R.H., 1996, Nutrient dynamics in Amazon shelf waters: results from AMASSEDS: Continental Shelf Research, v. 16, no. 3, p. 263–289.

DeMaster, D.J., Kuehl, S.A., and Nittrouer, C.A., 1986, Effects of suspended sediments on geochemical processes near the mouth of the Amazon River: examination of biological silica uptake and the fate of particle-reactive elements: Continental Shelf Research, v. 6, no. 1, p. 107–125.

DeMaster, D.J., McKee, B.A., Nittrouer, C.A., Brewster, D.C., and Biscaye, P.E., 1985, Rates of sediment reworking at the HEBBLE site based on measurements of Th-234, Cs-137 and Pb-210: Marine Geology, v. 66, no. 1, p. 133–148.

DeMaster, D.J., Smith, W.O., Jr, Nelson, D.M., and Aller, J.Y., 1996, Biogeochemical processes in Amazon shelf waters: chemical distributions and uptake rates of silicon, carbon and nitrogen: Continental Shelf Research, v. 16, no. 5, p. 617–643.

Deuser, W.G., Muller-Karger, F.E., and Hemleben, C., 1988, Temporal variations of particle fluxes in the deep subtropical and tropical North Atlantic: Eulerian versus Lagrangian effects: Journal of Geophysical Research, v. 93, no. C6, p. 6857–6862.

Deuser, W.G., Muller-Karger, F.E., Evans, R.H., Brown, O.B., Esaias, W.E., and Feldman, G.C., 1990, Surface-ocean color and deep-ocean carbon flux: how close a connection?: Deep Sea Research Part A. Oceanographic Research Papers, v. 37, no. 8, p. 1331–1343.

Druffel, E.R.M., 2005, Input of particulate organic and dissolved inorganic carbon from the Amazon to the Atlantic Ocean: Geochemistry Geophysics Geosystems, v. 6, no. 3, p. Q03009, doi: 10.1029/2004GC000842.

Foster, R.A., Subramaniam, A., Mahaffey, C., Carpenter, E.J., Capone, D.G., and Zehr, J.P., 2007, Influence of the Amazon River plume on distributions of free-living and symbiotic cyanobacteria in the western tropical north Atlantic Ocean: Limnology and Oceanography,, p. 517–532.

François, R., Altabet, M.A., Yu, E.-F., Sigman, D.M., Bacon, M.P., Frank, M., Bohrmann, G., Bareille, G., and Labeyrie, L.D., 1997, Contribution of Southern Ocean surface-water stratification to low atmospheric CO2 concentrations during the last glacial period: Nature, v. 389, no. 6654, p. 929–936.

François, R., Frank, M., Rutgers van der Loeff, M.M., and Bacon, M.P., 2004, 230Th normalization: An essential tool for interpreting sedimentary fluxes during the late Quaternary: Paleoceanography, v. 19, no. 1, p. PA1018, doi: doi:10.1029/2003PA000939.

François, R., Honjo, S., Krishfield, R., and Manganini, S.J., 2002, Factors controlling the flux of organic carbon to the bathypelagic zone of the ocean: Global Biogeochemical Cycles, v. 16, no. 4, p. 1087–1107, doi: doi:10.1029/2001GB001722.

Freudenthal, T., Wagner, T., Wenzhöfer, F., Zabel, M., and Wefer, G., 2001, Early diagenesis of organic matter from sediments of the eastern subtropical Atlantic: Evidence from stable nitrogen and carbon isotopes: Geochimica et Cosmochimica Acta, v. 65, no. 11, p. 1795–1808.

Froelich, P.N., Atwood, D., and Giese, G., 1978, Influence of Amazon River discharge on surface salinity and dissolved silicate concentration in the Caribbean Sea: Deep Sea Research, v. 25, no. 8, p. 735–744.

Gardner, W.D., Biscaye, P.E., and Richardson, M.J., 1997, A sediment trap experiment in the Vema Channel to evaluate the effect of horizontal particle fluxes on measured vertical fluxes: Journal of Marine Research, v. 55, no. 5, p. 995–1028, doi: 10.1357/0022240973224139.

Gaye, B., Wiesner, M., and Lahajnar, N., 2009, Nitrogen sources in the South China Sea, as discerned from stable nitrogen isotopic ratios in rivers, sinking particles, and sediments: Marine Chemistry, v. 114, p. 72–85.

Gibbs, R., 1976, Amazon River sediment transport in the Atlantic Ocean: Geology, v. 4, no. 1, p. 45–48, doi: 10.1130/0091-7613(1976)4<45:ARSTIT>2.0.CO;2.

Gough, M.A., Fauzi, R., Mantoura, C., and Preston, M., 1993, Terrestrial plant biopolymers in marine sediments: Geochimica et Cosmochimica Acta, v. 57, no. 5, p. 945–964, doi: 10.1016/0016-7037(93)90032-R.

Green, M.A., Aller, R.C., Cochran, J.K., Lee, C., and Aller, J.Y., 2002, Bioturbation in shelf/slope sediments off Cape Hatteras, North Carolina: the use of 234 Th, Chl-a, and Br− to evaluate rates of particle and solute transport: Deep Sea Research Part II: Topical Studies in Oceanography, v. 49, no. 20, p. 4627–4644.

Guinasso, N.L., and Schink, D.R., 1975, Quantitative estimates of biological mixing rates in abyssal sediments: Journal of Geophysical Research: Oceans (1978–

2012), v. 80, no. 21, p. 3032–3043.

Gust, G., Byrne, R.H., Bernstein, R.E., Betzer, P.R., and Bowles, W., 1992, Particles fluxes and moving fluids: experience from synchronous trap collection in the Sargassso sea: Deep Sea Research Part A. Oceanographic Research Papers, v. 39, no. 7, p. 1071–1083.

Hedges, J.I., and Keil, R.G., 1995, Sedimentary organic matter preservation: an assessment and speculative synthesis: Marine Chemistry, v. 49, p. 81–115.

Hedges, J.I., Clark, W.A., and Cowie, G.L., 1988, Fluxes and reactivities of organic matter in a coastal marine bay.: Limnology and Oceanography, v. 33, no. 5, p. 1137–1152.

Hedges, J.I., Clark, W.A., Quay, P.D., Richey, J.E., Devol, A.H., and Santos, U. de M., 1986, Compositions and fluxes of particulate organic material in the Amazon River: Limnology and Oceanography,, p. 717–738.

Honjo, S., 1980, Material fluxes and modes of sedimentation in the mesopelagic and bathypelagic zones: Journal of Marine Research, v. 38, p. 53–97.

Howard, M.T., Winguth, A., Klaas, C., and Maier-Reimer, E., 2006, Sensitivity of ocean carbon tracer distributions to particulate organic flux parameterizations: Global Biogeochemical Cycles, v. 20, no. 3.

Hu, C., Montgomery, E., Schmitt, R., and Muller-Karger, F.E., 2004, The dispersal of the Amazon and Orinoco River water in the tropical Atlantic and Caribbean Sea: Observation from space and S-PALACE floats: Deep Sea Research Part II, v. 51, no. 10-11, p. 1151–1171.

Kineke, G.C., Sternberg, R.W., Trowbridge, J.H., and Geyer, W.R., 1996, Fluid-mud processes on the Amazon continental shelf: Continental Shelf Research, v. 16, no. 5, p. 667–696.

Knauer, G.A., Martin, J.H., and Bruland, K.W., 1979, Fluxes of particulate carbon, nitrogen, and phosphorus in the upper water column of the northeast Pacific: Deep Sea Research Part A. Oceanographic Research Papers, v. 26, no. 1, p. 97–108.

Kuehl, S.A., Fuglseth, T.J., and Thunell, R.C., 1993, Sediment mixing and accumulation rates in the Sulu and South China Seas: implications for organic carbon preservation in deep-sea environments: Marine Geology, v. 111, no. 1, p. 15–35.

Lentz, S.J., and Limeburner, R., 1995, The Amazon River plume during AMASSEDS: Spatial characteristics and salinity variability: Journal of Geophysical Research, v. 100, no. C2, p. 2355–2375.

Martin, J., Knauer, G., Karl, D.M., and Broenkow, W., 1987, VERTEX: carbon cycling in the northeast Pacific: Deep Sea Research Part A. Oceanographic Research Papers, v. 34, no. 2, p. 267–285.

Martin, P., Lampitt, R.S., Jane Perry, M., Sanders, R., Lee, C., and D'Asaro, E., 2011, Export and mesopelagic particle flux during a North Atlantic spring diatom bloom: Deep Sea Research Part I: Oceanographic Research Papers, v. 58, no. 4, p. 338–349.

Meade, R.H., Dunne, T., Richey, J.E., Santos, U. de M., and Salati, E., 1985, Storage and remobilization of suspended sediment in the lower Amazon River of Brazil: Science, v. 228, no. 4698, p. 488–490.

Mikaloff Fletcher, S.E., Gruber, N., Jacobson, A.R., Gloor, M., Doney, S.C., Dutkiewicz, S., Gerber, M., Follows, M.J., Joos, F., Lindsay, K., Menemenlis, D., Mouchet, A., Müller, S.A., and Sarmiento, J.L., 2007, Inverse estimates of the oceanic sources and sinks of natural CO 2and the implied oceanic carbon transport: Global Biogeochemical Cycles, v. 21, no. 1, p. GB1010–19, doi: 10.1029/2006GB002751.

Milliman, J.D., Summerhayes, C., and Barretto, H., 1975, Quaternary sedimentation on the Amazon continental margin: a model: Bulletin of the Geological Society of America, v. 86, no. 5, p. 610–614.

Montoya, J.P., Carpenter, E.J., and Capone, D.G., 2002, Nitrogen fixation and nitrogen isotope abundances in zooplankton of the oligotrophic North Atlantic: Limnology and Oceanography, v. 47, no. 6, p. 1617–1628.

Muller-Karger, F.E., Mcclain, C., and Richardson, P.L., 1988, The dispersal of the Amazon's water: Nature, v. 333, p. 56–59, doi: doi:10.1038/333056a0.

Nakatsuka, T., Handa, N., Harada, N., Sugimoto, T., and Imaizumi, S., 1997, Origin and decomposition of sinking particulate organic matter in the deep water column inferred from the vertical distributions of its δ15N, δ13C and δ14C: Deep-sea research. Part 1. Oceanographic research papers, v. 44, no. 12, p. 1957–1979.

Neumann, G., 1969, Seasonal salinity variations in the upper Strata of the western tropical Atlantic Ocean - Sea surface salinities: Deep Sea Research, v. Supplement to Vol 16, p. 165–177.

Nittrouer, C.A., Kuehl, S.A., Sternberg, R.W., and Figueiredo, A.G., 1995, An introduction to the geological significance of sediment transport and accumulation on the Amazon continental shelf: Marine Geology, v. 125, no. 3-4, p. 177–192.

Opsahl, S., and Benner, R., 1997, Distribution and cycling of terrigenous dissolved organic matter in the ocean: Nature, v. 386, no. 6624, p. 480–482, doi: 10.1038/386480a0.

Premuzic, E.T., Benkovitz, C.M., Gaffney, J.S., and Walsh, J.J., 1982, The nature and distribution of organic matter in the surface sediments of world oceans and seas: Organic Geochemistry, v. 4, no. 2, p. 63–77.

Rama, M.K., and Goldberg, E.D., 1961, Lead-210 in natural waters: Science, v. 134, no. 3472, p. 98–99.

Reimer, P.J., Baillie, M.G., Bard, E., Bayliss, A., Beck, J.W., Blackwell, P.G., Ramsey, C.B., Buck, C.E., Burr, G.S., and Edwards, R.L., 2009, IntCal09 and Marine09 radiocarbon age calibration curves, 0–50,000 years cal BP: Radiocarbon, v. 51, no. 4, p. 1111–1150.

Reimers, C.E., Jahnke, R.A., and McCorkle, D.C., 1992, Carbon fluxes and burial rates over the continental slope and rise off central California with implications for the global carbon cycle: Global Biogeochemical Cycles, v. 6, no. 2, p. 199–224.

Rhoads, D.C., 1974, Organism-sediment relations on the muddy sea floor, *in* Oceanography and Marine Biology: An Annual Review, Aberdeen University Press, p. 263–300.

Richey, J.E., Hedges, J.I., Devol, A.H., and Quay, P.D., 1990, Biogeochemistry of carbon in the Amazon River: Limnology and Oceanography, v. 35, no. 2, p. 352–371.

Salisbury, J., Vandemark, D., Campbell, J., Hunt, C., Wisser, D., Reul, N., and Chapron, B., 2011, Spatial and temporal coherence between Amazon River discharge, salinity, and light absorption by colored organic carbon in western tropical Atlantic surface waters: Journal of Geophysical Research: Oceans (1978–2012), v. 116, no. C7.

Schlitzer, R., 2002, Carbon export fluxes in the Southern Ocean: Results from inverse modeling and comparison with satellite-based estimates: Deep Sea Research Part II: Topical Studies in Oceanography, v. 49, no. 9, p. 1623–1644.

Schneider, B., Schlitzer, R., Fischer, G., and Nöthig, E.-M., 2003, Depth-dependent elemental compositions of particulate organic matter (POM) in the ocean: Global Biogeochemical Cycles, v. 17, no. 2, p. 1032.

Seiter, K., 2005, Benthic carbon mineralization on a global scale: Global Biogeochemical Cycles, v. 19, no. 1, p. 1–26, doi: 10.1029/2004GB002225.

Seiter, K., Hensen, C., Schröter, J., and Zabel, M., 2004, Organic carbon content in surface sediments—defining regional provinces: Deep Sea Research Part I: Oceanographic Research Papers, v. 51, no. 12, p. 2001–2026.

Shipe, R.F., Curtaz, J., Subramaniam, A., Carpenter, E.J., and Capone, D.G., 2006, Diatom biomass and productivity in oceanic and plume-influenced waters of the western tropical Atlantic ocean: Deep Sea Research Part I: Oceanographic

Research Papers, v. 53, no. 8, p. 1320–1334.

Showers, W.J., and Angle, D.G., 1986, Stable isotopic characterization of organic carbon accumulation on the Amazon continental shelf: Continental Shelf Research, v. 6, no. 1, p. 227–244.

Siegel, D.A., and Deuser, W.G., 1997, Trajectories of sinking particles in the Sargasso Sea: Modeling of statistical funnels above deep-ocean sediment traps: Deep Sea Research Part I: Oceanographic Research Papers, v. 44, no. 9, p. 1519–1541.

Siegel, D.A., Granata, T.C., Michaels, A.F., and Dickey, T.D., 1990, Mesoscale eddy diffusion, particle sinking, and the interpretation of sediment trap data: Journal of Geophysical Research, v. 95, no. C4, p. 5305–5311.

Silver, M.W., and Gowing, M.M., 1991, The "particle" flux: origins and biological components: Progress in Oceanography, v. 26, no. 1, p. 75–113.

Smith, W.O., Jr, and DeMaster, D.J., 1996, Phytoplankton biomass and productivity in the Amazon River plume: correlation with seasonal river discharge: Continental Shelf Research, v. 16, no. 3, p. 291–319.

Smoak, J.M., DeMaster, D.J., Kuehl, S.A., Pope, R.H., and McKee, B.A., 1996, The behavior of particle-reactive tracers in a high turbidity environment: 234 Th and 210 Pb on the Amazon continental shelf: Geochimica et Cosmochimica Acta, v. 60, no. 12, p. 2123–2137.

Stanley, R.H., Buesseler, K.O., Manganini, S.J., Steinberg, D.K., and Valdes, J.R., 2004, A comparison of major and minor elemental fluxes collected in neutrally buoyant and surface-tethered sediment traps: Deep Sea Research Part I: Oceanographic Research Papers, v. 51, no. 10, p. 1387–1395.

Stephens, M.P., Kadko, D.C., Smith, C.R., and Latasa, M., 1997, Chlorophyll-a and pheopigments as tracers of labile organic carbon at the central equatorial Pacific seafloor: Geochimica et Cosmochimica Acta, v. 61, no. 21, p. 4605–4619.

Stramma, L., and England, M., 1999, On the water masses and mean circulation of the South Atlantic Ocean: Journal of Geophysical Research, v. 104, no. C9, p. 20863–20–883, doi: doi:10.1029/1999JC900139.

Strickland, J., 1968, A practical handbook of seawater analysis: Fisheries Research Board of Canada, Halifax.

Stuiver, M., and Braziunas, T.F., 1993, Modeling atmospheric (super 14) C influences and (super 14) C ages of marine samples to 10,000 BC.: Radiocarbon, v. 35, no. 1, p. 137–189, doi: 10.2458/azu_js_rc.v35i1.1558.

Stuiver, M., and Reimer, P.J., 1993, Extended 14C data base and revised Calib 3.0 14C

age calibration program: Radiocarbon, v. 35, no. 1, p. 215–230.

Subramaniam, A., Yager, P.L., Carpenter, E.J., Mahaffey, C., Björkman, K.M., Cooley, S.R., Kustka, A., Montoya, J.P., Sañudo-Wilhelmy, S.A., Shipe, R.F., and Capone, D.G., 2008, Amazon River enhances diazotrophy and carbon sequestration in the tropical North Atlantic Ocean: Proceedings of the National Academy of Sciences of the United States of America, v. 105, no. 30, p. 10460–10465.

Sun, M.-Y., Lee, C., and Aller, R.C., 1993, Laboratory studies of oxic and anoxic degradation of chlorophyll- a in Long Island Sound sediments: Geochimica et Cosmochimica Acta, v. 57, no. 1, p. 147–157.

Takahashi, T., Sutherland, S.C., Sweeney, C., Poisson, A., Metzl, N., Tilbrook, B., Bates, N.R., Wanninkhof, R., Feely, R.A., and Sabine, C., 2002, Global sea-air CO2 flux based on climatological surface ocean pCO2, and seasonal biological and temperature effects: Deep Sea Research Part II: Topical Studies in Oceanography, v. 49, no. 9-10, p. 1601–1622.

Teal, L.R., Bulling, M.T., Parker, E.R., and Solan, M., 2008, Global patterns of bioturbation intensity and mixed depth of marine soft sediments: Aquatic Biology, v. 2, no. 3, p. 207–218.

Ternon, J., Oudot, C., Dessier, A., and Diverres, D., 2000, A seasonal tropical sink for atmospheric CO2 in the Atlantic Ocean: the role of the Amazon River discharge: Marine Chemistry, v. 68, no. 3, p. 183–201.

Thomson, J., Colley, S., Anderson, R.F., Cook, G.T., and Mackensen, A., 1993, 210 Pb in the sediments and water column of the Northeast Atlantic from 47 to 59° N along 20° W: Earth and Planetary Science Letters, v. 115, no. 1, p. 75–87.

Thomson, J., Wallace, H.E., Colley, S., and Toole, J., 1990, Authigenic uranium in Atlantic sediments of the last glacial stage—a diagenetic phenomenon: Earth and Planetary Science Letters, v. 98, no. 2, p. 222–232.

Wells, J., and Coleman, J., 1981, Periodic mudflat progradation, northeastern coast of South America; a hypothesis: Journal of Sedimentary Research, v. 51, no. 4, p. 1069.

Yeung, L.Y., Berelson, W.M., Young, E.D., Prokopenko, M.G., Rollins, N., Coles, V.J., Montoya, J.P., Carpenter, E.J., Steinberg, D.K., Foster, R.A., Capone, D.G., and Yager, P.L., 2012, Impact of diatom-diazotroph associations on carbon export in the Amazon River plume: Geophysical Research Letters, v. 39, no. 18, p. L18609, doi: 10.1029/2012GL053356.

Chapter 4: Suboxic organic matter diagenesis in the sediments from the Western Tropical North Atlantic

ABSTRACT

Gravity cores were collected from the Demerara Abyssal plain to examine the downcore features of early diagenesis in the sediments and relate them to the location of the Amazon River plume. At all sites, the oxygen penetration depth was ~10-20 cm and nitrate was depleted within ~30 cm. Most of the cores also had a secondary nitrate maximum (4-13μM) at ~50 cm depth that we suggest is produced by Mn-oxide reduction and consumed by Fe oxidation at depth. Four sites also had shallow peaks in Fe (<35 cm) that are indicative of localized Fe cycling, which may involve nitrate and/or Mn oxides. Dissolved silica profiles decreased with depth below a maximum to an asymptotic concentration, most likely due to reverse weathering processes. Pore water gradients of Fe suggest that Fe oxidation may be responsible for dissolved Si uptake. A semi-lithified iron crust appeared at the base of the Fe production gradient at nearly all sites. This feature is an indicator of the relative position of the transition from glacial to interglacial sediments, however its exact position depends on the C_{org} content of both Glacial and Holocene sediment and the kinetic potential of mobilization-reoxidation processes.

INTRODUCTION

Of all the organic material produced by primary production in the surface ocean, only a small fraction settles on the sea floor, approximately 17% on the upper slopes, but only 1-1.5% in the deep, open ocean (Wollast, 1998). When organic matter reaches the ocean floor, it is subjected to a variety of mineralization processes. Marine sediments record the sequence of these degradation processes in the shape and positioning of profiles of oxidants and metabolites in pore waters (Froelich et al., 1979; Goloway and Bender, 1982; Heggie et al., 1987; Jahnke et al., 1982). In the upper mm's and cm's of the sediment column, organic matter is most plentiful, macrofauna and microbiota are most abundant, and the pathway for solute diffusion to the overlying water column is the shortest. The suite of reactions occurring in these sediments is termed 'early diagenesis'. As the pore water realm goes to a few meters, the reaction rates presumably are much slower, yet we know much less about what reactions occur at these depths since cores obtained for pore water analysis are not usually longer than 50 cm.

The objective of this chapter is to examine the downcore features of organic matter diagenesis in sediments in the Western North Atlantic Ocean that were obtained by gravity coring. Long cores have previously been studied from sites on the Amazon Fan (~5.14˚N, 46.58˚W), in an area that currently experiences little influence from the modern river plume (Schulz et al., 1994). In that study, pore waters revealed that the NO_3^- zone extends to ~40 cm into the sediments, reflecting the relatively low C_{org} input during the Holocene, and profiles of dissolved metals

were found to be closely related to both the degradation of organic matter and Fe oxides contained within Glacial-aged sediments (Schulz et al., 1994).

Throughout the Demerara Abyssal Slope and Plain, sedimentation rates are fairly uniform at 2-4 cm kyr^{-1} (Damuth, 1977), but C_{org} remineralization rates vary throughout the region (Chapter 2). We previously discussed the degradation of C_{org} over the length scale of a multi-core, 30-50 cm, where C_{org} degradation is dominated by oxygen and nitrate. Here we use gravity cores to examine the diagenetic zonation deeper in the sediments and explore what suboxic and possibly anoxic processes may occur at depth. Multi-cores from the same stations were used to assemble coherent geochemical profiles and correct for core-top loss (Lebel et al., 1982).

STUDY AREA AND METHODS

Seven gravity cores were collected aboard the R/V Melville in 2011 as part of the ANACONDAS project (Fig. 1, Table 1). Six of these stations also had multi-cores collected at the same station. Upon recovery, the gravity cores were placed upright on the deck of the ship and secured for immediate processing. After measuring the overall core length, the overlying water was drained from the core tube. Holes were drilled below the core top at 10 cm intervals for the first 5 samples, and then at 20 cm intervals thereafter. Rhizon soil samplers (Rhizosphere Resarch Products) were used to extract pore waters directly into acid cleaned plastic syringes with polyethylene plungers (Norm-Ject). Overall sample volume varied between 5 to 20

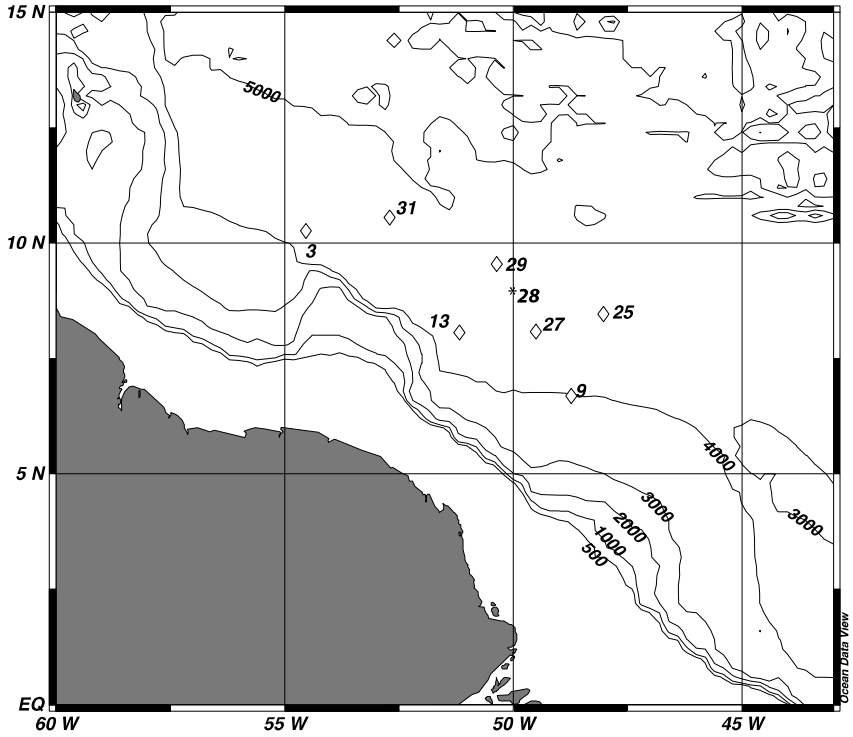

Figure 1. Map of study sites. *The multi-core data from station 28 was used to correct the depth assignments of the gravity core from station 29.

Table 1. Site Descriptions

Station	Latitude (˚N)	Longitude (˚W)	Depth (m)	MC Length (cm)	GC Length (cm)	GC Core-top Loss cm
3	10.27	54.53	4393	47	420	10
9	6.69	48.73	4030	44	120	15
13	8.07	51.18	4450	38	230	17
25	8.47	48.03	4526	44	310	3
27	8.08	49.53	4415	27	265	0
29	9.55	50.36	4784	42*	290	7
31	10.55	52.70	4889	49	320	0

* Multi-core from station 28

mL, which were split into separate samples bottles for subsequent analysis of dissolved Mn and Fe, NO_3^-,and $Si(OH)_4$.

At stations 25, 27, 29, and 31, porosity samples were taken from 5-6 depths throughout the length of the gravity core by drilling a 1.5 cm diameter hole into the core tube and extracting mud with a spatula. An aliquot of mud from each interval was collected in a pre-weighed glass container and used to determine the porosity by weight loss after drying. Dried sediment was subsequently ground to a fine powder with an agate mortar and pestle and used for solid phase analyses. After collecting the pore waters, the gravity core was packaged for transport back to USC.

Dissolved Si was analyzed shipboard on a flow-through spectrophotometer as discussed in Chapter 2 (analytical uncertainty for standard replicates was < ±6 %). There is a 2.5% increase in silicic acid concentration per ˚C above *in situ* temperatures (McManus et al., 1995). We measured the temperature of the OLW of each gravity core using a temperature probe, and continued to measure the temperature as the core warmed over time during sample collection. To correct our samples for warming, we took the midpoint of the total collection time and assumed an average temperature correction based on a plot of temperature vs. time. The midpoint temperature was generally ~7˚C. The uncertainty in temperature correction may add up to a 10% increase in the uncertainty for the Si profiles.

NO_3^- was analyzed on 100 µL samples using a Teledyne NO_x box with a chemiluminescence detector (Braman and Hendrix, 1989). The detection limit for NO_3^- was 0.1 µM. Uncertainty in replicate samples was < 3%.

Analyses for dissolved metals were performed either on a Thermo Elemental X-Series II ICP-MS or a Leeman Labs Prodigy ICP-OES at Oregon State University. Samples were acidified with trace metal clean HCl to pH ~2 prior to analysis. The detection limit for Mn ranged from 0.19 – 3.6 μM over the different runs, and from 0.16 – 4.8 μM for Fe. For samples above the detection limit, average uncertainties for Mn were 5% and for Fe 9% (average of all samples).

At stations 13 and 31, wt% and $\delta^{13}C$(TIC) of inorganic carbon (TIC) were determined by acidification of 40-70 mg of material and analysis of the evolved CO_2 with a Picarro G2121-i isotopic CO_2 analyzer (following the procedure discussed in Chapter 3). Sediment samples from station 13 were also analyzed for Total C content (TC) using an Elantech 1110 Elemental Analyzer (EA) connected to the Picarro, and C_{org} was determined by the difference between TC and TIC.

The depths of the gravity cores were adjusted to 'true depth' by matching the pore water profiles from the gravity cores of all four constituents (NO_3^-, $Si(OH)_4$, Mn^{2+}, and Fe^{2+}) as well as by using profiles of magnetic susceptibility measurements on the solid phase (Mortazavi, 2012). For the pore waters, the depth was adjusted until the best agreement between the multi-core profiles and gravity core profiles was found. As an additional check of our correlation between multi-cores and gravity cores, 8 magnetic susceptibility 'features' observed in the sediment profiles were used for depth correlation (Mortazavi, 2012).

RESULTS

Porosity

The porosity measured from the gravity cores at stations 25, 27, 29, and 31 had values ranging from 0.64 to 0.85 across all four cores (Table 2). The mean porosity at each station was 0.72, 0.79, 0.78, and 0.81 respectively and there was little change downcore. Since porosity was not directly measured at stations 3, 9 and 13, we took the porosity data measured from the multi-cores, selecting the deepest few depths that overlapped with the gravity core depths (Appendix A), and used this data for the subsequent flux calculations.

Pore water results

Adjusting the depth of gravity core horizons requires an adjustment for the amount of core-top lost by the 'bow wave' effect during coring. Correlations with multi-cores indicate that the amount of core-top loss varied from 0 to 17 cm (Table 1). There was good agreement between independent depth corrections performed by simultaneously correlating four pore water constituents (Figure 2). At station 29, there is no multi-core, so multi-core data from the next nearest station (28) was used for comparison to the gravity core. The adjusted depth assigned by pore water matching was compared to solid phase magnetic susceptibility profiles (Mortazavi, 2012) for all cores and there was also good coherence in all cases. We are confident

that the depth assignments used in the subsequent discussion are accurate to ± 3-5 cm. All gravity core data are presented in Appendix C.

Table 2.1. Gravity core porosity. Depths corrected for core-top loss.

Station	Depth (cm)	Porosity
3	20*	0.75
	26*	0.75
	30*	0.75
	34*	0.75
	38*	0.74
	mean:	**0.75**
9	38*	**0.71**
13	34*	**0.76**
25	35	0.73
	75	0.77
	120	0.80
	160	0.71
	200	0.66
	260	0.64
	mean:	**0.72**
27	30	0.74
	55	0.75
	95	0.81
	135	0.82
	195	0.80
	235	0.81
	mean:	**0.79**
29	35	0.76
	70	0.82
	110	0.85
	170	0.82
	210	0.81
	250	0.64
	mean:	**0.78**
31	28	0.78
	62	0.79
	102	0.83
	162	0.81
	225	0.82
	263	0.83
	mean:	**0.81**

*Samples taken from multi-cores

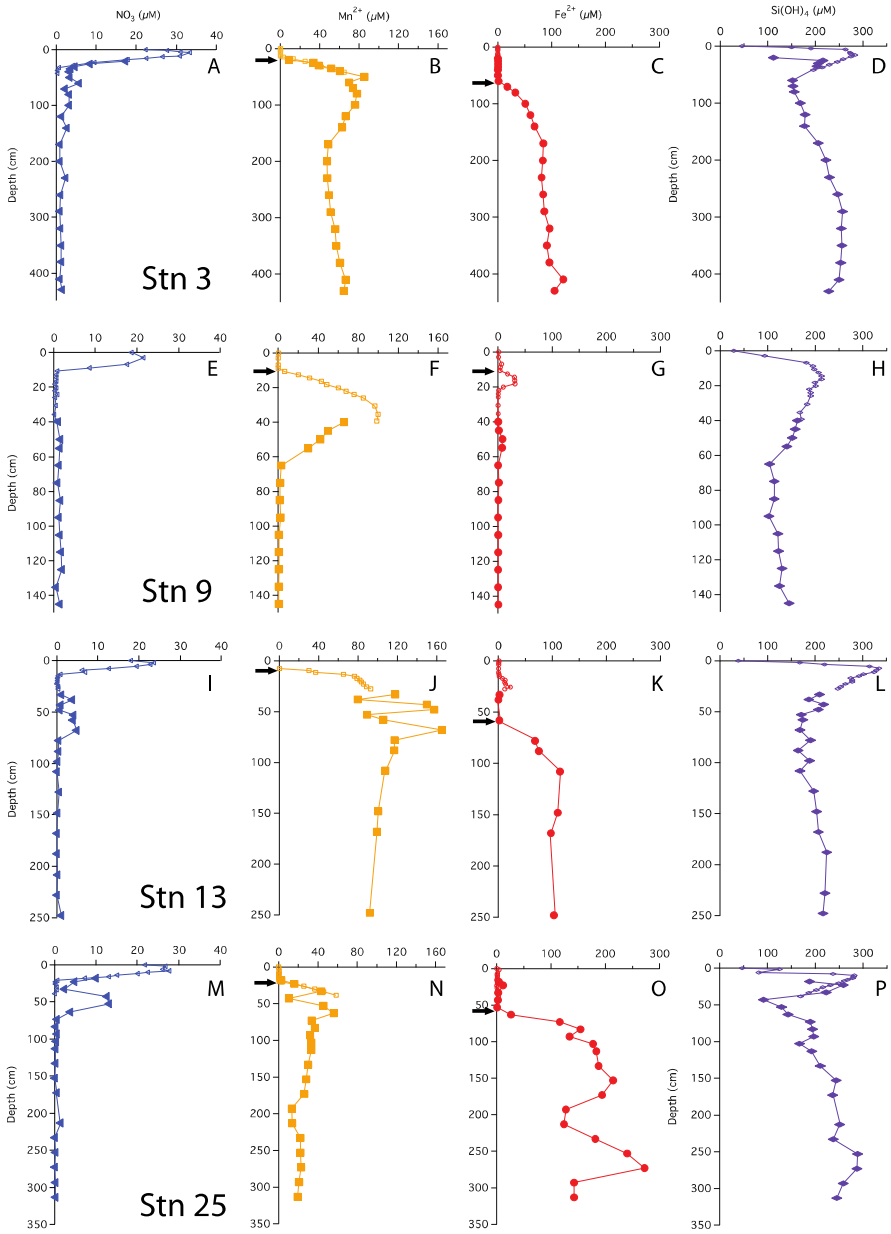
NO_3 (μM)
Mn^{2+} (μM)
Fe^{2+} (μM)
$Si(OH)_4$ (μM)
Depth (cm)
A
B
C
D
Stn 3
E
F
G
H
Stn 9
I
J
K
L
Stn 13
M
N
O
P
Stn 25

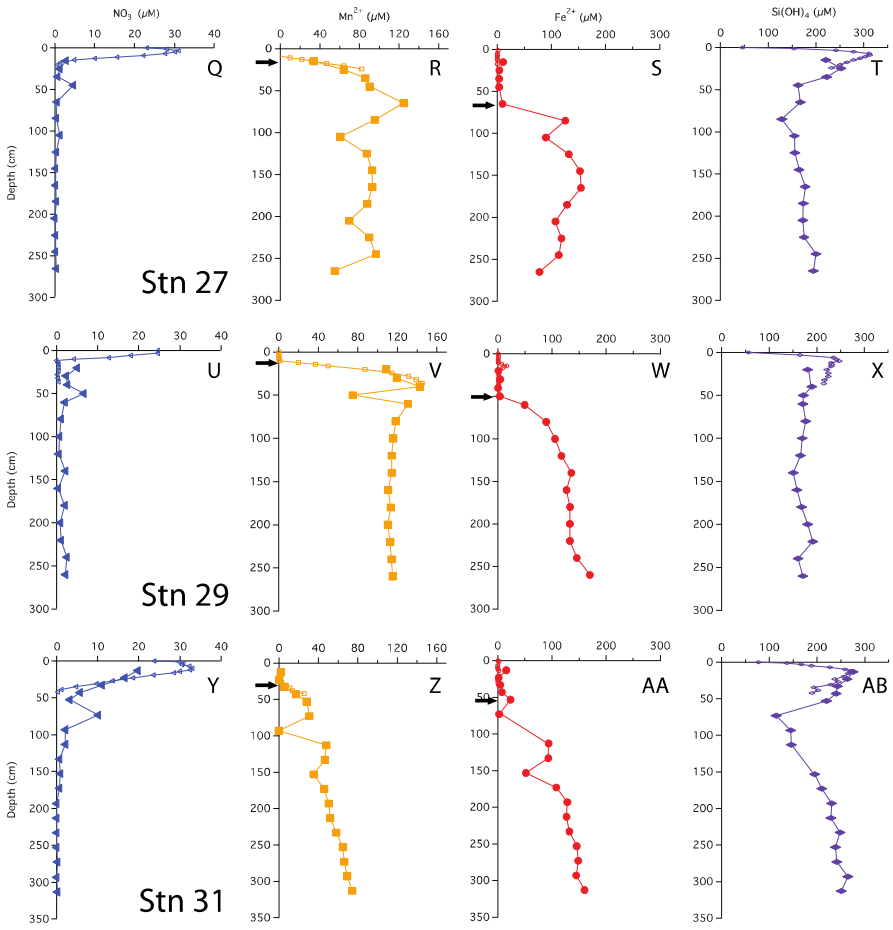

Figure 2. Pore water profiles of NO_3^- ◀, Mn^{2+} ■, Fe^{2+} ●, and $Si(OH)_4$ ◆. Arrows indicate depths where the flux was calculated following Fick's first law.

The multi-core pore water NO_3^- profiles have been discussed extensively in Chapter 2; all profiles showed an increase just below the SWI to a maximum ranging from 20-35 μM. The depth of the maximum ranged from 2 to 10 cm. Below this maximum, nitrate concentrations decreased, reaching near-zero values at a depths of 10-40 cm. Few gravity core profiles showed NO_3^- values of zero at depth, but the value measured was generally <2 μM. Some ammonium oxidation during sampling may explain this non-zero value. All of the stations, except station 9, had a 4-14 μM NO_3^- peak that appeared at a depth between 50-60 cm. As discussed below, we believe that this peak is not a sampling artifact.

The appearance depth of Mn^{+2} in the multi-cores has also been discussed extensively in chapter 2. It is assumed to be the depth where O_2 goes to zero and at the stations discussed in this study, ranged from 8-30 cm. The gravity core profiles were in good agreement with the multi-core profiles, and many of the profiles (station 3, 13, 25, 27, 29) showed an Mn^{+2} maximum before decreasing to an asymptotic value. The maxima appeared at depths between 40-70 cm. At station 9, Mn increased to a maximum of 100 μM at ~40cm after which it decreased to zero values. At station 31, the Mn profile steadily increased with depth. There may be a spurious Mn value in this core at ~90 cm.

The multi-cores generally had very little (<1μM) to no measureable dissolved Fe in the pore waters, however four stations (9, 13, 25 and 29) showed a small peak in dissolved Fe between 10-35 cm. At station 9, dissolved Fe appeared at 16 cm, rose to a concentration of 30 μM at 18 cm and then disappeared by 22 cm. At station 13,

dissolved Fe appeared at 15 cm, rising to 22 μM at 25 cm and disappearing at approximately 30 cm. At station 25, dissolved Fe rose to 12 μM at 23 cm and disappeared by 33 cm. At station 29, dissolved Fe appeared at 12 cm, reached a peak of 16 μM at 14 cm and disappeared at 24 cm.

The iron appearance depth, defined as the depth where we observed a continuous increase (not including the minor peaks discussed above) in concentration with depth, ranged from 60 – 80 cm. At stations 3, 13, 27, 29, and 31, the iron profiles increased to a generally asymptotic value with depth. The profile from station 31 increased with depth starting at ~50 cm and steadily increased to a concentration of ~150 μM at depth. At station 9, the concentrations of dissolved Fe remained at or near zero throughout the gravity core, although there was the aforementioned peak at 14-16 cm and a second, small maximum at ~50 cm depth.

Dissolved silica profiles all increased with depth throughout the multi-cores, reaching a maximum value between 9 and 15 cm, and then decreased thereafter. The gravity core data matched quite well with this decrease. The profiles appear to reach an asymptotic value with depth, although at stations 3, 25, and 31, dissolved Si decreased to a minimum before increasing back to the asymptotic concentration.

Solid Phase Results

Solid phase analyses were only performed on two gravity cores, 13 and 31. Matching solid phase properties, as discussed above, is yet another way to assess

the position of the gravity core relative to the multi-core. The alignment of pore water, magnetic and solid phase properties all agree with one another.

These sites are separated by 340 km; station 13 lies closer to the primary axis of the river plume, and station 31 lies off this axis and further to the NW (Chapter 2 and 3). The wt% $CaCO_3$ from stations 13 and 31 show very similar patterns, both increased and then decreased with depth. At station 13, the profile reached a maximum (33 wt%) at ~50 cm and decreased to <1 wt% around 90 cm depth (Figure 3). The wt% C_{org} measured at this station shows the opposite trend, decreasing with depth, reaching a minimum (0.2 wt%) at 60-70 cm. Values increased below this depth. At station 31, the $CaCO_3$ profile followed a similar pattern, reaching a maximum (35 wt%) at ~30 cm, decreasing to near zero at 50-60 cm depth.

The $\delta^{13}C$(TIC) values from both stations decreased with depth below a maximum. However, slight differences between the two profiles were evident; the maximum was somewhat shallower at station 31, occurring at ~15 cm with an isotopic value of ~1.2‰ while at station 13, the maximum was at ~20 cm with a value of ~1.5‰. The surface isotopic concentration also differed, with a value of 0.8 ‰ at station 31 compared to a value of 1.2 ‰ at station 13.

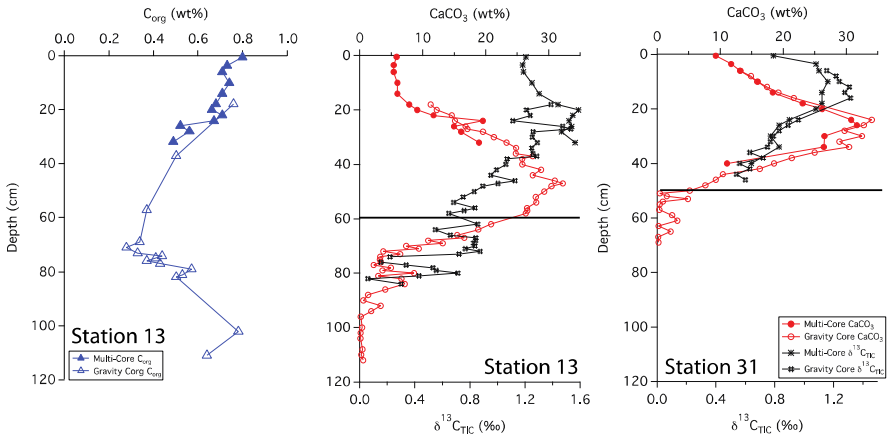

Figure 3. Downcore profiles of C_{org}, $CaCO_3$ and $\delta^{13}C_{(TIC)}$. Black lines indicate the depth of the indurated iron crust.

DISCUSSION

Fluxes, diagenetic zonation and profile shape

Oxygen and Nitrate

Generally, the gravity cores reflected pore water zonations expected from C_{org} diagenesis (Froelich et al., 1979), though due to the low C_{org} content, the zones were expanded over several meters (Fig 2). Based on the appearance of dissolved Mn in the pore waters (Froelich et al., 1979), we assumed that the maximum depth of oxygen penetration was between 10-30 cm, similar to previous observations (Schulz et al., 1994). As discussed in Chapter 2, this is consistent with the depth at which denitrification begins. All nitrate profiles reached a maximum below the SWI and then nitrate was consumed and depleted by 30 cm (Fig 4. feature A). A secondary nitrate peak (Fig. 4 features B and C) was a consistent feature in 6 cores and is discussed below in the context of oxidation of ammonium at depth.

Dissolved Mn and Fe

The fluxes of reduced metals within the sediment column can be used to assess possible reaction stoichiometries. We calculated fluxes of Mn^{2+}, and Fe^{2+} using Fick's first law following Hammond et al., (1996):

$$J = -\phi^n D_{sw} \frac{dC}{dz} \quad (1)$$

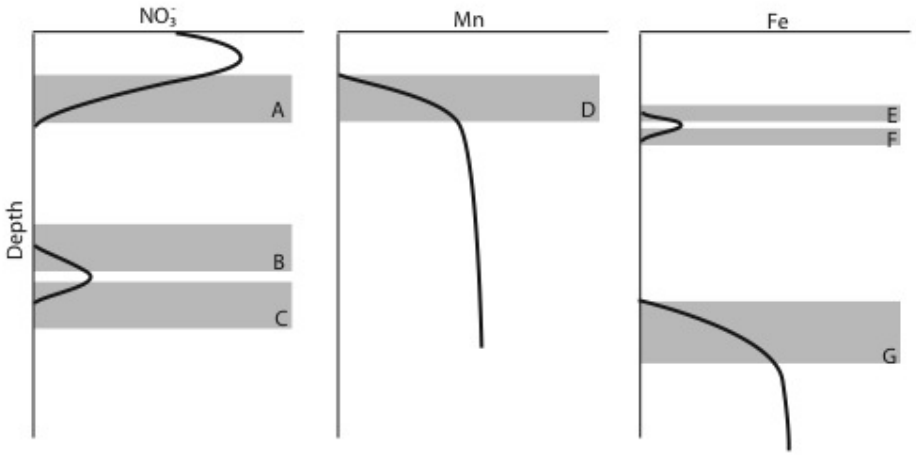

Figure 4. Schematic model of the major features observed in most of the gravity core pore water profiles. A) Consumption zone of the primary NO_3- peak. B) Upper zone of the secondary NO_3- peak. C) Lower zone of the secondary NO_3- peak. D) Manganese appearance depth. E) Upper zone of the primary Fe peak. F) Lower zone of the primary Fe peak. G) Appearance of the secondary Fe production zone.

where □ is the average porosity from the gravity core, D_{sw} is the molecular diffusivity in seawater ($cm^2\ sec^{-1}$), and dC/dz is the concentration gradient. dC/dz was determined by fitting a line through 3-6 points within the depth range of the selected concentration gradient. We used a value n = 2.6 following previous work to correct for tortuosity(Hammond et al., 1996; McManus et al., 1995). Molecular diffusivities at 2 ˚C were calculated following Li and Gregory (1974) and Schulz (1994) and the values we used in these calculations were: Mn^{2+} = 3.20 x 10^{-6} cm^2 sec^{-1}, Fe^{2+} = 3.20 x 10^{-6} cm^2 sec^{-1}.

The flux of Mn^{2+} at the position of the arrow (Fig. 2 and Fig. 4 feature D) ranged from 1.2 – 7.5 μmol m^{-2} d^{-1} with the highest flux at station 29 and the lowest at station 25 (Table 3). There does not appear to be a geographic pattern in the fluxes, and so Mn reduction is likely controlled by processes in the sediment rather than by the location of the river plume. Most of the pore water Mn profiles reached a near constant concentration at depth, and hence a near zero flux. The value of this asymptotic concentration ranged between 0 and 110 μM, with station 29 having the highest value. The lack of appreciable production or consumption at depth is different than was observed on the Amazon Fan, where dissolved Mn gradually decreased with depth to near zero values at 700 cm depth (Schulz et al., 1994). It is possible that the sediments become carbon limited at depth resulting in little carbon diagenesis at these depths. Another possibility is that Mn mineral solubility could be playing a role in the quasi-constant value obtained.

Below the depth of the gradient of Mn^{2+}, most of the nitrate profiles (except at station 9) had a secondary nitrate peak (4-13 μM) (Fig. 4 feature D). Since all of the nitrate produced from aerobic nitrification is subsequently consumed (feature A Fig. 4), the production of this additional nitrate is curious. It is possible that this feature is an artifact stemming from the oxidation of ammonium during sampling under aerobic conditions, but the fact that this secondary nitrate appears over a limited depth range and at the same depth across all gravity cores makes it less likely. It is also possible that this is an artifact of rhizon sampling water derived from the overlying water, trapped and perhaps channeled down the inside of the gravity core tube. We rule out this artifact because dissolved Si does not show an interruption in its profile. Bioirrigation is also ruled out for the same reason.

Feature D (Fig. 4) is perhaps created by anoxic nitrification coupled to Mn-oxide reduction (Hulth et al., 1999). Although there is no obvious change in the concentration gradient within the Mn profile, it is possible that anoxic nitrification could be the only method of Mn reduction occurring in the sediments due to the low availability of C_{org} in the sediments at depth. However, the stoichiometry of the flux of the secondary nitrate peak and the production flux of Mn^{2+} don't match the reaction stoichiometry for anoxic nitrification (Table 4). Thus, if this reaction is taking place, some of the dissolved Mn must be removed from the pore waters. Since the secondary nitrate peak also coincides with the consumption of dissolved silica, which is removed via reverse weathering as discussed below, the dissolved Mn could be removed by adsorption onto these newly formed authigenic aluminosilicates.

Table 4. Stoichiometries of known and hypothetical pathways of sedimentary redox processes.
Organic matter is represented as CH_2O for simplicity.[a]

Reaction	Process	Reaction	$\Delta G^{\circ\prime}$ (kJ mol^{-1})
	N Oxidation		
I	Nitrification	$2O_2 + NH_4^+ \rightarrow 2H^+ + NO_3^- + H_2O$	-353
II	Anoxic Nitrification	$\frac{3}{2}MnO_2 + NH_4^+ + 6H^+ \rightarrow 4Mn^{2+} + NO_3^- + 5H_2O$	-141
	N Reduction		
III	Denitrification	$\frac{5}{4}CH_2O + NO_3^- + H^+ \rightarrow \frac{5}{4}CO_2 + \frac{1}{2}N_2 + \frac{7}{4}H_2O$	-590
IV	NH_4^+ oxidation	$\frac{5}{3}NH_4^+ + NO_3^- \rightarrow \frac{4}{3}N_2 + 3H_2O + \frac{2}{3}H^+$	-550
V	Fe^{2+} oxidation	$NO_3^- + 5Fe^{2+} + 12H_2O \rightarrow 5Fe(OH)_3 + \frac{1}{2}N_2 + 9H^+$	-370
VI	Anoxic Mn^{2+} oxidation	$NO_3^- + \frac{5}{2}Mn^{2+} + 2H_2O \rightarrow \frac{5}{2}MnO_2 + \frac{1}{2}N_2 + 4H^+$	-71.4
	Metal Reduction		
VII	Mn Reduction (microbial)	$\frac{1}{2}CH_2O + \frac{3}{2}CO_2 + \frac{1}{2}H_2O + MnO_2 \rightarrow Mn^{2+} + 2HCO_3^-$	-190
VIII	Mn Reduction (abiotic)[b]	$2Fe^{2+} + MnO_2 + H_2O \rightarrow 2FeOOH + Mn^{2+} + 2H^+$	+80
IX	Fe Reduction (microbial)	$CH_2O + 7CO_2 + 4Fe(OH)_3 \rightarrow 4Fe^{2+} + 8HCO_3^- + 3H_2O$	-107

[a] Adapted from Hulth et al., 1999. Values of standard free energy of formation are at 25˚C and pH=8.
[b] Reaction from Postma (1985). Free energy calculated assuming $[Fe^{2+}]$ = 5 µM; $[Mn^{2+}]$ = 100 µM.

The secondary nitrate peak is consumed both above and below the depth of its appearance (Fig. 4, features B and C, respectively). In feature B, the secondary nitrate diffuses upwards and is likely consumed by denitrification (Table 4 Eq. III), though it is also possible that nitrate is involved in the oxidation of ammonium or in the anoxic reoxidation of Mn^{2+} (Table 4 Eq. IV and VI, respectively). The lower boundary of the secondary nitrate max (feature C) could be caused by diffusion and consumption by reduction with Fe^{2+} (Table 4 Eq. V). The depth of feature C is nearly coincident with the depth of the disappearance of the major Fe^{2+} gradient (Table 5). For example, the concentration gradients of feature C and G at station 25 (Fig. 2) appear to have the stoichiometry expected from Fe oxidation coupled to nitrate reduction (Table 4, Eq. V).

The fluxes of dissolved Fe at the position of the arrow in Fig. 2 (and feature G in Fig. 4) ranged from 0.06 – 3.7 μmol m^{-2} d^{-1}. The flux was the lowest at station 9 and the highest at station 25. As with dissolved Mn, there did not appear to be a spatial pattern in Fe^{+2} fluxes. The profiles of dissolved Fe reached a near constant concentration of ~100 μM at stations 3, 13, 29 and 31. The profiles from stations 25 and 27 showed more variation, indicating that there may be more iron recycling downcore at these sites. At station 9, very little dissolved iron was produced at depth, perhaps removed by the production of Fe-sulfides as has been observed on the Amazon Fan (Schulz et al., 1994). It was noted that sediments in this core were very dark colored.

Stations 9, 13, and 29 all had small peaks (between 16-31 uM) in dissolved iron appear very shallow in the sediment column (Fig. 4 feature E, F), 20-40 cm above the major gradient of dissolved Fe (feature G) and within the zone of Mn

Table 5. Depths of the features observed in the pore water profiles of NO_3^-, Mn and Fe as defined in Figure 4.
All values are in (cm).

Station	A	B, C	D	E,F	G	G-D
3	32	50-60	15	-	60	45
9	11	-	8	10-14	12	4
13	13	53-78	8	15-18	78	70
25	17	43-63	20	-	63	43
27	14	45-65	10	-	65	55
29	10	40-50	10	12-16	50	40
31	42	43-63	29	-	43	14

A. Consumption zone of the primary NO_3^- peak
B. Upper zone of the secondary NO_3^- peak
C. Lower zone of the secondary NO_3^- peak
D. Manganese Appearance Depth
E. Upper zone of the primary Fe peak
F. Lower zone of the primary Fe peak
G. Appearance of the secondary Fe production zone
G-D The amount of seperation between the appearance of Mn and Fe in pore waters

reduction (Table 5). These primary peaks in Fe imply local production and consumption of dissolved Fe. Generally, Fe reduction is not expected to take place at the same depth as Mn reduction due to the lower energy yield of the reaction (Froelich et al., 1979). However, the free energy calculations used to generate the expected energetic yield from anaerobic diagenetic reactions generally assume that the metal oxides are well-characterized, crystalline minerals (Burdige, 1993). It could be possible for localized Fe reduction to occur at concurrent depths with Mn reduction if the Fe oxides were poorly crystallized, amorphous solids. The shallow peaks of dissolved Fe are also coincident with the depth at which the primary NO_3^- peak goes to zero (Fig.4 feature A, Table 5). In feature E, the newly produced Fe^{2+} is consumed as it diffuses upwards, likely oxidized by the NO_3^- (Table 4 Eq. V). In feature F, just below the primary Fe peak, it is unclear what reaction is responsible for Fe consumption, as by this depth, the NO_3^- from feature A has been consumed. Postma (1985) proposed a reaction between Fe^{2+} and Mn-oxides (Table 4 Eq. VIII). While this reaction is unfavorable at standard temperature and pressure, Postma (1985) found that the reaction kinetics were fastest at pH <4, but still feasible to at least pH 6.5; at pH 6.3+ the precipitation of Fe oxyhydroxides begins to compete with the Mn-oxide reaction. The Fe^{2+} oxidation-NO_3^- reduction reaction occurring in nearby feature E could produce the acidic conditions necessary for abiotic Mn reduction to consume the remaining Fe^{2+}.

It has been generally found that iron reduction occurs at a depth coinciding with the disappearance of NO_3^- from pore waters (Burdige, 1993; Lyle, 1983). However, here, only stations 9 and 31 displayed this type of pattern. At the other

stations, dissolved Fe appeared 30-65 cm below the depth of 'major' nitrate disappearance (Table 5). We also examined the difference between the depths of appearance of the major gradients of Mn and Fe and found that while stations 9 and 31 had very little separation (4 and 14 cm, respectively), the other stations showed a separation ranging from 40-70 cm. This large spacing between the diagenetic zones indicates that at many stations, the C_{org} load of the sediments is quite low. At station 13, we measured the C_{org} wt% of the upper 120 cm of the gravity core, and found that concentrations decreased with depth to 70 cm, after which concentrations increased (Fig. 3). This minimum in C_{org} correlates to the appearance of Fe in the pore waters (feature G). Thus, at many stations, C_{org} limitation hinders Fe reduction until depths in the sediment where C_{org} is more prevalent. Previous work has shown that this is a ubiquitous phenomenon in the sediments of the equatorial Atlantic (Funk et al., 2003). We propose that the production of Fe^{+2} is occurring in Glacial-aged sediments containing higher C_{org} content.

Dissolved Silica

While all of the profiles of dissolved silica rapidly increased with depth, they did not immediately reach a constant value, instead decreasing from a maximum to values ranging from 100-250 μM. The dissolution of biogenic opal in sediments typically reaches an asymptotic value within 5-30 cm below the SWI that can range from 100 to 850 μM throughout the global ocean (Archer et al., 1993; Dixit et al., 2001; Fanning and Pilson, 1974; McManus et al., 1995; Rabouille et al., 1997; Sayles

et al., 1996), though these values are well below the solubility of fresh plankton (Lawson et al., 1978; Van Cappellen and Qiu, 1997). One possible explanation is that the there is a kinetic 'competition' between the dissolution of bSi and the formation of alumino-silicate minerals (Mackenzie and Garrels, 1966; Mackenzie et al., 1981; Ristvet, 1978; McManus et al., 1995). Clay formation produced by reverse weathering has been documented experimentally (Dixit et al., 2001), and has also been identified as an important reaction in the sediments of the Brazilian continental shelf underlying the Amazon Plume (Michalopoulos and Aller, 1995; Michalopoulos et al., 2000; Michalopoulos and Aller, 2004). Thus, it is quite possible that reverse weathering also plays an important role in opal preservation in the deep-sea sediments underlying the plume. The rapid dissolution of bSi in the surface sediments could be curtailed by the production of Al(III) from the remineralization of detrital minerals, as Al(III) has been shown to reduce silica solubility and induce precipitation of authigenic alumino-silicates (Dixit et al., 2001). The asymptotic value at depth could represent the new balance between the kinetics of dissolution and reverse weathering processes. The co-occurrence of the dissolved Si minimum and the steep Fe^{+2} gradient may imply the Fe oxidation processes involve a sink for dissolved Si.

Location of the indurated iron crust vs. pore water profiles

Previous work in this region has revealed that indurated, or semi-lithified, metal-rich layers are fairly common in the sediments of the Western Equatorial

Atlantic (Damuth, 1977; Flood et al., 1995; Mcgeary and Damuth, 1973). Metal-rich layers can form either within sediments from enrichment due to post-depositional redistribution of metals or at the SWI from direct precipitation or deposition from the water column. Observations of iron-rich crusts in this area indicated that the crusts appeared to correlate to the Pleistocene-Holocene boundary and were suggested to have been formed by the oxidation of reduced iron at the SWI after the post-glacial sea level rise (Mcgeary and Damuth, 1973). More recent studies have suggested that the crust is formed within the sediments due to non-steady state diagenetic processes resulting from the downward progression of redox boundaries stemming from the reduction in sedimentation rates following the last glacial/interglacial transition (Schulz et al., 1994; Kasten et al., 1998; Kasten et al., 2003) and penetration of oxygen. Under steady state conditions, solid-phase enrichments gradually migrate upwards as ongoing sedimentation moves these layers into increasingly reducing conditions and they are dissolved. However, a decrease in C_{org} burial over time can cause a fixation of the redox boundaries at a particular depth in the sediments for a prolonged period of time, thus creating higher solid-phase concentrations of the metal than would be produced during steady state (Kasten et al., 1998; Kasten et al., 2003). In the equatorial Atlantic, the active Fe(II)/Fe(III) redox boundary has become trapped at the upper boundary of the most recent change in TOC deposition, while the Mn enrichment has migrated upwards due to the faster reduction kinetics of Mn compared to Fe (Funk et al., 2003; Kasten et al., 2003).

Four of the cores from this study have a semi-hardened crust and one (Station 9) has a distinct color change from tan (above) to grey but no crust (Mortazavi 2012). The crust was defined by texture and visual inspection, and these observations matched those of previous workers whose subsequent measurements identified this as an Fe-rich layer (Damuth, 1977; Flood et al., 1995; Kasten et al., 1998; Mcgeary and Damuth, 1973). Mortazavi concluded that while the crust occurs near the Pleistocene-Holocene transition, it is not a direct marker of the exact boundary. Her means of age control were some ^{14}C dates and correlations established using magnetic stratigraphy.

The best-developed iron crusts were identified in cores from the central region of the study area (south of 10˚N and west of 50˚W) at sites influenced by both the spring plume and fall retroflection but not in the axis of the plume. While not at the same exact depth across all cores, the iron crust consistently appeared at the depth where dissolved iron appeared in the pore waters (Fig. 5). We can infer that there is likely an iron crust at stations 25 and 27 located where the Fe^{2+} gradient begins, however there was no sedimentary analysis of these cores.

Solid phase $CaCO_3$ measurements can also be used to infer where the transition between glacial and interglacial sediments occurs. Clay deposition in the Atlantic was higher during glacial times, resulting in lower $CaCO_3$ concentrations in glacial sediments (Bacon, 1984; Balsam and McCoy, 1987; Thomson et al., 1990). Based on ^{14}C age measurements made from bulk 200 μm sieved material (Chapter 3), the age of sediments at 38 cm from station 31 is ~10400 ypb, right at the

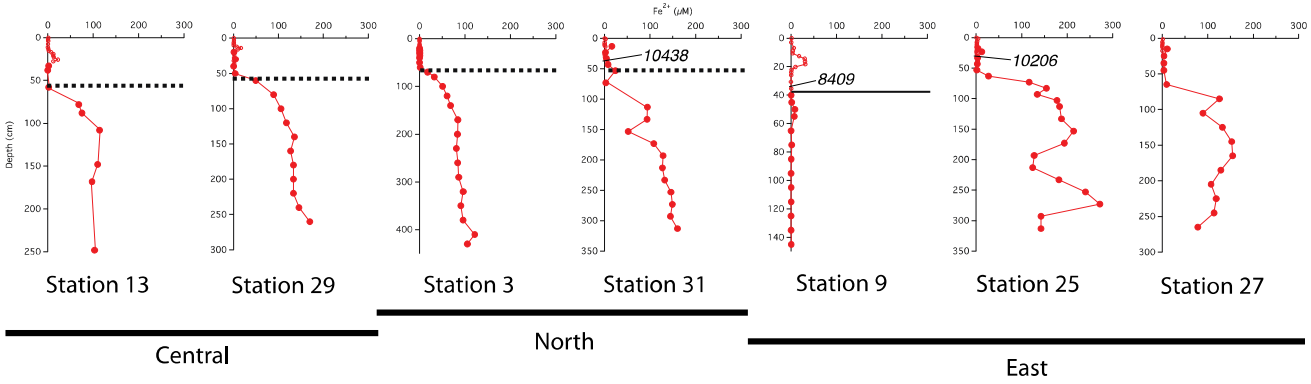

Figure 5. Comparison of the location of the indurated iron crust with the pore water profiles. Dashed lines represent the iron crust identified by Mortazavi (2012). The solid line at station 9 represents the depth of the color change from tan to grey. Central refers to stations south of 10˚N and west of 50˚W; North refers to stations above 10˚N; East refers to stations east of 50˚W. Calendar ages measured from bulk 200 μm sieved material are indicated where available.

boundary between the Pleistocene and Holocene (Mercer, 1972; Mörner, 1976). The $CaCO_3$ profile at this site rapidly decreases, reaching zero at 50 cm (Fig. 3); thus the depletion of $CaCO_3$ downcore is a good indicator of the transition from glacial to interglacial sediments. At station 31, the depth of disappearance of $CaCO_3$ from the sediment correlates quite well to the location of the iron crust, but at station 13, there is a ~30 cm offset between the disappearance of $CaCO_3$ and the depth of the iron crust (Fig. 3). It is possible that station 13 has somewhat higher concentrations of C_{org} in early Holocene sediments; thus the iron layer was able to migrate upwards over time at this site. Higher concentrations of C_{org} downcore may also explain why station 9, located at the base of the Amazon Fan, has a color change from tan to grey but no observable crust. Additional Corg would make the reaction kinetics of Fe reduction more favorable, allowing for the complete dissolution of the crust. Overall, these results confirm that the iron crust can be used as a relative, but not exact, indicator of the transition from glacial to interglacial sediments.

Knowing that the age of the sediments near the crust horizon is ~10,000 ybp, we tried to determine if the Fe^{2+} flux is sufficient to create the crust in this length of time. We used the porosity from the depth interval closest to the crust depth (~50cm) to determine the sediment density at that depth, assuming an overall grain density of 2.5 g cm^{-3}. Using a sediment Fe concentration of 30 g Fe(III) kg^{-1} from measurements on the Amazon Fan (Kasten et al., 1998), and crust thicknesses from Mortazavi (2012), we calculated the length of time it would take to create the observed crust (Table 6). At stations 13 and 25, the flux of Fe^{+2} is sufficient to produce the Fe crust within ~10,000 years, while stations 27 and 31 require

Table 6. Iron crust formation times. Calculations assumed a concentration of 30 g kg^{-1} within the crust.

Station	Fe^{2+} ($\mu mol\ m^{-2}d^{-1}$)	Porosity at 50 cm	Density ($g\ cm^{-3}$)	Crust Thickness (cm)	[Fe] ($g\ cm^{-3}$)	Formation Time (years)
3	0.7	0.74	0.65	4	0.020	51711
9[a]	0.06	0.71	0.725	-		
13	3.5	0.76	0.6	4	0.018	10179
25	3.7	0.73	0.675	5	0.020	13498
27	2.1	0.75	0.625	5	0.019	21798
29	1.9	0.82	0.45	0.5	0.014	1716
31	1.9	0.79	0.525	7	0.016	29080

[a] Station 9 did not have a visible Fe crust and was not used in this simulation

~20,000 years, and station 3 requires 50,000 years. The results show that the flux at station 29 is sufficiently large, and the crust sufficiently small that it could form in ~2000 years (Mortazavi, 2012). It is possible that there is additional Fe in the sediments surrounding the 0.5 cm lithified crust, and that the actual thickness of the crust is larger than what can be visually observed. A 4 cm crust depth at station 29 would take approximately 13,000 years to form. At stations 3, 27 and 31, it is possible that the concentration of Fe is lower than our assumed value, this would result is shorter time-of-formation. The results of this simulation indicate that the Fe crust is likely a relic of the change from glacial to interglacial sedimentation, where low C_{org} deposition during the Holocene has effectively trapped Fe diagenesis at this horizon.

CONCLUSIONS

Throughout the sites examined here, the depth of oxygen penetration was generally 10-20 cm below the SWI as indicated by the transition from nitrification to denitrification and consistent with the appearance of Mn+2 in pore waters. Nitrate is present in pore waters to ~ 30 cm. Nearly all of the cores also had a secondary nitrate maximum (4-13 μM) at ~50 cm depth perhaps stemming from the oxidation of ammonium. We propose that Mn-oxide reduction may be responsible for the secondary nitrate maximum. The disappearance of the secondary peak of nitrate coincided with the production of dissolved Fe at depth. Stoichiometric flux budgets are consistent with Fe^{+2} oxidation and nitrate consumption at this boundary. Most

of the profiles of dissolved metals generally showed a near zero flux at depth, and at most sites, the major gradient of iron occurred well below the depth of the major nitrate disappearance, indicating that the sediments are likely carbon limited at depth but that there is sufficient organic C to drive denitrification.

Dissolved silica profiles indicate rapid dissolution within the upper 30 cm followed by dissolved Si consumption, settling at a much lower constant concentration. The decrease in $Si(OH)_4$ concentration is likely attributable to reverse weathering and the asymptotic concentration is indicative of the balance between the kinetic competition between dissolution and the formation of authigentic alumino-silicate minerals. Pore water gradients are consistent with the hypothesis that iron oxidation is also responsible for dissolved Si uptake.

The depth of an indurated iron-rich crust is a relative indicator of the transition from glacial to interglacial sediments that agrees fairly well with an assessment of this boundary based on $CaCO_3$ content and ^{14}C dates. However, the actual location of the crust depends on the amount of C_{org} present in the sediments. At sites with sufficient C_{org} content, the crust can migrate upwards due to reduction-reoxidation processes. Simulations show that 10,000 years is a sufficient amount of time to form the observed crusts given the fluxes of dissolved Fe calculated at each site.

ACKNOWLEDGEMENTS

This work was supported by NSF grant #OCE-0934073 awarded to WB. We are grateful to the captain and crew of the R/V Melville. We would also like to acknowledge the members of the at-sea and shore-based science party and all contributors to the ANACONDAS project especially Chief Scientist Patricia Yager. We thank Nick Rollins, James McManus, Jesse Muratli, Steve Lund, Emily Mortazavi, Troy Gunderson, Alice Bitzer, Cara Fassino, and Jake Porter for their assistance and contributions to this work.

References

Archer, D.E., Lyle, M.W., Rodgers, K., and Froelich, P.N., 1993, What controls opal preservation in tropical deep-sea sediments: Paleoceanography, v. 8, no. 1, p. 7–21.

Bacon, M.P., 1984, Glacial to interglacial changes in carbonate and clay sedimentation in the Atlantic Ocean estimated from 230 Th measurements: Chemical Geology, v. 46, no. 2, p. 97–111.

Balsam, W.L., and McCoy, F.W., 1987, Atlantic sediments: Glacial/interglacial comparisons: Paleoceanography, v. 2, no. 5, p. 531–542.

Braman, R., and Hendrix, S., 1989, Nanogram nitrite and nitrate determination in environmental and biological materials by vanadium (III) reduction with chemiluminescence detection: Analytical Chemistry, v. 61, no. 24, p. 2715–2718.

Burdige, D.J., 1993, The biogeochemistry of manganese and iron reduction in marine sediments: Earth Science Reviews, v. 35, no. 3, p. 249–284.

Damuth, J.E., 1977, Late Quaternary sedimentation in the western equatorial Atlantic: GSA Bulletin, v. 88, no. 5, p. 695, doi: 10.1130/0016-7606(1977)88<695:LQSITW>2.0.CO;2.

Dixit, S., Van Cappellen, P., and van Bennekom, A.J., 2001, Processes controlling solubility of biogenic silica and pore water build-up of silicic acid in marine sediments: Marine Chemistry, v. 73, no. 3, p. 333–352.

Fanning, K.A., and Pilson, M.E., 1974, The diffusion of dissolved silica out of deep-sea sediments: Journal of Geophysical Research: Oceans (1978–2012), v. 79, no. 9, p. 1293–1297.

Flood, R.D., Piper, D., and Klaus, A., 1995, Proceedings of the Ocean Drilling Program, Initial Reports: College Station, TX.

Froelich, P.N., Klinkhammer, G.P., Bender, M.L., Luedtke, N.A., Heath, G.R., Cullen, D., Dauphin, P., Hammond, D.E., Hartman, B., and Maynard, V., 1979, Early oxidation of organic matter in pelagic sediments of the eastern equatorial Atlantic: suboxic diagenesis: Geochimica et Cosmochimica Acta, v. 43, no. 7, p. 1075–1090.

Funk, J.A., Dobeneck, Von, T., Wagner, T., and Kasten, S., 2003, Late quaternary sedimentation and early diagenesis in the Equatorial Atlantic Ocean: Patterns, trends and processes deduced from rock magnetic and geochemical records, *in* South Atlantic in the Late Quaternary, Springer, Berlin, p. 461–497.

Goloway, F., and Bender, M.L., 1982, Diagenetic models of interstitial nitrate profiles in deep sea suboxic sediments: Limnology and Oceanography,, p. 624–638.

Hammond, D.E., McManus, J., Berelson, W.M., Kilgore, T.E., and Pope, R.H., 1996, Early diagenesis of organic material in equatorial Pacific sediments: stoichiometry and kinetics: Deep Sea Research Part II: Topical Studies in Oceanography, v. 43, no. 4-6, p. 1365–1412.

Heggie, D.T., Maris, C., Hudson, A., Dymond, J., Beach, R., and Cullen, J.L., 1987, Organic carbon oxidation and preservation in NW Atlantic continental margin sediments: Geological Society, London, Special Publications, v. 31, no. 1, p. 215–236.

Hulth, S., Aller, R.C., and Gilbert, F., 1999, Coupled anoxic nitrification/manganese reduction in marine sediments: Geochimica et Cosmochimica Acta, v. 63, no. 1, p. 49–66.

Jahnke, R.A., Emerson, S.R., and Murray, J.W., 1982, A model of oxygen reduction, denitrification, and organic matter mineralization in marine sediments: Limnology and Oceanography, v. 27, no. 4, p. 610–623.

Kasten, S., Freudenthal, T., Gingele, F.X., and Schulz, H.D., 1998, Simultaneous formation of iron-rich layers at different redox boundaries in sediments of the Amazon deep-sea fan: Geochimica et Cosmochimica Acta, v. 62, no. 13, p. 2253–2264.

Kasten, S., Zabel, M., Heuer, V., and Hensen, C., 2003, Processes and signals of nonsteady-state diagenesis in deep-sea sediments and their pore waters: The South Atlantic in the Late Quaternary: Reconstruction of material budget and current systems,, p. 431–459.

Lawson, D.S., Hurd, D.C., and Pankratz, H.S., 1978, Silica dissolution rates of decomposing phytoplankton assemblages at various temperatures: American Journal of Science, v. 278, no. 10, p. 1373–1393.

Lebel, J., Silverberg, N., and Sundby, B., 1982, Gravity core shortening and pore water chemical gradients: Deep Sea Research Part A. Oceanographic Research Papers, v. 29, no. 11, p. 1365–1372.

Li, Y., and Gregory, S., 1974, Diffusion of ions in sea water and in deep-sea sediments: Geochimica et Cosmochimica Acta, v. 38, no. 5, p. 703–714.

Lyle, M.W., 1983, The brown-green color transition in marine sediments: A marker of the Fe (III)-Fe (II) redox boundary: Limnology and Oceanography, v. 28, no. 5, p. 1026–1033.

Mackenzie, F.T., and Garrels, R.M., 1966, Chemical mass balance between rivers and oceans: American Journal of Science, v. 264, no. 7, p. 507–525.

Mackenzie, F.T., Ristvet, B.L., Thorstenson, D.C., Lerman, A., and Leeper, R.H., 1981, Reverse weathering and chemical mass balance in a coastal environment, *in* Martin, J., Burton, J.D., and Eisma, D. eds., River inputs from Ocean Systems, United Nations Environmental Programme, United Nations Educational, Scientific, and Cultural Organization, Geneva, Switzerland, p. 152–187.

Mcgeary, D., and Damuth, J.E., 1973, Postglacial Iron-Rich Crusts in Hemipelagic Deep-Sea Sediment: GSA Bulletin, v. 84, no. 4, p. 1201–1212, doi: 10.1130/0016-7606(1973)84<1201:PICIHD>2.0.CO;2.

McManus, J., Hammond, D.E., Berelson, W.M., Kilgore, T.E., DeMaster, D.J., Ragueneau, O.G., and Collier, R.W., 1995, Early diagenesis of biogenic opal: Dissolution rates, kinetics, and paleoceanographic implications: Deep Sea Research II, v. 42, no. 2-3, p. 871–903.

Mercer, J.H., 1972, The lower boundary of the Holocene: Quaternary Research, v. 2, no. 1, p. 15–24.

Michalopoulos, P., and Aller, R.C., 2004, Early diagenesis of biogenic silica in the Amazon delta: alteration, authigenic clay formation, and storage: Geochimica et Cosmochimica Acta, v. 68, no. 5, p. 1061–1085.

Michalopoulos, P., and Aller, R.C., 1995, Rapid clay mineral formation in Amazon delta sediments: reverse weathering and oceanic elemental cycles: Science,, p. 614–614.

Michalopoulos, P., Aller, R.C., and Reeder, R., 2000, Conversion of diatoms to clays during early diagenesis in tropical, continental shelf muds: Geology, v. 28, no. 12, p. 1095–1098.

Mortazavi, E., 2012, Western Equatorial Atlantic Sedimentation: A Study of Magnetic Properties: University of Southern California.

Mörner, N.-A., 1976, The Pleistocene/Holocene boundary: a proposed boundary-stratotype in Gothenburg, Sweden: Boreas, v. 5, no. 4, p. 193–275.

Postma, D., 1985, Concentration of Mn and separation from Fe in sediments—I. Kinetics and stoichiometry of the reaction between birnessite and dissolved Fe (II) at 10 C: Geochimica et Cosmochimica Acta, v. 49, no. 4, p. 1023–1033.

Rabouille, C., Gaillard, J.-F., Treguer, P., and Vincendeau, M.-A., 1997, Biogenic silica recycling in surficial sediments across the Polar Front of the Southern Ocean (Indian Sector): Deep Sea Research Part II: Topical Studies in Oceanography, v. 44, no. 5, p. 1151–1176, doi: 10.1016/S0967-0645(96)00108-7.

Ristvet, B.L., 1978, Reverse weathering reactions within recent nearshore marine sediments, Kaneohe Bay, Oahu: University of Hawaii, Honolulu.

Sayles, F.L., Deuser, W.G., Goudreau, J.E., DIckinson, W.H., Jickells, T.D., and King, P., 1996, The benthic cycle of biogenic opal at the Bermuda Atlantic Time Series site: Deep Sea Research Part I: Oceanographic Research Papers, v. 43, no. 4, p. 383–409.

Schulz, H.D., Dahmke, A., Schinzel, U., Wallmann, K., and Zabel, M., 1994, Early diagenetic processes, fluxes, and reaction rates in sediments of the South Atlantic: Geochimica et Cosmochimica Acta, v. 58, no. 9, p. 2041–2060.

Thomson, J., Wallace, H.E., Colley, S., and Toole, J., 1990, Authigenic uranium in Atlantic sediments of the last glacial stage—a diagenetic phenomenon: Earth and Planetary Science Letters, v. 98, no. 2, p. 222–232.

Van Cappellen, P., and Qiu, L., 1997, Biogenic silica dissolution in sediments of the Southern Ocean. I. Solubility: Deep Sea Research Part II: Topical Studies in Oceanography, v. 44, no. 5, p. 1109–1128.

Wollast, R., 1998, Evaluation and comparison of the global carbon cycle in the coastal zone and in the open ocean: The sea, v. 10, p. 213–252–252.

Chapter 4: Nitrogen cycling within suboxic and anoxic sediment from the continental margin of Western North America

(published January 2012, Marine Chemistry)

Chong, L.S., Prokopenko, M.G., Berelson, W.M., Townsend-Small, A., McManus, J.

ABSTRACT

Here we report rates of benthic nitrogen (N) cycling and assess controls on biological NO_3^- sequestration and transport in sediments underlying oxygen deficient regions of the ocean ranging from anoxic/suboxic ([O_2] of 0-2μM) to more oxic (57 μM [O_2]) conditions. N mass balances were constructed based on benthic flux measurements (N_2, NH_4^+ and NO_3^-) and pore water profile determinations (N_2, NO_3^-, NO_2, N_2O, Fe and HS^-) at sites in the Southern California Borderland and the Mexican Margin. Fluxes across the sediment-water interface for N_2, NO_3^- and NH_4^+ were determined directly by whole core incubations, and fluxes of N_2 were also determined by modeling mm-scale pore water profiles. Estimates of the N_2 flux by these two methods agree to ±50%, thereby establishing a range of net N_2 production in these settings. The average N_2 efflux was four times larger at a site with high pore water H_2S concentrations (Soledad Basin 3.14 ± 1.10 mmol N $m^{-2}day^{-1}$) compared to an iron-rich site (Santa Monica Basin 0.74 ± 0.21 mmol N m^{-2} day^{-1}) despite both sites having comparable NO_3^- uptake fluxes (-0.93 ± 0.14 vs. -0.82 ± 0.08 mmol N m^{-2} day^{-1} respectively). Pore water profiles from both sulfidic and iron-rich sites reveal

subsurface maxima in NO_3^-, NO_2^-, and N_2O that are likely caused by the presence of reactive NO_3^- sequestered by infaunal microbiota. In Soledad Basin, the sequestered pool of microbial NO_3^- contributes to NH_4^+ production via DNRA resulting in an NH_4^+ efflux (2.66 ± 0.52 mmol N m^{-2} day^{-1}) to the overlying water. This flux exceeds the rate of NH_4^+ production by C_{org} degradation by 10 times. At the suboxic sites, a total N balance can only be achieved if the flux of NO_3^- into sediments is comprised of two components: diffusive and biologically mediated transport. The more oxic site shows no evidence of a sequestered microbial NO_3^- pool and diffusive fluxes can account for all N transformations. Core incubations do not capture the total NO_3^- flux where biological transport is important as they do not account for NO_3^- sequestered prior to the start of the incubation. Pore water N_2O concentrations of up to 500 nM in sub-surface sediments greatly exceed the background concentration (7 nM) and are likely generated by the metabolic reduction of the intracellular nitrate pool, however, there was no measurable efflux of N_2O from sediments to the overlying water. Biological NO_3^- transport is a ubiquitous process in suboxic and anoxic sediments, however the magnitude of its importance appears to be linked to the presence of dissolved iron or sulfide in the pore waters.

INTRODUCTION

Nitrogen (N) is an essential nutrient in the ocean and is limiting for biological productivity in many marine ecosystems. Large uncertainties exist in estimates of both fixed N inputs and removal (Brandes and Devol, 2002; Gruber, 2004). Benthic

denitrification, where denitrification refers to the successive reduction of fixed N from NO_3^- to N_2, contributes > 50% of the total fixed N removal in the oceans, while the remainder of N loss occurs in the water column (Devol, 2008). Past approaches to constrain global rates of fixed N losses in marine sediments resulted in a broad range of estimates, from 180 to >300 Tg N yr^{-1} (Codispoti, 2007; Codispoti et al., 2001; Deutsch, 2004; Gruber, 2004). The large uncertainty of current estimates stems from sparse spatial coverage of field measurements, variability in isotopic fractionation factors for contributing processes, and overall insufficient knowledge of biogeochemical pathways and microbial processes involved in sedimentary N cycling (Brandes and Devol, 2002; Codispoti, 2007; Deutsch, 2004).

Pathways of fixed N removal include: heterotrophic (canonical) denitrification, anammox, Fe-driven denitrification, and dissimilatory nitrate reduction coupled to sulfide oxidation, as reviewed by Burgin and Hamilton (2007). In addition, NO_3^- can be reduced via dissimilatory nitrate reduction to ammonium (DNRA) without a net fixed N loss. DNRA may proceed via two pathways: one involving fermentation (Tiedje, 1988), and the other linked to sulfur oxidation (Brunet and Garcia Gil, 1996; Otte et al., 1999). Both processes result in the production of NH_4^+. DNRA has also been associated with microbial NO_3^- storage and transport by large sulfur bacteria, e.g. *Thioploca, Beggiatoa* and *Thiomargarita* (Fossing et al., 1995; Mchatton et al., 1996; Schulz, 1999).

In this paper, we define 'sequestration' as the micro-biological intracellular uptake and concentration of NO_3^- and 'biological transport' as its transport below

the SWI by a moving organism. The environmental parameters that promote NO_3^- bio-sequestration and transport are not well understood and are the focus of this study. In sulfidic sediments, transport may occur by large sulfur bacteria via the gliding of individual filaments within a sheath or movement as a free-living cell; in either case, sequestered intracellular NO_3^- is used to oxidize HS^-, producing NH_4^+ and SO_4^{2-} or S^0 (Fossing et al., 1995; Jorgensen and D'hondt, 2006; Otte et al., 1999; Sayama et al., 2005; Thamdrup and Canfield, 1996; Zopfi et al., 2001). Benthic foraminifera from a wide range of environments have also been found to store NO_3^- in vacuoles with internal concentrations of up to 500 mM and reduce it to N_2 via heterotrophic denitrification (Piña-Ochoa, 2010; Risgaard-Petersen et al., 2006). These organisms can migrate within sediments to find 'optimal' geochemical conditions (Koho et al., 2010), transporting this intracellular pool of NO_3^- to depths of at least 3-4 cm. Prokopenko et al. (2011) demonstrated that denitrification of biologically sequestered and transported NO_3^- contributes between 30 and 60% of total NO_3^- uptake in two sites in the Southern California Borderland. These are otherwise diffusively dominated sediments as there is no macrofaunal or meiofaunal bio-irrigation.

We present our analyses of N cycling by the sediment community in the Eastern Tropical North Pacific (ETNP), which is recognized as an important region for fixed N removal within its strong oxygen minimum zone (OMZ) and underlying suboxic sediments (Altabet et al., 1999; Emmer and Thunell, 2000; Liu and Kaplan, 1989; Sigman et al., 2005; Yamagishi et al., 2007). We have measured fluxes of N_2, NO_3^-, and NH_4^+ as well as pore water profiles of N_2 and NO_3^-, and important

intermediates, N_2O and NO_2^-, in order to characterize the geochemical regimes that are favorable for biological NO_3^- sequestration and transport. There are currently very few studies that report high-resolution pore water profiles of dissolved N_2 and N_2O (Hartnett and Seitzinger, 2003; Prokopenko et al., 2011); here we present profiles of these species at mm-scale resolution to a depth of 10 cm from a variety of continental margin sites (540-1900 m). We show that biological NO_3^- sequestration and transport occurs in a range of reducing geochemical conditions, and we present an assessment of the controls on this process.

STUDY AREA

The study area includes sites from the Southern California Borderland and Mexican margin that are within the OMZ of the eastern North Pacific (Fig. 1). Sites were selected based on the previous work done by Berelson et al. (2005)and Prokopenko et al. (2006) and general properties of these sites are described in Table 1. The sites range from depths of 540 to 1900 m, and overlying waters (OLW) are very low in O_2 (0 - 2 μM O_2) except for San Clemente Basin, which is more oxygenated, but still hypoxic (57μM O_2) (Bender et al., 1989; Berelson et al., 2005). Since it has been shown that bottom water O_2 concentrations can vary temporally (Berelson, 1991), oxygen concentrations were measured at each site at the time of sampling and other indicators of long-term anoxia, such as the presence of fine laminae, were recorded. The absence of macrofauna is a feature of all sites, except San Clemente Basin.

Table 1 – Site Descriptions.

	Pescadero	Magdelena	Soledad	Santa Monica	San Clemente
Latitude	24º 16.880' N	23º 27.594' N	25º 12.490' N	33º 50.21' N	32º 34.723' N
Longitude	108º 11.790' W	111º 34.540' W	112º 42.269' W	119º 01.75' W	118º 70.537' W
Depth (m)	616	692	544	892	1920
Bottom Water O_2 (µM)	0.4	0.9	0	< 3	57
Bottom Water NO_3^- (µM)	39.6	39.1	18.7	30.3	41.0

Figure 1. Map of study sites. Contours indicate depth in meters. Solid dots indicate stations.

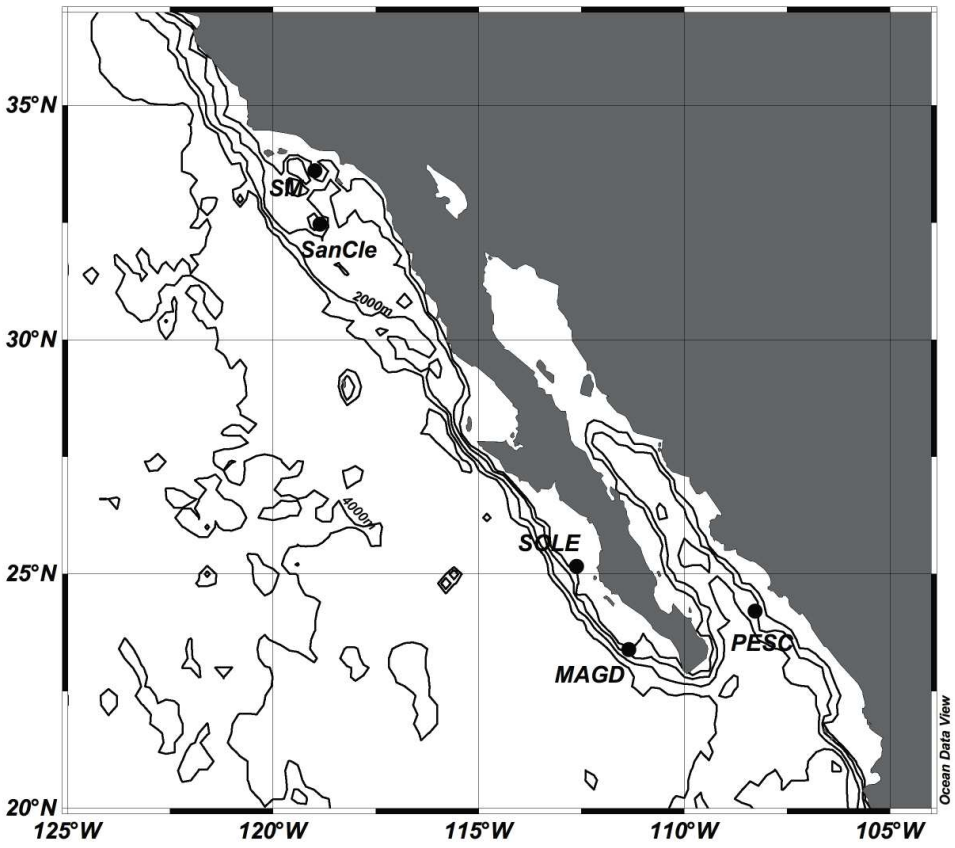

The Pescadero slope lies near the eastern side of the mouth of the Gulf of California, an area with high productivity and an OMZ centered at 600 m that limits sedimentary reworking by macrofauna (Baumgartner et al., 1985). Cores were taken at a depth of 616 m where sediments are laminated and organic rich (2.5 - 4.3 wt. % C_{org}) (Gonzalez-Yajimovich et al., 2005). Sediment supply to the Pescadero region includes the runoff from continental drainage of the Sierra Madre Occidental Mountains. Outside the Gulf, two sites that have been previously described by Van Geen et al. (2003) lie off the south-western coast of the Baja peninsula. The Magdalena Margin is an open margin site where cores were collected from a depth of 692 m. Here, sediments showed signs of bioturbation to a depth of 1-2 cm. However, no macrofauna were evident in any of the recovered cores. Soledad Basin is 545 m deep and is isolated from the ocean by a sill at approximately 250 m depth (Silverberg et al., 2004), leading to near 0 μM O_2 below this depth. Both Magdalena and Soledad sites receive little clastic sediment input and yet have high sediment accumulation rates (1 m /1000 years in Soledad (Van Geen, 2003), with an estimated C_{org} of ~ 6 wt. %), most likely caused by high productivity due to coastal upwelling (Douglas et al., 2007; Gonzalez-Yajimovich et al., 2005).

Santa Monica Basin lies just offshore Los Angeles; the basin is ~900 m deep, with a sill at 740 m that restricts circulation. This basin receives hemipelagic sediments derived from water column production and particulate material transported off the shelf (Jahnke, 1990). San Clemente Basin is further offshore, deeper and more oxic compared to the other sites examined here, and has a lower C_{org} rain rate (70 μmol C_{org} cm^{-2} yr^{-1}) compared to Santa Monica Basin (140 μmol C_{org}

cm^{-2} yr^{-1}) (Bender et al., 1989; Huh et al., 1993). However, the C_{org} flux at San Clemente is comparable to that of Soledad Basin (27-121 μmol C_{org} cm^{-2} yr^{-1}) (Silverberg et al., 2004).

METHODS

Core Collection

Sediment cores were collected using a multicorer with 10 cm diameter core tubes (Barnett et al., 1984) during a cruise in October-November of 2009 on the *R/V New Horizon*. Upon recovery, cores were immediately transferred to a cold van and were visually inspected to examine the sediment-water interface (SWI) to judge whether or not a core was usable for whole-core squeezing (WCS) (Bender et al., 1987) or for whole-core incubations (INC) (Hammond et al., 2004). Cores selected for sampling, had a visibly undisturbed, level SWI and clear OLW. All work with the cores was conducted inside a temperature-controlled van.

Core Sectioning

At each site, cores were sectioned in 1cm intervals and slices were divided into two splits. To examine the distribution of sequestered NO_3^-, one of the aliquots was transferred to acid-cleaned 50-mL centrifuge tubes and frozen at -80 ºC. Back at USC these sediments were thawed, sonicated for 1 minute at 22.5 kHz and 6 W, centrifuged and then the pore waters were decanted and analyzed for NO_3^- and NO_2^-. Freezing and thawing, followed by sonication, should break any cells present, releasing the intracellular contents into the pore water. Another aliquot of mud was

placed in a pre-weighed glass container and was used to determine porosity by weight loss after drying.

Whole Core Squeezing

Pore water was obtained by WCS in two ways. In one method, water was expressed from whole, intact cores into sample syringes as described in Berelson et al. (2005). Other cores selected for squeezing were partially extruded and then 'beheaded', removing the top 3 to 6 centimeters to allow squeezing of deeper sediments. To extract deep pore waters from these cores, a whole core squeezer was designed around the use of a hydraulic jack to apply pressure similar to that described by Kalil and Goldhaber (1973). Here, a piston was inserted at the bottom of the core, and a plug with a 1/8" hole in the center was inserted into the top. The entire core was placed atop a hydraulic jack inside an aluminum frame. Water was expressed through nylon tubing directly into sample syringes by forcing the sediment column up against the top-plug via motion of the hydraulic jack.

The cumulative volume of water expressed was used as a measure of the depth at which each sample was located. Assignment of the SWI (z=0) depends on the visual inspection of the piston and depth assignment depends on sediment porosity; also, it is assumed that pore waters flow uniformly upward through the sediment as pressure is applied (Bender et al., 1987; Berelson et al., 1990). The distance the piston traveled was also measured and compared to the depth calculated; the overall uncertainty in WCS depth assignments was ± 0.2 cm.

Samples of the expressed pore water were collected directly into gas-tight 20 mL glass syringes (Popper® Micro-mate®) for N_2/Ar analysis and were kept in a water bath in a temperature-controlled van prior to analysis. N_2O samples were collected in 10 mL syringes with stopcock closures and water was immediately transferred to pre-evacuated 20 mL crimp vials with gray butyl rubber stoppers and preserved with $HgCl_2$. All other samples (NO_3^-, NO_2^-) were collected in 20 mL syringes and then filtered through a 0.8/0.2 μm Acrodisk syringe filter directly into sample bottles and frozen. The time from a core's arrival on deck to the collection of the last WCS sample ranged from 4-8 hours.

Whole Core Incubations

Cores selected for INCs were also chosen for having an interface that appeared to be undisturbed and that were fairly level (<1 cm relief). The cores were set up to incubate 0.5-1.0 liters of water as described in Hammond et al. (2004). Samples for N_2/Ar, N_2O, NO_3^-, and NH_4^+ were collected every 5-6 hours for 24-30 hours. Typically, ~40 ml were drawn during each sample period by pushing down on a piston, thus shortening the overlying water column. The cores were incubated at ~5 ºC; the *in situ* value was ~9 ºC. When calculating fluxes based on concentration change vs. time, we applied a correction to address differences in the *in situ* and incubation temperatures assuming molecular diffusivity changes of ~2.5% per ºC for N_2 and ~3.5% per ºC for NO_3^- and NH_4^+(Hammond et al., 2004; Li and Gregory, 1974). We report INC fluxes as an average ± 1 standard deviation of all cores incubated (3-5) from each station. It should be noted that potential pressure

effects on NO_3^-, such as a change in the rate of NO_3^- uptake by denitrifiers resulting from decompression, have not conclusively been documented. However, results from Hammond et al. (2004) suggest that ship-board incubations result in decreased NO_3^- fluxes compared to *in situ* values.

Fluxes from INCs were calculated by fitting a regression line or quadratic function to concentration plotted against elapsed time/height (Hammond et al., 2004). The use of time/height accounts for the diminishing volume of OLW due to sampling and the slope of such a plot is the flux. In cases where it appeared that there was a spurious data point, the Cook's distance (D_i) was used to measure the effect of deleting a single data point on the regression model (Cook, 1979). This parameter is defined as:

$$D_i = \frac{\sum_{j=1}^{n} (\hat{Y}_j - \hat{Y}_{j(i)})^2}{n \times MSE} \qquad (1)$$

where $\hat{Y}_j$ is the predicted value from the full regression model for data point j; $\hat{Y}_{j(i)}$ is the predicted value for data point j from a refitted regression model in which point i has been omitted; n is the number of points used in the regression, and MSE is the mean square error of the model. Data points were considered outliers and omitted if they exceeded the operational guideline of $D_i > 4/n$ (Lorenz, 1987).

Uncertainties in the INC flux value included the standard deviation of replicate analyses for NO_3^- and NH_4^+ and the uncertainty in the regression fit. N_2/Ar uncertainties were determined from the propagation of error from analyses (the

standard error of the standard curves at each station) and included the uncertainty from temperature fluctuation (±2 ºC) as applied to uncertainty in Ar concentrations.

Rhizon Sampling

At each station, one core was sampled using Rhizon soil samplers (Rhizosphere Research Products) inserted into pre-drilled holes in the core tube and pore water was collected using plastic syringes with a polyethylene plunger (Norm-Ject) that would draw and hold vacuum while pore waters were expressed. Sample volume ranged from 5-10 ml and sampling duration was 20-60 minutes. Samples extracted this way were used for metal and HS^- analyses. Syringes showed no sign of Fe oxidation at Fe-rich (Fe-rich is defined as containing high concentrations of Fe^{2+}) sites, indicating a state of anoxia within the syringe.

Sample Analyses

Samples for N_2/Ar were analyzed shipboard on a membrane-inlet mass spectrometer (MIMS) modified from Kana et al. (1994). Water was sampled directly from gas tight syringes, and masses 28, 32, and 40 were detected on a quadrupole mass spectrometer (Pffeifer PrismaPlus™ QMG220) using the Secondary Electron Multiplier (SEM) detector and Quadera software (Inficon). Approximately 8 mL of each standard and sample were used to determine the average ratio of masses 28/40 and 32/40. The first two minutes of data were discarded as the ion currents required ~90-120 seconds to stabilize for each sample as previously documented by Kana et al. (1998). Mass ratios were converted to dissolved gas ratios by comparison to the ratios measured in standard solutions equilibrated with

atmosphere at constant temperatures (Emerson et al., 1999; Hamme and Emerson, 2004).

Standards were prepared by bubbling water of specific salinity (0 ppt, 20 ppt, 50 ppt NaCl) with atmospheric air for 12 hours at constant temperature. It has been shown previously that the presence of oxygen in the quadrupole mass spectrometer chamber may result in isobaric interferences that will affect measured 28/40 ratios (Eyre et al., 2002; Kana, 2004). We confirmed this effect by testing a series of standards containing variable amounts of sodium sulfite (Appendix D.1). Due to the lack of reproducibility and high variability in the magnitude of this effect, no correction could be applied. Therefore, O_2 was removed from standard water by adding approximately 0.2 g of sodium sulfite to each standard bottle prior to sealing. INC samples had 0.2 mL of a 30 mM sodium sulfite solution added prior to analysis. WCS samples were expected to have low to zero [O_2] and were not amended with sodium sulfite.

The bottom water value of N_2/Ar was determined from samples collected with Niskin bottles triggered within 10 m of the sea floor. Measured N_2/Ar ratios were converted to N_2 % saturation assuming [Ar] is at equilibrium with atmosphere as follows:

$$N_2\ \%saturation = 100 \times \frac{\left(N_2/Ar\right)_{measured}}{\left(N_2/Ar\right)_{equilibrium}} \qquad (2)$$

While the last assumption of Ar being in equilibrium may not be completely valid (Hamme and Severinghaus, 2007), the error it introduces into the final [N_2]

calculations is smaller than uncertainties arising from analytical procedures. The equilibrium (or 100% saturation) value for N_2/Ar was calculated from the expected concentrations of N_2 and Ar at the *in situ* bottom water temperature and salinity. To convert degree of saturation to concentration, values obtained from equation 2 were multiplied by equilibrium [N_2] values (Emerson et al., 1999; Hamme and Emerson, 2004; Weiss, 1970). Uncertainty in measured % saturation was ±2% at Magdelena and ± 1.5% at the other stations; this uncertainty represents the propagation of error from replicate standards, the error in fitting the standard curves, and uncertainty due to temperature variability.

Dissolved N_2O measurements were made shipboard on a Shimadzu Scientific Instruments GC-2014 Nitrous Oxide Analyzer with electron capture detector using headspace extraction with ultra-high purity N_2. The extraction was performed using a ratio of 10 mL water to 10 mL headspace. Sample concentrations were determined using calibrated N_2O standards bracketing the concentrations of samples (100-1000 ppb in air). The uncertainty in N_2O measurements was ±5%.

Samples for NO_3^- and NO_2^- were analyzed on a Teledyne NO_x box with a chemiluminescence detector. NO_3^- samples (100 µl) were injected into a heated reaction vessel containing a solution of reduced vanadyl sulfate (Braman and Hendrix, 1989). NO_2^- samples (100 µl) were injected into the same apparatus, but into a solution of hot potassium iodide and acetic acid (Cox, 1980). Uncertainty in replicate NO_3^- and NO_2^- analyses was < ± 3%. NH_4^+ samples were analyzed colorimetrically on a flow-through spectrophotometer following the salicylate-

hypochlorite method (Bower and Holm-Hansen, 1980). Uncertainty in replicate NH_4^+ was ± 3%. HS^- samples were also analyzed colorimetrically using the Cline method with an uncertainty of ± 5% (Cline, 1969). Splits of pore water were analyzed for Fe concentration (± 2%, an average of all samples) by ICP-OES at Oregon State University. The detection limit for Fe was ± 0.05 μM. Porosity was determined by weight loss after drying at 60 ºC. Bottom water O_2 concentrations were measured with an optode (Presens) calibrated with water equilibrated with atmospheric air at known temperatures.

Thioploca Incubations

While sectioning sediments at Soledad and Magdalena, we observed populations of *Thioploca* bacteria. To address the potential origin of the high N_2O measured in pore waters, a series of eleven 8-mL vials were prepared to determine if there was production of N_2O from *Thioploca* filaments and/or their associated bacterial consortia (Table 2). Bundles of trichomes were removed from a Soledad Basin sediment core using tweezers and were rinsed with bottom water. The active experiments (4 vials) contained approximately 10 bundles of trichomes of *Thioploca* in 1 mL bottom water. We also conducted control experiments with Thioploca + poison ($HgCl_2$), seawater and rinsate from *Thioploca* bundles washed with bottom water (Table 2). The vial headspace was flushed with high purity N_2 gas, and then incubated for at least 22 hours. The headspace was subsequently analyzed for N_2O concentration.

Table 2 – *Thioploca* experiment description and results. N_2O concentrations are dissolved N_2O concentrations corrected for the volume of the vial and the volume of N_2O-free headspace.

Experiment	Description	Incubation Time (hours)	N_2O (nM)
1	10 *Thioploca* in 1 mL bottom water (BW)	21.3	24
2	10 *Thioploca* in 1 mL BW	22.0	45
3	10 *Thioploca* in 1 mL BW	48.0	103
4	10 *Thioploca* in 1 mL BW	48.1	69
5	10 *Thioploca* in 1 mL BW + 0.1 mL $HgCl_2$	21.6	9
6	10 *Thioploca* in 1 mL BW + 0.1 mL $HgCl_2$	22.2	9
7	1 mL BW	22.1	7
8	1 mL BW + 0.1 mL $HgCl_2$	21.7	7
9	.2 mL *Thioploca* rinsate + 1 mL BW	21.5	6
10	.2 mL *Thioploca* rinsate + 1 mL BW	21.8	6
11	.2 mL *Thioploca* rinsate + 1 mL BW + 0.1 mL $HgCl_2$	22.4	10

RESULTS

Core Sectioning and Porosity

The porosity data (Fig. 2) were fit with either equation 3 or 4 in order to achieve the best fit to observed data:

$$\phi = a + be^{c*z} \quad (3)$$

$$\phi = a + bz^{c} \quad (4)$$

where ϕ is the porosity, z is depth, and a, b and c are fitting parameters. Profiles showed strong similarities to porosity profiles determined previously at the same sites (Berelson et al., 2005; Jahnke, 1990). The extrapolated porosity at the SWI was used in calculating the diffusive flux. Turbidite deposits have been documented in Santa Monica Basin (Berelson et al., 2005; Christensen et al., 1994) and their porosity was lower than the trend established by the hemipelagic sediment; therefore, these horizons were excluded in the porosity vs. depth fit.

Pore Water Profiles

Bottom water N_2 % saturation was typically close to 100% (± 1%), but all of the pore water profiles of N_2 showed an increase with depth (Fig. 3). At San Clemente Basin, the increase in % saturation from the OLW was about 4% occurring over a depth of 6 cm. At the suboxic and anoxic sites, the increase in % saturation of N_2 was much higher; at Magdalena, the increase was 12% above bottom water values, at Soledad there was an increase to ~30% supersaturation, and Santa

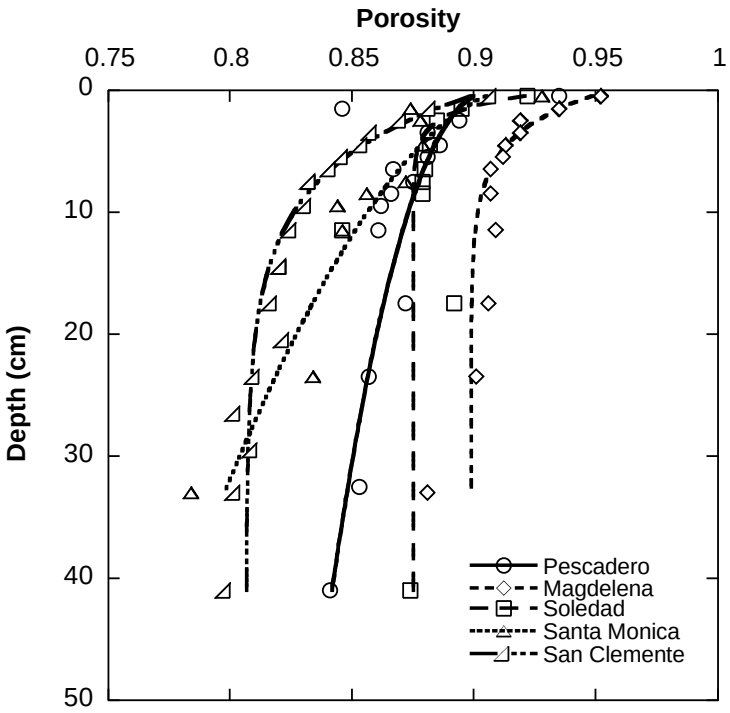

Figure 2. Profiles of porosity vs. depth. In Santa Monica Basin, data points associated with turbidite deposits were excluded from the model fit. Pescadero, Magdelena and San Clemente porosity profiles were fit with equation 4; Soledad and Santa Monica data were fit with equation 3.

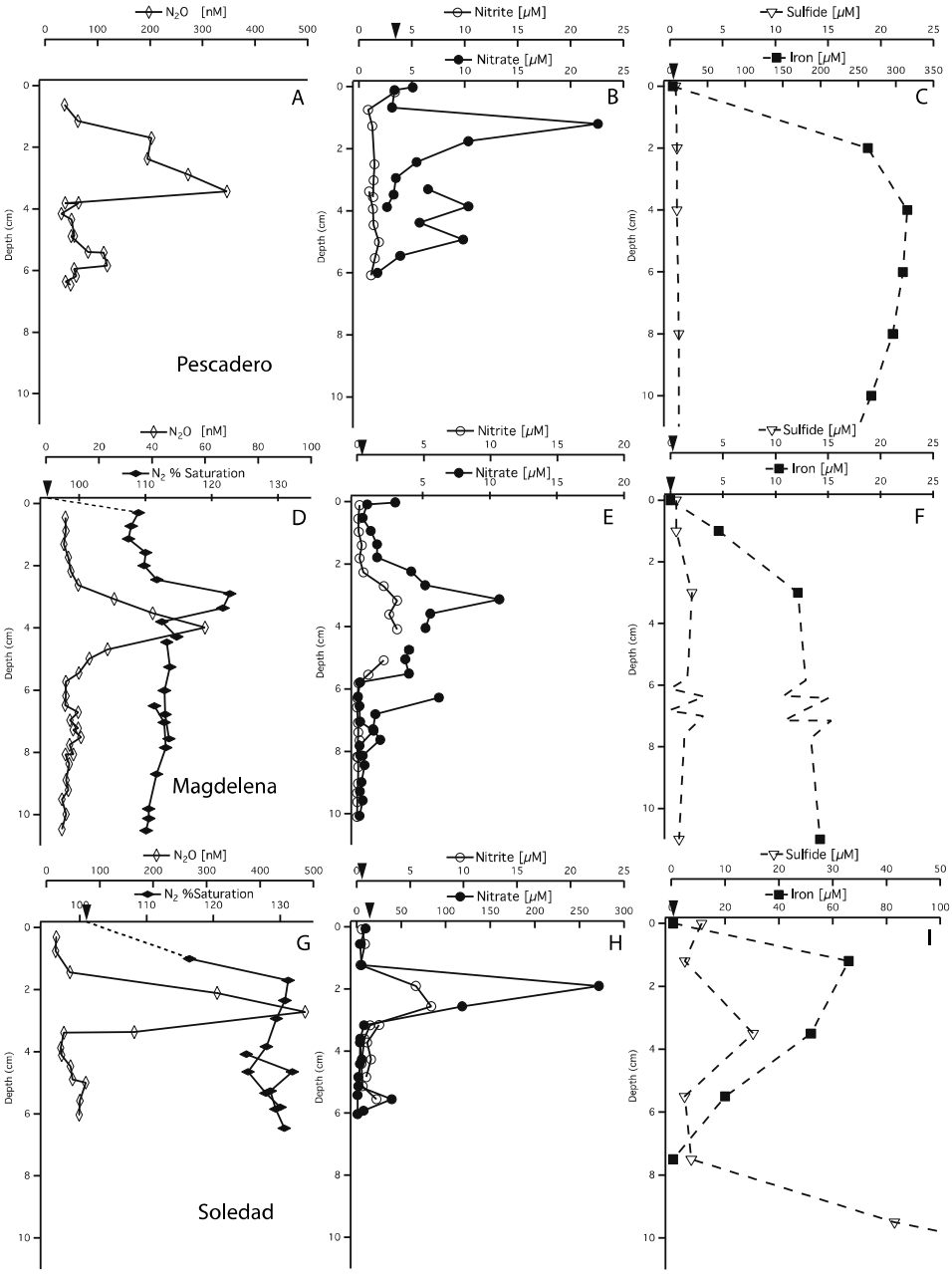
N2O [nM]
Nitrite [μM]
Nitrate [μM]
Sulfide [μM]
Iron [μM]
N2 % Saturation
N2 %Saturation
Depth (cm)
A
B
C
D
E
F
G
H
I
Pescadero
Magdelena
Soledad

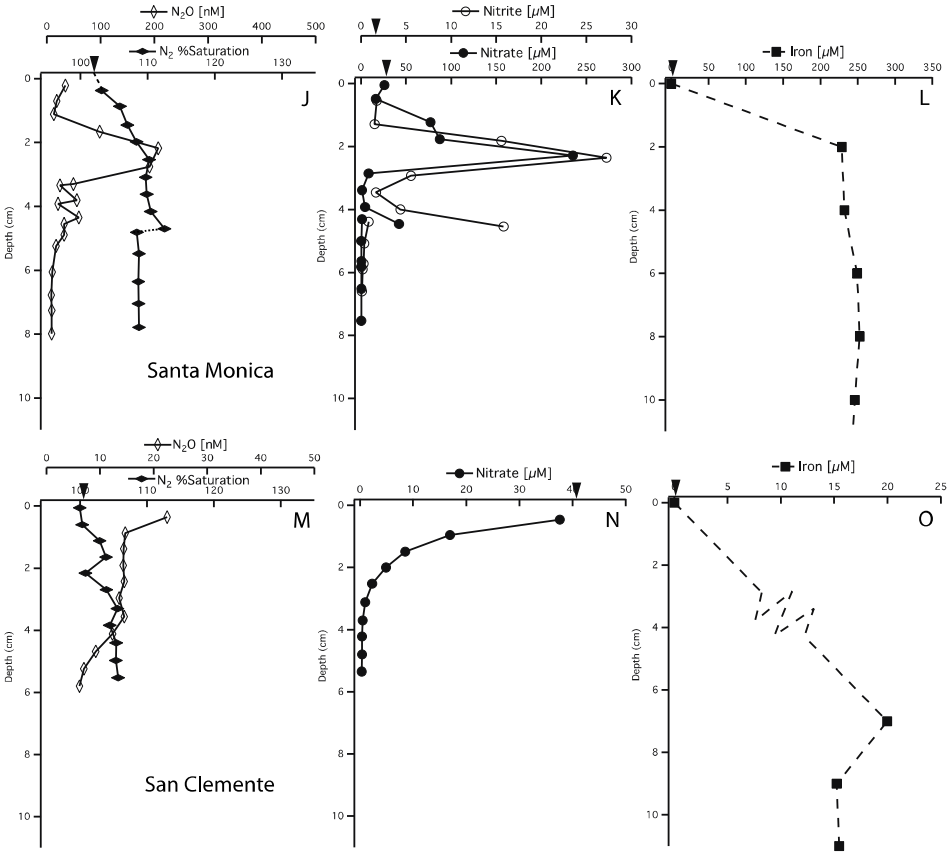

Figure 3. Porewater profiles of N_2, N_2O, NO_3-, NO_2-, HS- and dissolved Fe for each site. Profiles of N_2, N_2O, NO_3-, and NO_2- show data from 2 or 3 WCS cores, with data from each core connected by a solid line. Dissolved Fe and HS- were measured on pore water extracted with Rhizon samplers and the profiles are denoted with a dashed line. Filled triangles indicate bottom water concentration where measured and within the scale of the horizontal axis. Values of dissolved Fe that are 0 are below the detection limit of 0.05 μM.

Monica Basin showed an increase up to ~8-12% relative to the OLW values. At Magdalena, Soledad and Santa Monica sites, the 'beheaded' cores showed N_2 concentrations consistent with the values obtained in the regular WCS cores, the profiles lined up reasonably well, and N_2 values remained fairly constant with depth.

A monotonic decline in NO_3^-+NO_2^- (N+N) from the bottom water values to zero was only observed in the sediments of San Clemente Basin (Fig. 3 and Appendix D.2). At the suboxic sites, there was a pronounced maxima in NO_3^- concentration appearing 1-4 cm below the SWI that ranged in magnitude from 10-25 μM at Pescadero and Magdalena to ~ 280 μM at Soledad and Santa Monica. Profiles of NO_2^- also showed maxima at similar depths to the NO_3^- peak, however, NO_2^- was undetectable at San Clemente and quite low at Pescadero.

The concentration of N_2O in the pore water from San Clemente at the SWI was about 25 nM, and dropped to bottom water levels (about 7 nM) within 5 cm of the SWI. However, N_2O profiles from the suboxic and anoxic sites showed a subsurface maximum (Fig. 3). The elevated concentrations ranged from 60 nM at Magdalena to 200 nM at Santa Monica and 350-450 nM at Pescadero and Soledad.

Dissolved Fe within San Clemente sediments was undetectable at the SWI, and was present at low (~20 μM Fe) concentrations at >7 cm below the surface. Pescadero also had near-zero concentrations of dissolved Fe at the SWI, but it rose to 260 μM Fe within the first 2 cm. At Magdalena, dissolved Fe concentrations were zero at the SWI, but rose to ~10 μM Fe at 3 cm. Soledad Basin had zero dissolved Fe at the SWI, and concentrations rose to ~65 μM Fe within the upper 1 cm and fell

back to zero by 8 cm. In Santa Monica Basin, dissolved Fe rose from near zero at the SWI to ~230 μM Fe at 2 cm and remained at this value (± 20 μM) throughout the top 10 cm.

Dissolved HS^- was not measured at San Clemente Basin, but there was no H_2S odor observed. At Pescadero, dissolved HS^- concentrations were 0 μM throughout the upper 10 cm of the sediment core. The HS^- concentration was also consistently low at Magdalena, only rising to ~2 μM at 3 cm depth below which HS^- stayed relatively constant. In Soledad Basin, there was ~10 μM HS^- at the SWI, and a significant increase (to >40 μM) starting at ~8 cm. HS^- was not measured at Santa Monica Basin, but previous studies (Jahnke, 1990) have reported <5 μM HS^- in the upper 10 cm of pore waters from this location.

Whole Core Incubations

Both linear and quadratic fits were applied to the incubation data (Fig. 4, Appendix D.3) and data from later in the incubation period (typically beyond 24 hours) were omitted as described previously (Bender et al., 1989). The slope at t=0 was taken as the flux, and the quality of the fit and uncertainty in the flux was based on the reduced chi squared value (Hammond et al., 2004). The average fluxes of N_2, NO_3^-, and NH_4^+ for 3-5 cores per station are reported in Table 3. The N_2 flux ranged from 0.72 ± 0.42 mmol N m^{-2} day^{-1} at San Clemente to 2.68 ± 0.40 mmol N m^{-2} day^{-1} at Soledad; NO_3^- fluxes ranged from -0.05 ± 0.04 mmol N m^{-2} day^{-1} at San Clemente to -0.93 ± 0.14 mmol N m^{-2} day^{-1} at Soledad (negative fluxes indicating transport

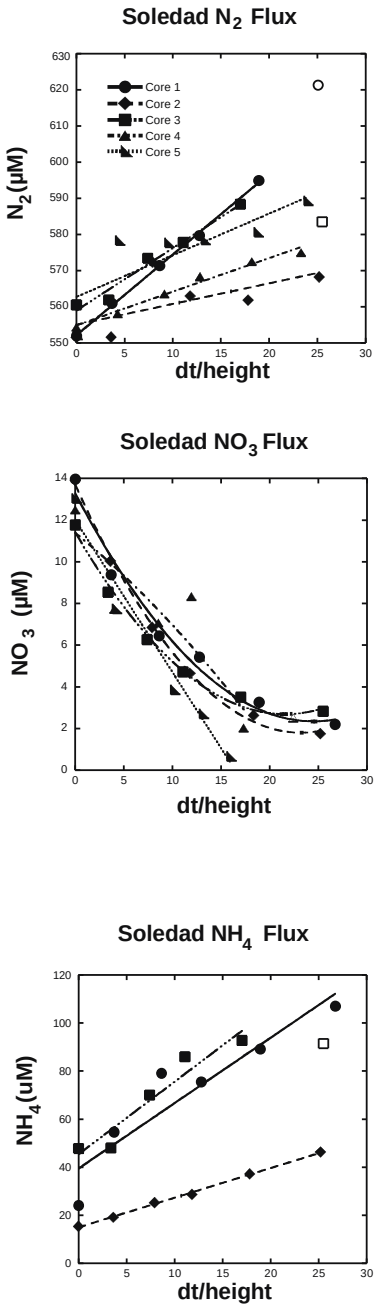

Figure 4. Results of INC data from Soledad Basin. Data from 3 to 5 cores were fit with linear or quadratic regressions as described in the text. Open symbols show data that were omitted from the regression model. The x-axis is the cumulative change in time plotted against the incubation core water column height, such that the slope of the regression line at x=0 is the flux.

into the sediments). In Soledad Basin, there was a high efflux of NH_4^+ of 2.66 ± 0.52 mmol N m^{-2} day^{-1}, whereas the NH_4^+ flux was near zero at the other sites.

Thioploca Incubations

We observed a dense *Thioploca* population (about 5-10 x 10^4 bundles m^{-2}) with sheaths that extended to approximately 6 cm within Soledad Basin sediments. The depth below which no trichomes were found was within 2 cm of the zone of the marked increase in HS^- concentration. The incubations at this site showed that samples with 10 *Thioploca* bundles in 1 mL bottom water started with 7.7 nM N_2O and produced 24-45 nM after 22 hours, and 69-108 nM after 48 hours (Fig. 8). Samples poisoned with $HgCl_2$, or containing only the rinsate from *Thioploca* trichome bundles started with an average concentration of 7.7 ± 1.4 nM N_2O and this value did not change with incubation time (Table 2).

DISCUSSION

Benthic N_2 Production in Pore Waters

N_2 fluxes determined from INCs were compared to fluxes determined from a model fit to high-resolution WCS pore water data (Fig. 6, Table 3). Pore water profiles of N_2 concentration were modeled by fitting measured data with the following equation:

$$C_z = C_0 + \beta * (1 - e^{-\kappa z}) \qquad (5)$$

where z is depth down core, C_0 is the bottom water N_2 concentration established from either Niskin or, in case of Magdalena site, OLW measurements and β and κ are

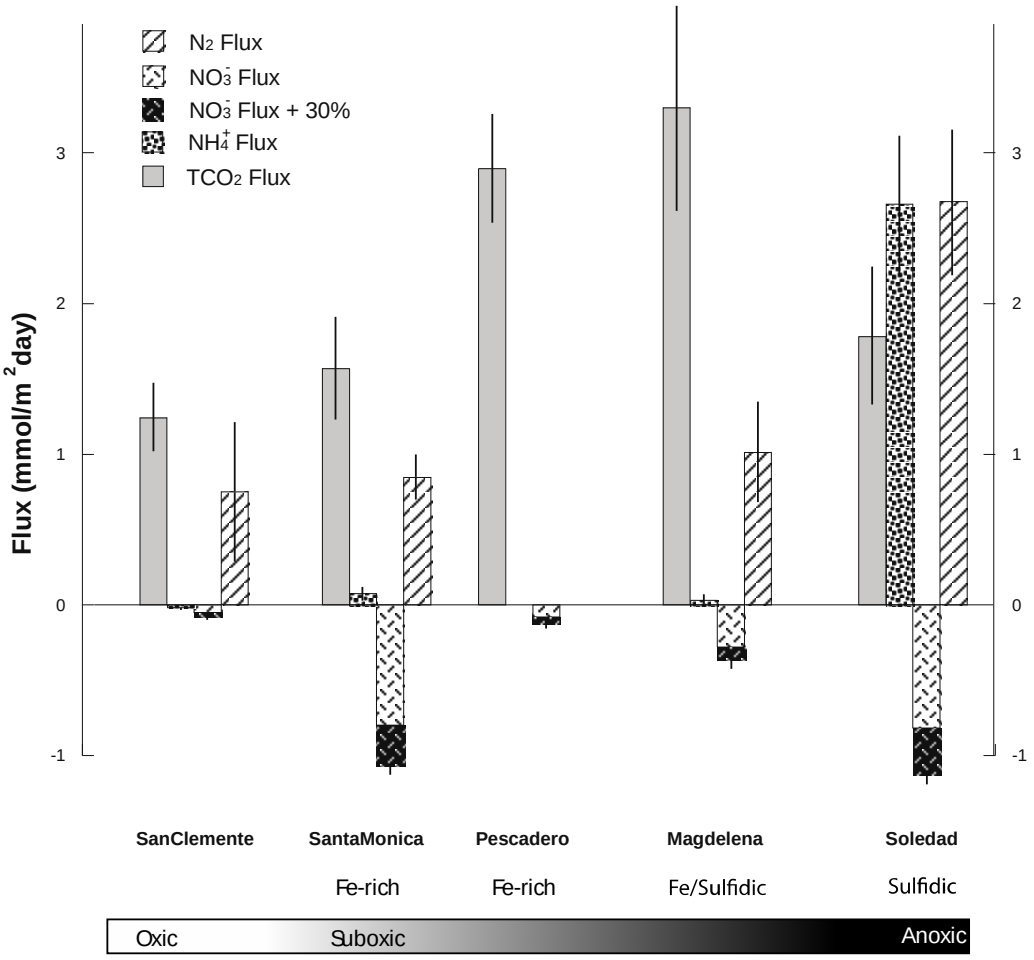

Figure 5. Net fluxes of N_2, NO_3^-, NH_4^+ across the SWI from the core incubations measured in this study, error bars are standard deviation of mean. TCO_2 fluxes from Berelson et al., (2005). Units for N_2, NO_3^- and NH_4^+ are in mmol N m^{-2} day^{-1}, and for TCO_2 in mmol C m^{-2} day^{-1}. Positive values indicate a net efflux, and negative values a net influx. A bar of relative oxygenation state of the sediments is intended as a schematic representation.

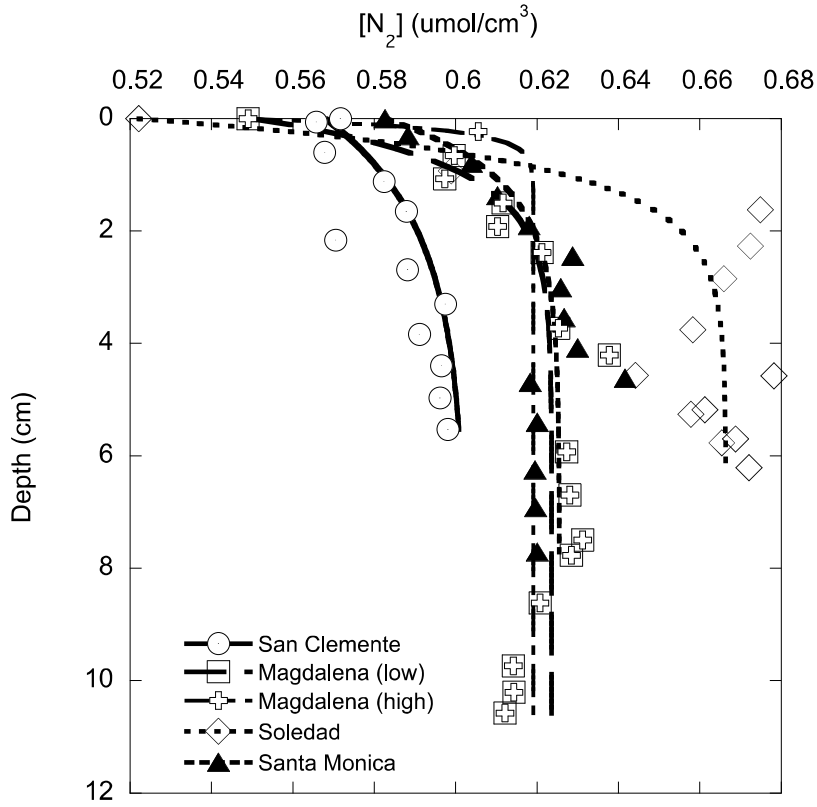

Figure 6. Diffusion-reaction model fits of N_2 WCS data. C_0 was fixed using measured bottom water values. Magdelena is modeled excluding the two 'high' points seen in the porewater profile (Figure 3D), as well as with and without the first point below the SWI.

Table 3 – Flux estimates of N_2, NO_3^-, NH_4^+, TCO_2. Number of cores incubated in ( ). Units for N_2, NO_3^- and NH_4^+ are in mmol N m^{-2} day^{-1}, and for TCO_2, mmol C m^{-2} day^{-1}. The error in the modeled N_2 flux from WCS is ±50%.

	N_2		NO_3^-				
	INC	WCS	INC	INC + 30%	Lander	NH_4^+	TCO_2
Pescadero			-0.12 ± .03 (3)	-0.16		<0.01	2.9 ± 0.39[χ]
Magdelena	1.02 ± .32 (3)	1.50 – 5.96	-0.28 ± .06 (3)	-0.36		0.03 ± .01 (3)	3.3 ± 0.82[χ]
Soledad	2.68 ± .40 (5)	3.6	-0.93 ± .14 (5)	-1.2		2.66 ± .52 (3)	1.78 ± 0.44[χ]
Santa Monica	0.82 ± .10 (5)	0.66	-0.82 ± .08 (5)	-1.1	-0.91 ± .09[ß] -1.1 ± 0.3 [¥]	0.08 ± .04 (5)	1.57 ± 0.39[χ]
San Clemente	0.72 ± .42 (3)	0.30	-0.05 ± .04 (3)	-0.06	-0.1 ± .02[α]	-0.02 ± .10 (3)	1.24 ± 0.31[a]

[a] From Bender et al., (1989)

[ß] From Berelson et al., (1996)

[χ] From Berelson et al., (2005)

[¥] From Jahnke (1990), an average of lander measurements and 6 core incubations.

fitting parameters. This equation is a steady-state solution to a reaction-diffusion model of the form dC/dt = D*(dC/dz) + kC, and was chosen as a good visual fit to the observed data. The diffusive flux was calculated using Fick's first law:

$$J = \phi^3 D_{sw} \frac{dC}{dz} \quad (6)$$

where the diffusivity in seawater (D_{sw}) of N_2 used in the calculations was 1.07 x 10^{-5} cm^2 sec^{-1} at 5 ºC and of 1.29 x 10^{-5} cm^2 sec^{-1} at 10 ºC (Schulz and Zabel, 2000). A correction for tortuosity in sediments, as the porosity squared (ϕ^2), was applied following other workers (Ullman and Aller, 1982). Uncertainty in the diffusive flux of N_2 was approximately 50% after propagating the additive uncertainties in temperature, depth assignment, model fit, and porosity.

All of the pore water profiles of N_2 show monotonic, generally exponentially increasing N_2 concentrations with depth (Fig. 3). These profiles define the depth of N_2 production. For example, the Soledad Basin site clearly shows the deepest and greatest N_2 production. Estimates of the diffusive flux of N_2 agree with our measured values from core incubations to within 50% (Table 3). At Magdalena, we observed a two-point maximum in N_2; it appears that these data were affected by atmospheric contamination within the sample syringes, and were therefore omitted from the calculation of diffusive fluxes. We also note that the first point below the SWI at Magdalena was more supersaturated than the next point below it, giving it significant weight in the curve fit and yielding a large N_2 flux value. Without a reason to dismiss this data point, we have calculated the N_2 flux from this site with and without this point (Fig. 6, Table 3). Since the length scale of an N_2 profile is

greater than 2 cm, the time for the N_2 profile to adjust to a new steady state is on the order of several days. Thus, even if there were a change in metabolic reaction rate upon bringing the cores to the surface, our modeled and measured N_2 fluxes should still reflect reasonable estimates of the *in situ* production rate.

Mass balance between NO_3^- supply and N_2 production at each site

We compared benthic N_2 and NO_3^- fluxes in suboxic and anoxic sediments to determine if there was a balance between the supply of NO_3^- from the overlying water column and the net production of N_2, as one likely reaction in these settings is heterotrophic denitrification in which 2 moles of NO_3^- yield one mole of N_2. As noted earlier, INC method tends to underestimate the *in situ* diffusive flux of NO_3^- by approximately 30% (Hammond et al., 2004), hence our NO_3^- INC fluxes have been increased by this amount (Table 3).

The flux of NO_3^- of -0.06 ± .04 mmol N m^{-2} day^{-1} obtained in this study for San Clemente Basin (Fig. 5) is comparable with fluxes (-0.1 ± 0.2 mmol N m^{-2} day^{-1}) reported previously based on diffusive models, and benthic lander studies (Bender et al., 1989; Berelson et al., 1996) (Table 3). However, our estimates of N_2 fluxes from this basin of 0.30-0.72 mmol N m^{-2} d^{-1} would predict equivalent fluxes of NO_3^- if denitrification were the only N_2 producing reaction. The excess N_2 production requires another source. One potential source of the additional N_2 is the oxic nitrification and subsequent denitrification of NH_4^+ generated from organic matter degradation, with the possible involvement of anammox (Bender et al., 1989; Prokopenko et al., 2006). Based on the previously measured TCO_2 flux (Bender et al.,

1989) of 1.24 mmol C m^{-2} day^{-1}, and assuming Redfield stoichiometry of organic matter decomposition (C:N = 7), we predict 0.2 mmol N m^{-2} day^{-1} can be generated by these processes. Thus, N_2 production and flux from these sediments is accounted for by the sum of denitrification supported by diffusive NO_3^- supply from the OLW and the nitrification and denitrification of an NH_4^+ flux generated via N_{org} decomposition.

In Santa Monica Basin, we measured NO_3^- fluxes (-1.1 ± .08 mmol m^{-2} day^{-1}) into the sediments that are consistent with those measured previously (-0.91 ± .09 Berelson et al., 1996; -1.1 ± 0.3 Jahnke 1990). N_2 flux from these sediments (0.66 - 0.82 mmol N m^{-2} day^{-1}) is approximately ½ the flux of NO_3^-, implying that all N_2 could be supplied by denitrification. However, the small NH_4^+ flux (0.08 ± 0.04 mmol N m^{-2} day^{-1}) from Santa Monica sediments (Table 3) does not account for all the NH_4^+ produced by C_{org} respiration (0.22 mmol N m^{-2} day^{-1} Berelson et al., 2005; 0.38 Jahnke 1990), which suggests that NH_4^+ is mostly oxidized and denitrified below the SWI. Moreover, Prokopenko et al., (2011) reported isotopic enrichment of NH_4^+ at depths much greater than O_2 penetration depths implying oxidation of the pore water NH_4^+ pool. These observations suggest that, similar to San Clemente basin, combined aerobic/anaerobic NH_4^+ oxidation contributes an additional N_2 flux of 0.14 - 0.3 mmol N m^{-2} day^{-1}. Thus the N_2 fluxes measured in Santa Monica are smaller than expected, but we note that our prior work in San Pedro Basin (Prokopenko et al., 2011), which is geochemically similar to Santa Monica, has larger N_2 fluxes (1.40 ± 0.28 mmol N m^{-2} day^{-1}). We consider it likely that the Santa Monica Basin N_2 fluxes reported here are anomalously low, for unknown reasons.

In contrast to the mass balances constructed for San Clemente and Santa Monica, when we examine the NO_3^- fluxes in and N_2 fluxes out of INC cores in Soledad and Magdalena sediments (Fig. 5), we find a large imbalance. At both sites, high N_2 fluxes are well in excess of what could be provided by denitrification of NO_3^- supplied by diffusion across the SWI from bottom waters. The excess of N_2 generated over the NO_3^- benthic flux may be explained by either one or a combination of the following scenarios: 1) NO_3^- flux determined in INCs is underestimated, as it does not include NO_3^- transport that occurred prior to the start of the incubation 2) Ammonium oxidation contributes to N_2 production via nitrification/denitrification pathway or anammox.

At Magdalena, the range in N_2 flux estimates from the two techniques (1.02 mmol N m^{-2} day^{-1} from INC; 1.50 – 5.96 mmol N m^{-2} day^{-1} from WCS; Table 3) makes it difficult to establish a clear picture of N cycling. As mentioned earlier, there is a data point just below the SWI that has a high concentration and including it inflates our model-fit estimate of the N_2 flux to 5.96 mmol N m^{-2} day^{-1}, as opposed to the flux of 1.50 mmol N $m^{-2}d^{-1}$ calculated without this data point. Regardless of which value is used, the N_2 flux cannot be supported by NO_3^- uptake from the OLW alone (-0.4 mmol N m^{-2} day^{-1}; Table 3). There is a negligible flux of NH_4^+, yet previous estimates of TCO_2 flux predict the production of 0.50 mmol NH_4^+ m^{-2} day^{-1} (Berelson et al., 2005). Combining the N_2 sourced from organic matter degradation and from denitrification of OLW-supplied NO_3^- totals to 0.90 mmol N m^{-2} day^{-1}, which is not hugely different from our estimate of N_2 flux determined by core incubations or the

lower estimate of the diffusive flux from WCS. However, the elevated N_2 fluxes are still suggestive of additional N_2-producing mechanisms at work at this site.

Soledad Basin also has a high N_2 flux that is not accounted for by the diffusive NO_3^- influx. Moreover, Soledad Basin is unique in that we measured a NH_4^+ flux that exceeds the NH_4^+ produced by C_{org} remineralization by an order of magnitude (Table 3). The fluxes of diffusive NO_3^- uptake and NH_4^+ produced through C_{org} decomposition only account for half of the observed N_2 flux and none of the observed NH_4^+ efflux. The imbalances we observe between N products and reactants at Magdalena and Soledad suggest that some input terms are missing from the budgets described above. We propose that the reduction of biologically sequestered and transported NO_3^- accounts for the apparent imbalances in our budget, driving the production of excess N_2 and NH_4^+. The associated metabolic pathway is likely the sulfur-based reduction of intracellular NO_3^- as discussed below. Measurements of the NO_3^- flux from core incubations do not capture the total influx of NO_3^- because they do not account for NO_3^- that is sequestered prior to the start of the incubation.

Evidence of Biological NO_3^- Sequestration and Transport

It is evident that in Soledad Basin, there must be a source of N in addition to the diffusive supply of NO_3^- from the OLW to explain the observed N_2 profiles and fluxes. This is very likely true at Magdalena and Pescadero as well. While our data do not indicate excess N_2 production in Santa Monica Basin, the presence of a subsurface NO_3^- pool is suggestive of a sequestration mechanism operating there, which is consistent with previous work in the geochemically similar San Pedro

Basin (Prokopenko et al., in press). The depth of N_2 production shown in the pore water profiles extends to 1-3 cm, which coincides with the depth range of elevated NO_3^- in pore waters extracted with WCS. The presence of elevated N_2 at depths well below the depth of NO_3^- penetration via diffusion point to a sequestration and transport mechanism at work. Another piece of evidence in support of sequestration and transport are the measured maxima in N_2O and NO_2^-, coincident with or slightly below the maxima in NO_3^-. As a 'control' station, San Clemente Basin sediments, though processed in the same manner at the suboxic sites, show no anomalously high concentrations of NO_2^- or N_2O.

Combined nitrate + nitrite (N+N) maxima appear to be ubiquitous in suboxic and anoxic sediments despite large differences in sediment geochemistry. They consistently appear at approximately 1-3 cm in the WCS profiles. Based on the N_2 profiles, we think it likely that this is the depth range at which sequestered NO_3^- is utilized, yielding the metabolic intermediates NO_2^- and N_2O. However, it is probable that the observed depth in these profiles is also subject to an artifact of the squeezing technique – at a certain pressure, microbial cells will burst and release intracellular material into the pore water (Aller et al., 1998; Alperin et al., 1999; Carignan et al., 1985; Martin and Sayles, 2006). The cells that contain sequestered NO_3^- may actually reside shallower than the WCS profiles would suggest, but they burst when the squeezing pressure is equivalent to the extrusion of pore waters from 1-3 cm. This is confirmed in Figure 7, where we have measured a pool of sequestered NO_3^- in the top 0-1 cm of suboxic sediments, though relatively low values (≤30 μM) from the San Clemente Basin core suggest that the high NO_3^-

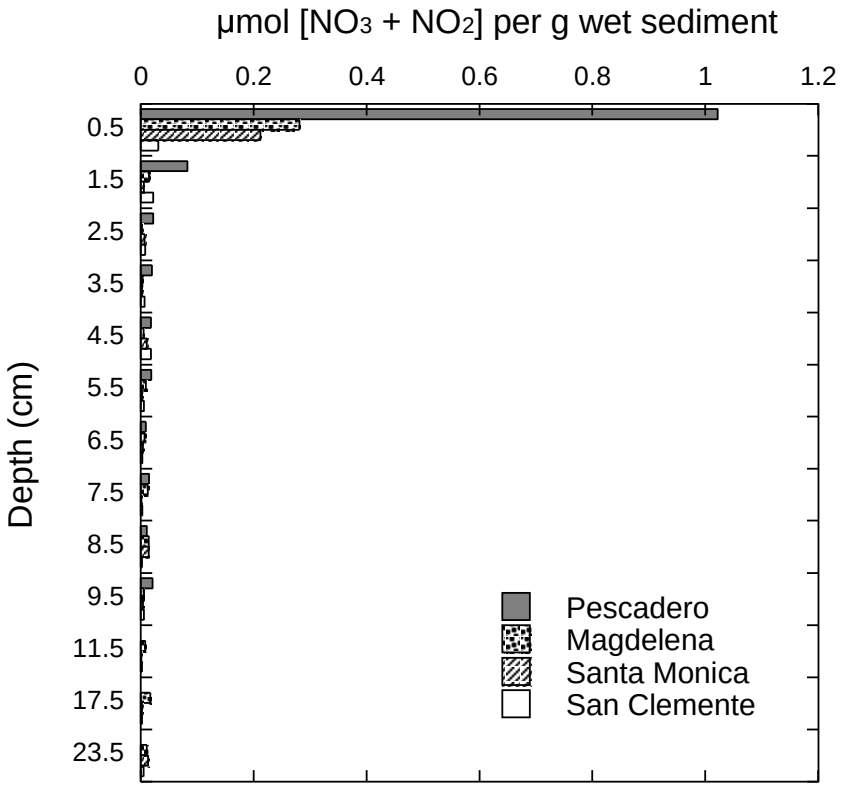

Figure 7. Measurements of combined NO_3^- + NO_2^- in µmol N g^{-1} wet sediment from frozen, thawed and sonicated sediments. Depth assignment is the midpoint of a 1 cm section.

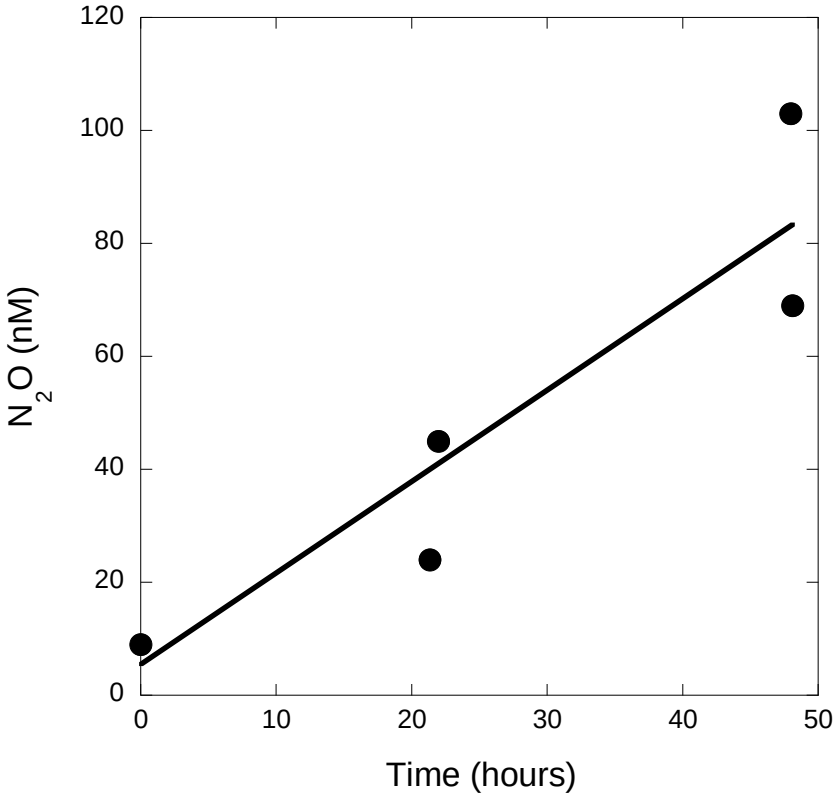

Figure 8. Results of N_2O production from the Thioploca incubation experiments described in the text. Data represent individual measurements of [N_2O].

concentrations observed in WCS profiles are not simply a squeezing artifact as they are only associated with the suboxic/anoxic sites.

The presence of N_2O in the WCS profiles at depths similar to the N+N maxima provides further evidence for reactions that involve sequestered and biologically transported NO_3^-. It is unlikely that N_2O is actively sequestered within cells, and thus we interpret the measured maxima as evidence of *in situ* reactions driven by the intracellular NO_3^- pool at depth. However, we cannot exclude the possibility that, as intracellular NO_3^- is extracted under pressure of WCS, rapid transformations may occur in the time squeezing takes place, approximately 5 minutes per depth horizon. In that scenario, some denitrification may occur and we capture the intermediary species, NO_2^- and N_2O. Still, whether the pools of the N_2O and NO_2^- are *in situ* phenomena or are generated during squeezing, the presence of these metabolites requires that a source, such as NO_3^-, is readily available.

In Soledad Basin, the sulfidic sediments support a community of *Thioploca* spp. Bacteria (Bernhard et al., 2000; Prokopenko et al., 2006) that are known to sequester NO_3^-, transport and utilize it at depth (Fossing et al., 1995; Zopfi et al., 2001). The results of *Thioploca* incubations indicate N_2O production associated with live filaments (Table 4, Fig. 8). Previous studies of *Thioploca* physiology found that this organism did not produce N_2 or N_2O and utilized the DNRA pathway to produce NH_4^+, (Hogslund et al., 2009; Otte et al., 1999), though Bleakley and Tiedje (1982) and Smith and Zimmerman (1981) have shown that some of the organisms that utilize the DNRA pathway can produce N_2O. Prokopenko et al. (2006) suggested

that anammox bacteria living in symbiosis with *Thioploca* could be significant contributors to the total fixed N removal through the formation of N_2. As anammox does not produce N_2O, we conclude that other members of the bacterial consortia living within or in association with the filament sheath are likely contributors to the production of N_2O via denitrification.

Comparing NO_3^- transport in sulfidic vs. Fe-rich pore waters

Biological NO_3^- sequestration and transport is likely significant in sediments that have very low O_2 in the OLW. While O_2 concentrations in San Clemente Basin are well below saturation, we did not observe any evidence of significant biological sequestration of NO_3^- at this site (Fig. 3). Foraminifera residing in oxygenated sediments have been observed to sequester NO_3^- (Piña-Ochoa et al., 2010), however, Glud et al., (2009) found that denitrification attributable to foraminiferal NO_3^- sequestration only accounted for 4% of total N_2 production. Glud et al. worked in sediments with BW O_2 (~60μM) comparable to San Clemente Basin. Thus, the degree of sediment oxygenation must be key to the NO_3^- sequestration process. Under lower O_2 conditions, the type of suboxic or anoxic geochemical environment does not appear to dictate the size of the sequestered NO_3^- pool. Though Santa Monica and Soledad Basins are quite different geochemically, at both sites the sequestered NO_3^- peaks are comparable in magnitude (~280 μM) and appear at similar depths in the sediment. At both sites, NO_3^- is sequestered by microbiota in the upper sediments, N_2 production occurs at a depth of 1-3 cm, and high

concentrations of reaction intermediates are present in the pore water in this same zone.

While both anoxic and suboxic sediments in this study contain intracellular NO_3^- pools, the observed differences in some aspects of the sedimentary N cycling between these sites are likely related to the variability in microbiota inhabiting the sediments at these sites, which in turn is likely to be controlled by the difference in the geochemical conditions at these sites. Comparing Soledad and Santa Monica Basins, we find that *Thioploca* were only present at Soledad. In Santa Monica Basin, we did not observe *Thioploca*, which is consistent with the absence of measurable HS^- in the upper > 50 cm of sediments. Instead, we speculate that undetermined species of foraminifera (Piña-Ochoa et al., 2010) are the source of sequestered NO_3^- since we have found benthic foraminifera that sequester NO_3^- in Fe-rich San Pedro Basin (Prokopenko, et al. 2011). The utilization of NO_3^- as the oxidant and Fe as the reduced species, with N_2 or N_2O as final products, is also an energetically favorable reaction, demonstrated in a beta-proteobacteria group (Kappler et al., 2005; Straub et al., 1996; Weber et al., 2001). These species may contribute to the reduction of sequestered NO_3^- we observe in Fe-rich sediments like Santa Monica Basin and Pescadero.

In addition to the degree of bottom water oxygenation, the amount of C_{org} input to the seafloor is an important factor determining geochemistry of the sediments and as such has the potential to influence the amount and type of biological NO_3^- transport in the sediments. Regional denitrification rates are

generally correlated with the amount of carbon supply (Liu and Kaplan, 1984), and C_{org} flux appears to be an important control on pelagic denitrification (Ward et al., 2008). However, our data show that the amount of N sequestration is not directly coupled to the amount of C_{org} input (Fig. 5). Moreover, C_{org} deposition does not appear to be the master variable controlling the magnitude of NO_3^- transport. The sites with the highest C_{org} input, Pescadero and Magdalena, show only moderate concentrations of NO_3^- in the subsurface 'pool'. In contrast, the magnitude of TCO_2 flux at Soledad and Santa Monica is only half that of Pescadero and Magdalena but sediments in these basins have much higher concentrations of subsurface NO_3^- and are characterized by higher rates of N_2 production.

Implications to the global nitrogen cycle

Despite advances in the methodologies used to study the N cycle, the magnitude of sedimentary fixed N losses remains the most poorly constrained term in the global marine N budget (Devol, 2008; Gruber and Sarmiento, 1997). Our results indicate that the amount of N removed at sites where biological sequestration and transport is important may be greater than would be predicted based on diffusive supply of NO_3^- estimated from pore water profiles or benthic fluxes alone. We have documented a range of concentrations of the sequestered NO_3^- pool, but the transport rates are difficult to estimate, as it may not be a steady-state process that can be described by simple diffusive models.

Models of global N cycling indicate that sediments underlying areas of high NO_3^- (40 μM) and low oxygen (<80 μM) will act as net sinks for fixed N (Middelburg

et al., 1996), and the magnitude of this sink is proportional to the rate of C_{org} rain to the sea floor. In Santa Monica Basin, where C_{org} input is high (>120 μmol cm^{-2} $year^{-1}$), biological sequestration of NO_3^- occurs, but it is not clear that N_2 production greatly exceeds the supply of NO_3^- from the OLW plus the N supplied by C_{org} remineralization. In contrast, Soledad Basin has a moderate (30-120 μmol cm^{-2} $year^{-1}$) amount of C_{org} input, but reduction of sequestered NO_3^- constitutes a much larger fraction of the total N transformations, greatly enhancing the formation of NH_4^+ by DNRA as well as the overall production of N_2. Sulfidic sites that support DNRA appear to have a higher capacity for transformations that retain N in the biologically available pool, but also have very high N_2 production rates. This may be attributable to sulfur-driven NO_3^- reduction that produces N_2 at low levels of HS^-, but generates NH_4^+ as NO- and N_2O-reductase become inhibited at high concentrations of HS^- (Brunet and Garcia Gil, 1996; Cardoso et al., 2006). Hence, it is the availability of HS^- in the sediment column that makes this pathway possible, and it may be the absence of significant detrital Fe in a system that holds the key to sedimentary N transformations.

CONCLUSIONS

We have made pore water measurements of N_2 at mm scale resolution from sites in the Southern California Borderland and the Mexican Margin that have low bottom water O_2 concentrations (0-2 μM) but different pore water dissolved Fe and HS^- concentrations. Estimates of N_2 flux were made in two ways, by direct

measurement of incubated core fluxes and by pore water profile diffusive modeling. These approaches yield fluxes that agree with each other within 50%. By establishing the N_2 flux and its depth distribution, we have constrained potential net N_2-producing reactions. Our results indicate that the overall supply of NO_3^- into suboxic sediments is most likely comprised of two components: diffusive and biologically mediated transport. Core incubations do not capture the total NO_3^- flux into the sediments, apparently underestimating the bio-transport component. N_2O production during incubations of *Thioploca* bacteria reveals that a consortium of currently unknown microorganisms living within the trichome sheath is able to utilize sequestered NO_3^-. Biological NO_3^- sequestration and transport appears to be ubiquitous in suboxic and anoxic sediments, though the specific N transformation pathways are likely to be controlled by the availability of HS^- vs. Fe in the pore waters. Where HS^- is present in shallow pore waters, a large fraction of NO_3^- sequestered from the overlying water column is converted to NH_4^+ via DNRA resulting in a large efflux to the overlying water.

ACKNOWLEDGEMENTS

Financial support for this work was provided by NSF grant # OCE-0727123 awarded to WB and MP. JM's participation was supported by NSF grant # OCE-0624777. We are thankful to the captain and crew of the R/V New Horizon. We would also like to acknowledge the members of the at-sea and shore-based science party for their efforts. In particular, we thank Nick Rollins, Tim Riedel, Sean Loyd,

Jesse Muratli, Loreto De Brabandere, Heidi Grøn Jensen, and Paige Green for their assistance.

REFERENCES

Aller, R.C., Hall, P.O., Rude, P., and Aller, J.Y., 1998, Biogeochemical heterogeneity and suboxic diagenesis in hemipelagic sediments of the Panama Basin: Deep Sea Research Part I, v. 45, no. 1, p. 133–165.

Alperin, M.J., Martens, C., Albert, D., Suayah, I.B., Benninger, L.K., Blair, N.E., and Jahnke, R.A., 1999, Benthic fluxes and porewater concentration profiles of dissolved organic carbon in sediments from the North Carolina continental slope: Geochimica et Cosmochimica Acta, v. 63, no. 3-4, p. 427–448.

Altabet, M.A., Pilskaln, C.H., Thunell, R.C., Pride, C.J., Sigman, D.M., Chavez, F.P., and François, R., 1999, The nitrogen isotope biogeochemistry of sinking particles from the margin of the Eastern North Pacific: Deep Sea Research Part I: Oceanographic Research Papers, v. 46, no. 4, p. 655–679.

Barnett, P., Watson, J., and Connelly, D., 1984, A multiple corer for taking virtually undisturbed samples from shelf, bathyal and abyssal sediments.: Oceanologica Acta, v. 7, p. 399–408.

Baumgartner, T.R., Ferreira-Bartrina, V., Schrader, H., and Soutar, A., 1985, A 20-year carve record of siliceous phytoplankton variability in the central Gulf of California: Marine Geology, v. 64, no. 1-2, p. 113–129.

Bender, M.L., Jahnke, R.A., Weiss, R., Martin, W.R., Heggie, D.T., Orchardo, J., and Sowers, T., 1989, Organic carbon oxidation and benthic nitrogen and silica dynamics in San Clemente Basin, a continental borderland site: Geochimica et Cosmochimica Acta, v. 53, p. 685–697.

Bender, M.L., Martin, W.R., Hess, J., Sayles, F.L., Ball, L., and Lambert, C.E., 1987, A whole-core squeezer for interfacial pore-water sampling: Limnology and Oceanography,, p. 1214–1225.

Berelson, W.M., 1991, The flushing of two deep-sea basins, southern California borderland: Limnology and Oceanography, v. 36, no. 6, p. 1150–1166.

Berelson, W.M., Hammond, D.E., Xu, X., O'Neill, D., Chin, C., and Zukin, J., 1990, Benthic fluxes and pore water studies from sediments of the central equatorial north Pacific: Nutrient diagenesis: Geochimica et Cosmochimica Acta, v. 54, p.

3001–3012.

Berelson, W.M., McManus, J., Coale, K.H., Johnson, K.S., Kilgore, T.E., Burdige, D.J., and Pilskaln, C.H., 1996, Biogenic matter diagenesis on the sea floor: A comparison between two continental margin transects: Journal of Marine Research, v. 54, p. 731–762.

Berelson, W.M., Prokopenko, M.G., Sansone, F.J., Graham, A.W., McManus, J., and Bernhard, J.M., 2005, Anaerobic diagenesis of silica and carbon in continental margin sediments: discrete zones of TCO2 production: Geochimica et Cosmochimica Acta, v. 69, no. 19, p. 4611–4629, doi: 10.1016/j.gca.2005.05.011.

Bernhard, J.M., Buck, K., Farmer, M., and Bowser, S.S., 2000, The Santa Barbara Basin is a symbiosis oasis: Nature, v. 403, p. 77–80.

Bleakley, B.H., and Tiedje, J.M., 1982, Nitrous oxide production by organisms other than nitrifiers or denitrifiers: Applied and Environmental Microbiology, v. 44, no. 6, p. 1342–1348.

Bower, C., and Holm-Hansen, T., 1980, A salicylate-hypochlorite method for determining ammonia in seawater: Canadian Journal of Fisheries and Aquatic Sciences, v. 37, p. 794–798.

Braman, R., and Hendrix, S., 1989, Nanogram nitrite and nitrate determination in environmental and biological materials by vanadium (III) reduction with chemiluminescence detection: Analytical Chemistry, v. 61, no. 24, p. 2715–2718.

Brandes, J.A., and Devol, A.H., 2002, A global marine-fixed nitrogen isotopic budget: Implications for Holocene nitrogen cycling: Global Biogeochemical Cycles, v. 16, no. 4, p. 1–14, doi: 10.1029/2001GB001856br.

Brunet, R., and Garcia Gil, L., 1996, Sulfide-induced dissimilatory nitrate reduction to ammonia in anaerobic freshwater sediments: FEMS Microbiology Ecology, v. 21, no. 2, p. 131–138.

Burgin, A., and Hamilton, S.K., 2007, Have we overemphasized the role of denitrification in aquatic ecosystems? A review of nitrate removal pathways: Frontiers in Ecology and the Environment, v. 5, no. 2, p. 89–96.

Cardoso, R.B., Sierra-Alvarez, R., Rowlette, P., Flores, E.R., Gomez, J., and Field, J.A., 2006, Sulfide oxidation under chemolithoautotrophic denitrifying conditions: Biotechnology and Bioengineering, v. 95, no. 6, p. 1148–1157, doi: 10.1002/bit.21084.

Carignan, R., Rapin, F., and Tessier, A., 1985, Sediment porewater sampling for metal analysis: a comparison of techniques: Geochimica et Cosmochimica Acta, v. 49, no. 11, p. 2493–2497.

Christensen, C., Gorsline, D.S., Hammond, D.E., and Lund, S.P., 1994, Non-annual laminations and expansion of anoxic basin-floor conditions in Santa Monica Basin, California Borderland: Marine Geology, v. 116, no. 3-4, p. 399–418.

Cline, J.D., 1969, Spectrophotometric determination of hydrogen sulfide in natural waters: Limnology and Oceanography,, p. 454–458.

Codispoti, L.A., 2007, An oceanic fixed nitrogen sink exceeding 400 Tg N/a vs the concept of homeostasis in the fixed-nitrogen inventory: Biogeosciences, v. 4, p. 233–253.

Codispoti, L.A., Brandes, J.A., Christensen, J.P., Devol, A.H., Naqvi, S.W.A., Paerl, H.W., and Yoshinari, T., 2001, The oceanic fixed nitrogen and nitrous oxide budgets: Moving targets as we enter the anthropocene?: Scientia Marina, v. 65, p. 85–105.

Cook, R., 1979, Influential observations in linear regression: Journal of the American Statistical Association, v. 74, no. 365, p. 169–174.

Cox, R., 1980, Determination of nitrate and nitrite at the parts per billion level by chemiluminescence: Analytical Chemistry, v. 52, no. 2, p. 332–335.

Deutsch, C., 2004, Isotopic constraints on glacial/interglacial changes in the oceanic nitrogen budget: Global Biogeochemical Cycles, v. 18, no. 4, p. GB4012, doi: 10.1029/2003GB002189.

Devol, A.H., 2008, Denitrification including anammox, *in* Capone, D.G., Bronk, D., Mulholland, M., and Carpenter, E.J. eds., Nitrogen in the Marine Environment, Elsevier, Inc, p. 263–301.

Douglas, R.G., Gonzalez-Yajimovich, O., Ledesma-Vazquez, J., and Staines-Urias, F., 2007, Climate forcing, primary production and the distribution of Holocene biogenic sediments in the Gulf of California: Quaternary Science Reviews, v. 26, no. 1-2, p. 115–129, doi: 10.1016/j.quascirev.2006.05.003.

Emerson, S.R., Stump, C., Wilbur, D., and Quay, P.D., 1999, Accurate measurement of O2, N2, and Ar gases in water and the solubility of N2: Marine Chemistry, v. 64, p. 337–347.

Emmer, E., and Thunell, R.C., 2000, Nitrogen isotope variations in Santa Barbara Basin sediments: Implications for denitrification in the eastern tropical North Pacific during the last 50,000 years: Paleoceanography, v. 15, no. 4, p. 377–387.

Eyre, B., Rysgaard, S., Dalsgaard, T., and Christensen, P.B., 2002, Comparison of isotope pairing and N 2: Ar methods for measuring sediment denitrification—Assumptions, Modifications, and Implications: Estuaries and Coasts, v. 25, no. 6A, p. 1077–1087.

Fossing, H., Gallardo, V.A., Jorgensen, B.B., Hüttel, M., Nielsen, L.P., Schulz, H.N., Canfield, D.E., Forster, S., Glud, R.N., and Gundersen, J., 1995, Concentration and transport of nitrate by the mat-forming sulphur bacterium Thioploca: Nature, v. 374, no. April, p. 713–715.

Gonzalez-Yajimovich, O., Douglas, R.G., and Gorsline, D.S., 2005, The preserved carbonate record in Holocene sediments of the Alfonso and Pescadero basins, Gulf of California: Proceedings of the Geologists Association, v. 116, no. 3-4, p. 315–330.

Gruber, N., 2004, The dynamics of the marine nitrogen cycle and its influence on atmospheric CO2 variations: The Ocean Carbon Cycle and Climate.

Gruber, N., and Sarmiento, J.L., 1997, Global patterns of marine nitrogen fixation and denitrification: Global Biogeochemical Cycles, v. 11, p. 235–266.

Hamme, R.C., and Emerson, S.R., 2004, The solubility of neon, nitrogen and argon in distilled water and seawater: Deep Sea Research Part I: Oceanographic Research Papers, v. 51, no. 11, p. 1517–1528, doi: 10.1016/j.dsr.2004.06.009.

Hamme, R.C., and Severinghaus, J., 2007, Trace gas disequilibria during deep-water formation: Deep Sea Research Part I: Oceanographic Research Papers, v. 54, no. 6, p. 939–950.

Hammond, D.E., Cummins, K.M., McManus, J., Berelson, W.M., Smith, G., and Spagnoli, F., 2004, Methods for measuring benthic nutrient flux on the California Margin: Comparing shipboard core incubations to in situ lander results: Limnology and Oceanography: Methods.

Hartnett, H.E., and Seitzinger, S.P., 2003, High-resolution nitrogen gas profiles in sediment porewaters using a new membrane probe for membrane-inlet mass spectrometry: Marine Chemistry, v. 83, no. 1-2, p. 23–30, doi: 10.1016/S0304-4203(03)00093-8.

Hogslund, S., Peter Revsbech, N., Gijs Kuenen, J., Jorgensen, B.B., Gallardo, V.A., van de Vossenberg, J., Nielsen, J.L., Holmkvist, L., Arning, E.T., and Peter Nielsen, L., 2009, Physiology and behaviour of marine Thioploca: The ISME Journal, v. 3, no. 6, p. 647, doi: doi:10.1038/ismej.2009.17.

Huh, C., Ku, T., Luo, S., Landry, M.R., and Williams, P.M., 1993, Fluxes of Th isotopes in the Santa Monica Basin, offshore California: Earth and Planetary Science Letters, v. 116, no. 1-4, p. 155–164.

Jahnke, R.A., 1990, Early diagenesis and recycling of biogenic debris at the seafloor, Santa Monica Basin, California: Journal of Marine Research, v. 48, no. 2, p. 413–436.

Jorgensen, B.B., and D'hondt, S., 2006, ECOLOGY: A Starving Majority Deep Beneath the Seafloor: Science, v. 314, no. November, p. 932–934.

Kalil, E., and Goldhaber, M., 1973, A sediment squeezer for removal of pore waters without air contact: Journal of Sedimentary Research, v. 43, no. 2, p. 553.

Kana, T.M., 2004, Comment on "Comparison of isotope pairing and N 2: Ar methods for measuring sediment denitrification" by BD Eyre, S. Rysgaard, T. Dalsgaard, and P. Bondo Christensen. 2002. Estuaries 25: 1077–1087: Estuaries and Coasts, v. 27, no. 1, p. 173–176.

Kana, T.M., Darkangelo, C., Hunt, M., and Oldham, J., 1994, Membrane Inlet Mass Spectrometer for Rapid High-Precision Determination of N2, O2, and Ar in environmental water samples: Analytical Chemistry, v. 66, p. 4166–4170.

Kana, T.M., Sullivan, M., Cornwell, J.C., and Groszkowski, K., 1998, Denitrification in estuarine sediments determined by membrane inlet mass spectrometry: Limnology and Oceanography, v. 43, no. 2, p. 334–339.

Kappler, A., Pasquero, C., Konhauser, K.O., and Newman, D.K., 2005, Deposition of banded iron formations by anoxygenic phototrophic Fe (II)-oxidizing bacteria: Geology, v. 33, no. 11, p. 865–868.

Koho, K.A., Piña-Ochoa, E., Geslin, E., and Risgaard-Petersen, N., 2010, Vertical migration, nitrate uptake and denitrification: survival mechanisms of foraminifers (Globobulimina turgida) under low oxygen conditions: FEMS Microbiology Ecology, v. 75, no. 2, p. 273–283, doi: 10.1111/j.1574-6941.2010.01010.x.

Li, Y., and Gregory, S., 1974, Diffusion of ions in sea water and in deep-sea sediments: Geochimica et Cosmochimica Acta, v. 38, no. 5, p. 703–714.

Liu, K.K., and Kaplan, I.R., 1984, Denitrification rates and availability of organic matter in marine environments: Earth and Planetary Science Letters, v. 68, p. 88–100.

Liu, K.K., and Kaplan, I.R., 1989, The eastern tropical Pacific as a source of 15N-enriched nitrate in seawater off southern California: Limnology and Oceanography,, p. 820–830.

Lorenz, F.O., 1987, Teaching about influence in Simple Regression: Teaching Sociology,, p. 173–177.

Martin, W.R., and Sayles, F.L., 2006, Organic matter oxidation in deep-sea sediments: distribution in the sediment column and implications for calcite dissolution: Deep Sea Research Part II, v. 53, p. 771–792.

Mchatton, S., Barry, J., Jannasch, H.W., and Nelson, D.C., 1996, High Nitrate Concentrations in Vacuolate, Autotrophic Marine Beggiatoa spp: Applied and Environmental Microbiology, v. 62, no. 3, p. 954–958.

Middelburg, J.J., Soetaert, K., Herman, P.M., and Heip, C.H.R., 1996, Denitrification in marine sediments: A model study: Global Biogeochemical Cycles, v. 10, no. 4, p. 661–673.

Otte, S., Kuenen, J.G., Nielsen, L.P., Paerl, H.W., Zopfi, J., Schulz, H.N., Teske, A., Strotmann, B., Gallardo, V.A., and Jorgensen, B.B., 1999, Nitrogen, Carbon, and Sulfur Metabolism in Natural Thioploca Samples: Applied and Environmental Microbiology, v. 65, no. 7, p. 3148–3157.

Piña-Ochoa, E., 2010, Supplemental Information:.

Piña-Ochoa, E., Hogslund, S., Geslin, E., Cedhagen, T., Revsbech, N.P., Nielsen, L.P., Schweizer, M., Jorissen, F.J., Rysgaard, S., and Risgaard-Petersen, N., 2010, Widespread occurrence of nitrate storage and denitrification among Foraminifera and Gromiida: Proceedings of the National Academy of Sciences, v. 107, no. 3, p. 1148–1153, doi: 10.1073/pnas.0908440107.

Prokopenko, M.G., Hammond, D.E., Berelson, W.M., Bernhard, J.M., Stott, L., and Douglas, R.G., 2006, Nitrogen cycling in the sediments of Santa Barbara basin and Eastern Subtropical North Pacific: Nitrogen isotopes, diagenesis and possible chemosymbiosis between two lithotrophs (Thioploca and Anammox)—"riding on a glider": Earth and Planetary Science Letters, v. 242, no. 1-2, p. 186–204, doi: 10.1016/j.epsl.2005.11.044.

Prokopenko, M.G., Sigman, D.M., Berelson, W.M., Hammond, D.E., Barnett, B.A., Chong, L.S., and Townsend-Small, A., 2011, Denitrification in anoxic sediments supported by biological nitrate transport: Geochimica et Cosmochimica Acta, v. 75, no. 22, p. 7180–7199.

Risgaard-Petersen, N., Langezaal, A.M., Ingvardsen, S., Schmid, M.C., Jetten, M.S.M., Op Den Camp, H.J.M., Derksen, J.W.M., Piña-Ochoa, E., Eriksson, S.P., Peter Nielsen, L., Peter Revsbech, N., Cedhagen, T., and van der Zwaan, G.J., 2006, Evidence for complete denitrification in a benthic foraminifer: Nature, v. 443, no. 7107, p. 93–96, doi: 10.1038/nature05070.

Sayama, M., Risgaard-Petersen, N., Nielsen, L.P., Fossing, H., and Christensen, P.B., 2005, Impact of Bacterial NO3- Transport on Sediment Biogeochemistry: Applied and Environmental Microbiology, v. 71, no. 11, p. 7575–7577, doi: 10.1128/AEM.71.11.7575-7577.2005.

Schulz, H.D., and Zabel, M., 2000, Marine Geochemistry: Springer-Verlag.

Schulz, H.N., 1999, Dense Populations of a Giant Sulfur Bacterium in Namibian Shelf

Sediments: Science, v. 284, no. 5413, p. 493–495, doi: 10.1126/science.284.5413.493.

Sigman, D.M., Granger, J., DiFiore, P.J., Lehmann, M.M., Ho, R., Cane, G., and Van Geen, A., 2005, Coupled nitrogen and oxygen isotope measurements of nitrate along the eastern North Pacific margin: Global Biogeochemical Cycles, v. 19, no. 4, p. GB4022.

Silverberg, N., Martínez, A., Aguíñiga, S., Carriquiry, J.D., Romero, N., Shumilin, E., and Cota, S., 2004, Contrasts in sedimentation flux below the southern California Current in late 1996 and during the El Niño event of 1997–1998: Estuarine, Coastal and Shelf Science, v. 59, no. 4, p. 575–587, doi: 10.1016/j.ecss.2003.11.003.

Smith, M.S., and Zimmerman, K., 1981, Nitrous Oxide Production by Nondenitrifying Soil Nitrate Reducers: Soil Science Society of America Journal, v. 45, no. 5, p. 865.

Straub, K.L., Benz, M., Schink, B., and Widdel, F., 1996, Anaerobic, nitrate-dependent microbial oxidation of ferrous iron: Applied and Environmental Microbiology, v. 62, no. 4, p. 1458–1460.

Thamdrup, B., and Canfield, D.E., 1996, Pathways of carbon oxidation in continental margin sediments off central Chile: Limnology and Oceanography, v. 41, no. 8, p. 1629–1650.

Tiedje, J.M., 1988, Ecology of denitrification and dissimilatory nitrate reduction to ammonium, *in* Zehnder, J. ed., Biology of anaerobic microorganisms, John Wiley & Sons, p. 179–244.

Ullman, W., and Aller, R.C., 1982, Diffusion coefficients in nearshore marine sediments: Limnology and Oceanography, v. 27, no. 3, p. 552–556.

Van Geen, A., 2003, On the preservation of laminated sediments along the western margin of North America: Paleoceanography, v. 18, no. 4, p. 1098, doi: 10.1029/2003PA000911.

Ward, B.B., Tuit, C.B., Jayakumar, A., Rich, J.J., Moffett, J., and Naqvi, S.W.A., 2008, Organic carbon, and not copper, controls denitrification in oxygen minimum zones of the ocean: Deep Sea Research Part I: Oceanographic Research Papers, v. 55, no. 12, p. 1672–1683, doi: 10.1016/j.dsr.2008.07.005.

Weber, K.A., Picardal, F.W., and Roden, E.E., 2001, Microbially Catalyzed Nitrate-Dependent Oxidation of Biogenic Solid-Phase Fe(II) Compounds: Environmental Science & Technology, v. 35, no. 8, p. 1644–1650, doi: 10.1021/es0016598.

Weiss, R., 1970, The solubility of nitrogen, oxygen and argon in water and seawater: Deep Sea Research and Oceanographic Abstracts, v. 17, no. 4, p. 721–735.

Yamagishi, H., Westley, M.B., Popp, B.N., Toyoda, S., Yoshida, N., Watanabe, S., Koba, K., and Yamanaka, Y., 2007, Role of nitrification and denitrification on the nitrous oxide cycle in the eastern tropical North Pacific and Gulf of California: Journal of Geophysical Research, v. 112, no. G2, p. G02015, doi: 10.1029/2006JG000227.

Zopfi, J., Kjar, T., Nielsen, L.P., and Jorgensen, B.B., 2001, Ecology of Thioploca spp.: Nitrate and Sulfur Storage in Relation to Chemical Microgradients and Influence of Thioploca spp. on the Sedimentary Nitrogen Cycle: Applied and Environmental Microbiology, v. 67, no. 12, p. 5530–5537, doi: 10.1128/AEM.67.12.5530-5537.2001.

Chapter 6: Summary

The work presented in this dissertation has examined C and N cycling in marine sediments. The first and major portion of this study has focused on the impact the Amazon River has on the export of organic material from a pore water and sedimentary perspective. The second examined the effect of biological nitrate transport on the overall nitrogen budget of suboxic and anoxic sediments and how this process may affect estimations of nitrogen removal in the global ocean.

Following the first theme, this work examined the spatial patterns of carbon and biogenic silica in the surface sediments underlying the Amazon River plume. We sought to determine how the Amazon River affects biogenic export and sedimentation throughout the Western Tropical Atlantic by quantifying the amount of material arriving at the sea floor, using the sediments as the ultimate sediment trap. We also wanted to identify any links between the deposition of C_{org} and bSi in the sediments, which may indicate whether or not diatom-diazotroph-associations are an important vector for C_{org} export.

Our assessment of export first relied on studies of the products of C_{org} degradation in the sediments, focusing on the production and consumption of nitrate in the pore waters. A multi-G, diffusion-reaction model, which assumes that fractions of C_{org} have different reactivities, was used to estimate carbon oxidation rates from pore water profiles of nitrate. Pore water dissolved Mn was used to determine the depth where oxygen went to zero, the depth of denitrification.

The Amazon River Plume leaves a distinct footprint of C_{org} and bSi remineralization in the underlying sediments as far as 1200 km from the river mouth. There is an axis of C_{org} and bSi deposition that corresponds to the axis of the spring plume as it travels to the northwest towards the Caribbean. The sedimentary patterns reveal much steeper gradients in the remineralization fluxes of C_{org} and bSi than would be predicted from an analysis of the surface plume salinity alone.

Benthic carbon oxidation fluxes ranged from 0.16 – 1.92 mmol m^{-2} d^{-1} throughout the study region, with the highest fluxes localized in sediments beneath the core axis of the Amazon River Plume extending to the northwest. Benthic $Si(OH)_4$ fluxes ranged from 0.14 – 1.35 mmol m^{-2} d^{-1}, and covered a wider latitudinal expanse towards the northwest while to the east, fluxes were consistently low. Deposition follows a pattern of high-C/high-Si near the axis of the plume, low-C/high-Si as plume waters move away from the central axis, and low-C/low-Si throughout the rest of the area. The region underlying the fall retroflection plume appears to be of minor importance to C_{org} and bSi export compared to the spring plume. The disconnect between the patterns of C_{org} and bSi deposition indicates that their export is somewhat decoupled from one another. Diatom-diazotroph-associations may increase bSi export, but it does not appear that mesohaline waters (salinity = 30-32) provide a zone of elevated C_{org} export to the deep ocean.

There is a fast-reacting pool of organic matter that is highest within the plume axis, and accounts for >90% of the total C_{org} flux. Sites quite distal from this axis also receive a high fraction of fast-reaction C_{org}, though there is a region,

primarily in the retroflection, where fast C_{org} constitutes only 40-50% of the total C_{org} flux. Overall, 0.15 Tmol C y^{-1} is remineralized in abyssal sediments in the 900,000 km^2 region influenced by the Amazon River Plume, constituting ~7% of the estimated 2.3 Tmol C yr^{-1} of total surface C_{org} export suggested by Subramaniam et al., (2008).

We performed an analysis of the downcore composition and properties of the sediment cores across the region. The sedimentary studies provided an assessment of burial fluxes and examined how patterns of deposition have changed throughout the Holocene. Surface sediment concentrations showed that elevated amounts of C_{org} and bSi are found in an area near 10˚N 50˚W, and the expanse of this zone covers a larger longitudinal space than covered by the modern river plume. The surface sediment C_{org} content decreases by a factor of 2 to the north and east. Our study area had higher average surface sediment C_{org} and bSi content and lower $CaCO_3$ concentrations compared to other sites in the North Atlantic.

We examined sediment mixing using profiles of excess ^{210}Pb, and found the sediment mixed layer was generally 10-12 cm deep. Sediment mixing coefficients ranged from 0.06 – 3.1 cm^2 yr^{-1}, agreeing with other values from the deep ocean, but no spatial patterns were evident. The normalized excess ^{210}Pb inventory in the sediments was higher than that of the water column by ~2X at sites south of 10˚N 50˚W, but outside this zone, the stations were generally deficient in excess ^{210}Pb. ^{230}Th-derived focusing factors (from the similar stations) revealed a pattern of sediment focusing and winnowing throughout the region that was not

geographically systematic. Sites with high values of normalized excess ^{210}Pb inventories in absence of high focusing derived from ^{230}Th indicate that there is a significant amount of ^{210}Pb moved to these areas through lateral transport.

Sedimentation rates were determined using ^{14}C calendar ages measured from bulk sieved material (200 μm, comprised primarily of foraminifera) and were calculated assuming a sediment mixed layer of 10 cm. Box model simulations indicate that sedimentation rates within the mixed layer, which reflect the last few thousand years, are roughly the same as those determined at depth. The sedimentation rates calculated below the sediment mixed layer agreed with previous measurements from the Western Tropical Atlantic, ranging from 1.2 – 4.6 cm kyr^{-1}. The average sedimentation rate was highest in the central zone (4.3 ± 0.4 cm kyr^{-1}), south of 10˚N and west of 50˚W, while rates to the north and east were comparable to each other (2.8 ±1.4 and 3.0 ± 1.2 cm kyr^{-1}, respectively). The sedimentation rates calculated from 7 sites were extrapolated to the study region and combined with sediment composition data to estimate burial fluxes of C_{org} and bSi, which ranged from 0.01-0.08 mmol C m^{-2}d^{-1} and 0.01-0.04 mmol SiO_2 m^{-2}d^{-1}, respectively. The burial fluxes comprised 4-16% of the total C_{org} rain and 2-10% of the total bSi rain arriving on the sea floor.

Downcore, sediments in the south and west generally contain higher amounts of both C_{org} and bSi as compared to the east, a trend that persisted throughout most of the study area, though at 10˚N, the composition was fairly uniform between the west and east. $CaCO_3$ followed an inverse pattern, where

greater amounts of $CaCO_3$ are in the sediments at eastern stations. The NW plume axis is a key area for the deposition of Corg and bSi, where in the south, both sedimentation rates and biogenic content are high compared to the rest of the region. Detrital material makes up the majority of the material arriving at the sea floor except at the most northerly and easterly stations. Detrital deposition has remained fairly constant throughout the Holocene, except at the easternmost stations where there was rapid increase in detrital concentrations at a depth of ~20cm likely corresponding to an age of approximately 10,000 years.

Deep-sea POC rain rates (determined from the sum of remineralization flux + burial flux) were extrapolated back to the surface using the Martin Curve. With a b-value of 0.86, the export fluxes predicted by this method were 7-17X greater than those recorded by floating sediment traps deployed at the same site. A smaller attenuation coefficient increased the coherence between the surface and benthic values. This result indicates that sediment traps may be under-collecting, there may be very little attenuation in the POC flux with depth, export fluxes may have decreased in this region over the last few decades, or our traps just happened to be deployed during low flux events. A comparison of estimates of total surface C_{org} export from previous work, from the extrapolations of C_{org} rain back to the surface, and from the sediment traps showed that there is approximately 3.5 Tmol C yr^{-1} exported from the surface ocean in waters influenced by the Amazon River plume.

The material captured by the sediment traps had $\delta^{13}C$ values that indicated the sinking POC is primarily of marine origin at most sites, however sites in the zone

of the retroflection plume appeared to have a significant contribution from terrestrial material, likely from C3 plants. The $\delta^{15}N$ of the trap material was generally around 4.5 ‰, though lighter values (~2 ‰) at select stations point to contributions from N_2-fixation.

We continued our examination of the importance of the Amazon plume to sedimentary processes by looking at the suboxic diagenetic reactions occurring in the deep sediment pore waters of gravity cores. Pore water nitrate profiles revealed a secondary nitrate maximum occurring at ~50 cm depth. We are not sure if such a feature has been previously reported from pore water profiles (and not attributable to bioturbation). Though it is possible that this feature is an artifact of sampling in an aerobic environment, the consistency of its appearance at the same depth throughout all of the cores suggest it may be real. This secondary nitrate peak may be produced by Mn-reduction and consumed by a combination of denitrification and/or Fe-oxidation. Most of the profiles of dissolved Mn and Fe had a near zero flux at depth, indicating that the sediments are likely carbon limited with 10's of cm's below the nitrate reduction zone.

Dissolved silica profiles show rapid dissolution within the upper 30 cm followed by dissolved $Si(OH)_4$ consumption, and then settled at a constant concentration. The decrease in $Si(OH)_4$ concentration is likely attributable to reverse weathering and the asymptotic concentration is indicative of the balance between the kinetic competition between dissolution and the formation of

authigentic alumino-silicate minerals. Pore water gradients are consistent with the hypothesis that iron oxidation is responsible for dissolved Si uptake.

An indurated, iron-rich crust is a common feature observed in the sediments of the equatorial Atlantic. Others have shown that the depth of the crust is a relative indicator of the transition from glacial to interglacial sediments, and our analysis of this boundary using $CaCO_3$ profiles and ^{14}C dating agrees with this finding. Additionally, simulations indicate that the flux of Fe is sufficient to create an Fe crust within ~10,000 years. The actual location of the crust depends on the amount of C_{org} present in the sediments. At sites with sufficient C_{org} content within Holocene sediments, the crust can migrate upwards due to reduction-reoxidation processes. At other sites, the boundary is fixed at the Glacial-Holocene.

The Amazon River leaves a clear footprint in the sediments with sharp gradients that would not have been expected from analysis of the surface plume alone. While C_{org} export in sediments underlying the plume is high when compared to other sites, it appears to be somewhat decoupled from bSi export and the areas of highest export do not correlate to the areas with surface salinities favorable for diatom-diazotroph associations. Suboxic diagenetic processes revealed complex interactions between nitrate, manganese and iron, as well as reverse weathering affecting the downcore profile of bSi. The river plume has played a key role in biogenic sedimentation throughout the Holocene, depositing high concentrations of C_{org} and bSi in the sediments along the NW plume axis. Overall, sedimentation rates

in this region do not appear to depend on the river plume, and instead appear to be controlled by sediment focusing.

Early in my graduate student career, I studied N cycling in coastal sediments. This work reported rates of benthic nitrogen cycling and assessed the controls on biological nitrate sequestration and transport in sediments underlying oxygen deficient areas of the Eastern North Pacific along the Western Coast of North America. Pore water measurements of N_2 were made at mm-scale resolution from sites with low bottom water O_2 (0-2 μM) but at sites with different pore water concentrations of dissolved Fe and HS^-. Estimates of N_2 fluxes were made by direct measurements from core incubations and by modeling of pore water profiles. The average N_2 efflux was four times larger at a site with high pore water H_2S concentrations (Soledad Basin 3.14 ± 1.10 mmol N m^{-2} d^{-1}) compared to an iron-rich site (Santa Monica Basin 0.74 ± 0.21 mmol N m^{-2} d^{-1}) despite both sites having comparable NO_3^- uptake fluxes (− 0.93 ± 0.14 vs. − 0.82 ± 0.08 mmol N m^{-2} d^{-1} respectively).

Pore water profiles of NO_3^-, NO_2^-, and N_2O from both sulfidic and iron-rich sites contained subsurface maxima that were likely caused by the presence of NO_3^- sequestered by infaunal microbiota. In Soledad Basin, the flux of NH_4^+ exceeded the rate that could be produced from C_{org} degradation by 10 times, and was instead likely produced by dissimilatory nitrate reduction to ammonium (DNRA) fueled by the sequestered pool of NO_3^-.

The results indicated that the overall supply of NO_3^- into suboxic and anoxic sediments must have two components: diffusive and biologically mediated nitrate transport. Core incubations do not capture the total NO_3^- flux, due to their inability to account for NO_3^- sequestered prior to the start of the experiment. Biological nitrate sequestration and transport appears to be a ubiquitous process in suboxic and anoxic sediments, though the specific N pathways and transformations are likely to be controlled by the availability of Fe or HS^- in the pore waters.

This dissertation was aimed at improving on the sparse spatial coverage of sedimentary field measurements and increasing knowledge of the biogeochemical pathways involved in sedimentary cycling in order to expand on our ability to understand the global cycling of C and N. In doing this, I have produced one of the most extensive datasets of deep ocean pore water and sedimentary data from a single region, and also characterized the importance of biological nitrate transport to the removal of fixed N. While these datasets have answered questions regarding the importance of the Amazon River to deep ocean export, and of biological nitrate transport to the benthic nitrogen cycle, many questions remain or have emerged as result of these findings:

1) Does the POC carried by the retroflection plume contain a larger fraction of terrestrial material than the NW plume?
2) Is there terrestrial POC present in the river plume that is not captured by the $\delta^{13}C$ values (C4 plants).
3) While DDAs appear to be important for increasing surface production, we do

not observe elevated fluxes of C_{org} rain in the deep ocean in areas where we would expect to find DDAs. Does any of the DDA-related production reach the deep ocean?

4) How does our estimation of C_{org} kinetics derived from remineralization compare to the kinetics derived from sedimentation and burial?
5) Is there a defined pattern in the sedimentation rates throughout the region?
6) How complex is N diagenesis in the deep sediments below the Amazon Plume? Is there anoxic nitrification? Is the secondary nitrate maximum real or an artifact?
7) How prevalent is biological nitrate transport throughout the global ocean?

While these are only a few questions that stem from this work, they are a starting point for future studies. With regards to the influence of the Amazon Plume, in going forward, we should look at the delivery of refractory and potentially terrestrial material to the deep ocean, particularly in the region of the retroflection plume. Focus should also be placed on characterizing the composition of the refractory POC that is buried in the sediments as well as in the plume itself so that we can try to predict the potential impact of anthropogenic changes on the delivery of POC to the deep ocean in this region. Future studies of surface export within the river plume need to account for the speed of the surface currents and complex hydrodynamics of the region. The PITS style traps employed in this study are likely not accurately capturing the material sinking out of the surface ocean within the plume, and thus a change in the trap design is likely warranted. To continue studies of biological nitrate transport, analyses of dissolved N_2 should be performed in

sediments below major OMZs, like off the coast of Peru and in the Arabian Sea, in order to establish the overall importance of this process to benthic N removal on a global scale.

Bibliography

Aller, R.C., 1982. The effects of macrobenthos on chemical properties of marine sediment and overlying water, in: McCall, P.L., Tevesz, M. (Eds.), Animal-Sediment Relations. Plenum, NY, pp. 53–102.

Aller, R.C., 1998. Mobile deltaic and continental shelf muds as suboxic, fluidized bed reactors. Marine Chemistry 61, 143–155.

Aller, R.C., Blair, N.E., 2006. Carbon remineralization in the Amazon-Guianas tropical mobile mudbelt: A sedimentary incinerator. Continental Shelf Research 26, 2241–2259.

Aller, R.C., Blair, N.E., Xia, Q., Rude, P., 1996. Remineralization rates, recycling, and storage of carbon in Amazon shelf sediments. Continental Shelf Research 16, 753–786.

Aller, R.C., Hall, P.O., Rude, P., Aller, J.Y., 1998. Biogeochemical heterogeneity and suboxic diagenesis in hemipelagic sediments of the Panama Basin. Deep Sea Research Part I 45, 133–165.

Aller, R.C., Heilbrun, C., Panzeca, C., Zhu, Z., Baltzer, F., 2004. Coupling between sedimentary dynamics, early diagenetic processes, and biogeochemical cycling in the Amazon–Guianas mobile mud belt: coastal French Guiana. Marine Geology 208, 331–360.

Alperin, M.J., Martens, C., Albert, D., Suayah, I.B., Benninger, L.K., Blair, N.E., Jahnke, R.A., 1999. Benthic fluxes and porewater concentration profiles of dissolved organic carbon in sediments from the North Carolina continental slope. Geochimica et Cosmochimica Acta 63, 427–448.

Altabet, M.A., François, R., 1994. Sedimentary nitrogen isotopic ratio as a recorder for surface ocean nitrate utilization. Global Biogeochemical Cycles 8, 103–116.

Altabet, M.A., Pilskaln, C.H., Thunell, R.C., Pride, C.J., Sigman, D.M., Chavez, F.P., François, R., 1999. The nitrogen isotope biogeochemistry of sinking particles from the margin of the Eastern North Pacific. Deep Sea Research Part I: Oceanographic Research Papers 46, 655–679.

Anderson, L.A., Sarmiento, J.L., 1994. Redfield ratios of remineralization determined by nutrient data analysis. Global Biogeochemical Cycles.

Archer, D.E., 1996. An atlas of the distribution of calcium carbonate in sediments of the deep sea. Global Biogeochemical Cycles 10, 159–174.

Archer, D.E., Lyle, M.W., Rodgers, K., Froelich, P.N., 1993. What controls opal preservation in tropical deep-sea sediments. Paleoceanography 8, 7–21.

Bacon, M.P., 1984. Glacial to interglacial changes in carbonate and clay sedimentation in the Atlantic Ocean estimated from 230 Th measurements. Chemical Geology 46, 97–111.

Balsam, W.L., McCoy, F.W., 1987. Atlantic sediments: Glacial/interglacial comparisons. Paleoceanography 2, 531–542.

Barnett, P., Watson, J., Connelly, D., 1984. A multiple corer for taking virtually undisturbed samples from shelf, bathyal and abyssal sediments. Oceanologica Acta 7, 399–408.

Barsanti, M., Delbono, I., Schirone, A., Langone, L., Miserocchi, S., Salvi, S., Delfanti, R., 2011. Sediment reworking rates in deep sediments of the Mediterranean Sea. Science of The Total Environment 409, 2959–2970.

Basso, D., Thomson, J., Corselli, C., 2004. Indications of low macrobenthic activity in the deep sediments of the eastern Mediterranean Sea. Scientia Marina 68, 53–62.

Baumgartner, T.R., Ferreira-Bartrina, V., Schrader, H., Soutar, A., 1985. A 20-year carve record of siliceous phytoplankton variability in the central Gulf of California. Marine Geology 64, 113–129.

Bender, M.L., Fanning, K., Froelich, P.N., Heath, G.R., Maynard, V., 1977. Interstitial nitrate profiles and oxidation of sedimentary organic matter in the eastern equatorial Atlantic. Science 198, 605–609.

Bender, M.L., Heggie, D.T., 1984. Fate of organic carbon reaching the deep sea floor: a status report. Geochimica et Cosmochimica Acta 48, 977–986.

Bender, M.L., Jahnke, R.A., Weiss, R., Martin, W.R., Heggie, D.T., Orchardo, J., Sowers, T., 1989. Organic carbon oxidation and benthic nitrogen and silica dynamics in San Clemente Basin, a continental borderland site. Geochimica et Cosmochimica Acta 53, 685–697.

Bender, M.L., Martin, W.R., Hess, J., Sayles, F.L., Ball, L., Lambert, C.E., 1987. A whole-core squeezer for interfacial pore-water sampling. Limnology and Oceanography 1214–1225.

Berelson, W.M., 1991. The flushing of two deep-sea basins, southern California borderland. Limnology and Oceanography 36, 1150–1166.

Berelson, W.M., Hammond, D.E., Xu, X., O'Neill, D., Chin, C., Zukin, J., 1990. Benthic fluxes and pore water studies from sediments of the central equatorial north Pacific: Nutrient diagenesis. Geochimica et Cosmochimica Acta 54, 3001–3012.

Berelson, W.M., McManus, J., Coale, K.H., Johnson, K.S., Kilgore, T.E., Burdige, D.J., Pilskaln, C.H., 1996. Biogenic matter diagenesis on the sea floor: A comparison between two continental margin transects. Journal of Marine Research 54, 731–762.

Berelson, W.M., Prokopenko, M.G., Sansone, F.J., Graham, A.W., McManus, J., Bernhard, J.M., 2005. Anaerobic diagenesis of silica and carbon in continental margin sediments: discrete zones of TCO2 production. Geochimica et Cosmochimica Acta 69, 4611–4629.

Berner, E.K., Berner, R.A., 2012. Global environment: water, air and geochemical cycles. Princeton University Press, Princeton, NJ.

Berner, R.A., 1980. Early Diagenesis: A Theoretical Approach. Princeton University Press, Princeton, NJ.

Bernhard, J.M., Buck, K., Farmer, M., Bowser, S.S., 2000. The Santa Barbara Basin is a symbiosis oasis. Nature 403, 77–80.

Blair, N.E., Aller, R.C., 2012. The fate of terrestrial organic carbon in the marine environment. Annual Review of Marine Science 4, 401–423.

Blair, N.E., Leithold, E., Aller, R.C., 2004. From bedrock to burial: the evolution of particulate organic carbon across coupled watershed-continental margin systems. Marine Chemistry 91, 141–156.

Bleakley, B.H., Tiedje, J.M., 1982. Nitrous oxide production by organisms other than nitrifiers or denitrifiers. Applied and Environmental Microbiology 44, 1342–1348.

Boudreau, B.P., Ruddick, B.R., 1991. On a reactive continuum representation of

organic matter diagenesis. American Journal of Science 291, 507–538.

Bower, C., Holm-Hansen, T., 1980. A salicylate-hypochlorite method for determining ammonia in seawater. Canadian Journal of Fisheries and Aquatic Sciences 37, 794–798.

Boyd, P.W., Ellwood, M.J., 2010. The biogeochemical cycle of iron in the ocean. Nature Geoscience 3, 675–682.

Braman, R., Hendrix, S., 1989. Nanogram nitrite and nitrate determination in environmental and biological materials by vanadium (III) reduction with chemiluminescence detection. Analytical Chemistry 61, 2715–2718.

Brandes, J.A., Devol, A.H., 2002. A global marine-fixed nitrogen isotopic budget: Implications for Holocene nitrogen cycling. Global Biogeochemical Cycles 16, 1–14.

Brandes, J.A., Devol, A.H., Deutsch, C., 2007. New developments in the marine nitrogen cycle. Chemical Reviews 107, 577–589.

Broecker, W.S., Matsumoto, K., Clark, E., Hajdas, I., Bonani, G., 1999. Radiocarbon age differences between coexisting foraminiferal species. Paleoceanography 14, 431–436.

Broecker, W.S., Peng, T.-H., 1982. Tracers in the sea 690.

Brunet, R., Garcia Gil, L., 1996. Sulfide-induced dissimilatory nitrate reduction to ammonia in anaerobic freshwater sediments. FEMS Microbiology Ecology 21, 131–138.

Buesseler, K.O., Antia, A.N., Chen, M., Fowler, S.W., Gardner, W.D., Gustafsson, O., Harada, K., Michaels, A.F., van der Loeff, M.M., Sarin, M., 2007a. An assessment of

the use of sediment traps for estimating upper ocean particle fuxes. Journal of Marine Research 65, 345–416.

Buesseler, K.O., Boyd, P.W., 2009. Shedding light on processes that control particle export and flux attenuation in the twilight zone of the open ocean. Limnology and Oceanography 54, 1210.

Buesseler, K.O., Lamborg, C.H., Boyd, P.W., Lam, P.J., Trull, T.W., Bidigare, R.R., Bishop, J.K., Casciotti, K.L., DeHairs, F., Elskens, M., Honda, M.C., Karl, D.M., Siegel, D.A., Silver, M.W., Steinberg, D.K., Valdes, J.R., Van Mooy, B.A., Wilson, S., 2007b. Revisiting Carbon Flux Through the Ocean's Twilight Zone. Science 316, 567–570.

Buesseler, K.O., Steinberg, D.K., Michaels, A.F., Johnson, R.J., Andrews, J.E., Valdes, J.R., Price, J.F., 2000. A comparison of the quantity and composition of material caught in a neutrally buoyant versus surface-tethered sediment trap. Deep Sea Research Part I: Oceanographic Research Papers 47, 277–294.

Burdige, D.J., 1993. The biogeochemistry of manganese and iron reduction in marine sediments. Earth Science Reviews 35, 249–284.

Burdige, D.J., 2007. Preservation of organic matter in marine sediments: controls, mechanisms, and an imbalance in sediment organic carbon budgets? Chemical Reviews-Columbus 107, 467–485.

Burgin, A., Hamilton, S.K., 2007. Have we overemphasized the role of denitrification in aquatic ecosystems? A review of nitrate removal pathways. Frontiers in Ecology and the Environment 5, 89–96.

Cai, W.-J., Reimers, C.E., Shaw, T., 1995. Microelectrode studies of organic carbon

degradation and calcite dissolution at a California continental rise site. Geochimica et Cosmochimica Acta 59, 497–511.

Canfield, D.E., 1994. Factors influencing organic carbon preservation in marine sediments. Chemical Geology 114, 315–329.

Canfield, D.E., Kristensen, E., Thamdrup, B., 2005. Aquatic Geomicrobiology. Academic Press.

Capone, D.G., Burns, J.A., Montoya, J.P., Subramaniam, A., Mahaffey, C., Gunderson, T., Michaels, A.F., Carpenter, E.J., 2005. Nitrogen fixation by Trichodesmium spp.: An important source of new nitrogen to the tropical and subtropical North Atlantic Ocean. Global Biogeochemical Cycles 19, GB2024.

Cardoso, R.B., Sierra-Alvarez, R., Rowlette, P., Flores, E.R., Gomez, J., Field, J.A., 2006. Sulfide oxidation under chemolithoautotrophic denitrifying conditions. Biotechnol. Bioeng. 95, 1148–1157.

Carignan, R., Rapin, F., Tessier, A., 1985. Sediment porewater sampling for metal analysis: a comparison of techniques. Geochimica et Cosmochimica Acta 49, 2493–2497.

Carpenter, E.J., Capone, D.G., 1992. Nitrogen fixation in Trichodesmium blooms, in: Carpenter, E.J., Capone, D.G. (Eds.), Marine Pelagic Cyanobacteria. Kluwer Academic Publishers, pp. 211–218.

Carpenter, E.J., Montoya, J.P., Burns, J.A., Mulholland, M., Subramaniam, A., Capone, D.G., 1999. Extensive bloom of a N2 fixing symbiotic association in the tropical Atlantic Ocean. Marine Ecology Progress Series 188, 273–283.

Carpenter, E.J., Romans, K., 1991. Major role of the cyanobacterium Trichodesmium

in nutrient cycling in the North Atlantic Ocean. Science 254, 1356.

Carvalho, F.P., Oliveira, J.M., Soares, A.M.M., 2011. Sediment accumulation and bioturbation rates in the deep Northeast Atlantic determined by radiometric techniques. ICES Journal of Marine Science 68, 427–435.

Chong, L.S., Prokopenko, M.G., Berelson, W.M., Townsend-Small, A., McManus, J., 2012. Nitrogen cycling within suboxic and anoxic sediments from the continental margin of Western North America. Marine Chemistry 128-129, 13–25.

Christensen, C., Gorsline, D.S., Hammond, D.E., Lund, S.P., 1994. Non-annual laminations and expansion of anoxic basin-floor conditions in Santa Monica Basin, California Borderland. Marine Geology 116, 399–418.

Cline, J.D., 1969. Spectrophotometric determination of hydrogen sulfide in natural waters. Limnology and Oceanography 454–458.

Cochran, J.K., McKibbin-Vaughan, T., Dornblaser, M.M., Hirschberg, D., Livingston, H.D., Buesseler, K.O., 1990. 210 Pb scavenging in the North Atlantic and North Pacific Oceans. Earth and Planetary Science Letters 97, 332–352.

Codispoti, L.A., 2007. An oceanic fixed nitrogen sink exceeding 400 Tg N/a vs the concept of homeostasis in the fixed-nitrogen inventory. Biogeosciences 4, 233–253.

Codispoti, L.A., Brandes, J.A., Christensen, J.P., Devol, A.H., Naqvi, S.W.A., Paerl, H.W., Yoshinari, T., 2001. The oceanic fixed nitrogen and nitrous oxide budgets: Moving targets as we enter the anthropocene? Scientia Marina 65, 85–105.

Cook, R., 1979. Influential observations in linear regression. Journal of the American

Statistical Association 74, 169–174.

Cooley, S.R., Coles, V.J., Subramaniam, A., Yager, P.L., 2007. Seasonal variations in the Amazon plume-related atmospheric carbon sink. Global Biogeochemical Cycles 21, GB3014.

Cooley, S.R., Yager, P.L., 2006. Physical and biological contributions to the western tropical North Atlantic Ocean carbon sink formed by the Amazon River plume. Journal of Geophysical Research 111, 1–14.

Cox, R., 1980. Determination of nitrate and nitrite at the parts per billion level by chemiluminescence. Analytical Chemistry 52, 332–335.

Craig, H., Krishnaswami, S., Somayajulu, B., 1973. 210 Pb 226 Ra: Radioactive disequilibrium in the deep sea. Earth and Planetary Science Letters 17, 295–305.

Damuth, J.E., 1977. Late Quaternary sedimentation in the western equatorial Atlantic. GSA Bulletin 88, 695.

Damuth, J.E., Embley, R., 1981. Mass-transport processes on Amazon Cone: western equatorial Atlantic. AAPG Bulletin 65, 629.

Damuth, J.E., Kumar, N., 1975. Late Quaternary depositional processes on the continental rise of the western equatorial Atlantic: Comparison with the western North Atlantic and implications for reservoir-rock distribution. AAPG Bulletin 59, 2172–2181.

Davey, M., Tarran, G.A., Mills, M.M., Ridame, C., Geider, R.J., LaRoche, J., 2008. Nutrient limitation of picophytoplankton photosynthesis and growth in the tropical North Atlantic. Limnology and Oceanography 1722–1733.

de Baar, H.J.W., de Jong, J.T.M., 2001. Distributions, sources, and sinks of iron in

seawater, in: IUPAC Series on Analytical and Physical Chemistry of Environmental Systems. pp. 123–254.

Del Vecchio, R., Subramaniam, A., 2004. Influence of the Amazon River on the surface optical properties of the western tropical North Atlantic Ocean. Journal of Geophysical Research 109, C11001.

DeMaster, D.J., 1981. The supply and accumulation of silica in the marine environment. Geochimica et Cosmochimica Acta 45, 1715–1732.

DeMaster, D.J., Kuehl, S.A., Nittrouer, C.A., 1986. Effects of suspended sediments on geochemical processes near the mouth of the Amazon River: examination of biological silica uptake and the fate of particle-reactive elements. Continental Shelf Research 6, 107–125.

DeMaster, D.J., McKee, B.A., Nittrouer, C.A., Brewster, D.C., Biscaye, P.E., 1985. Rates of sediment reworking at the HEBBLE site based on measurements of Th-234, Cs-137 and Pb-210. Marine Geology 66, 133–148.

DeMaster, D.J., Pope, R.H., 1996. Nutrient dynamics in Amazon shelf waters: results from AMASSEDS. Continental Shelf Research 16, 263–289.

DeMaster, D.J., Smith, W.O., Jr, Nelson, D.M., Aller, J.Y., 1996. Biogeochemical processes in Amazon shelf waters: chemical distributions and uptake rates of silicon, carbon and nitrogen. Continental Shelf Research 16, 617–643.

Deuser, W.G., 1986. Seasonal and interannual variations in deep-water particle fluxes in the Sargasso Sea and their relation to surface hydrography. Deep Sea Research Part A. Oceanographic Research Papers 33, 225–246.

Deuser, W.G., Brewer, P.G., Jickells, T.D., Commeau, R., 1983. Biological control of the

removal of abiogenic particles from the surface ocean. Science 219, 388.

Deuser, W.G., Muller-Karger, F.E., Evans, R.H., Brown, O.B., Esaias, W.E., Feldman, G.C., 1990. Surface-ocean color and deep-ocean carbon flux: how close a connection? Deep Sea Research Part A. Oceanographic Research Papers 37, 1331–1343.

Deuser, W.G., Muller-Karger, F.E., Hemleben, C., 1988. Temporal variations of particle fluxes in the deep subtropical and tropical North Atlantic: Eulerian versus Lagrangian effects. Journal of Geophysical Research 93, 6857–6862.

Deuser, W.G., Ross, E.H., 1980. Seasonal change in the flux of organic carbon to the deep Sargasso Sea. Nature 283, 364–365.

Deuser, W.G., Ross, E.H., Anderson, R.F., 1981. Seasonality in the supply of sediment to the deep Sargasso Sea and implications for the rapid transfer of matter to the deep ocean. Deep Sea Research Part A. Oceanographic Research Papers 28, 495–505.

Deutsch, C., 2004. Isotopic constraints on glacial/interglacial changes in the oceanic nitrogen budget. Global Biogeochemical Cycles 18, GB4012.

Devol, A.H., 2008. Denitrification including anammox, in: Capone, D.G., Bronk, D., Mulholland, M., Carpenter, E.J. (Eds.), Nitrogen in the Marine Environment. Elsevier, Inc, pp. 263–301.

Dixit, S., Van Cappellen, P., van Bennekom, A.J., 2001. Processes controlling solubility of biogenic silica and pore water build-up of silicic acid in marine sediments. Marine Chemistry 73, 333–352.

Douglas, R.G., Gonzalez-Yajimovich, O., Ledesma-Vazquez, J., Staines-Urias, F., 2007.

Climate forcing, primary production and the distribution of Holocene biogenic sediments in the Gulf of California. Quaternary Science Reviews 26, 115–129.

Druffel, E.R.M., 2005. Input of particulate organic and dissolved inorganic carbon from the Amazon to the Atlantic Ocean. Geochem. Geophys. Geosyst. 6, Q03009.

Emerson, S.R., Jahnke, R.A., Bender, M.L., Froelich, P.N., Klinkhammer, G.P., Bowser, C., Setlock, G., 1980. Early diagenesis in sediments from the eastern equatorial Pacific, I. Pore water nutrient and carbonate results. Earth and Planetary Science Letters 49, 57–80.

Emerson, S.R., Stump, C., Wilbur, D., Quay, P.D., 1999. Accurate measurement of O2, N2, and Ar gases in water and the solubility of N2. Marine Chemistry 64, 337–347.

Emmer, E., Thunell, R.C., 2000. Nitrogen isotope variations in Santa Barbara Basin sediments: Implications for denitrification in the eastern tropical North Pacific during the last 50,000 years. Paleoceanography 15, 377–387.

Eppley, R., Peterson, B., 1979. Particulate organic matter flux and planktonic new production in the deep ocean. Nature 282, 677–680.

Eyre, B., Rysgaard, S., Dalsgaard, T., Christensen, P.B., 2002. Comparison of isotope pairing and N 2: Ar methods for measuring sediment denitrification—Assumptions, Modifications, and Implications. Estuaries and Coasts 25, 1077–1087.

Falkowski, P.G., Barber, R.T., Smetacek, V., 1998. Biogeochemical controls and feedbacks on ocean primary production. Science 281, 200–206.

Falkowski, P.G., Scholes, R.J., Boyle, E.A., Canadell, J.G., Canfield, D., Elser, J., Gruber,

N., Hibbard, K., Hogberg, P., Linder, S., 2000. The global carbon cycle: a test of our knowledge of earth as a system. Science 290, 291–296.

Fanning, K.A., Pilson, M.E., 1974. The diffusion of dissolved silica out of deep-sea sediments. Journal of Geophysical Research: Oceans (1978–2012) 79, 1293–1297.

Flood, R.D., Piper, D., Klaus, A., 1995. Proceedings of the Ocean Drilling Program, Initial Reports. College Station, TX.

Fossing, H., Gallardo, V.A., Jorgensen, B.B., Hüttel, M., Nielsen, L.P., Schulz, H.N., Canfield, D.E., Forster, S., Glud, R.N., Gundersen, J., 1995. Concentration and transport of nitrate by the mat-forming sulphur bacterium Thioploca. Nature 374, 713–715.

Foster, R.A., Subramaniam, A., Mahaffey, C., Carpenter, E.J., Capone, D.G., Zehr, J.P., 2007. Influence of the Amazon River plume on distributions of free-living and symbiotic cyanobacteria in the western tropical north Atlantic Ocean. Limnology and Oceanography 517–532.

François, R., Altabet, M.A., Yu, E.-F., Sigman, D.M., Bacon, M.P., Frank, M., Bohrmann, G., Bareille, G., Labeyrie, L.D., 1997. Contribution of Southern Ocean surface-water stratification to low atmospheric CO2 concentrations during the last glacial period. Nature 389, 929–936.

François, R., Frank, M., Rutgers van der Loeff, M.M., Bacon, M.P., 2004. 230Th normalization: An essential tool for interpreting sedimentary fluxes during the late Quaternary. Paleoceanography 19, PA1018.

François, R., Honjo, S., Krishfield, R., Manganini, S.J., 2002. Factors controlling the

flux of organic carbon to the bathypelagic zone of the ocean. Global Biogeochemical Cycles 16, 1087–1107.

Freudenthal, T., Wagner, T., Wenzhöfer, F., Zabel, M., Wefer, G., 2001. Early diagenesis of organic matter from sediments of the eastern subtropical Atlantic: Evidence from stable nitrogen and carbon isotopes. Geochimica et Cosmochimica Acta 65, 1795–1808.

Froelich, P.N., Atwood, D., Giese, G., 1978. Influence of Amazon River discharge on surface salinity and dissolved silicate concentration in the Caribbean Sea. Deep Sea Research 25, 735–744.

Froelich, P.N., Klinkhammer, G.P., Bender, M.L., Luedtke, N.A., Heath, G.R., Cullen, D., Dauphin, P., Hammond, D.E., Hartman, B., Maynard, V., 1979. Early oxidation of organic matter in pelagic sediments of the eastern equatorial Atlantic: suboxic diagenesis. Geochimica et Cosmochimica Acta 43, 1075–1090.

Funk, J.A., Dobeneck, Von, T., Wagner, T., Kasten, S., 2003. Late quaternary sedimentation and early diagenesis in the Equatorial Atlantic Ocean: Patterns, trends and processes deduced from rock magnetic and geochemical records, in: South Atlantic in the Late Quaternary. Springer, Berlin, pp. 461–497.

Gardner, W.D., Biscaye, P.E., Richardson, M.J., 1997. A sediment trap experiment in the Vema Channel to evaluate the effect of horizontal particle fluxes on measured vertical fluxes. Journal of Marine Research 55, 995–1028.

Gaye, B., Wiesner, M., Lahajnar, N., 2009. Nitrogen sources in the South China Sea, as discerned from stable nitrogen isotopic ratios in rivers, sinking particles, and sediments. Marine Chemistry 114, 72–85.

Gibbs, R., 1972. Water chemistry of the Amazon River. Geochimica et Cosmochimica Acta 36, 1061–1066.

Gibbs, R., 1976. Amazon River sediment transport in the Atlantic Ocean. Geology 4, 45–48.

Goloway, F., Bender, M.L., 1982. Diagenetic models of interstitial nitrate profiles in deep sea suboxic sediments. Limnology and Oceanography 624–638.

Gonzalez-Yajimovich, O., Douglas, R.G., Gorsline, D.S., 2005. The preserved carbonate record in Holocene sediments of the Alfonso and Pescadero basins, Gulf of California. Proceedings of the Geologists Association 116, 315–330.

Gough, M.A., Fauzi, R., Mantoura, C., Preston, M., 1993. Terrestrial plant biopolymers in marine sediments. Geochimica et Cosmochimica Acta 57, 945–964.

Granger, J., Sigman, D.M., 2009. Removal of nitrite with sulfamic acid for nitrate N and O isotope analysis with the denitrifier method. Rapid Communications in Mass Spectrometry 23, 3753–3762.

Green, M.A., Aller, R.C., Cochran, J.K., Lee, C., Aller, J.Y., 2002. Bioturbation in shelf/slope sediments off Cape Hatteras, North Carolina: the use of 234 Th, Chl-a, and Br− to evaluate rates of particle and solute transport. Deep Sea Research Part II: Topical Studies in Oceanography 49, 4627–4644.

Gruber, N., 2004. The dynamics of the marine nitrogen cycle and its influence on atmospheric CO2 variations. The Ocean Carbon Cycle and Climate.

Gruber, N., Sarmiento, J.L., 1997. Global patterns of marine nitrogen fixation and denitrification. Global Biogeochemical Cycles 11, 235–266.

Guinasso, N.L., Schink, D.R., 1975. Quantitative estimates of biological mixing rates

in abyssal sediments. Journal of Geophysical Research: Oceans (1978–2012) 80, 3032–3043.

Gust, G., Byrne, R.H., Bernstein, R.E., Betzer, P.R., Bowles, W., 1992. Particles fluxes and moving fluids: experience from synchronous trap collection in the Sargassso sea. Deep Sea Research Part A. Oceanographic Research Papers 39, 1071–1083.

Hales, B., Emerson, S.R., Archer, D.E., 1994. Respiration and dissolution in the sediments of the western North Atlantic: estimates from models of in situ microelectrode measurements of porewater oxygen and pH. Deep Sea Research I 41, 695–719.

Hamme, R.C., Emerson, S.R., 2004. The solubility of neon, nitrogen and argon in distilled water and seawater. Deep Sea Research Part I: Oceanographic Research Papers 51, 1517–1528.

Hamme, R.C., Severinghaus, J., 2007. Trace gas disequilibria during deep-water formation. Deep Sea Research Part I: Oceanographic Research Papers 54, 939–950.

Hammond, D.E., Cummins, K.M., McManus, J., Berelson, W.M., Smith, G., Spagnoli, F., 2004. Methods for measuring benthic nutrient flux on the California Margin: Comparing shipboard core incubations to in situ lander results. Limnology and Oceanography: Methods.

Hammond, D.E., McManus, J., Berelson, W.M., Kilgore, T.E., Pope, R.H., 1996. Early diagenesis of organic material in equatorial Pacific sediments: stoichiometry and kinetics. Deep Sea Research Part II: Topical Studies in Oceanography 43, 1365–1412.

Hartnett, H.E., Seitzinger, S.P., 2003. High-resolution nitrogen gas profiles in sediment porewaters using a new membrane probe for membrane-inlet mass spectrometry. Marine Chemistry 83, 23–30.

Hedges, J.I., Clark, W.A., Cowie, G.L., 1988. Fluxes and reactivities of organic matter in a coastal marine bay. Limnology and Oceanography 33, 1137–1152.

Hedges, J.I., Clark, W.A., Quay, P.D., Richey, J.E., Devol, A.H., Santos, U. de M., 1986. Compositions and fluxes of particulate organic material in the Amazon River. Limnology and Oceanography 717–738.

Hedges, J.I., Keil, R.G., 1995. Sedimentary organic matter preservation: an assessment and speculative synthesis. Marine Chemistry 49, 81–115.

Heggie, D.T., Maris, C., Hudson, A., Dymond, J., Beach, R., Cullen, J.L., 1987. Organic carbon oxidation and preservation in NW Atlantic continental margin sediments. Geological Society, London, Special Publications 31, 215–236.

Henrichs, S., Reeburgh, W.S., 1987. Anaerobic mineralization of marine sediment organic matter: Rates and the role of anaerobic processes in the oceanic carbon economy. Geomicrobiology Journal 5, 191–237.

Herman, P.M., Soetaert, K., Middelburg, J.J., Heip, C.H.R., Lohse, L., Epping, E., Helder, W., Antia, A.N., Peinert, R., 2001. The seafloor as the ultimate sediment trap—using sediment properties to constrain benthic–pelagic exchange processes at the Goban Spur. Deep Sea Research Part II: Topical Studies in Oceanography 48, 3245–3264.

Hogslund, S., Peter Revsbech, N., Gijs Kuenen, J., Jorgensen, B.B., Gallardo, V.A., van de Vossenberg, J., Nielsen, J.L., Holmkvist, L., Arning, E.T., Peter Nielsen, L., 2009.

Physiology and behaviour of marine Thioploca. The ISME Journal 3, 647.

Holstein, J.M., Hensen, C., 2010. Microbial mediation of benthic biogenic silica dissolution. Geo-Marine Letters 30, 477–492.

Honjo, S., 1980. Material fluxes and modes of sedimentation in the mesopelagic and bathypelagic zones. Journal of Marine Research 38, 53–97.

Howard, M.T., Winguth, A., Klaas, C., Maier-Reimer, E., 2006. Sensitivity of ocean carbon tracer distributions to particulate organic flux parameterizations. Global Biogeochemical Cycles 20.

Hu, C., Montgomery, E., Schmitt, R., Muller-Karger, F.E., 2004. The dispersal of the Amazon and Orinoco River water in the tropical Atlantic and Caribbean Sea: Observation from space and S-PALACE floats. Deep Sea Research Part II 51, 1151–1171.

Huh, C., Ku, T., Luo, S., Landry, M.R., Williams, P.M., 1993. Fluxes of Th isotopes in the Santa Monica Basin, offshore California. Earth and Planetary Science Letters 116, 155–164.

Hulth, S., Aller, R.C., Gilbert, F., 1999. Coupled anoxic nitrification/manganese reduction in marine sediments. Geochimica et Cosmochimica Acta 63, 49–66.

Jahnke, R.A., 1990. Early diagenesis and recycling of biogenic debris at the seafloor, Santa Monica Basin, California. Journal of Marine Research 48, 413–436.

Jahnke, R.A., Emerson, S.R., Murray, J.W., 1982. A model of oxygen reduction, denitrification, and organic matter mineralization in marine sediments. Limnology and Oceanography 27, 610–623.

Jahnke, R.A., Jahnke, D., 2004. Calcium carbonate dissolution in deep sea sediments:

reconciling microelectrode, pore water and benthic flux chamber results. Geochimica et Cosmochimica Acta 68, 47–59.

Jahnke, R.A., Reimers, C.E., Craven, D.B., 1990. Intensification of recycling of organic matter at the sea floor near ocean margins. Nature 348, 50–54.

James, R.H., Palmer, M.R., 2000. Marine geochemical cycles of the alkali elements and boron: the role of sediments. Geochimica et Cosmochimica Acta 64, 3111–3122.

Johns, W.E., Lee, T.N., Beardsley, R.C., Candela, J., Limeburner, R., Castro, B., 1998. Annual cycle and variability of the North Brazil Current. Journal of physical Oceanography 28, 103–128.

Jorgensen, B.B., D'hondt, S., 2006. ECOLOGY: A Starving Majority Deep Beneath the Seafloor. Science 314, 932–934.

Kalil, E., Goldhaber, M., 1973. A sediment squeezer for removal of pore waters without air contact. Journal of Sedimentary Research 43, 553.

Kana, T.M., 2004. Comment on “Comparison of isotope pairing and N 2: Ar methods for measuring sediment denitrification” by BD Eyre, S. Rysgaard, T. Dalsgaard, and P. Bondo Christensen. 2002. Estuaries 25: 1077–1087. Estuaries and Coasts 27, 173–176.

Kana, T.M., Darkangelo, C., Hunt, M., Oldham, J., 1994. Membrane Inlet Mass Spectrometer for Rapid High-Precision Determination of N2, O2, and Ar in environmental water samples. Analytical Chemistry 66, 4166–4170.

Kana, T.M., Sullivan, M., Cornwell, J.C., Groszkowski, K., 1998. Denitrification in estuarine sediments determined by membrane inlet mass spectrometry. Limnology and Oceanography 43, 334–339.

Kappler, A., Pasquero, C., Konhauser, K.O., Newman, D.K., 2005. Deposition of banded iron formations by anoxygenic phototrophic Fe (II)-oxidizing bacteria. Geology 33, 865–868.

Kasten, S., Freudenthal, T., Gingele, F.X., Schulz, H.D., 1998. Simultaneous formation of iron-rich layers at different redox boundaries in sediments of the Amazon deep-sea fan. Geochimica et Cosmochimica Acta 62, 2253–2264.

Kasten, S., Zabel, M., Heuer, V., Hensen, C., 2003. Processes and signals of nonsteady-state diagenesis in deep-sea sediments and their pore waters. The South Atlantic in the Late Quaternary: Reconstruction of material budget and current systems 431–459.

Keil, R.G., Mayer, L., Quay, P.D., Richey, J.E., Hedges, J.I., 1997. Loss of organic matter from riverine particles in deltas. Geochimica et Cosmochimica Acta 61, 1507–1511.

Kineke, G.C., Sternberg, R.W., Trowbridge, J.H., Geyer, W.R., 1996. Fluid-mud processes on the Amazon continental shelf. Continental Shelf Research 16, 667–696.

Knauer, G.A., Martin, J.H., Bruland, K.W., 1979. Fluxes of particulate carbon, nitrogen, and phosphorus in the upper water column of the northeast Pacific. Deep Sea Research Part A. Oceanographic Research Papers 26, 97–108.

Koho, K.A., Piña-Ochoa, E., Geslin, E., Risgaard-Petersen, N., 2010. Vertical migration, nitrate uptake and denitrification: survival mechanisms of foraminifers (Globobulimina turgida) under low oxygen conditions. FEMS Microbiology Ecology 75, 273–283.

Kuehl, S.A., DeMaster, D.J., Nittrouer, C.A., 1986. Nature of sediment accumulation on the Amazon continental shelf. Continental Shelf Research 6, 209–225.

Kuehl, S.A., Fuglseth, T.J., Thunell, R.C., 1993. Sediment mixing and accumulation rates in the Sulu and South China Seas: implications for organic carbon preservation in deep-sea environments. Marine Geology 111, 15–35.

Kuehl, S.A., Nittrouer, C.A., Allison, M.A., Faria, L.E.C., Dukat, D.A., Jaeger, J.M., Pacioni, T.D., Figueiredo, A.G., Underkoffler, E.C., 1996. Sediment deposition, accumulation, and seabed dynamics in an energetic fine-grained coastal environment. Continental Shelf Research 16, 787–815.

la Rocha, de, C., 2003. The Biological Pump, in: Holland, H.D., Turekian, K.K. (Eds.), Treatise on Geochemistry. Elsevier, pp. 84–107.

Lawson, D.S., Hurd, D.C., Pankratz, H.S., 1978. Silica dissolution rates of decomposing phytoplankton assemblages at various temperatures. American Journal of Science 278, 1373–1393.

Lebel, J., Silverberg, N., Sundby, B., 1982. Gravity core shortening and pore water chemical gradients. Deep Sea Research Part A. Oceanographic Research Papers 29, 1365–1372.

Lentz, S.J., Limeburner, R., 1995. The Amazon River plume during AMASSEDS: Spatial characteristics and salinity variability. Journal of Geophysical Research 100, 2355–2375.

Li, Y., Gregory, S., 1974. Diffusion of ions in sea water and in deep-sea sediments. Geochimica et Cosmochimica Acta 38, 703–714.

Liu, K.K., Kaplan, I.R., 1984. Denitrification rates and availability of organic matter in

marine environments. Earth and Planetary Science Letters 68, 88–100.

Liu, K.K., Kaplan, I.R., 1989. The eastern tropical Pacific as a source of 15N-enriched nitrate in seawater off southern California. Limnology and Oceanography 820–830.

Lorenz, F.O., 1987. Teaching about influence in Simple Regression. Teaching Sociology 173–177.

Lyle, M.W., 1983. The brown-green color transition in marine sediments: A marker of the Fe (III)-Fe (II) redox boundary. Limnology and Oceanography 28, 1026–1033.

Mackenzie, F.T., Garrels, R.M., 1966. Chemical mass balance between rivers and oceans. American Journal of Science 264, 507–525.

Mackenzie, F.T., Ristvet, B.L., Thorstenson, D.C., Lerman, A., Leeper, R.H., 1981. Reverse weathering and chemical mass balance in a coastal environment, in: Martin, J., Burton, J.D., Eisma, D. (Eds.), River Inputs From Ocean Systems. United Nations Environmental Programme, United Nations Educational, Scientific, and Cultural Organization, Geneva, Switzerland, pp. 152–187.

Martin, J., Knauer, G., Karl, D.M., Broenkow, W., 1987. VERTEX: carbon cycling in the northeast Pacific. Deep Sea Research Part A. Oceanographic Research Papers 34, 267–285.

Martin, P., Lampitt, R.S., Jane Perry, M., Sanders, R., Lee, C., D'Asaro, E., 2011. Export and mesopelagic particle flux during a North Atlantic spring diatom bloom. Deep Sea Research Part I: Oceanographic Research Papers 58, 338–349.

Martin, W.R., Bender, M.L., 1988. The variability of benthic fluxes and sedimentary

remineralization rates in response to seasonally variable organic carbon rain rates in the deep sea: A modeling study. American Journal of Science 288, 561–574.

Martin, W.R., Bender, M.L., Leinen, M., Orchardo, J., 1991. Benthic organic carbon degradation and biogenic silica dissolution in the central equatorial Pacific. Deep Sea Research Part A. Oceanographic Research Papers 38, 1481–1516.

Martin, W.R., Sayles, F.L., 1996. CaCO3 dissolution in sediments of the Ceara Rise, western equatorial Atlantic. Geochimica et Cosmochimica Acta 60, 243–263.

Martin, W.R., Sayles, F.L., 2004. Organic matter cycling in sediments of the continental margin in the northwest Atlantic Ocean. Deep Sea Research Part I 51, 457–489.

Martin, W.R., Sayles, F.L., 2006. Organic matter oxidation in deep-sea sediments: distribution in the sediment column and implications for calcite dissolution. Deep Sea Research Part II 53, 771–792.

Mcgeary, D., Damuth, J.E., 1973. Postglacial Iron-Rich Crusts in Hemipelagic Deep-Sea Sediment. GSA Bulletin 84, 1201–1212.

Mchatton, S., Barry, J., Jannasch, H.W., Nelson, D.C., 1996. High Nitrate Concentrations in Vacuolate, Autotrophic Marine Beggiatoa spp. Applied and Environmental Microbiology 62, 954–958.

McManus, J., Berelson, W.M., Severmann, S., Poulson, R.L., Hammond, D.E., Klinkhammer, G.P., Holm, C., 2006. Molybdenum and uranium geochemistry in continental margin sediments: Paleoproxy potential. Geochimica et Cosmochimica Acta 70, 4643–4662.

McManus, J., Hammond, D.E., Berelson, W.M., Kilgore, T.E., DeMaster, D.J., Ragueneau, O.G., Collier, R.W., 1995. Early diagenesis of biogenic opal: Dissolution rates, kinetics, and paleoceanographic implications. Deep Sea Research II 42, 871–903.

Meade, R.H., Dunne, T., Richey, J.E., Santos, U. de M., Salati, E., 1985. Storage and remobilization of suspended sediment in the lower Amazon River of Brazil. Science 228, 488–490.

Mercer, J.H., 1972. The lower boundary of the Holocene. Quaternary Research 2, 15–24.

Michalopoulos, P., Aller, R.C., 1995. Rapid clay mineral formation in Amazon delta sediments: reverse weathering and oceanic elemental cycles. Science 614–614.

Michalopoulos, P., Aller, R.C., 2004. Early diagenesis of biogenic silica in the Amazon delta: alteration, authigenic clay formation, and storage. Geochimica et Cosmochimica Acta 68, 1061–1085.

Michalopoulos, P., Aller, R.C., Reeder, R., 2000. Conversion of diatoms to clays during early diagenesis in tropical, continental shelf muds. Geology 28, 1095–1098.

Middelburg, J.J., Meysman, F.J., 2007. Burial at sea. Science (Washington) 316.

Middelburg, J.J., Soetaert, K., Herman, P.M., Heip, C.H.R., 1996. Denitrification in marine sediments: A model study. Global Biogeochemical Cycles 10, 661–673.

Middelburg, J.J., Vlug, T., Jaco, F., Van Der Nat, W.A., 1993. Organic matter mineralization in marine systems. Global and Planetary Change 8, 47–58.

Mikaloff Fletcher, S.E., Gruber, N., Jacobson, A.R., Gloor, M., Doney, S.C., Dutkiewicz, S., Gerber, M., Follows, M.J., Joos, F., Lindsay, K., Menemenlis, D., Mouchet, A.,

Müller, S.A., Sarmiento, J.L., 2007. Inverse estimates of the oceanic sources and sinks of natural CO 2and the implied oceanic carbon transport. Global Biogeochemical Cycles 21, GB1010–19.

Milliman, J.D., Meade, R.H., 1983. World-wide delivery of river sediment to the oceans. The Journal of Geology 1–21.

Milliman, J.D., Summerhayes, C., Barretto, H., 1975. Quaternary sedimentation on the Amazon continental margin: a model. Bulletin of the Geological Society of America 86, 610–614.

Montoya, J.P., Carpenter, E.J., Capone, D.G., 2002. Nitrogen fixation and nitrogen isotope abundances in zooplankton of the oligotrophic North Atlantic. Limnology and Oceanography 47, 1617–1628.

Moré, J.J., Sorensen, D.C., 1983. Computing a trust region step. SIAM Journal on Scientific and Statistical Computing 4, 553–572.

Mortazavi, E., 2012. Western Equatorial Atlantic Sedimentation: A Study of Magnetic Properties. University of Southern California, Los Angeles.

Mörner, N.-A., 1976. The Pleistocene/Holocene boundary: a proposed boundary-stratotype in Gothenburg, Sweden. Boreas 5, 193–275.

Muller-Karger, F.E., Mcclain, C., Richardson, P.L., 1988. The dispersal of the Amazon's water. Nature 333, 56–59.

Muller-Karger, F.E., Richardson, P.L., McGillicuddy, D., 1995. On the offshore dispersal of the Amazon's Plume in the North Atlantic: Comments on the paper by A. Longhurst,'Seasonal cooling and blooming in tropical oceans'. Deep Sea Research Part I: Oceanographic Research Papers 42, 2127–2137.

Nakatsuka, T., Handa, N., Harada, N., Sugimoto, T., Imaizumi, S., 1997. Origin and decomposition of sinking particulate organic matter in the deep water column inferred from the vertical distributions of its δ15N, δ13C and δ14C. Deep-sea research. Part 1. Oceanographic research papers 44, 1957–1979.

Neumann, G., 1969. Seasonal salinity variations in the upper Strata of the western tropical Atlantic Ocean - Sea surface salinities. Deep Sea Research Supplement to Vol 16, 165–177.

Nittrouer, C.A., Kuehl, S.A., Sternberg, R.W., Figueiredo, A.G., 1995. An introduction to the geological significance of sediment transport and accumulation on the Amazon continental shelf. Marine Geology 125, 177–192.

Opsahl, S., Benner, R., 1997. Distribution and cycling of terrigenous dissolved organic matter in the ocean. Nature 386, 480–482.

Otte, S., Kuenen, J.G., Nielsen, L.P., Paerl, H.W., Zopfi, J., Schulz, H.N., Teske, A., Strotmann, B., Gallardo, V.A., Jorgensen, B.B., 1999. Nitrogen, Carbon, and Sulfur Metabolism in Natural Thioploca Samples. Applied and Environmental Microbiology 65, 3148–3157.

Passow, U., Carlson, C.A., 2012. The biological pump in a high CO 2 world. Marine Ecology Progress Series 470, 249–271.

Perry, G.D., Duffy, P.B., Miller, N.L., 1996. An extended data set of river discharges for validation of general circulation models. Journal of Geophysical Research: Oceans (1978–2012) 101, 21339–21349.

Pfannkuche, O., 1993. Benthic response to the sedimentation of particulate organic matter at the BIOTRANS station, 47ºN, 20ºW. Deep Sea Research II 40, 135–149.

Piña-Ochoa, E., 2010. Supplemental Information.

Piña-Ochoa, E., Hogslund, S., Geslin, E., Cedhagen, T., Revsbech, N.P., Nielsen, L.P., Schweizer, M., Jorissen, F.J., Rysgaard, S., Risgaard-Petersen, N., 2010. Widespread occurrence of nitrate storage and denitrification among Foraminifera and Gromiida. Proceedings of the National Academy of Sciences 107, 1148–1153.

Postma, D., 1985. Concentration of Mn and separation from Fe in sediments—I. Kinetics and stoichiometry of the reaction between birnessite and dissolved Fe (II) at 10 C. Geochimica et Cosmochimica Acta 49, 1023–1033.

Premuzic, E.T., Benkovitz, C.M., Gaffney, J.S., Walsh, J.J., 1982. The nature and distribution of organic matter in the surface sediments of world oceans and seas. Organic Geochemistry 4, 63–77.

Prokopenko, M.G., Hammond, D.E., Berelson, W.M., Bernhard, J.M., Stott, L., Douglas, R.G., 2006. Nitrogen cycling in the sediments of Santa Barbara basin and Eastern Subtropical North Pacific: Nitrogen isotopes, diagenesis and possible chemosymbiosis between two lithotrophs (Thioploca and Anammox)—"riding on a glider." Earth and Planetary Science Letters 242, 186–204.

Prokopenko, M.G., Sigman, D.M., Berelson, W.M., Hammond, D.E., Barnett, B.A., Chong, L.S., Townsend-Small, A., 2011. Denitrification in anoxic sediments supported by biological nitrate transport. Geochimica et Cosmochimica Acta 75, 7180–7199.

Rabouille, C., Gaillard, J.-F., Treguer, P., Vincendeau, M.-A., 1997. Biogenic silica recycling in surficial sediments across the Polar Front of the Southern Ocean

(Indian Sector). Deep Sea Research Part II: Topical Studies in Oceanography 44, 1151–1176.

Rama, M.K., Goldberg, E.D., 1961. Lead-210 in natural waters. Science 134, 98–99.

Rauch, J.N., Pacyna, J.M., 2009. Earth's global Ag, Al, Cr, Cu, Fe, Ni, Pb, and Zn cycles. Global Biogeochemical Cycles 23.

Raymond, P.A., Cole, J.J., 2003. Increase in the export of alkalinity from North America's largest river. Science 301, 88–91.

Redfield, A., 1934. On the proportions of organic derivatives in sea water and their relation to the composition of plankton. University Press of Liverpool, Liverpool, UK.

Redfield, A., Ketchum, B., Richards, F.A., 1963. The influence of organisms on the composition of sea water, in: The Sea, Ideas and Observations on the Progress in the Study of the Seas. Interscience, pp. 26–77.

Reimer, P.J., Baillie, M.G., Bard, E., Bayliss, A., Beck, J.W., Blackwell, P.G., Ramsey, C.B., Buck, C.E., Burr, G.S., Edwards, R.L., 2009. IntCal09 and Marine09 radiocarbon age calibration curves, 0–50,000 years cal BP. Radiocarbon 51, 1111–1150.

Reimers, C.E., Jahnke, R.A., McCorkle, D.C., 1992. Carbon fluxes and burial rates over the continental slope and rise off central California with implications for the global carbon cycle. Global Biogeochemical Cycles 6, 199–224.

Rhoads, D.C., 1974. Organism-sediment relations on the muddy sea floor, in: Oceanography and Marine Biology: an Annual Review. Aberdeen University Press, pp. 263–300.

Richey, J.E., Hedges, J.I., Devol, A.H., Quay, P.D., 1990. Biogeochemistry of carbon in

the Amazon River. Limnology and Oceanography 35, 352–371.

Risgaard-Petersen, N., Langezaal, A.M., Ingvardsen, S., Schmid, M.C., Jetten, M.S.M., Op Den Camp, H.J.M., Derksen, J.W.M., Piña-Ochoa, E., Eriksson, S.P., Peter Nielsen, L., Peter Revsbech, N., Cedhagen, T., van der Zwaan, G.J., 2006. Evidence for complete denitrification in a benthic foraminifer. Nature 443, 93–96.

Ristvet, B.L., 1978. Reverse weathering reactions within recent nearshore marine sediments, Kaneohe Bay, Oahu. University of Hawaii, Honolulu.

Salisbury, J., Vandemark, D., Campbell, J., Hunt, C., Wisser, D., Reul, N., Chapron, B., 2011. Spatial and temporal coherence between Amazon River discharge, salinity, and light absorption by colored organic carbon in western tropical Atlantic surface waters. Journal of Geophysical Research: Oceans (1978–2012) 116.

Sayama, M., Risgaard-Petersen, N., Nielsen, L.P., Fossing, H., Christensen, P.B., 2005. Impact of Bacterial NO3- Transport on Sediment Biogeochemistry. Applied and Environmental Microbiology 71, 7575–7577.

Sayles, F.L., 1979. The composition and diagenesis of interstitial solutions--I. Fluxes across the seawater-sediment interface in the Atlantic Ocean. Geochimica et Cosmochimica Acta 43, 527–545.

Sayles, F.L., Deuser, W.G., Goudreau, J.E., DIckinson, W.H., Jickells, T.D., King, P., 1996. The benthic cycle of biogenic opal at the Bermuda Atlantic Time Series site. Deep Sea Research Part I: Oceanographic Research Papers 43, 383–409.

Sayles, F.L., Martin, W.R., Deuser, W.G., 1994. Response of benthic oxygen demand to particulate organic carbon supply in the deep sea near Bermuda.

Schlitzer, R., 2002. Carbon export fluxes in the Southern Ocean: Results from inverse modeling and comparison with satellite-based estimates. Deep Sea Research Part II: Topical Studies in Oceanography 49, 1623–1644.

Schlünz, B., Schneider, R.R., Müller, P.J., Showers, W.J., 1999. Terrestrial organic carbon accumulation on the Amazon deep sea fan during the last glacial sea level low stand. Chemical Geology 159, 263–281.

Schneider, B., Schlitzer, R., Fischer, G., Nöthig, E.-M., 2003. Depth-dependent elemental compositions of particulate organic matter (POM) in the ocean. Global Biogeochemical Cycles 17, 1032.

Schulz, H.D., Dahmke, A., Schinzel, U., Wallmann, K., Zabel, M., 1994. Early diagenetic processes, fluxes, and reaction rates in sediments of the South Atlantic. Geochimica et Cosmochimica Acta 58, 2041–2060.

Schulz, H.D., Zabel, M., 2000. Marine Geochemistry. Springer-Verlag.

Schulz, H.N., 1999. Dense Populations of a Giant Sulfur Bacterium in Namibian Shelf Sediments. Science 284, 493–495.

Seiter, K., 2005. Benthic carbon mineralization on a global scale. Global Biogeochemical Cycles 19, 1–26.

Seiter, K., Hensen, C., Schröter, J., Zabel, M., 2004. Organic carbon content in surface sediments—defining regional provinces. Deep Sea Research Part I: Oceanographic Research Papers 51, 2001–2026.

Shipe, R.F., Curtaz, J., Subramaniam, A., Carpenter, E.J., Capone, D.G., 2006. Diatom biomass and productivity in oceanic and plume-influenced waters of the western tropical Atlantic ocean. Deep Sea Research Part I: Oceanographic

Research Papers 53, 1320–1334.

Showers, W.J., Angle, D.G., 1986. Stable isotopic characterization of organic carbon accumulation on the Amazon continental shelf. Continental Shelf Research 6, 227–244.

Siegel, D.A., Deuser, W.G., 1997. Trajectories of sinking particles in the Sargasso Sea: Modeling of statistical funnels above deep-ocean sediment traps. Deep Sea Research Part I: Oceanographic Research Papers 44, 1519–1541.

Siegel, D.A., Granata, T.C., Michaels, A.F., Dickey, T.D., 1990. Mesoscale eddy diffusion, particle sinking, and the interpretation of sediment trap data. Journal of Geophysical Research 95, 5305–5311.

Sigman, D.M., Granger, J., DiFiore, P.J., Lehmann, M.M., Ho, R., Cane, G., Van Geen, A., 2005. Coupled nitrogen and oxygen isotope measurements of nitrate along the eastern North Pacific margin. Global Biogeochemical Cycles 19, GB4022.

Silver, M.W., Gowing, M.M., 1991. The "particle" flux: origins and biological components. Progress in Oceanography 26, 75–113.

Silverberg, N., Martínez, A., Aguíñiga, S., Carriquiry, J.D., Romero, N., Shumilin, E., Cota, S., 2004. Contrasts in sedimentation flux below the southern California Current in late 1996 and during the El Niño event of 1997–1998. Estuarine, Coastal and Shelf Science 59, 575–587.

Smith, K.L., Jr, Baldwin, R.J., 1984. Seasonal fluctuations in deep-sea sediment community oxygen consumption: central and eastern North Pacific. Nature 307, 624–626.

Smith, M.S., Zimmerman, K., 1981. Nitrous Oxide Production by Nondenitrifying Soil

Nitrate Reducers. Soil Science Society of America Journal 45, 865.

Smith, S.M., Hitchcock, G.L., 1994. Nutrient enrichments and phytoplankton growth in the surface waters of the Louisiana Bight. Estuaries 17, 740–753.

Smith, W.O., Jr, DeMaster, D.J., 1996. Phytoplankton biomass and productivity in the Amazon River plume: correlation with seasonal river discharge. Continental Shelf Research 16, 291–319.

Smoak, J.M., DeMaster, D.J., Kuehl, S.A., Pope, R.H., McKee, B.A., 1996. The behavior of particle-reactive tracers in a high turbidity environment: 234 Th and 210 Pb on the Amazon continental shelf. Geochimica et Cosmochimica Acta 60, 2123–2137.

Stanley, R.H., Buesseler, K.O., Manganini, S.J., Steinberg, D.K., Valdes, J.R., 2004. A comparison of major and minor elemental fluxes collected in neutrally buoyant and surface-tethered sediment traps. Deep Sea Research Part I: Oceanographic Research Papers 51, 1387–1395.

Stephens, M.P., Kadko, D.C., Smith, C.R., Latasa, M., 1997. Chlorophyll-a and pheopigments as tracers of labile organic carbon at the central equatorial Pacific seafloor. Geochimica et Cosmochimica Acta 61, 4605–4619.

Stramma, L., England, M., 1999. On the water masses and mean circulation of the South Atlantic Ocean. Journal of Geophysical Research 104, 20863–20–883.

Straub, K.L., Benz, M., Schink, B., Widdel, F., 1996. Anaerobic, nitrate-dependent microbial oxidation of ferrous iron. Applied and Environmental Microbiology 62, 1458–1460.

Strickland, J., 1968. A practical handbook of seawater analysis. Fisheries Research Board of Canada, Halifax.

Strickland, J.D.H., Parsons, T.R., 1972. A Practical Handbook of Seawater Analysis. Fisheries Research Board of Canada, Ottowa, Canada.

Stuiver, M., Braziunas, T.F., 1993. Modeling atmospheric (super 14) C influences and (super 14) C ages of marine samples to 10,000 BC. Radiocarbon 35, 137–189.

Stuiver, M., Reimer, P.J., 1993. Extended 14C data base and revised Calib 3.0 14C age calibration program [WWW Document]. Radiocarbon. URL https://www.google.com/url?sa=t&rct=j&q=&esrc=s&source=web&cd=2&cad=rja&ved=0CDsQFjAB&url=https%3A%2F%2Fjournals.uair.arizona.edu%2Findex.php%2Fradiocarbon%2Farticle%2Fdownload%2F1561%2F1565&ei=kfI3UcnhIsTfyQHlqoC4Bg&usg=AFQjCNFh09fJJfNVmqkzejE-vmRrcNEFPw&bvm=bv.43287494,d.aWc (accessed 3.6.13).

Subramaniam, A., Yager, P.L., Carpenter, E.J., Mahaffey, C., Björkman, K.M., Cooley, S.R., Kustka, A., Montoya, J.P., Sañudo-Wilhelmy, S.A., Shipe, R.F., Capone, D.G., 2008. Amazon River enhances diazotrophy and carbon sequestration in the tropical North Atlantic Ocean. Proceedings of the National Academy of Sciences of the United States of America 105, 10460–10465.

Sun, M.-Y., Lee, C., Aller, R.C., 1993. Laboratory studies of oxic and anoxic degradation of chlorophyll- a in Long Island Sound sediments. Geochimica et Cosmochimica Acta 57, 147–157.

Takahashi, T., Sutherland, S.C., Sweeney, C., Poisson, A., Metzl, N., Tilbrook, B., Bates, N.R., Wanninkhof, R., Feely, R.A., Sabine, C., 2002. Global sea-air CO2 flux based on climatological surface ocean pCO2, and seasonal biological and temperature effects. Deep Sea Research Part II: Topical Studies in Oceanography 49, 1601–

1622.

Teal, L.R., Bulling, M.T., Parker, E.R., Solan, M., 2008. Global patterns of bioturbation intensity and mixed depth of marine soft sediments. Aquatic Biology 2, 207–218.

Ternon, J., Oudot, C., Dessier, A., Diverres, D., 2000. A seasonal tropical sink for atmospheric CO2 in the Atlantic Ocean: the role of the Amazon River discharge. Marine Chemistry 68, 183–201.

Thamdrup, B., 2012. New Pathways and Processes in the Global Nitrogen Cycle. Annu. Rev. Ecol. Evol. Syst. 43, 407–428.

Thamdrup, B., Canfield, D.E., 1996. Pathways of carbon oxidation in continental margin sediments off central Chile. Limnology and Oceanography 41, 1629–1650.

Thomson, J., Colley, S., Anderson, R.F., Cook, G.T., Mackensen, A., 1993. 210 Pb in the sediments and water column of the Northeast Atlantic from 47 to 59° N along 20° W. Earth and Planetary Science Letters 115, 75–87.

Thomson, J., Wallace, H.E., Colley, S., Toole, J., 1990. Authigenic uranium in Atlantic sediments of the last glacial stage—a diagenetic phenomenon. Earth and Planetary Science Letters 98, 222–232.

Tiedje, J.M., 1988. Ecology of denitrification and dissimilatory nitrate reduction to ammonium, in: Zehnder, J. (Ed.), Biology of Anaerobic Microorganisms. John Wiley & Sons, pp. 179–244.

Ullman, W., Aller, R.C., 1982. Diffusion coefficients in nearshore marine sediments. Limnology and Oceanography 27, 552–556.

Van Cappellen, P., Qiu, L., 1997. Biogenic silica dissolution in sediments of the

Southern Ocean. I. Solubility. Deep Sea Research Part II: Topical Studies in Oceanography 44, 1109–1128.

Van Geen, A., 2003. On the preservation of laminated sediments along the western margin of North America. Paleoceanography 18, 1098.

Volk, T., Hoffert, M.L., 1984. Ocean carbon pumps - Analysis of relative strengths and efficiencies in ocean-driven atmospheric CO2 changes, in:. Presented at the The carbon cycle and atmospheric CO2: Natural variations archean to present; Proceedings of the Chapman Conference on Natural Variations in Carbon Dioxide and the Carbon Cycle, Tarpon Springs, FL, January 9-13, 1984 (A86-39426 18-46), Tarpon Springs, FL, pp. 99–110.

Ward, B.B., Tuit, C.B., Jayakumar, A., Rich, J.J., Moffett, J., Naqvi, S.W.A., 2008. Organic carbon, and not copper, controls denitrification in oxygen minimum zones of the ocean. Deep Sea Research Part I: Oceanographic Research Papers 55, 1672–1683.

Ward, N.D., Keil, R.G., Medeiros, P.M., Brito, D.C., Cunha, A.C., Dittmar, T., Yager, P.L., Krusche, A.V., Richey, J.E., 2013. Degradation of terrestrially-derived lignin macromolecules in the Amazon River. Nature Geoscience.

Weber, K.A., Picardal, F.W., Roden, E.E., 2001. Microbially Catalyzed Nitrate-Dependent Oxidation of Biogenic Solid-Phase Fe(II) Compounds. Environ. Sci. Technol. 35, 1644–1650.

Weiss, R., 1970. The solubility of nitrogen, oxygen and argon in water and seawater. Deep Sea Research and Oceanographic Abstracts 17, 721–735.

Wells, J., Coleman, J., 1981. Periodic mudflat progradation, northeastern coast of

South America; a hypothesis. Journal of Sedimentary Research 51, 1069.

Wenzhöfer, F., Glud, R.N., 2002. Benthic carbon mineralization in the Atlantic: a synthesis based on in situ data from the last decade. Deep Sea Research Part I 49, 1255–1279.

Wenzhöfer, F., Holby, O., Kohls, O., 2001. Deep penetrating benthic oxygen profiles measured in situ by oxygen optodes. Deep Sea Research I 48, 1741–1755.

WOCE Data Products Committee, 2002. WOCE Global Data, Version 3.0. WOCE International Project Office.

Wollast, R., 1998. Evaluation and comparison of the global carbon cycle in the coastal zone and in the open ocean. The sea 10, 213–252–252.

Yamagishi, H., Westley, M.B., Popp, B.N., Toyoda, S., Yoshida, N., Watanabe, S., Koba, K., Yamanaka, Y., 2007. Role of nitrification and denitrification on the nitrous oxide cycle in the eastern tropical North Pacific and Gulf of California. Journal of Geophysical Research 112, G02015.

Yeung, L.Y., Berelson, W.M., Young, E.D., Prokopenko, M.G., Rollins, N., Coles, V.J., Montoya, J.P., Carpenter, E.J., Steinberg, D.K., Foster, R.A., Capone, D.G., Yager, P.L., 2012. Impact of diatom-diazotroph associations on carbon export in the Amazon River plume. Geophysical Research Letters 39, L18609.

Zehr, J.P., Ward, B.B., 2002. Nitrogen Cycling in the Ocean: New Perspectives on Processes and Paradigms. Applied and Environmental Microbiology 68, 1015–1024.

Zopfi, J., Kjar, T., Nielsen, L.P., Jorgensen, B.B., 2001. Ecology of Thioploca spp.: Nitrate and Sulfur Storage in Relation to Chemical Microgradients and Influence

of Thioploca spp. on the Sedimentary Nitrogen Cycle. Applied and Environmental Microbiology 67, 5530–5537.

Supplemental Information to Chapter 2

A.1 COMPARISON OF OLW DATA TO THE WOCE DATABASE

OLW $Si(OH)_4$ and NO_3^- from the WCS and Rhizon samples was compared to deep water samples in the WOCE database (WOCE Data Products Committee, 2002).

A1.1 OLW NO_3^- vs water depth

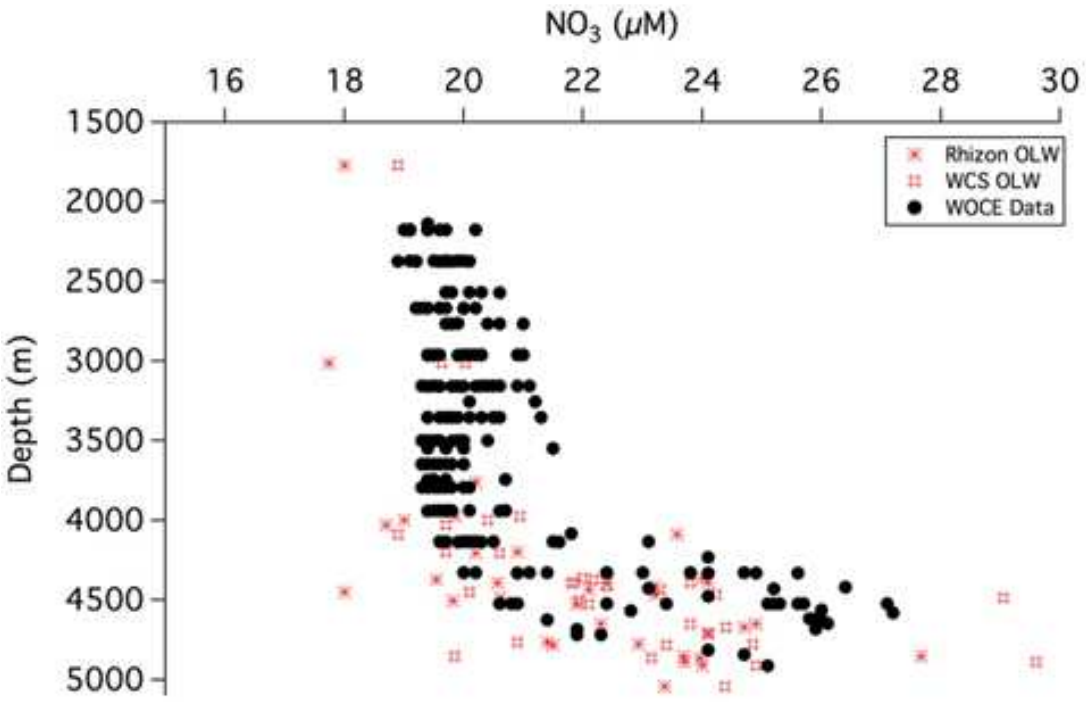

A1.2 OLW $Si(OH)_4$ vs water depth

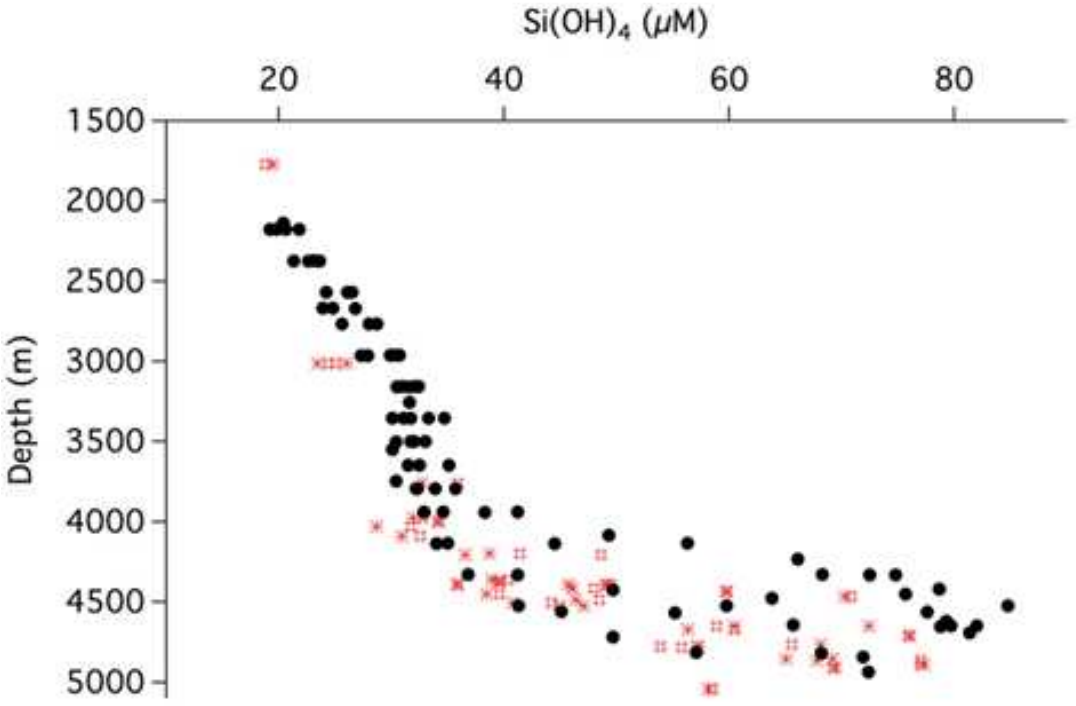

A.2 THE NO_3^- MODEL MATLAB® CODE

The matlab code below is prepared for the 3-layer model applied to station 2011-3.

```
function numeric_a11s3_t3

%Numeric 2 carbon model, AN2011 station 3

%define the constants, etc
global Gm N0 xhat p xmin xmax Dno3 g2 pfinal DO2 O2zero m1 m2 m3 porosity Dn_swi
Dsedo por_prime xm
tic
%Data - column 1 is depth, column 2 is concentration in umol/cm3
Data = ...
[0      0.02
0.29  0.0253
0.92  0.0291
1.91  0.0278
```

```
3.81  0.0310
5.72  0.0335
11.42   0.0310
13.32   0.0267
15.23   0.0225
18.08   0.0180
22.85   0.0096
27.61   0.0043
32.37   0.0007
37.13   0.0004
41.90   0.0004];

%Error from the measurements of each data point
Error = ...
[9.04797E-05
 0.000241871
 4.63002E-05
 2.1765E-05
 0.000220982
 0.000169815
 0.000147274
 0.000289288
 0.000183732
 0.000121047
 1.46259E-06
 3.23007E-05
 0.000112165
 0.000212054
 0.000104576];

%Manganese data
Mn=[0.0000
        0.0000
        0.0000
        0.0000
        0.0000
        0.0000
        0.0031
        0.0131
        0.0251
        0.0352
        0.0418
        0.0548
        0.0649];
Mndepth=[0
            1.905
            3.81
            5.72
            11.42
            13.32
            15.23
```

```
            18.08
            22.85
            27.61
            32.37
            37.13
            41.90];

xdata = Data(:,1);
ydata = Data(:,2);
xmin=min(Data(:,1));
xmax=max(Data(:,1));
ymax = max(Data(:,2));

%concentration gradient at deepest depth
Gm = (Data(end-1,2)-Data(end,2))/(Data(end-1,1)-Data(end,1));

%Static parameters
Dno3=1.05e-05; %molecular diffusion of NO3 cm2/sec
DO2=1.2e-05; %molecular diffusion of O2 cm2/sec
O2zero=.240; %concentration of O2 at SWI
N0=0.022;  %NO3 concentration at the surface
g2 = .1; %gamma2 the ratio of NO3:O2
xhat = 18.4;%Lower boundary of NO3 production
xm=22.85;%Upper boundary of NO3 consumption
m1=.74661; %m1 - m3 are fitting parameters for porosity
m2=.15658;
m3=.14947;

%vector of initial guesses for the parameters
p = [-.00000001 .3 -.00000001 .7 -.0000001 .2]; %initial guess for parameters p1-6
%parameter bounds
lb = [-1e-05 .01 -1e-6 .01 -1e-04 .001];
ub = [-1e-10 3.5 -1e-12 3.5 -1e-12 2];

%setup for global optimization
problem =
createOptimProblem('lsqcurvefit','objective',@fitN,'xdata',xdata,'ydata',ydata,'x0',p,'lb',lb,'
ub',ub,'options',optimset('Algorithm','trust-region-reflective','TolX',1e-14,'TolFun',1e-14))

[pfinal fval]=lsqcurvefit(problem)

ms = MultiStart('Display','iter','PlotFcns',{@NumberToNextBest,@gsplotbestf});

[pfinal fval output solutions manymins] = run(ms,problem,30)

%Figures to show the result of each run and the best three %results
figure;hist([manymins.Fval])
pvalues=manymins.X
bestf=[manymins.Fval];
figure;hist(bestf(1:3))
```

```
%Setup to fit the data with the solution of the ODE
options=optimset('FunValCheck','on','MaxIter',5000,'MaxFunEvals',4000,'TolX',1e-
14,'Tolfun',1e-14);

[pfinal,resnorm,exitflag,output]=lsqcurvefit(@fitN,p,xdata,ydata,lb,ub,options);

pfinal
xlswrite('pfinal.xls',pfinal); %save final parameters

%Plot output of lsqcurvefit
xsim = linspace(xmin,xmax,100);
yout = fitN(pfinal,xsim);
xsim2=xsim';

xnitr=linspace(xmin,xhat,100);
yout2= fitN(pfinal,xnitr);

xnitr2=linspace(xmin,xhat,500);

Nconc=[xsim2(:,1),yout(:,1)];
save NO3concentration Nconc
xlswrite('No3conc.xls',Nconc);

% Calculation of the diffusive flux and integrated flux for %nitrification
Pnitr=@(x) pfinal(1,1)*exp(-pfinal(1,2)*x)+ pfinal(1,3)*exp(-pfinal(1,4)*x) ;
Pnitr2 = m1*pfinal(1,1).*exp(-pfinal(2)*xnitr2)+m1*pfinal(1,3).*exp(-
pfinal(4)*xnitr2)+m2*pfinal(1,1).*exp(-m3*xnitr2).*exp(-
pfinal(2)*xnitr2)+m2*pfinal(1,3).*exp(-m3*xnitr2).*exp(-pfinal(4)*xnitr2);

Pxn2 = SWIporosity^3*Dno3*((Nconc(1,2)-Nconc(2,2))/(Nconc(1,1)-Nconc(2,1)));
Pxn3 = trapz(xnitr2,Pnitr2);

Rn2=-Pxn2*10*60*60*24
Rn3 = Pxn3*60*60*24*10*g2
CtoN=6.95
Cn= Rn*CtoN
Ro = -Rn3/g2

%Calculate the depth integrated reaction rate for denitrification
xdenitr=linspace(xm,xmax,500);
yout3=fitN(pfinal,xdenitr);

Pxd = pfinal(1,5)*yout3'.*exp(-xdenitr.*pfinal(1,6)).*(m1+m2.*exp(-m3*xdenitr));
Px2=trapz(xdenitr,Pxd);

Rdenitr=Px2*60*60*24*10*g2
Ctotal=(Rn3*(CtoN))+(Rdenitr*1.02)

%plot the solution to the ODE from bvp4c
figure
clf
```

```
plot(xsim,yout,'b-',xnitr,yout2,'r--');
hold on
plot(xdata,ydata,'go');
xlabel('Depth')
ylabel('Nitrate (mol/cm3)')
legend('Nitrate model a','Nitrate model b','Nitrate data')

print('-depsc2','-r300','model.eps')

%Chisquare
obs_depth = Data(:,1);
observable=Data(:,2);
model=fitN(pfinal,obs_depth);
Error;
Rawr= ((observable-model)/Error);
[row,col]=find(Rawr);
Rawr2=Rawr(:,col(1,1));
Rawr3=Rawr2.^2;

Chisquare=(sum(Rawr3))
Red_Chisquare = Chisquare/(length(Data)-6)

results=[Rn2 Rn3 CtoN Cn Ro Rdenitr Ctotal Chisquare Red_Chisquare];
%save results results
xlswrite('results.xls',results);

%solve differential for oxygen
solinitO2 = bvpinit(linspace(xmin,xmax,500),[0.240,0]);
solO2 = bvp4c(@odeO2, @bcO2, solinitO2);

O2x=linspace(xmin,xmax,100);
O2 = deval(solO2,O2x);
O2conc=O2(1,:)';
O2depth=O2x(1,:)';
O2conc2=[O2conc O2depth];
%save O2concentration O2conc2
xlswrite('O2concentration.xls',O2conc2);

oxygen=O2(1,:);

figure
clf
plot (O2x,oxygen,'r-')
hold on
plot (Mndepth, Mn, 'bo')
axis([xmin xmax 0 .250])
xlabel('Depth')
ylabel('Oxygen')

print('-depsc2','-r300','oxygen.eps')
toc
```

```
%ODE for O2
function dO2dx = odeO2(x,y)
global Gm N0 xhat pfinal xmin xmax DO2 O2zero Dno3 g2 m1 m2 m3 porosity Dn_swi
Dsedo por_prime xm
pfinalO = pfinal./(g2);
PO2 = (pfinal(1)*exp(-pfinal(2)*x)+ pfinal(3)*exp(-pfinal(4)*x) );

dO2dx= [y(2); -(3/porosity)*por_prime*y(2) - (1/(porosity^.6*DO2))* PO2];

function boundary = bcO2(ya,yb)
global Gm N0 xhat p xmin xmax DO2 pfinal O2zero m1 m2 m3 porosity Dsedo
por_prime Dn_swi xm
boundary = [ya(1) - O2zero
                    yb(2)];

%connects bvp4c to lsqcurvefit
function F = fitN(x,xdata)
global Gm N0 xhat p xmin xmax Dno3 g2 m1 m2 m3 porosity Dn_swi Dsedo por_prime
xm

p=x;
options= bvpset('Stats','off','RelTol',1e-7,'abstol',1e-7);
solinit = bvpinit(linspace(xmin,xmax,100),[0.022,0.03]);
sol = bvp4c(@ode, @bc, solinit,options);

ydata_sim = deval(sol,xdata)'; %evaluates solution of bvp at the xdata points
F = ydata_sim(:,1);

%The ODE for Nitrogen
function dydx = ode(x,y)
global Gm N0 xhat p xmin xmax Dno3 g2 m1 m2 m3 porosity Dn_swi Dsedo por_prime
xm

f=zeros(length(x),1);
for i=1:length(x)
if (x(i) <= xhat)
A = 1;
B= 1;
elseif (x(i) >= xm)
A = 0;
B=1;
else
A = 0;
B=0;
end
end

porosity = m1 + m2*(exp(-m3*x(i))); %porosity fitting equation (either parabolic or
exponential)
por_prime = -m2*m3*(exp(-m3*x(i)));
```

```
P = ((A))*(p(1,1)*exp(-p(1,2)*x(i))+ p(1,3)*exp(-p(1,4)*x(i)) )- ((1-A))*(p(1,5)*exp(-
p(1,6)*x(i)))*y(1);

dydx= [y(2); -(3/porosity)*por_prime*y(2) + g2*(1/(porosity.^.6*Dno3))*P*B];

%The boundary conditions for Nitrogen
function boundary = bc(ya,yb)
global Gm N0 xhat p xmin xmax Dno3 g2 m1 m2 m3 porosity Dn_swi Dsedo por_prime
xm
boundary = [ya(1) - N0
yb(2)- Gm];

%ya(2) - .021138

%Code for mid-run figures
function stop = NumberToNextBest(optimValues, state)
persistent bestfv bestcounter

stop = false;
switch state
case 'init'
% Initialize variable to record best function value.
bestfv = [];

% Initialize counter to record number of
% local solver runs to find next best minimum.
bestcounter = 1;

% Create the histogram.
bar(log(bestcounter),'tag','NumberToNextBest');
xlabel('Number of New Best Fval Found');
ylabel('Log Number of Local Solver Runs');
title('Number of Local Solver Runs to Find Lower Minimum')
case 'iter'
% Find the axes containing the histogram.
NumToNext = ...
findobj(get(gca,'Children'),'Tag','NumberToNextBest');

% Update the counter that records number of local
% solver runs to find next best minimum.
if ~isequal(optimValues.bestfval, bestfv)
bestfv = optimValues.bestfval;
bestcounter = [bestcounter 1];
else
bestcounter(end) = bestcounter(end) + 1;
end

% Update the histogram.
set(NumToNext,'Ydata',log(bestcounter))
end
```

A.3 2-CARBON MODEL VS. 1-CARBON MODEL

The 2-carbon model was employed here following prior work (Goloway and Bender, 1982; Hales et al., 1994; Hammond et al., 1996; Martin and Sayles, 2006; 2004; 1996). The 2-carbon model produced a better model fit than a 1-carbon model, as shown by the table below, where nearly every station results in a lower reduced χ^2 value by using the 2-carbon model. '#-rhiz' refer to stations where a better fit was obtained after omitting WCS data – see 'Pore water models – Nitrate' from Chapter 2.

Year	Station	Model	2C Model Red-χ^2	1C Model Red-χ^2
2010	1	2L	5.8	10
2010	1-rhiz	2L	3.1	
2010	5	2L	9.7	7.4
2010	5	3L	7.1	
2010	6	2L	17	21
2010	6	3L	16	
2010	7	2L	0.6	2.0
2010	7-rhiz	2L	1.7	
2010	9	2L	32	36
2010	9	3L	33	
2010	19	2L	1.2	15
2010	19-rhiz	2L	3.7	
2010	20	2L	72	147
2010	20	3L	125	
2010	21	2L	174	392
2010	21	3L	192	
2010	23	2L	7.1	0.1
2010	23	3L	0.1	
2010	25	2L	27	27
2010	35	3L	65	
2010	26	2L	106	65

2010	27	2L	20	223
2011	1	2L	3.8	33
2011	3	2L	45	51
2011	3	3L	15	
2011	6	2L	23	67
2011	6	3L	24	
2011	8	2L	38	105
2011	8	3L	261	
2011	9	2L	6.0	10
2011	9	3L	6.1	
2011	13	2L	64	85
2011	13	3L	100	
2011	19	2L	17	45
2011	19-rhiz	2L	6.9	
2011	20	2L	24	26
2011	20	3L	36	
2011	22	2L	7.6	44
2011	22	3L	4.1	
2011	23	2L	0.4	31
2011	23	3L	28	
2011	24	2L	43	49
2011	24	3L	13	
2011	25	2L	111	366
2011	25	3L	55	
2011	27	2L	25	129
2011	27	3L	56	
2011	28	2L	30	16
2011	28	3L	3.1	
2011	30	2L	7.7	11
2011	30	3L	32	
2011	31	2L	2.3	11
2011	31	3L	1.3	
2011	33	2L	67	38
2011	33	3L	8.5	
2012	1	2L	38	65
2012	2	2L	19	63
2012	2-rhiz	2L	37	
2012	5	2L	4.8	22
		3L	9.8	

A.4 2-LAYER VS. 3-LAYER MODEL

The 3-layer formulation of the NO_3^- model was employed at every station demonstrating NO_3^- consumption. The best fit, and thus, the best flux, was determined by examining the reduced χ^2 value for each model fit. The table below shows the model results from using both the 2-layer and 3-layer formulation along with the reduced χ^2 of the model fit.

Year	Station	Model	Ctot	Red-X^2
2010	1	2L	0.73	5.8
2010	1	2L - Rhiz	0.15	3.1
2010	5	2L	0.47	9.7
2010	5	3L	0.53	7.1
2010	6	2L	0.36	17
2010	6	3L	0.35	16
2010	7	2L	0.79	0.6
2010	7	2L - Rhiz	0.40	1.7
2010	9	2L	1.13	32
2010	9	3L	1.13	33
2010	19	2L	1.18	1.2
2010	19	2L - Rhiz	0.45	3.7
2010	20	2L	0.41	72
2010	20	3L	0.41	125
2010	21	2L	0.47	174
2010	21	3L	0.51	192
2010	23	2L	0.61	7.1
2010	23	3L	0.74	0.1
2010	25	2L	0.23	27
2010	25	3L	0.31	65
2010	26	2L	0.16	106
2010	27	2L	0.16	20
2011	1	2L	0.29	3.8
2011	3	2L	0.76	45.0
2011	3	3L	0.64	15
2011	6	2L	1.38	23
2011	6	3L	1.41	24
2011	8	2L	0.59	38

2011	8	3L	0.63	261
2011	9	2L	0.47	6.0
2011	9	3L	0.45	6.1
2011	13	2L	0.75	64
2011	13	3L	0.83	100
2011	19	2L	0.85	17
2011	19	2L - Rhiz	0.21	6.9
2011	20	2L	0.23	24
2011	20	3L	0.36	36
2011	22	2L	0.51	7.6
2011	22	3L	0.46	4.1
2011	23	2L	0.44	0.4
2011	23	3L	0.32	28
2011	24	2L	0.56	43
2011	24	3L	0.65	13
2011	25	2L	0.28	111
2011	25	3L	0.34	55
2011	27	2L	0.53	25
2011	27	3L	0.50	56
2011	28	2L	0.33	30
2011	28	3L	0.32	3.1
2011	30	2L	0.54	7.7
2011	30	3L	0.59	32
2011	31	2L	0.16	2.3
2011	31	3L	0.39	1.3
2011	33	2L	0.30	67
2011	33	3L	0.44	8.5
2012	1	2L	0.22	38
2012	2	2L	1.96	19
2012	2	2L - Rhiz	1.04	7.5
2012	5	2L	1.92	2.0
2012	5	3L	1.53	9.8

A.5 EXPONENTIAL VS POLYNOMIAL FITS OF PORE WATER $Si(OH)_4$

The WCS $Si(OH)_4$ data was fit with either an exponential or polynomial equation. The best fit was determined by which fit produced the lowest χ^2 as shown in the following table. The flux discussed in Chapter 2 is listed in bold.

	Exponential		Polynomial	
Station	Flux	Chi^2	Flux	Chi^2
AN2010				
1	**0.16**	45.9	0.16	44.8
5	1.65	60.2	**0.74**	46.1
6	**0.21**	14.1	0.18	23.4
7	**0.29**	66.8	0.22	81.7
9	**1.30**	301.3	1.15	410.1
19	**2.13**	130.5	1.45	192.9
20	0.25	74.8	**0.25**	61.5
21	**1.08**	38.5	0.56	45.2
23	0.55	102.4	**0.48**	165.8
25	**0.34**	14.8	0.30	30.6
26	**0.36**	61	0.30	68.2
27	**0.40**	34.3	0.42	105.25
AN2011				
1	**0.64**	46.6	0.48	76.2
3	1.11	111.2	**0.94**	31.6
6	1.06	9.5	**0.95**	6.9
8	0.57	145.7	**0.49**	112.6
9	**0.56**	4.0	0.46	18.8
13	**1.34**	123.7	0.99	379.9
19	0.35	7.9	**0.34**	7.4
20	**0.56**	18.6	0.40	64.1
22	**0.30**	148	0.23	177.2
23	**0.41**	52.6	0.36	66.9
24	0.26	72.2	**0.25**	71.1
25	0.54	90.8	**0.51**	60.0
27	0.60	36.6	**0.55**	25.4
28	0.36	50.6	**0.35**	48.2
30	**0.34**	7.6	0.26	20.1
31	**0.39**	34.5	0.36	42.8
33	**0.33**	12.5	0.32	14.5
AN2012				
1	0.32	1153.9	**0.29**	1110.5
2	**0.91**	146.7	0.71	236.7
5	**1.17**	146.17	0.76	795.2

A.6 SEDIMENT Chl-a MEASUREMENTS

Chlorophyll-a was measured in the sediments from four stations from the 2010 cruise. Sediments were extracted by adding 90% acetone to 1mL of wet sediments followed by vortexing to create a slurry. Chl-a was measured by fluorometry. The results show concentrations of Chl-a ranging from 260-370 μg L^{-1}, indicating that 'fresh' organic material does reach the deep ocean. Using the C/Chl-a ratio of Sun et al., (1991) of 60, our results are equivalent to 15.8-22.4 μg planktonic-C cm^{-3}.

The concentrations of Chl-a in the surface sediments underlying the Amazon River plume are equivalent to 0.63-0.98 μg Chl-a g-$sediment^{-1}$. These values are higher than those observed by Smith et al., (1996) in the equatorial pacific, 0.01-0.44 μg Cl-a g-$sediment^{-1}$, but are comparable to estimates from the NE Atlantic of 0.53 μg Chl-a g-$sediment^{-1}$ (Lochte and Turley, 1986; Rice et al., 1986).

A6.1 Downcore sediment Chl-a measurements

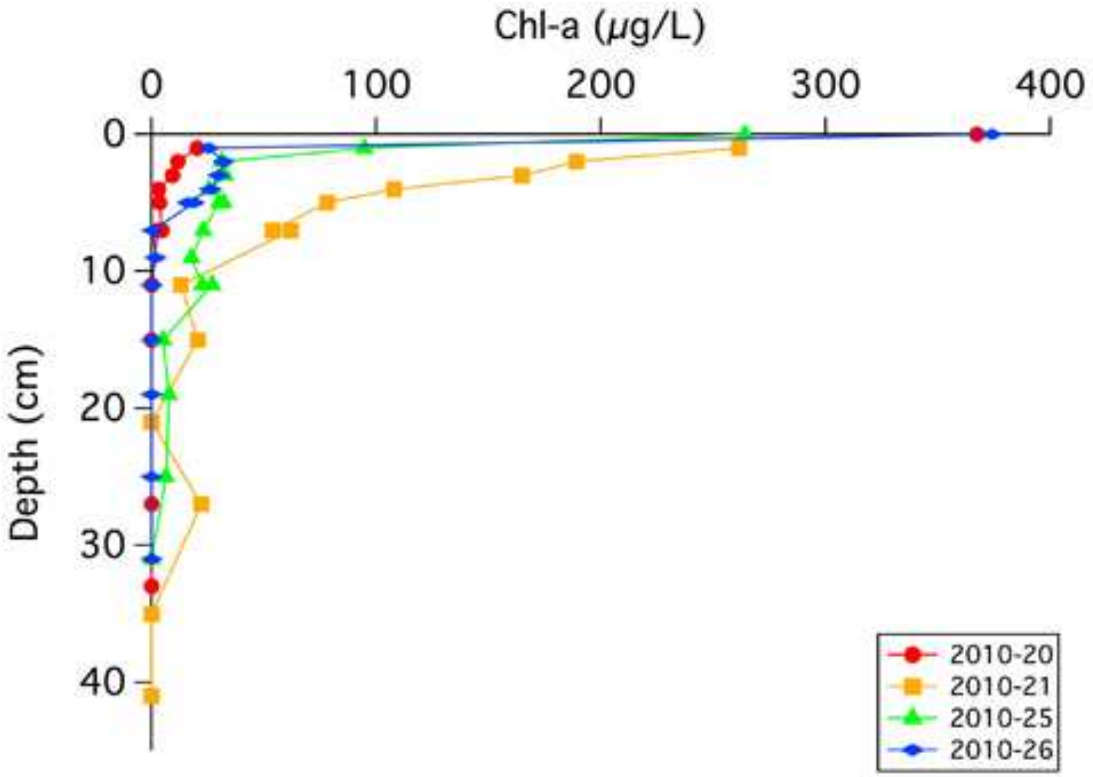

A.7 POROSITY FITTING PARAMETERS

Porosity fitting parameters from Eqs. 1 and 2.							
Station	Fit to upper 5cm of f profile				Eq. 1 fit to full f profile		
	Fitting Eqn	a	b	c	a	b	c
2010							
1	Eq.1	0.8160	0.0840	1.0165	0.8160	0.0840	1.0165
5	Eq.1	0.8043	0.1026	0.4143	0.8043	0.1026	0.4143
6	Eq.1	0.7801	0.1117	0.8943	0.7801	0.1117	0.8943
7	Eq.2	0.8903	-0.0367	0.5734	0.7445	0.1395	0.6989
9	Eq.1	0.8411	0.0913	0.9624	0.8411	0.0913	0.9624
19	Eq.1	0.7445	0.1395	0.6989	0.7887	0.0944	0.3778
20	Eq.1	0.8082	0.1127	0.7788	0.8082	0.1127	0.7788
21	Eq.2	0.9401	-0.0446	0.4178	0.8561	0.0568	0.9438
23	Eq.1	0.8069	0.0921	0.5860	0.8069	0.0921	0.0586
25	Eq.1	0.7992	0.1318	0.8073	0.7992	0.1318	0.8073
26	no samples, used data from 2010-27				0.7763	0.1180	1.2718
27	Eq.1	0.7763	0.1180	1.2718	0.7763	0.1180	1.2718
2011							
1	Eq.2	0.6582	0.1836	-0.1902	0.7455	0.1457	0.2298

3	Eq.2	0.6322	0.2436	-0.1269	0.7466	0.1566	0.1495
6	Eq.2	0.9272	-0.0386	0.6483	0.7190	0.1952	0.1365
8	Eq.1	0.8008	0.1286	0.6483	0.7301	0.1749	0.1289
9	Eq.2	0.9536	-0.0677	0.3760	0.7080	0.1767	0.1077
13	Eq.2	0.5287	0.3336	-0.0307	0.7570	0.1281	0.0677
19	Eq.2	0.6165	0.2037	-0.1571	0.7081	0.1370	0.1725
20	Eq.1	0.6913	0.1260	0.1801	0.6913	0.1260	0.1801
22	Eq.2	0.6131	0.2036	-0.1722	0.7294	0.1228	0.2905
23	Eq.2	0.7309	0.0795	-0.6557	0.7253	0.1394	0.3427
24	Eq.1	0.8115	0.0917	0.2609	0.7522	0.1520	0.1324
25	Eq.2	0.5221	0.3172	-0.0765	0.7185	0.1365	0.0944
27	Eq.1	0.7859	0.1053	0.5589	0.7349	0.1204	0.1289
28	Eq.2	0.5905	0.2963	-0.1156	0.7313	0.1637	0.0751
30	Eq.1	0.7862	0.1089	0.2993	0.7725	0.1129	0.2002
31	Eq.1	0.8221	0.1183	0.7153	0.7690	0.1347	0.1884
33	Eq.1	0.7898	0.0749	0.3987	0.7677	0.0898	0.2125
2012							
1	Eq.1	0.8023	0.1469	1.3530	0.7316	0.1383	0.1743
2	Eq.1	0.8285	0.0904	0.6115	0.7613	0.1350	0.1424
5	Eq.2	0.6885	0.1957	-0.1172	0.7493	0.1298	0.0566

A.8 NITRATE MODEL RATE CONSTANTS

Supplemental Table ST-2. Reaction rate constants and depth attenuation coefficients determined by the NO_3^- model.
J_f and J_s are the fluxes of fast and slow carbon oxidation attributable to nitrification.

Station	Latitude	Longitude	Depth (m)	κ_f µmol N $cm^{-3}yr^{-1}$	κ_s µmol N $cm^{-3}yr^{-1}$	α_f cm^{-1}	α_s cm^{-1}	$J_f(\kappa_f\alpha_f^{-1})$ mmol C $m^{-2}d^{-1}$	$J_s(\kappa_s\alpha_s^{-1})$ mmol C $m^{-2}d^{-1}$
Zone A									
2010-5	6.81	49.98	3975	1.23	0.0000033	0.44	3.50	0.54	0.00
2010-9	5.92	50.73	3014	16.99	0.05	2.72	0.14	1.19	0.07
2010-19	8.29	50.75	4854	1.73	0.0000032	0.64	3.50	0.51	0.00
2010-21	9.77	50.75	4863	3.79	0.13	3.50	0.02	0.21	1.05
2011-6	6.85	51.35	3760	22.80	2.80	3.20	3.20	1.36	0.17
2011-8	6.86	49.92	3997	7.17	0.19	3.50	0.01	0.39	2.94[c]
2011-13	8.07	51.18	4450	9.03	0.41	3.50	0.17	0.49	0.45
2011-30	10.00	50.99	4910	8.09	0.06	2.94	0.01	0.52	1.07[c]
2012-2	39.59	9.42	4764	9.53	0.44	3.50	0.01	0.52	8.43[c]
2012-5	0.60	4.82	1770	33.57	0.51	3.50	0.01	1.83	9.75[c]
Zone B									
2010-1	11.57	56.79	4373	0.05	0.00032	0.01	3.50	0.95[c]	0.00
2010-23	10.62	54.39	4486	5.34	0.06	2.01	0.01	0.51	1.20[c]
2010-25	11.41	56.36	4465	1.02	0.04	1.11	0.07	0.18	0.11
2010-26	11.80	54.21	4777	1.48	0.07	3.50	0.12	0.08	0.12
2010-27	12.16	52.13	5044	3.15	0.07	2.13	0.18	0.28	0.08
2011-1	11.60	56.86	4362	0.05	0.00006	3.50	0.23	0.003	0.00
2011-3	10.27	54.53	4393	8.11	0.21	3.50	0.13	0.44	0.30
2011-31	10.55	52.70	4889	5.53	0.07	3.50	0.08	0.30	0.16
2011-33	11.32	55.00	4650	7.43	0.05	3.50	0.07	0.40	0.13

2012-1	48.62	11.57	4390	0.14	0.0000032	0.09	3.50	0.32	0.00
Zone C									
2010-6	6.82	47.63	4088	0.21	0.00033	0.01	0.01	0.40[c]	0.01[c]
2010-7[a]	7.00	45.02	4394	2.30	0.09	1.28	0.11	0.34	0.16
2010-20	10.00	49.97	4854	9.28	0.12	3.50	0.12	0.50	0.18
2011-9	6.69	48.73	4030	2.37	0.27	3.50	0.01	0.13	5.11[c]
2011-19[a]	6.78	45.96	4205	2.15	0.16	3.49	0.13	0.12	0.22
2011-20[a]	6.19	45.43	4197	0.34	0.34	0.23	3.50	0.28	0.02
2011-22[a]	7.00	44.90	4435	8.03	0.13	3.50	0.20	0.44	0.12
2011-23	8.50	45.00	4709	5.03	0.19	3.50	0.16	0.27	0.23
2011-24	9.45	46.99	4784	7.30	0.62	3.48	0.37	0.40	0.32
2011-25	8.47	48.03	4526	0.98	0.10	0.90	0.06	0.21	0.33
2011-27	8.08	49.53	4415	3.81	0.20	3.50	0.01	0.21	3.79[c]
2011-28	9.00	50.00	4672	1.22	0.37	3.50	0.19	0.07	0.37
Ceara Rise[b]									
Kn142-2 B-1	5.27	44.15	3279	0.18	0.02	3.20	0.30	0.01	0.01
Kn142-2-E	5.45	44.02	3772	8.67	0.14	3.50	0.26	0.47	0.10
Kn142-2-A-1	5.28	43.57	3990	0.57	0.00	0.40		0.27	
Kn142-2-A-2	5.28	43.57	3990	3.45	0.41	3.00	0.36	0.22	0.22
Kn142-2-F	5.55	43.60	4164	3.64	0.24	3.00	0.28	0.23	0.17
Kn142-2-H	5.77	43.63	4267	0.54	0.11	0.46	0.31	0.22	0.07
Kn142-2-J	5.75	43.40	4342	8.18	0.18	3.50	0.21	0.45	0.16
Kn142-2-G-1	6.17	42.88	4675	2.18	0.19	3.00	0.24	0.14	0.15

[a] Indicates ANACONDAS stations closest to Ceara Rise

[b] Data from Martin and Sayles (2006)

[c] These fluxes cannot be directly compared to the model derived fluxes of C_{tot} because the scale length is greater than that of the average depth of our data (~40cm)

A.9 ANACONDAS MULTI-CORE PORE WATER DATA

The following table lists all multi-core pore water data (WCS and Rhizon) of NO_3^-, $Si(OH)_4$, and dissolved Mn collected from the three cruises of the ANACONDAS project.

Year	Station	Type	Depth	NO3 (µM)	±	Si (µM)	±	Mn (µM)	±
2010	1	WCS	0.0	21.1	0.1	39.2	2.3		
2010	1	WCS	0.0	23.2	0.2	40.0	2.4		
2010	1	WCS	0.1	22.0	0.2	43.8	2.6		
2010	1	WCS	0.5	23.8	2.2	56.9	3.4		
2010	1	WCS	0.8	26.7	0.3	75.4	4.5		
2010	1	WCS	1.0	28.0	0.0	78.8	4.7		
2010	1	WCS	1.3	28.9	0.2	85.8	5.1		
2010	1	WCS	1.6	29.0	0.1	86.6	5.2		
2010	1	WCS	1.8	29.7	0.0	94.2	5.7		
2010	1	WCS	2.0	30.2	0.1	94.6	5.7		
2010	1	WCS	2.2	30.5	0.2	90.8	5.4		
2010	1	Rhizon	0.0	19.5	0.1	39.1	2.3	0.02	0.01
2010	1	Rhizon	2.0	20.9	0.3	74.7	4.5	0.05	0.01
2010	1	Rhizon	3.9	26.4	0.5	182.2	10.9	0.04	0.01
2010	1	Rhizon	5.8	27.7	0.2	210.3	12.6	0.02	0.01
2010	1	Rhizon	7.7	34.9	0.2	251.2	15.1	0.03	0.01
2010	1	Rhizon	11.5	39.4	0.5	247.6	14.9	0.02	0.01
2010	1	Rhizon	13.4	37.5	0.5	265.5	15.9	0.01	0.01
2010	1	Rhizon	17.2	36.7	0.4	247.4	14.8	0.04	0.02
2010	1	Rhizon	19.1	35.7	1.7	228.3	13.7	0.02	0.01
2010	1	Rhizon	21.1	32.3	1.1	214.6	12.9	0.03	0.00
2010	1	Rhizon	23.0	37.3	1.7	215.0	12.9	0.03	0.01
2010	5	WCS	0.0	16.3	0.0	32.0	1.9		
2010	5	WCS	0.0	20.9	0.2	32.8	2.0		
2010	5	WCS	0.2	22.1	0.1	68.9	4.1		
2010	5	WCS	0.4	22.9	0.1	77.2	4.6		
2010	5	WCS	0.6	23.2	2.0	83.7	5.0		
2010	5	WCS	0.7	23.7	0.0	73.1	4.4		
2010	5	WCS	0.8	26.6	0.2	71.4	4.3		
2010	5	WCS	1.0	23.6	0.1	72.2	4.3		
2010	5	WCS	1.1	23.6	0.0	74.7	4.5		
2010	5	WCS	1.2	24.5	0.1	76.3	4.6		
2010	5	Rhizon	0.0	19.9	1.4	31.2	1.9	0.01	0.01
2010	5	Rhizon	1.0	25.0	1.5	107.5	6.5	0.27	0.01
2010	5	Rhizon	3.9	30.1	0.1	245.4	14.7	0.07	0.01
2010	5	Rhizon	6.7	28.4	0.5	311.1	18.7	0.07	0.00
2010	5	Rhizon	9.6	19.1	0.8	312.7	18.8	3.85	0.02

2010	5	Rhizon	12.4	12.5	1.3	293.9	17.6	26.30	0.06
2010	5	Rhizon	15.3	16.2	0.1	224.9	13.5	21.52	0.12
2010	5	Rhizon	18.1			265.9	16.0	56.18	0.26
2010	5	Rhizon	21.0	4.0	0.6	249.5	15.0	70.91	0.16
2010	5	Rhizon	23.9	5.6	0.3	237.2	14.2	79.50	0.18
2010	5	Rhizon	26.7			230.6	13.8	86.62	0.20
2010	5	Rhizon	29.6			228.2	13.7		
2010	5	Rhizon	32.4			221.6	13.3		
2010	6	WCS	0.0	20.5	0.7	31.4	1.9		
2010	6	WCS	0.0	17.3	0.4	34.6	2.1		
2010	6	WCS	0.2	23.2	0.2	44.9	2.7		
2010	6	WCS	0.4	25.4	0.2	56.7	3.4		
2010	6	WCS	0.6	27.6	0.1	60.7	3.6		
2010	6	WCS	0.8	27.4	0.0	62.2	3.7		
2010	6	WCS	0.9	25.8	0.5	66.2	4.0		
2010	6	WCS	1.1	25.9	0.1	68.6	4.1		
2010	6	WCS	1.2	25.7	0.2	71.7	4.3		
2010	6	WCS	1.3	25.5	0.1	74.9	4.5		
2010	6	Rhizon	0.0	23.6	0.1	29.9	1.8	0.02	0.01
2010	6	Rhizon	1.0	22.5	1.6	52.0	3.1	0.05	0.00
2010	6	Rhizon	2.9			129.4	7.8	0.09	0.01
2010	6	Rhizon	4.8	28.2	0.0	111.2	6.7	0.03	0.01
2010	6	Rhizon	6.7	30.8	0.0	161.0	9.7	0.07	0.01
2010	6	Rhizon	8.6	23.6	1.0	186.2	11.2	0.10	0.01
2010	6	Rhizon	10.5	30.7	1.0	196.5	11.8	0.03	0.01
2010	6	Rhizon	12.4	12.4	0.7	221.0	13.3	0.09	0.01
2010	6	Rhizon	14.3	7.1	0.2	219.4	13.2	3.34	0.02
2010	6	Rhizon	16.2	4.7	0.1	213.1	12.8	16.82	0.04
2010	6	Rhizon	18.1			198.1	11.9	28.74	0.09
2010	6	Rhizon	20.1	6.2	0.1	199.7	12.0	36.17	0.11
2010	6	Rhizon	22.0			194.9	11.7	52.44	0.15
2010	7	WCS	0.0	21.9	0.3	47.1	2.8		
2010	7	WCS	0.0	10.3	0.8	48.7	2.9		
2010	7	WCS	0.2	23.1	0.1	60.9	3.7		
2010	7	WCS	0.4	27.1	0.2	67.4	4.0		
2010	7	WCS	0.5	27.5	0.2	78.9	4.7		
2010	7	WCS	0.7	27.7	0.0	80.5	4.8		
2010	7	WCS	0.9	28.3	0.3	74.8	4.5		
2010	7	WCS	1.0	27.8	0.2	61.7	3.7		
2010	7	WCS	1.2	28.3	0.2	84.6	5.1		
2010	7	WCS	1.4	28.1	0.0	83.3	5.0		
2010	7	WCS	1.6	25.6	0.3	83.7	5.0		
2010	7	WCS	1.7	26.7	0.0	82.9	5.0		
2010	7	Rhizon	0.0	20.6	1.2	46.6	2.8	0.00	0.01
2010	7	Rhizon	1.0	27.1	1.5	88.6	5.3	0.52	0.01
2010	7	Rhizon	3.9	28.0	0.7	153.5	9.2	0.02	0.01
2010	7	Rhizon	5.8	30.3	0.6	187.3	11.2	0.04	0.01
2010	7	Rhizon	7.7	27.9	0.5	195.1	11.7	0.02	0.00
2010	7	Rhizon	9.6	26.2	0.3	162.0	9.7	0.02	0.00

2010	7	Rhizon	12.4	24.1	0.6	189.8	11.4	0.02	0.01
2010	7	Rhizon	15.3	22.6	0.6	113.1	6.8	0.02	0.01
2010	7	Rhizon	18.1			178.3	10.7	0.03	0.00
2010	7	Rhizon	21.0	14.1	0.3	162.8	9.8	0.04	0.01
2010	7	Rhizon	23.9			162.8	9.8	0.05	0.01
2010	7	Rhizon	26.4	6.1	0.0	160.4	9.6	0.02	0.00
2010	7	Rhizon	29.3			132.3	7.9	7.24	0.32
2010	7	Rhizon	32.1			140.0	8.4	18.33	0.16
2010	7	Rhizon	35.0			90.3	5.4	27.07	0.70
2010	9.1	WCS	0.0	19.2	0.4	24.5	1.5		
2010	9.1	WCS	0.0	17.2	0.1	26.9	1.6		
2010	9.1	WCS	0.1	22.9	0.0	78.1	4.7		
2010	9.1	WCS	0.3	25.5	0.2	100.9	6.1		
2010	9.1	WCS	0.4	25.1	0.5	126.9	7.6		
2010	9.1	WCS	0.6	23.9	0.4	148.2	8.9		
2010	9.1	WCS	0.7	18.0	0.6	173.0	10.4		
2010	9.1	WCS	0.9	21.5	0.1	192.3	11.5		
2010	9.1	WCS	1.1	15.6	0.3	205.3	12.3		
2010	9.1	WCS	1.2	16.9	1.1	214.4	12.9		
2010	9.1	WCS	1.3	17.2	0.3	219.9	13.2		
2010	9.1	WCS	1.4	18.7	0.1	225.4	13.5		
2010	9.1	WCS	1.6	16.1	0.4	227.0	13.6		
2010	9.3	WCS	0.0	19.8	0.3	24.0	1.4		
2010	9.3	WCS	0.0	19.5	0.1	26.3	1.6		
2010	9.3	WCS	0.1	21.7	0.1	59.0	3.5		
2010	9.3	WCS	0.2	24.4	0.3	85.8	5.1		
2010	9.3	WCS	0.3	15.5	1.2	88.0	5.3		
2010	9.3	WCS	0.5	21.4	0.2	94.1	5.6		
2010	9.3	WCS	0.6	21.7	1.1	103.5	6.2		
2010	9.3	WCS	0.7	22.1	0.1	106.9	6.4		
2010	9.3	WCS	0.9	21.7	0.7	119.7	7.2		
2010	9.3	WCS	1.0	19.2	0.9	124.2	7.5		
2010	9.3	WCS	1.1	21.0	0.2	134.7	8.1		
2010	9.3	WCS	1.3	20.9	0.2	142.2	8.5		
2010	9.3	WCS	1.4	20.4	0.2	145.3	8.7		
2010	9.3	WCS	1.5	19.0	0.4	144.5	8.7		
2010	9.3	WCS	1.7	19.5	0.1	143.8	8.6		
2010	9.3	WCS	1.8	20.0	0.2	146.0	8.8		
2010	9.3	WCS	1.9	20.4	0.0	145.3	8.7		
2010	9.3	WCS	2.0	20.3	0.8	146.0	8.8		
2010	9.3	WCS	2.2	20.3	0.0	142.2	8.5		
2010	9.1	Rhizon	0.0			22.9	1.4	0.02	0.01
2010	9.1	Rhizon	1.9			203.7	12.2	0.02	0.01
2010	9.1	Rhizon	2.9			245.1	14.7		
2010	9.1	Rhizon	4.8			288.0	17.3	0.02	0.00
2010	9.1	Rhizon	10.5			322.3	19.3	14.15	0.18
2010	9.1	Rhizon	13.3			324.3	19.5	16.53	0.23
2010	9.1	Rhizon	16.2			307.3	18.4	14.74	0.28
2010	9.1	Rhizon	19.1			333.7	20.0	17.07	0.28

2010	9.1	Rhizon	21.9			338.1	20.3	17.49	0.25
2010	9.1	Rhizon	25.7			323.5	19.4	13.88	0.09
2010	9.1	Rhizon	29.5			360.9	21.7	16.72	0.23
2010	9.1	Rhizon	33.3			325.5	19.5		
2010	9.1	Rhizon	37.1			293.9	17.6		
2010	9.3	Rhizon	0.0	17.7	0.1	22.5	1.4	0.02	0.02
2010	9.3	Rhizon	1.0	25.3	0.6	81.3	4.9	0.03	0.01
2010	9.3	Rhizon	2.9	25.2	0.1	117.4	7.0		
2010	9.3	Rhizon	4.8	22.3	0.1	129.4	7.8	0.05	0.02
2010	9.3	Rhizon	6.7	22.7	0.1	165.6	9.9	0.16	0.07
2010	9.3	Rhizon	8.6	17.9	0.4	195.7	11.7	0.16	0.02
2010	9.3	Rhizon	10.5	5.6	0.2	210.0	12.6	4.27	0.09
2010	9.3	Rhizon	12.4	16.0	0.3			13.34	0.07
2010	9.3	Rhizon	14.3	10.1	0.0	215.3	12.9	12.33	0.05
2010	9.3	Rhizon	17.1	12.6	0.2			16.79	0.11
2010	9.3	Rhizon	20.0	6.5	0.0				
2010	9.3	Rhizon	22.9	21.6	0.1				
2010	19	WCS	0.0	21.7	0.1	45.3	2.7		
2010	19	WCS	0.0	22.1	0.2	47.0	2.8		
2010	19	WCS	0.1	24.1	0.3	89.5	5.4		
2010	19	WCS	0.2	25.1	0.2	131.0	7.9		
2010	19	WCS	0.4	25.7	0.1	132.8	8.0		
2010	19	WCS	0.5	25.7	0.3	137.2	8.2		
2010	19	WCS	0.7	26.0	0.2	143.4	8.6		
2010	19	WCS	0.9	25.8	0.1	149.6	9.0		
2010	19	WCS	1.1	26.2	0.1	158.4	9.5		
2010	19	WCS	1.2	26.1	0.3	167.3	10.0		
2010	19	WCS	1.4	26.0	0.1	177.9	10.7		
2010	19	WCS	1.5	25.7	0.0	180.5	10.8		
2010	19	WCS	1.7	26.2	0.1	191.1	11.5		
2010	19	WCS	1.9	25.9	0.2	197.8	11.9		
2010	19	Rhizon	0.0	19.8	0.0	41.7	2.5	0.08	0.01
2010	19	Rhizon	1.9	25.4	0.4	151.8	9.1	0.13	0.01
2010	19	Rhizon	3.8	22.8	0.0	245.1	14.7	0.05	0.00
2010	19	Rhizon	11.4	7.2	0.0	314.5	18.9	16.15	0.08
2010	19	Rhizon	14.3	6.6	0.1	291.0	17.5	47.03	0.20
2010	19	Rhizon	17.1			290.2	17.4	79.40	0.74
2010	19	Rhizon	20.0			264.5	15.9	87.97	0.55
2010	19	Rhizon	22.9	7.6	0.0	252.1	15.1		
2010	19	Rhizon	26.7	4.8	0.1	240.6	14.4	126.09	0.68
2010	19	Rhizon	30.5	7.7	1.2	211.5	12.7	123.45	0.81
2010	19	Rhizon	34.3	5.6	0.0	223.0	13.4	161.29	0.35
2010	19	Rhizon	39.1			204.4	12.3	175.17	1.03
2010	20.1	WCS	0.0	19.8	0.2				
2010	20.1	WCS	0.0	19.9	0.1	59.8	3.6		
2010	20.1	WCS	0.1	21.3	0.0	43.9	2.6		
2010	20.1	WCS	0.2	26.1	0.2	69.8	4.2		
2010	20.1	WCS	0.4	27.2	0.1	87.6	5.3		
2010	20.1	WCS	0.5	28.2	0.2	96.5	5.8		

2010	20.1	WCS	0.7	28.7	0.1	103.0	6.2		
2010	20.1	WCS	0.8	28.8	0.1	107.0	6.4		
2010	20.1	WCS	1.0	29.5	0.1	107.8	6.5		
2010	20.1	WCS	1.1	29.4	0.0	113.5	6.8		
2010	20.1	WCS	1.3	29.4	0.0	116.7	7.0		
2010	20.1	WCS	1.5	29.5	0.1	121.6	7.3		
2010	20.1	WCS	1.6	29.8	0.1	124.4	7.5		
2010	20.1	WCS	1.8	30.2	0.1	126.5	7.6		
2010	20.1	WCS	1.9	29.4	0.1	125.6	7.5		
2010	20.1	WCS	2.1	29.9	0.0	120.4	7.2		
2010	20.1	Rhizon	0.0	23.7	0.1	58.0	3.5	0.01	0.00
2010	20.1	Rhizon	1.9	28.7	0.2	104.5	6.3	0.10	0.01
2010	20.1	Rhizon	3.8	29.7	0.0	123.5	7.4	0.29	0.01
2010	20.1	Rhizon	5.7			161.6	9.7	0.28	0.01
2010	20.1	Rhizon	7.6	42.9	0.0	172.1	10.3	0.01	0.00
2010	20.1	Rhizon	9.5	34.4	0.1	204.5	12.3	0.01	0.00
2010	20.1	Rhizon	12.4	32.8	0.1	215.8	12.9	0.00	0.00
2010	20.1	Rhizon	17.1	26.0	0.2	220.3	13.2	0.01	0.00
2010	20.1	Rhizon	21.0	24.0	0.1	221.5	13.3	0.01	0.00
2010	20.1	Rhizon	25.7			213.4	12.8	0.01	0.01
2010	20.1	Rhizon	30.5	12.9	0.0	207.7	12.5	0.01	0.01
2010	20.1	Rhizon	35.2			202.1	12.1	0.11	0.02
2010	20.1	Rhizon	40.0			190.3	11.4	15.47	0.11
2010	20.1	Rhizon	45.7	6.8	0.1			39.17	0.26
2010	20.2	Rhizon	0.0	27.7	0.3	61.6	3.7	0.00	0.00
2010	20.2	Rhizon	1.9	30.5	0.6	112.2	6.7	0.02	0.00
2010	20.2	Rhizon	3.8	27.6	0.5	139.7	8.4	0.04	0.01
2010	20.2	Rhizon	5.7	31.6	0.4	159.2	9.5	0.02	0.00
2010	20.2	Rhizon	8.6	28.5	0.2	167.3	10.0	0.03	0.00
2010	20.2	Rhizon	12.4	30.1	0.3	211.4	12.7	0.09	0.00
2010	20.2	Rhizon	15.2	28.4	0.1	216.6	13.0	0.21	0.01
2010	20.2	Rhizon	18.1	24.7	0.1	221.5	13.3	0.10	0.00
2010	20.2	Rhizon	21.0	22.6	0.1	226.3	13.6	0.13	0.00
2010	20.2	Rhizon	23.8	19.4	0.1	216.6	13.0	0.22	0.01
2010	20.2	Rhizon	26.7	16.3	0.3	211.0	12.7	0.20	0.00
2010	20.2	Rhizon	29.5			198.0	11.9	0.29	0.00
2010	20.2	Rhizon	32.4			200.4	12.0	0.04	0.00
2010	20.2	Rhizon	37.1	5.3	0.2	191.9	11.5		0.10
2010	20.2	Rhizon	41.9					25.20	
2010	21	WCS	0.0	23.9	0.2	61.2	3.7		
2010	21	WCS	0.0	22.3	0.1	55.0	3.3		
2010	21	WCS	0.1	23.9	0.2	74.9	4.5		
2010	21	WCS	0.2	26.7	0.1	84.5	5.1		
2010	21	WCS	0.4	27.7	0.2	96.2	5.8		
2010	21	WCS	0.5	28.2	0.0	102.3	6.1		
2010	21	WCS	0.7	27.5	0.2	109.9	6.6		
2010	21	WCS	0.8	28.7	0.1	117.1	7.0		
2010	21	WCS	0.9	27.8	0.1	121.6	7.3		
2010	21	WCS	1.1	28.2	0.0	127.0	7.6		

2010	21	WCS	1.2	27.8	0.1	129.8	7.8		
2010	21	WCS	1.4	27.4	0.1	136.3	8.2		
2010	21	WCS	1.5	25.6	0.0	139.4	8.4		
2010	21	WCS	1.6	27.9	0.2	144.2	8.7		
2010	21	WCS	1.8	26.4	0.1	148.3	8.9		
2010	21	WCS	1.9	26.9	0.2	151.4	9.1		
2010	21	WCS	2.0	26.0	0.1	153.1	9.2		
2010	21	Rhizon	0.0	24.0	0.1	51.2	3.1	0.03	0.01
2010	21	Rhizon	2.0	30.8	0.1	112.2	6.7	0.09	0.00
2010	21	Rhizon	3.9	30.5	0.0	134.2	8.1	0.07	0.01
2010	21	Rhizon	5.8	30.0	0.0	151.3	9.1	0.03	0.01
2010	21	Rhizon	8.7	30.1	0.0	176.7	10.6	0.04	0.00
2010	21	Rhizon	11.5	22.2	0.2	211.0	12.7	0.07	0.01
2010	21	Rhizon	14.4	19.7	0.0	218.6	13.1	0.02	0.00
2010	21	Rhizon	18.2			189.7	11.4	1.21	0.00
2010	21	Rhizon	22.0	4.8	0.1	203.5	12.2	13.89	0.04
2010	21	Rhizon	25.8			188.7	11.3	38.34	0.14
2010	21	Rhizon	29.6	6.4	0.1	180.1	10.8	59.22	0.26
2010	21	Rhizon	33.4	5.3	0.0	176.0	10.6	75.16	0.49
2010	21	Rhizon	37.2	6.9	0.1	171.2	10.3	91.76	0.33
2010	21	Rhizon	41.1	4.2	0.1	160.9	9.7	111.33	0.84
2010	21	Rhizon	45.8	4.8	0.1	155.4	9.3	124.54	0.73
2010	21	Rhizon	50.6	4.3	0.1	148.6	8.9	149.04	1.09
2010	23	WCS	0.0	21.8	0.1	47.8	2.9		
2010	23	WCS	0.0	29.1	1.1	55.1	3.3		
2010	23	WCS	0.1	30.5	1.6	79.7	4.8		
2010	23	WCS	0.2	26.2	0.2	87.0	5.2		
2010	23	WCS	0.4	26.9	0.0	97.0	5.8		
2010	23	WCS	0.5	27.7	0.1	106.1	6.4		
2010	23	WCS	0.7	28.9	0.1	114.3	6.9		
2010	23	WCS	0.8	29.0	0.0	121.6	7.3		
2010	23	WCS	1.0	29.8	0.1	125.2	7.5		
2010	23	WCS	1.1			135.3	8.1		
2010	23	WCS	1.3	30.8	0.2	148.0	8.9		
2010	23	WCS	1.4	30.5	0.1	145.3	8.7		
2010	23	WCS	1.6	30.4	30.4	133.4	8.0		
2010	23	WCS	1.7	30.7	0.5	128.0	7.7		
2010	23	WCS	1.9	30.6	0.2	122.5	7.3		
2010	23	WCS	2.1	30.4	1.3	116.6	7.0		
2010	23	Rhizon	0.0	20.6	0.1	47.8	2.9	0.01	0.01
2010	23	Rhizon	1.9	38.6	0.1	139.8	8.4	0.05	0.00
2010	23	Rhizon	4.8	33.9	0.2	233.7	14.0	0.02	0.01
2010	23	Rhizon	7.6	34.9	0.2	251.0	15.1		
2010	23	Rhizon	10.5	34.6	0.1	248.3	14.9	0.02	0.01
2010	23	Rhizon	13.3	31.5	0.1	261.0	15.7	0.04	0.01
2010	23	Rhizon	16.2					0.23	0.00
2010	23	Rhizon	19.1	24.1	0.2	253.7	15.2	1.09	0.01
2010	23	Rhizon	21.9			241.9	14.5	8.05	0.05
2010	23	Rhizon	25.7	16.5	0.1	235.5	14.1	17.45	0.10

2010	23	Rhizon	30.5	7.6	0.0	192.2	11.5	25.77	0.08
2010	25	WCS	0.0	24.2	0.1	70.7	4.2		
2010	25	WCS	0.0	24.3	0.2	74.9	4.5		
2010	25	WCS	0.1	27.1	0.0	87.2	5.2		
2010	25	WCS	0.2	27.8	0.4	91.9	5.5		
2010	25	WCS	0.4	28.7	0.2	100.3	6.0		
2010	25	WCS	0.5	29.0	0.1	104.6	6.3		
2010	25	WCS	0.7	29.4	0.6	108.8	6.5		
2010	25	WCS	0.8	29.5	0.0	112.2	6.7		
2010	25	WCS	1.0	29.9	0.2	112.2	6.7		
2010	25	WCS	1.1	29.8	0.2	124.1	7.4		
2010	25	WCS	1.3	30.1	0.0	124.1	7.4		
2010	25	WCS	1.5	30.3	0.0	125.7	7.5		
2010	25	WCS	1.6	30.0	0.8	132.5	8.0		
2010	25	WCS	1.8	29.4		125.7	7.5		
2010	25	WCS	2.0	30.8	0.6	130.0	7.8		
2010	25	WCS	2.1	30.0	0.1	127.9	7.7		
2010	25	Rhizon	0.0	23.2	0.0	69.0	4.1	0.01	0.01
2010	25	Rhizon	1.9	27.4	0.2	80.8	4.9	0.10	0.01
2010	25	Rhizon	6.7	30.8	0.0	142.7	8.6	0.02	0.00
2010	25	Rhizon	9.5	30.3	0.1	202.0	12.1	4.02	0.03
2010	25	Rhizon	12.4	33.3	0.3	172.4	10.3	0.37	0.02
2010	25	Rhizon	15.2	31.6	0.1	213.9	12.8		
2010	25	Rhizon	18.1	28.7	0.5	209.6	12.6	0.01	0.00
2010	25	Rhizon	21.0	28.5	0.1	243.5	14.6	0.02	0.00
2010	25	Rhizon	24.8	27.1	0.1	202.9	12.2	0.03	0.00
2010	25	Rhizon	28.6			214.7	12.9	0.03	0.01
2010	25	Rhizon	33.3	25.1	0.3	194.4	11.7	0.03	0.01
2010	25	Rhizon	38.1	17.8	0.0	230.4	13.8	0.04	0.01
2010	26	WCS	0.0	25.1	0.0	52.6	3.2		
2010	26	WCS	0.0	24.6	0.1	57.6	3.5		
2010	26	WCS	0.1	27.2	0.0	71.2	4.3		
2010	26	WCS	0.2	30.1	0.2	69.1	4.1		
2010	26	WCS	0.4	28.4	0.1	83.2	5.0		
2010	26	WCS	0.5	28.3	0.1	86.5	5.2		
2010	26	WCS	0.7	28.5	0.1	91.0	5.5		
2010	26	WCS	0.8	27.7	0.1	96.4	5.8		
2010	26	WCS	1.0	29.7	0.5	100.5	6.0		
2010	26	WCS	1.1	28.8	0.2	95.5	5.7		
2010	26	WCS	1.3	30.1	0.1	109.1	6.5		
2010	26	WCS	1.4	27.3	0.1	109.6	6.6		
2010	26	WCS	1.6	29.9	0.1	103.8	6.2		
2010	26	WCS	1.8	30.3	0.2	105.4	6.3		
2010	26	WCS	1.9	30.4	0.4	105.4	6.3		
2010	26	WCS	2.1	30.3	0.1	101.7	6.1		
2010	26	Rhizon	0.0	22.9	0.1	55.9	3.4	0.01	0.01
2010	26	Rhizon	1.4	24.7	0.1	68.3	4.1	0.03	0.00
2010	26	Rhizon	4.3	27.6	0.3	84.8	5.1	0.01	0.01
2010	26	Rhizon	7.1	33.0	0.1	166.5	10.0	0.01	0.00

2010	26	Rhizon	10.0	35.1	0.0	194.9	11.7	0.01	0.01
2010	26	Rhizon	13.8	35.1	0.2	213.5	12.8	0.01	0.01
2010	26	Rhizon	16.6	34.6	0.1	226.7	13.6	0.01	0.00
2010	26	Rhizon	19.5	34.3	0.0	224.2	13.5	0.00	0.00
2010	26	Rhizon	22.4	34.2	0.1	225.5	13.5	0.04	0.00
2010	26	Rhizon	26.2	31.1	0.1	225.1	13.5	0.01	0.00
2010	26	Rhizon	30.9	29.7	0.1	239.9	14.4	0.02	0.00
2010	26	Rhizon	35.7	28.1	0.1	242.4	14.5	0.01	0.01
2010	26	Rhizon	40.5	26.5	0.1	249.0	14.9	0.01	0.01
2010	26	Rhizon	45.2			243.2	14.6	0.22	0.01
2010	27	WCS	0.0	24.9	0.0	58.5	3.5		
2010	27	WCS	0.0	23.9	0.1	58.5	3.5		
2010	27	WCS	0.1	26.7	0.0	72.8	4.4		
2010	27	WCS	0.2	24.9	0.1	78.4	4.7		
2010	27	WCS	0.4	27.8	0.1	82.4	4.9		
2010	27	WCS	0.5	28.3	0.1	84.0	5.0		
2010	27	WCS	0.7	28.5	0.4	86.3	5.2		
2010	27	WCS	0.8	28.8	0.0	90.3	5.4		
2010	27	WCS	1.0	29.5	0.0	91.9	5.5		
2010	27	WCS	1.2	29.3	0.0	91.1	5.5		
2010	27	WCS	1.4	30.2	0.3	89.1	5.3		
2010	27	WCS	1.5	30.1	0.1	90.3	5.4		
2010	27	WCS	1.7	29.3	0.1	89.5	5.4		
2010	27	Rhizon	0.0	23.4	0.3	58.1	3.5	0.00	0.01
2010	27	Rhizon	1.9	27.8	0.1	76.8	4.6	0.02	0.01
2010	27	Rhizon	3.8	29.0	0.2	111.8	6.7	0.02	0.01
2010	27	Rhizon	6.7	33.4	0.1	138.0	8.3	0.04	0.01
2010	27	Rhizon	10.5			152.3	9.1	0.02	0.00
2010	27	Rhizon	14.3	32.8	0.1	153.1	9.2	0.03	0.01
2010	27	Rhizon	17.1	33.9	0.0	148.3	8.9	0.03	0.00
2010	27	Rhizon	21.0	34.6	0.3	156.2	9.4	0.01	0.01
2010	27	Rhizon	24.8	32.5	0.1	159.4	9.6	0.04	0.00
2010	27	Rhizon	28.6	35.3	0.2	159.4	9.6	0.02	0.01
2010	27	Rhizon	32.4	31.7	0.4	170.5	10.2	0.01	0.00
2010	27	Rhizon	36.2	36.5	0.2	161.8	9.7	0.05	0.00
2010	27	Rhizon	41.0	31.6	0.1	161.8	9.7	0.06	0.00
2011	1	WCS	0.0	22.6	0.2	37.4	2.2		
2011	1	WCS	0.0	21.3	0.1	40.4	2.4		
2011	1	WCS	0.1	24.5	0.1	59.7	3.6		
2011	1	WCS	0.3	25.9	0.4	67.1	4.0		
2011	1	WCS	0.4	26.8	0.1	78.9	4.7		
2011	1	WCS	0.6	27.0	0.1	83.4	5.0		
2011	1	WCS	0.8	27.3	0.0	90.8	5.4		
2011	1	WCS	0.9	27.3	0.0	90.8	5.4		
2011	1	WCS	1.2	27.6	0.0	89.3	5.4		
2011	1	WCS	1.4	27.5	0.1	83.4	5.0		
2011	1	WCS	1.6	27.7	0.1	81.9	4.9		
2011	1	WCS	1.8	28.1	0.1	81.9	4.9		
2011	1	WCS	2.0	28.4	0.1	83.4	5.0		

2011	1	Rhizon	0.0	24.0	0.4	38.9	2.3	0.24	0.06
2011	1	Rhizon	2.7	26.8	0.2	102.6	6.2	4.40	0.07
2011	1	Rhizon	4.6	32.5	0.3	153.0	9.2	0.05	0.06
2011	1	Rhizon	6.5	30.5	0.1	157.5	9.4	0.08	0.06
2011	1	Rhizon	8.4	27.6	0.2	141.2	8.5	0.05	0.06
2011	1	Rhizon	10.3	30.4	0.2	175.2	10.5	0.03	0.06
2011	1	Rhizon	12.2	29.6	0.2	181.2	10.9	0.04	0.06
2011	1	Rhizon	14.1	28.6	0.1	157.5	9.4	0.03	0.06
2011	1	Rhizon	17.9	28.7	0.2	166.3	10.0	0.07	0.06
2011	1	Rhizon	21.8	28.5	0.6	179.7	10.8	0.04	0.06
2011	1	Rhizon	25.6	28.9	0.9	207.8	12.5	0.11	0.06
2011	1	Rhizon	30.3	26.1	0.0	178.2	10.7	0.06	0.06
2011	3	WCS	0.0	22.2	0.1	50.8	3.0		
2011	3	WCS	0.0	21.4	0.1	49.1	2.9		
2011	3	WCS	0.1	23.5	0.2	81.1	4.9		
2011	3	WCS	0.3	24.8	0.6	106.4	6.4		
2011	3	WCS	0.5	27.5	0.3	136.7	8.2		
2011	3	WCS	0.7	28.7	0.1	158.6	9.5		
2011	3	WCS	0.8	28.9	0.1	167.0	10.0		
2011	3	WCS	1.0	29.2	0.1	165.4	9.9		
2011	3	WCS	1.2	29.5	0.2	167.0	10.0		
2011	3	Rhizon	0.0	22.4	0.1	45.7	2.7		
2011	3	Rhizon	1.9	27.8	0.0	150.2	9.0		
2011	3	Rhizon	3.8	31.0	0.3	190.6	11.4		
2011	3	Rhizon	5.7	33.5	0.2	263.1	15.8		
2011	3	Rhizon	11.4	31.0	0.2	273.2	16.4		
2011	3	Rhizon	13.3	26.7	0.4	274.9	16.5		
2011	3	Rhizon	15.2	22.5	0.3	283.3	17.0	3.1	0.8
2011	3	Rhizon	18.1	18.0	0.2	274.9	16.5	13.1	0.8
2011	3	Rhizon	22.8	9.6	0.0	258.0	15.5	25.1	0.8
2011	3	Rhizon	27.6	4.3	0.0	246.2	14.8	35.2	0.8
2011	3	Rhizon	32.4	0.7	0.2	229.4	13.8	41.8	0.8
2011	3	Rhizon	37.1	0.4	0.3	214.2	12.9	54.8	0.8
2011	3	Rhizon	41.9	0.4	0.1	195.7	11.7	64.9	0.8
2011	6	WCS	0.0	20.0	0.0	32.7	2.0		
2011	6	WCS	0.0	19.4	0.0	34.3	2.1		
2011	6	WCS	0.1	20.9	0.1	63.0	3.8		
2011	6	WCS	0.3	23.9	0.3	98.0	5.9		
2011	6	WCS	0.4	24.6	0.1	125.1	7.5		
2011	6	WCS	0.6	24.6	0.1	144.2	8.7		
2011	6	WCS	0.8	24.1	0.3	160.2	9.6		
2011	6	WCS	1.0	18.9	0.0	168.1	10.1		
2011	6	WCS	1.1	18.8	0.3	176.1	10.6		
2011	6	WCS	1.3	23.0	0.1	163.4	9.8		
2011	6	Rhizon	0.0	20.1	0.0	32.7	2.0	0.07	0.10
2011	6	Rhizon	1.9	19.0	0.3	243.0	14.6	0.06	0.10
2011	6	Rhizon	3.8	10.9	0.1	321.1	19.3	0.11	0.10
2011	6	Rhizon	6.0	0.4	0.1	364.1	21.8	32.9	0.5
2011	8	WCS	0.0	20.5	0.1	34.2	2.1		

2011	8	WCS	0.0	20.4	0.0	34.2	2.1		
2011	8	WCS	0.2	21.7	0.0	54.4	3.3		
2011	8	WCS	0.3	22.9	0.1	68.4	4.1		
2011	8	WCS	0.5	22.8	0.1	76.2	4.6		
2011	8	WCS	0.5	22.7	0.0	90.2	5.4		
2011	8	WCS	0.7	22.2	0.2	97.9	5.9		
2011	8	WCS	0.9	21.9	0.1	99.5	6.0		
2011	8	WCS	1.0	21.8	0.3	97.9	5.9		
2011	8	WCS	1.2	22.1	0.1	96.4	5.8		
2011	8	WCS	1.4	22.8	0.2	90.2	5.4		
2011	8	WCS	1.6	23.1	0.4	85.5	5.1		
2011	8	WCS	1.7	23.2	0.1	87.1	5.2		
2011	8	WCS	1.9	23.1	0.0				
2011	8	WCS	2.2	23.2	0.1				
2011	8	WCS	3.2	23.7	0.1	90.2	5.4		
2011	8	Rhizon	0.0	19.0	0.2	34.2	2.1	0.0	0.0
2011	8	Rhizon	1.9	22.0	0.1	132.2	7.9	0.0	0.0
2011	8	Rhizon	3.8	18.9	0.2	163.3	9.8	0.0	0.0
2011	8	Rhizon	5.7	16.2	0.1	188.2	11.3	0.0	0.0
2011	8	Rhizon	7.6	9.7	0.0	202.2	12.1	0.0	0.0
2011	8	Rhizon	9.5	4.5	0.0	213.0	12.8	14.2	0.8
2011	8	Rhizon	11.4	0.2	0.0	241.0	14.5	31.0	0.8
2011	8	Rhizon	13.3	1.7	0.1	231.7	13.9	40.1	0.8
2011	8	Rhizon	15.2	0.0	0.1	244.1	14.6	56.3	0.8
2011	8	Rhizon	17.1	0.0	0.1	233.3	14.0	67.8	0.8
2011	8	Rhizon	19.1	0.0	0.0	227.0	13.6	80.0	0.7
2011	8	Rhizon	21.0	0.0	0.0	213.0	12.8	96.4	0.7
2011	8	Rhizon	22.9	0.0	0.0	216.2	13.0	111.0	0.7
2011	8	Rhizon	24.8	0.0	0.0	220.8	13.2	124.1	0.8
2011	9.1	WCS	0.0	19.7	0.0	31.7	1.9		
2011	9.1	WCS	0.0	19.6	0.1	31.7	1.9		
2011	9.1	WCS	0.1	20.6	0.0	52.8	3.2		
2011	9.1	WCS	0.3	22.6	0.0	66.4	4.0		
2011	9.1	WCS	0.5	22.5	0.1	78.5	4.7		
2011	9.1	WCS	0.6	22.6	0.0				
2011	9.1	WCS	0.8	22.5	0.2	90.6	5.4		
2011	9.1	WCS	1.0	22.1	0.1	93.6	5.6		
2011	9.1	WCS	1.2	22.5	0.1	92.1	5.5		
2011	9.1	WCS	1.3	22.1	0.1	90.6	5.4		
2011	9.1	WCS	1.5	21.0	0.0	95.1	5.7		
2011	9.1	WCS	1.7	20.6	0.0	95.1	5.7		
2011	9.1	WCS	2.1	23.1	0.7	93.6	5.6		
2011	9.2	WCS	0.0	23.7	0.1	33.2	2.0		
2011	9.2	WCS	0.0	21.7	0.2	34.8	2.1		
2011	9.2	WCS	0.1	22.4	0.1	80.6	4.8		
2011	9.2	WCS	0.3	22.9	0.1	90.1	5.4		
2011	9.2	WCS	0.5	23.7	0.1	91.7	5.5		
2011	9.2	WCS	0.6	23.3	0.1	98.0	5.9		
2011	9.2	WCS	0.8	23.0	0.8	104.4	6.3		

2011	9.2	WCS	1.0	22.8	0.1	105.9	6.4		
2011	9.2	WCS	1.2	21.8	0.1	107.5	6.5		
2011	9.2	WCS	1.3	22.8	0.2	104.4	6.3		
2011	9.2	WCS	1.5	22.9	0.1	104.4	6.3		
2011	9.2	WCS	1.7	22.7	0.1	104.4	6.3		
2011	9.2	WCS	2.7	23.1	0.4	110.7	6.6		
2011	9.1	Rhizon	0.0	18.7	0.0	28.7	1.7	0.21	0.10
2011	9.1	Rhizon	2.9	21.7	0.0	93.6	5.6	0.10	0.10
2011	9.1	Rhizon	6.9	17.7	0.0	181.2	10.9	0.11	0.10
2011	9.1	Rhizon	8.8	8.7	0.0	194.8	11.7	0.12	0.10
2011	9.1	Rhizon	10.7	0.9	0.0	197.9	11.9	6.32	0.10
2011	9.1	Rhizon	12.6	0.8	0.1	206.9	12.4	20.06	0.13
2011	9.1	Rhizon	14.5	0.7	0.1	213.0	12.8	31.5	0.5
2011	9.1	Rhizon	16.4	0.7	0.1	213.0	12.8	43.1	0.5
2011	9.1	Rhizon	18.3	0.4	0.0	199.4	12.0	48.5	0.5
2011	9.1	Rhizon	20.2	0.7	0.3	200.9	12.1	60.0	0.5
2011	9.1	Rhizon	22.1	0.3	0.1	187.3	11.2	67.8	0.5
2011	9.1	Rhizon	24.0	0.9	0.0	190.3	11.4	75.8	0.7
2011	9.1	Rhizon	25.9	0.3	0.0	190.3	11.4	85.0	0.7
2011	9.1	Rhizon	30.7	0.5	0.0	182.8	11.0	96.6	0.9
2011	9.1	Rhizon	35.4	0.2	0.0	167.7	10.1	99.8	1.0
2011	9.1	Rhizon	39.2	0.5	0.1	170.7	10.2	98.6	0.7
2011	13	WCS	0.0	20.3	0.2	38.1	2.3		
2011	13	WCS	0.0	20.0	0.2	39.6	2.4		
2011	13	WCS	0.1	23.1	0.2	78.2	4.7		
2011	13	WCS	0.3	20.6	0.2	119.8	7.2		
2011	13	WCS	0.5	21.3	0.2	137.5	8.3		
2011	13	WCS	0.6	20.7	0.2	140.6	8.4		
2011	13	WCS	0.8	20.1	0.2	156.5	9.4		
2011	13	WCS	1.0	19.7	0.2	166.2	10.0		
2011	13	WCS	1.2	19.1	0.2	176.3	10.6		
2011	13	WCS	1.4	18.9	0.2	175.5	10.5		
2011	13	WCS	1.5	19.0	0.2	180.2	10.8		
2011	13	WCS	1.7	18.9	0.2	182.9	11.0		
2011	13	WCS	1.9	18.4	0.1	183.4	11.0		
2011	13	WCS	2.1	19.4	0.2	184.5	11.1		
2011	13	WCS	2.6	19.4	0.2	177.5	10.6		
2011	13	WCS	3.2	19.5	0.2	161.9	9.7		
2011	13	Rhizon	0.0	18.0	0.1	38.4	2.3		
2011	13	Rhizon	1.8	23.8	0.1	167.6	10.1		
2011	13	Rhizon	3.7	22.9	0.0	219.5	13.2		
2011	13	Rhizon	5.6	19.5	0.1	314.0	18.8		
2011	13	Rhizon	7.5	12.7	0.0	334.5	20.1	0.2	1.0
2011	13	Rhizon	9.4	6.1	0.0	328.2	19.7	30.1	0.9
2011	13	Rhizon	11.3	6.8	0.0	323.5	19.4	37.1	0.9
2011	13	Rhizon	13.2	0.9	0.1	301.4	18.1	65.3	1.0
2011	13	Rhizon	15.1	0.4	0.0	292.0	17.5	76.3	0.7
2011	13	Rhizon	17.0	0.2	0.0	274.7	16.5	78.8	0.8
2011	13	Rhizon	18.9	0.2	0.0	277.8	16.7	81.9	0.9

2011	13	Rhizon	20.9	0.2	0.0	277.8	16.7	83.6	0.8
2011	13	Rhizon	22.8	0.1	0.1	263.6	15.8	85.6	1.0
2011	13	Rhizon	25.6	0.4	0.0	254.2	15.3	88.7	0.9
2011	13	Rhizon	27.5	0.4	0.0	247.9	14.9	92.9	1.0
2011	19	WCS	0.0	20.6	0.1	48.9	2.9		
2011	19	WCS	0.0	15.3	0.2	48.6	2.9		
2011	19	WCS	0.2	21.4	0.0	54.4	3.3		
2011	19	WCS	0.3	25.4	0.1	68.1	4.1		
2011	19	WCS	0.5	25.1	0.0	85.7	5.1		
2011	19	WCS	0.8	26.5	0.1	101.4	6.1		
2011	19	WCS	1.0	26.9	0.1	111.9	6.7		
2011	19	WCS	1.2	26.6	0.0	113.0	6.8		
2011	19	WCS	1.4	26.6	0.1	115.1	6.9		
2011	19	WCS	1.6	26.6	0.2	113.9	6.8		
2011	19	WCS	1.8	26.8	0.0	110.8	6.6		
2011	19	WCS	2.0	26.7	0.3	109.2	6.6		
2011	19	WCS	2.2	26.9	0.1	115.0	6.9		
2011	19	WCS	2.4	27.0	0.3	120.7	7.2		
2011	19	WCS	2.6	27.4	0.0				
2011	19	WCS	2.8	27.8	0.1				
2011	19	WCS	3.0	28.3	0.1				
2011	19	WCS	3.2	28.5	0.1				
2011	19	WCS	3.4	28.7	0.2				
2011	19	WCS	3.6	28.9	0.4				
2011	19	WCS	3.8	29.2	0.2				
2011	19	WCS	4.0	29.1	0.4				
2011	19	Rhizon	0.0	20.2	0.2	36.5	2.2	0.10	0.11
2011	19	Rhizon	1.8	25.2	0.0	96.8	5.8	0.15	0.10
2011	19	Rhizon	3.7	26.1	0.4	145.4	8.7	0.13	0.10
2011	19	Rhizon	5.6	28.5	0.0	194.0	11.6	0.09	0.10
2011	19	Rhizon	7.5	28.4	0.1	215.3	12.9	0.07	0.10
2011	19	Rhizon	9.4	28.4	0.1	223.1	13.4	0.14	0.10
2011	19	Rhizon	11.3	24.5	0.1	221.2	13.3	0.14	0.10
2011	19	Rhizon	13.2	23.6	0.0	217.3	13.0	0.08	0.10
2011	19	Rhizon	16.1	20.0	0.0	209.5	12.6	0.14	0.10
2011	19	Rhizon	18.9	18.0	0.2	209.5	12.6	0.13	0.10
2011	19	Rhizon	21.8	12.8	0.1	197.8	11.9	0.11	0.10
2011	19	Rhizon	24.7	8.0	0.2	190.1	11.4	0.10	0.10
2011	19	Rhizon	27.5	3.2	0.1	186.2	11.2	0.12	0.10
2011	19	Rhizon	31.3	0.0	0.1	172.6	10.4	6.01	0.11
2011	20	WCS	0.0	19.5	0.2	39.6	2.4		
2011	20	WCS	0.0	19.9	0.0	43.2	2.6		
2011	20	WCS	0.1	23.2	0.1	64.1	3.8		
2011	20	WCS	0.3	24.2	0.1	76.2	4.6		
2011	20	WCS	0.5	24.6	0.0	82.5	5.0		
2011	20	WCS	0.7	24.7	0.2	90.8	5.4		
2011	20	WCS	0.8	25.3	0.0	95.1	5.7		
2011	20	WCS	1.1	25.6	0.0	96.3	5.8		
2011	20	WCS	1.3	25.9	0.1	102.4	6.1		

2011	20	WCS	1.4	26.3	0.0	102.9	6.2		
2011	20	WCS	1.7	26.5	0.2	105.6	6.3		
2011	20	WCS	1.9	26.8	0.1	105.7	6.3		
2011	20	WCS	2.1	27.2	0.2	110.6	6.6		
2011	20	WCS	2.3	27.8	0.2	113.5	6.8		
2011	20	WCS	2.4	27.5	0.2				
2011	20	WCS	2.6	27.7	0.2				
2011	20	WCS	2.8	25.9	0.1				
2011	20	WCS	3.0	28.0	0.2				
2011	20	WCS	3.2	28.2	0.1				
2011	20	WCS	3.4	28.3	0.0				
2011	20	WCS	3.6	28.4	0.1				
2011	20	WCS	4.7	28.4	0.1				
2011	20	WCS	5.2	28.5	0.2				
2011	20	Rhizon	0.0	20.9	0.1	38.7	2.3	0	
2011	20	Rhizon	1.5	24.1	0.0	102.0	6.1	0	
2011	20	Rhizon	3.4	26.2	0.0	151.8	9.1	0	
2011	20	Rhizon	5.3	31.6	0.1	184.4	11.1	0	
2011	20	Rhizon	7.2	27.7	0.1	207.4	12.4	0	
2011	20	Rhizon	9.1	29.7	0.4	213.1	12.8	0	
2011	20	Rhizon	11.0	29.3	0.0	215.0	12.9	0	
2011	20	Rhizon	12.9	26.0	0.1	217.0	13.0	0	
2011	20	Rhizon	14.8	22.6	0.0	215.0	12.9	0	
2011	20	Rhizon	17.7	17.5	0.1	207.4	12.4	0	
2011	20	Rhizon	20.6	14.2	0.1	197.8	11.9	0	
2011	20	Rhizon	23.4	11.4	0.1	192.0	11.5	0	
2011	20	Rhizon	26.3	8.9	0.1	197.8	11.9	0	
2011	20	Rhizon	28.2	6.8	0.1	184.4	11.1	0	
2011	22	WCS	0.0	23.5	0.2	61.2	3.7		
2011	22	WCS	0.0	23.1	0.1	59.8	3.6		
2011	22	WCS	0.1	24.4	0.0	75.7	4.5		
2011	22	WCS	0.4	26.7	0.1	84.6	5.1		
2011	22	WCS	0.5	27.3	0.1	89.5	5.4		
2011	22	WCS	0.7	27.9	0.1	95.5	5.7		
2011	22	WCS	0.9	28.4	0.3	90.6	5.4		
2011	22	WCS	1.1	29.0	0.0	109.0	6.5		
2011	22	WCS	1.2	29.2	0.0	108.0	6.5		
2011	22	WCS	1.4	29.1	0.0	105.7	6.3		
2011	22	WCS	1.6	29.1	0.1	107.1	6.4		
2011	22	WCS	1.8	29.5	0.2	108.1	6.5		
2011	22	WCS	2.0	29.6	0.1				
2011	22	WCS	2.2	29.7	0.1				
2011	22	WCS	2.4	29.9	0.2				
2011	22	WCS	2.6	30.2	0.1				
2011	22	WCS	2.8	30.4	0.1				
2011	22	WCS	3.0	30.9	0.1				
2011	22	WCS	3.8	31.5	0.0				
2011	22	WCS	4.2	32.2	0.1				
2011	22	Rhizon	0.0	22.1	0.2	59.8	3.6	0.21	0.06

2011	22	Rhizon	1.8	17.0	0.0	114.3	6.9	0.03	0.06
2011	22	Rhizon	5.8	18.4	0.1	199.7	12.0	0.07	0.06
2011	22	Rhizon	7.7	18.5	0.1	214.2	12.9	0.05	0.06
2011	22	Rhizon	9.6	18.2	0.0	236.0	14.2	0.10	0.06
2011	22	Rhizon	11.5	17.3	0.0	237.8	14.3	0.04	0.06
2011	22	Rhizon	13.4	16.4	0.0	236.0	14.2	0.04	0.06
2011	22	Rhizon	15.3	15.2	0.1	232.4	13.9	0.07	0.06
2011	22	Rhizon	17.2	14.2	0.1	228.7	13.7	0.04	0.06
2011	22	Rhizon	20.1	12.2	0.0			0.05	0.06
2011	22	Rhizon	22.9	10.2	0.1			0.22	0.06
2011	22	Rhizon	25.8	8.6	0.0			0.15	0.06
2011	22	Rhizon	28.7	5.9	0.1	210.6	12.6	0.04	0.06
2011	22	Rhizon	31.5	4.5	0.0	201.5	12.1	0.18	0.06
2011	22	Rhizon	34.4	2.5	0.1	205.1	12.3	0.08	0.06
2011	22	Rhizon	38.2	0.3	0.0	205.1	12.3	1.21	0.06
2011	23	WCS	0.0	24.3	0.0	74.9	4.5		
2011	23	WCS	0.0	23.9	0.0	76.0	4.6		
2011	23	WCS	0.1	25.1	0.3	95.4	5.7		
2011	23	WCS	0.3	26.8	0.1	101.3	6.1		
2011	23	WCS	0.5	29.1	0.2	110.2	6.6		
2011	23	WCS	0.7	27.9	0.1	120.7	7.2		
2011	23	WCS	0.8	16.0	0.2	126.9	7.6		
2011	23	WCS	1.0	28.3	0.1	132.9	8.0		
2011	23	WCS	1.2	28.7	0.4	138.9	8.3		
2011	23	WCS	1.4	28.1	0.2	142.2	8.5		
2011	23	WCS	1.6	28.8	0.1	139.9	8.4		
2011	23	WCS	1.8	28.8	0.1	136.9	8.2		
2011	23	WCS	2.0	28.8	0.1				
2011	23	WCS	2.2	28.8	0.2				
2011	23	WCS	3.2	20.9	0.1				
2011	23	WCS	4.3	17.1	0.1				
2011	23	Rhizon	0.0	24.1	0.1	76.0	4.6	0.08	0.10
2011	23	Rhizon	1.5	29.1	0.1	130.0	7.8	0.30	0.10
2011	23	Rhizon	5.9	32.5	0.1	226.6	13.6	0.16	0.10
2011	23	Rhizon	7.8	32.7	0.0	248.9	14.9	0.31	0.10
2011	23	Rhizon	9.7	30.9	0.2	248.9	14.9	0.15	0.10
2011	23	Rhizon	11.6	28.8	0.0	239.7	14.4	0.42	0.10
2011	23	Rhizon	13.5	27.0	0.2	234.1	14.0	0.10	0.10
2011	23	Rhizon	15.4	24.8	0.0	224.8	13.5	0.12	0.10
2011	23	Rhizon	17.3	22.3	0.2	204.3	12.3	0.23	0.10
2011	23	Rhizon	19.2	20.4	0.0			0.09	0.10
2011	23	Rhizon	21.1	17.8	0.1			0.48	0.10
2011	23	Rhizon	24.0	14.3	0.1			0.14	0.10
2011	23	Rhizon	26.9	10.5	0.1	196.9	11.8	0.12	0.10
2011	23	Rhizon	29.7	5.4	0.6	196.9	11.8	0.14	0.10
2011	23	Rhizon	32.6	0.0	0.0	178.3	10.7	0.21	0.10
2011	23	Rhizon	35.4	0.0	0.0	163.4	9.8	2.00	0.10
2011	23	Rhizon	38.3	0.0	0.0	165.3	9.9	2.71	0.10
2011	24	WCS	0.0	14.8	0.2	52.3	3.1		

2011	24	WCS	0.0	23.4	0.2	55.8	3.3		
2011	24	WCS	0.1	25.7	0.2	68.7	4.1		
2011	24	WCS	0.4	24.7	0.3	74.5	4.5		
2011	24	WCS	0.5	24.7	0.2	94.0	5.6		
2011	24	WCS	0.7	25.2	0.3	103.8	6.2		
2011	24	WCS	0.9	24.9	1.1	113.4	6.8		
2011	24	WCS	1.0	25.5	0.0	118.3	7.1		
2011	24	WCS	1.2	24.7	0.0	131.3	7.9		
2011	24	WCS	1.4	23.5	0.0	142.2	8.5		
2011	24	WCS	1.6	22.8	0.1	148.6	8.9		
2011	24	WCS	1.8	23.5	0.0	154.8	9.3		
2011	24	WCS	2.0	24.6	0.2				
2011	24	WCS	2.1	24.6	0.2				
2011	24	WCS	2.3	25.0	0.2				
2011	24	WCS	2.5	25.9	0.1				
2011	24	WCS	2.7	26.2	0.3				
2011	24	WCS	3.1	26.6	0.0				
2011	24	WCS	3.7	26.9	0.1				
2011	24	Rhizon	0.0	21.5	0.2	57.1	3.4	0.20	0.10
2011	24	Rhizon	1.2	24.8	0.3	115.6	6.9	0.06	0.10
2011	24	Rhizon	3.1	25.0	0.0	154.6	9.3	0.07	0.10
2011	24	Rhizon	5.0	24.7	0.2	181.9	10.9	0.11	0.10
2011	24	Rhizon	6.9	21.5	0.0	203.3	12.2	0.10	0.12
2011	24	Rhizon	8.8	18.1	0.0	224.8	13.5	0.08	0.10
2011	24	Rhizon	10.7	13.9	0.1	236.5	14.2	11.00	0.11
2011	24	Rhizon	15.5	3.2	0.2	228.7	13.7	20.39	0.15
2011	24	Rhizon	17.4	0.9	0.0	222.8	13.4	28.4	0.5
2011	24	Rhizon	19.3	0.6	0.0	220.9	13.3	36.5	0.5
2011	24	Rhizon	23.1	0.7	0.0	213.1	12.8	35.7	0.5
2011	24	Rhizon	27.0	0.5	0.0	203.3	12.2	29.7	0.5
2011	24	Rhizon	30.8	0.4	0.1	197.5	11.8	20.07	0.18
2011	24	Rhizon	34.6	0.4	0.0	187.7	11.3	12.20	0.15
2011	24	Rhizon	38.4	0.5	0.0	179.9	10.8	7.44	0.11
2011	24	Rhizon	42.2	0.3	0.0	166.3	10.0	8.33	0.11
2011	24	Rhizon	44.1	0.5	0.0	154.6	9.3	9.20	0.11
2011	24	Rhizon	47.9	0.2	0.0	148.7	8.9		
2011	25	WCS	0.0	22.3	0.1	43.4	2.6		
2011	25	WCS	0.0	22.0	0.0	45.0	2.7		
2011	25	WCS	0.1	23.5	0.2	63.7	3.8		
2011	25	WCS	0.3	24.4	0.0	84.6	5.1		
2011	25	WCS	0.5	25.5	0.1	103.1	6.2		
2011	25	WCS	0.7	26.8	0.0	127.1	7.6		
2011	25	WCS	0.8	26.7	0.1	135.9	8.2		
2011	25	WCS	1.1	26.9	0.2	139.5	8.4		
2011	25	WCS	1.2	17.5	0.1	156.0	9.4		
2011	25	WCS	1.4	27.7	0.3	172.5	10.4		
2011	25	WCS	1.6	27.8	0.1	169.3	10.2		
2011	25	WCS	1.8	27.9	0.2	157.6	9.5		
2011	25	WCS	2.0	22.4	0.0				

2011	25	WCS	2.2	28.1	0.2				
2011	25	WCS	2.6	27.7	0.2				
2011	25	WCS	3.3	28.4	0.2				
2011	25	Rhizon	0.0	21.9	0.0	47.1	2.8	0.03	0.06
2011	25	Rhizon	1.5	26.8	0.0	124.6	7.5	0.28	0.06
2011	25	Rhizon	6.1	26.2	0.1	82.0	4.9	0.35	0.06
2011	25	Rhizon	8.0	27.8	0.1	236.9	14.2	0.10	0.06
2011	25	Rhizon	9.9	22.6	0.2	281.5	16.9	0.16	0.06
2011	25	Rhizon	11.8	20.1	0.1	279.6	16.8	0.19	0.06
2011	25	Rhizon	13.7	15.2	0.0	277.6	16.7	0.15	0.06
2011	25	Rhizon	15.6	13.1	0.1	267.9	16.1	0.14	0.06
2011	25	Rhizon	17.5	7.2	0.0	260.2	15.6	0.13	0.06
2011	25	Rhizon	20.4	0.7	0.0	248.6	14.9	2.91	0.07
2011	25	Rhizon	23.2	0.2	0.1	231.1	13.9	14.7	0.5
2011	25	Rhizon	26.1	0.3	0.1	215.6	12.9	25.5	0.5
2011	25	Rhizon	29.9	0.5	0.0	202.1	12.1	36.7	0.5
2011	25	Rhizon	33.7	0.5	0.0	186.6	11.2	46.1	0.7
2011	25	Rhizon	38.5	0.0	0.0	169.1	10.1	58.5	0.6
2011	27	WCS	0.0	22.4	0.1	45.8	2.7		
2011	27	WCS	0.0	19.9	0.1	50.1	3.0		
2011	27	WCS	0.1	24.2	0.1	68.3	4.1		
2011	27	WCS	0.3	25.4	0.0	93.7	5.6		
2011	27	WCS	0.5	25.7	0.1	114.8	6.9		
2011	27	WCS	0.7	25.3	0.1	125.9	7.6		
2011	27	WCS	0.8	25.5	0.0	142.7	8.6		
2011	27	WCS	1.0	25.2	0.0	146.2	8.8		
2011	27	WCS	1.2	24.6	1.0	148.6	8.9		
2011	27	WCS	1.4	25.3	0.2	149.0	8.9		
2011	27	WCS	1.6	25.8	0.3	148.5	8.9		
2011	27	WCS	1.7	26.1	0.1	143.2	8.6		
2011	27	WCS	1.9	26.1	0.0				
2011	27	WCS	2.7	26.3	0.1				
2011	27	WCS	3.1	26.2	0.0				
2011	27	Rhizon	0.0	23.2	0.1	46.1	2.8	0.0	0.0
2011	27	Rhizon	1.4	28.1	0.1	153.9	9.2	0.0	0.0
2011	27	Rhizon	3.3	31.2	0.0	241.6	14.5	0.0	0.0
2011	27	Rhizon	5.2	30.2	0.1	278.5	16.7	0.0	0.0
2011	27	Rhizon	7.1	27.7	0.1	310.9	18.7	0.0	0.0
2011	27	Rhizon	9.0	22.3	0.1	312.4	18.7	0.0	0.0
2011	27	Rhizon	10.9	15.8	0.0	303.2	18.2	0.0	0.0
2011	27	Rhizon	12.8	10.0	0.1	292.4	17.5	21.8	0.8
2011	27	Rhizon	14.7	5.0	0.1	278.5	16.7	31.2	0.8
2011	27	Rhizon	17.6	1.4	0.1	264.7	15.9	46.7	0.8
2011	27	Rhizon	20.5	0.6	0.1	250.8	15.1	64.1	0.8
2011	27	Rhizon	24.3	1.0	0.1	232.4	13.9	82.1	0.8
2011	28	WCS	0.0	24.3	0.1	58.6	3.5		
2011	28	WCS	0.0	24.4	0.0	60.5	3.6		
2011	28	WCS	0.1	25.8	0.0	66.0	4.0		
2011	28	WCS	0.3	26.2	0.2	84.1	5.0		

2011	28	WCS	0.5	26.1	0.0	101.6	6.1		
2011	28	WCS	0.6	26.5	0.1	107.8	6.5		
2011	28	WCS	0.8	26.1	0.1	115.8	6.9		
2011	28	WCS	1.0	26.0	0.2	125.0	7.5		
2011	28	WCS	1.1	24.4	0.5	134.1	8.0		
2011	28	WCS	1.3	25.8	0.1	141.1	8.5		
2011	28	WCS	1.5	26.1	0.0	136.7	8.2		
2011	28	WCS	1.7	26.1	0.6	133.0	8.0		
2011	28	WCS	1.8	26.6	0.0				
2011	28	WCS	2.0	27.2	0.2				
2011	28	WCS	2.7	25.6	0.9				
2011	28	Rhizon	0.0	24.7	0.1	56.3	3.4	0.05	0.06
2011	28	Rhizon	3.0	24.8	0.1	164.6	9.9	0.12	0.06
2011	28	Rhizon	6.0	18.1	0.0	234.7	14.1	0.08	0.06
2011	28	Rhizon	8.1	12.7	0.0	240.8	14.4	0.20	0.06
2011	28	Rhizon	10.1	4.2	0.0	246.9	14.8	1.26	0.06
2011	28	Rhizon	12.1	0.0	0.1	230.1	13.8	20.0	0.5
2011	28	Rhizon	14.1	0.3	0.0	231.7	13.9	37.1	0.6
2011	28	Rhizon	16.1	0.6	0.1	230.1	13.8	49.9	0.6
2011	28	Rhizon	20.1	0.5	0.4	221.0	13.3	87.2	0.8
2011	28	Rhizon	24.1	0.5	0.0	224.0	13.4	114.5	1.1
2011	28	Rhizon	28.1	0.3	0.0	224.0	13.4	131.4	1.3
2011	28	Rhizon	32.1	0.3	0.0	216.4	13.0	139.2	0.9
2011	28	Rhizon	36.1	0.5	0.0	214.9	12.9	145.0	1.3
2011	30	WCS	0.0	24.7	0.1	69.3	4.2		
2011	30	WCS	0.0	25.0	0.1				
2011	30	WCS	0.0	17.6	0.0				
2011	30	WCS	0.0	27.0	0.2	94.6	5.7		
2011	30	WCS	0.1	22.1	0.1	105.1	6.3		
2011	30	WCS	0.3	28.1	0.1	116.4	7.0		
2011	30	WCS	0.5	28.6	0.2	123.7	7.4		
2011	30	WCS	0.6	28.8	0.0	124.4	7.5		
2011	30	WCS	0.8	29.3	0.1	128.6	7.7		
2011	30	WCS	1.0	29.7	0.0	131.1	7.9		
2011	30	WCS	1.2	29.5	0.0	135.5	8.1		
2011	30	WCS	1.4	29.6	0.2	143.6	8.6		
2011	30	WCS	1.5	29.4	0.0	134.6	8.1		
2011	30	WCS	1.7	17.2	0.1	129.9	7.8		
2011	30	Rhizon	0.0	24.0	0.2	69.4	4.2	0.36	0.06
2011	30	Rhizon	1.0	29.3	0.1	138.1	8.3	0.12	0.06
2011	30	Rhizon	2.9	29.6	0.3	168.4	10.1	0.06	0.06
2011	30	Rhizon	4.8	27.6	0.1	203.5	12.2	0.06	0.06
2011	30	Rhizon	6.7	29.3	0.2	224.2	13.5	0.03	0.06
2011	30	Rhizon	8.6	27.7	0.2	256.2	15.4	0.07	0.06
2011	30	Rhizon	10.5	24.4	0.0	257.7	15.5	0.04	0.06
2011	30	Rhizon	14.4	17.0	0.1	259.3	15.6	0.06	0.06
2011	30	Rhizon	18.2	9.9	0.2	243.4	14.6	4.87	0.08
2011	30	Rhizon	22.0	3.6	0.6	238.6	14.3	9.5	0.5
2011	30	Rhizon	25.8	0.4	0.0	230.6	13.8	20.4	0.5

2011	30	Rhizon	29.6	0.4	0.1	217.9	13.1	35.8	0.6
2011	30	Rhizon	33.4	0.4	0.0	209.9	12.6	47.4	0.7
2011	30	Rhizon	37.2	0.4	0.2	205.1	12.3	60.5	0.7
2011	30	Rhizon	41.0	0.1	0.0	185.9	11.2	74.8	0.7
2011	30	Rhizon	44.9	0.3	0.1	179.5	10.8	88.9	1.1
2011	30	Rhizon	46.8	0.2	0.0	165.2	9.9	97.0	0.8
2011	31	WCS	0.0	29.2	0.1	73.9	4.4		
2011	31	WCS	0.0	30.1	1.4	77.0	4.6		
2011	31	WCS	0.1	28.7	0.2	88.7	5.3		
2011	31	WCS	0.3	29.4	0.8	107.4	6.4		
2011	31	WCS	0.5	29.7	0.3	115.6	6.9		
2011	31	WCS	0.6	32.0	1.0	121.5	7.3		
2011	31	WCS	0.8	31.0	0.1	132.0	7.9		
2011	31	WCS	1.0	31.7	0.0	142.6	8.6		
2011	31	WCS	1.2	32.0	0.4	149.0	8.9		
2011	31	WCS	1.3	31.4	0.3	153.0	9.2		
2011	31	WCS	1.5	36.8	0.1	156.2	9.4		
2011	31	WCS	1.7	30.6	0.1	155.1	9.3		
2011	31	WCS	2.6	23.6	1.4				
2011	31	Rhizon	0.0	23.7	0.0	77.3	4.6	0.0	0.0
2011	31	Rhizon	1.1	29.9	0.1	137.1	8.2	0.0	0.0
2011	31	Rhizon	3.0	31.0	0.1	166.9	10.0	0.0	0.0
2011	31	Rhizon	4.9	30.7	1.2	188.0	11.3	0.0	0.0
2011	31	Rhizon	6.8	32.4	0.1	226.7	13.6	0.0	0.0
2011	31	Rhizon	9.7	33.0	0.0	258.3	15.5	0.0	0.0
2011	31	Rhizon	11.6	32.6	0.0	270.6	16.2	0.0	0.0
2011	31	Rhizon	13.5	30.1	0.4	268.9	16.1	0.0	0.0
2011	31	Rhizon	15.4	28.7	0.1	265.4	15.9	0.0	0.0
2011	31	Rhizon	19.2	23.7	0.2	256.6	15.4	0.0	0.0
2011	31	Rhizon	23.1	18.7	0.0	237.2	14.2	0.0	0.0
2011	31	Rhizon	26.9	13.7	0.4	244.3	14.7	3.0	0.8
2011	31	Rhizon	30.7	9.8	0.0	228.5	13.7	7.6	0.8
2011	31	Rhizon	34.5	4.9	0.0	193.3	11.6	10.8	0.8
2011	31	Rhizon	38.3	1.2	0.0	202.1	12.1	13.5	0.8
2011	31	Rhizon	42.1	0.3	0.1	189.8	11.4	25.5	0.8
2011	33	WCS	0.0	24.0	0.2	59.0	3.5		
2011	33	WCS	0.0	23.7	0.2	58.9	3.5		
2011	33	WCS	0.1	25.3	0.2	70.1	4.2		
2011	33	WCS	0.3	26.8	0.2	88.5	5.3		
2011	33	WCS	0.5	27.7	0.3	102.1	6.1		
2011	33	WCS	0.7	28.3	0.1	112.3	6.7		
2011	33	WCS	0.8	28.9	0.2	121.1	7.3		
2011	33	WCS	1.0	28.9	0.2	134.7	8.1		
2011	33	WCS	1.2	29.3	0.1	139.9	8.4		
2011	33	WCS	1.4	29.6	0.2	155.0	9.3		
2011	33	WCS	1.6	30.1	0.0	166.3	10.0		
2011	33	WCS	1.8	30.4	0.0	169.6	10.2		
2011	33	WCS	2.0	23.8	0.1				
2011	33	WCS	2.2	30.3	0.2				

2011	33	WCS	2.9	30.6	0.0				
2011	33.1	Rhizon	0.0	24.8	0.0	60.5	3.6	0.29	0.06
2011	33.1	Rhizon	1.5	28.3	0.1	67.3	4.0	0.08	0.06
2011	33.1	Rhizon	3.4	28.3	0.1	140.9	8.5	0.27	0.06
2011	33.1	Rhizon	5.3	30.3	0.2	149.4	9.0	0.66	0.06
2011	33.1	Rhizon	9.3	30.8	0.0	187.1	11.2	0.21	0.06
2011	33.1	Rhizon	11.2	30.7	0.1	202.5	12.1	0.09	0.06
2011	33.1	Rhizon	13.1	10.8	0.3	240.1	14.4		
2011	33.1	Rhizon	15.0	29.0	0.1	258.9	15.5	0.13	0.06
2011	33.1	Rhizon	18.8	26.7	0.1	269.2	16.2	0.06	0.06
2011	33.1	Rhizon	22.6	24.0	0.0	252.1	15.1	0.11	0.06
2011	33.1	Rhizon	26.5	20.7	0.1	257.2	15.4	0.16	0.06
2011	33.1	Rhizon	30.3	17.3	0.1	252.1	15.1	0.64	0.06
2011	33.1	Rhizon	36.0	12.4	0.1	245.2	14.7	0.08	0.06
2011	33.1	Rhizon	41.7	6.4	0.1	243.5	14.6	0.37	0.06
2011	33.2	Rhizon	0.0	22.3	0.4	72.5	4.3	0.04	0.06
2011	33.2	Rhizon	2.0	27.7	0.1	140.9	8.5	0.04	0.06
2011	33.2	Rhizon	9.0	31.6	0.2	207.6	12.5	0.02	0.06
2011	33.2	Rhizon	14.0	30.8	0.1	243.5	14.6		
2011	33.2	Rhizon	21.0	25.1	0.2	257.2	15.4	0.13	0.06
2011	33.2	Rhizon	28.0	23.0	0.3	226.4	13.6	0.02	0.06
2011	33.2	Rhizon	39.0	30.3	0.2	235.0	14.1	0.05	0.06
2012	1	WCS	0.0	23.2	0.0	35.9	2.2		
2012	1	WCS	0.0	24.1	0.2	35.9	2.2		
2012	1	WCS	0.1	24.3	0.3	34.1	2.0		
2012	1	WCS	0.3	26.2	0.4	34.1	2.0		
2012	1	WCS	0.4	28.1	0.2	83.7	5.0		
2012	1	WCS	0.6	29.1	0.1	83.7	5.0		
2012	1	WCS	0.8	31.4	0.0	81.9	4.9		
2012	1	WCS	1.0	30.4	0.2	81.9	4.9		
2012	1	WCS	1.1	32.3	1.5	97.8	5.9		
2012	1	WCS	1.3	29.2	0.1	99.6	6.0		
2012	1	WCS	1.5	29.3	0.1	99.6	6.0		
2012	1	WCS	1.6	29.3	0.4	99.6	6.0		
2012	1	Rhizon	0.0	24.1	0.2	35.9	2.2	0	
2012	1	Rhizon	2.7	28.8	0.2	103.7	6.2	0	
2012	1	Rhizon	4.6	32.3	0.2	144.1	8.6	0	
2012	1	Rhizon	6.5	35.4	0.0	170.5	10.2	0	
2012	1	Rhizon	8.4	38.3	0.3	195.1	11.7	0	
2012	1	Rhizon	10.3	36.0	0.0	198.0	11.9	0	
2012	1	Rhizon	12.2	32.9	0.0	210.6	12.6	0	
2012	1	Rhizon	16.0	28.4	0.1	202.0	12.1	0	
2012	1	Rhizon	19.8	23.1	0.0	196.3	11.8	0	
2012	1	Rhizon	23.7	18.8	0.1	181.2	10.9	0	
2012	2	WCS	0.0	20.5	0.1	51.0	3.1		
2012	2	WCS	0.0	14.4	0.2	65.6	3.9		
2012	2	WCS	0.1	28.9	1.6	100.3	6.0		
2012	2	WCS	0.3	33.3	0.2	114.5	6.9		
2012	2	WCS	0.4	30.1	0.3	126.4	7.6		

2012	2	WCS	0.6	30.1	0.0	139.4	8.4		
2012	2	WCS	0.7	30.4	0.0	145.8	8.7		
2012	2	WCS	0.8	31.0	0.3	152.9	9.2		
2012	2	Rhizon	0.0	21.4	0.1	68.1	4.1	0.0	
2012	2	Rhizon	1.4	28.1	0.5	227.1	13.6	0.0	
2012	2	Rhizon	3.3	29.5	0.6	318.0	19.1	0.0	
2012	2	Rhizon	5.2	26.5	0.2	372.1	22.3	0.0	
2012	2	Rhizon	7.1	18.2	0.2	373.9	22.4	0.0	
2012	2	Rhizon	9.0	8.6	0.0	400.1	24.0	13.3	0.1
2012	2	Rhizon	10.9	0.0		359.9	21.6	27.6	0.1
2012	2	Rhizon	14.7	0.0		279.5	16.8	42.9	0.7
2012	2	Rhizon	18.5	0.0		324.9	19.5	63.5	0.7
2012	2	Rhizon	26.2	0.0		286.5	17.2	72.5	0.7
2012	2	Rhizon	33.8	0.0		235.8	14.2	79.6	0.8
2012	2	Rhizon	37.6	0.0		256.8	15.4	89.3	0.7
2012	2	Rhizon	42.4	0.0		251.6	15.1	94.2	0.6
2012	5	WCS	0.0	19.7	0.2	15.2	0.9		
2012	5	WCS	0.0	18.8	0.1	18.8	1.1		
2012	5	WCS	0.1	17.0	0.9	75.8	4.5		
2012	5	WCS	0.2	26.3	0.1	99.2	6.0		
2012	5	WCS	0.4	25.4	0.1	114.0	6.8		
2012	5	WCS	0.6	22.2	0.7	134.6	8.1		
2012	5	WCS	0.8	24.6	0.1	147.3	8.8		
2012	5	WCS	1.0	22.4	1.0	151.7	9.1		
2012	5	WCS	1.1	24.0	0.7	154.7	9.3		
2012	5	WCS	1.3	24.0	0.0	162.1	9.7		
2012	5	WCS	1.5	20.4	0.9	163.9	9.8		
2012	5	WCS	1.6	20.9	1.4	162.1	9.7		
2012	5	WCS	1.7	19.7	0.1	178.7	10.7		
2012	5	Rhizon	0.0	18.0	0.0	39.5	2.4	0.0	
2012	5	Rhizon	1.8	19.9	0.2	182.4	10.9	0.0	
2012	5	Rhizon	3.7	8.0	0.0	280.4	16.8	0.0	
2012	5	Rhizon	5.6	0.0		353.1	21.2	7.0	0.1
2012	5	Rhizon	7.5	0.0		368.7	22.1	9.9	0.1
2012	5	Rhizon	9.4	0.0		401.6	24.1	11.2	0.1
2012	5	Rhizon	11.3	0.0		413.5	24.8	12.1	0.1
2012	5	Rhizon	14.1	0.0		398.6	23.9	12.1	0.1
2012	5	Rhizon	17.9	0.0		421.4	25.3	12.5	0.1
2012	5	Rhizon	21.7	0.0		410.3	24.6	12.5	0.1
2012	5	Rhizon	25.6	0.0		411.9	24.7	12.5	0.1
2012	5	Rhizon	31.3	0.0		413.6	24.8	12.8	0.1
2012	5	Rhizon	37.0	0.0		407.9	24.5	12.8	0.1
2012	5	Rhizon	42.7	0.0		409.6	24.6	12.8	0.1
2012	5	Rhizon	48.4	0.0		361.8	21.7		
2012	5	Rhizon	54.1	0.0		400.4	24.0	12.8	0.1
2012	5	Rhizon	60.8	0.0		393.1	23.6	14.0	0.1

REFERENCES

Goloway, F., Bender, M.L., 1982. Diagenetic models of interstitial nitrate profiles in deep sea suboxic sediments. Limnology and Oceanography 624–638.

Hales, B., Emerson, S.R., Archer, D.E., 1994. Respiration and dissolution in the sediments of the western North Atlantic: estimates from models of in situ microelectrode measurements of porewater oxygen and pH. Deep Sea Research I 41, 695–719.

Hammond, D.E., McManus, J., Berelson, W.M., Kilgore, T.E., Pope, R.H., 1996. Early diagenesis of organic material in equatorial Pacific sediments: stoichiometry and kinetics. Deep Sea Research Part II: Topical Studies in Oceanography 43, 1365–1412.

Lochte, K., Turley, C., 1986. Bacteria and cyanobacteria associated with phytodetritus in the deep sea. Nature 333, 67–69.

Martin, W.R., Sayles, F.L., 1996. CaCO3 dissolution in sediments of the Ceara Rise, western equatorial Atlantic. Geochimica et Cosmochimica Acta 60, 243–263.

Martin, W.R., Sayles, F.L., 2004. Organic matter cycling in sediments of the continental margin in the northwest Atlantic Ocean. Deep Sea Research Part I 51, 457–489.

Martin, W.R., Sayles, F.L., 2006. Organic matter oxidation in deep-sea sediments: distribution in the sediment column and implications for calcite dissolution. Deep Sea Research Part II 53, 771–792.

Rice, A.L., Billett, D.S.M., Fry, J.C., John, A., Lampitt, R.S., Mantoura, R.F.C., Morris, R., 1986. Seasonal deposition of phytodetritus to the deep-sea floor. Proceedings of the Royal Society of Edinburgh 88b, 265–279.

Smith, C.R., Hoover, D.J., Doan, S., Pope, R.H., DeMaster, D.J., Dobbs, F.C., Altabet, M.A., 1996. Phytodetritus at the abyssal seafloor across 10 of latitude in the central equatorial Pacific. Deep Sea Research Part II: Topical Studies in Oceanography 43, 1309–1338.

Sun, M., Aller, R.C., Lee, C., 1991. Early diagenesis of chlorophyll-a in Long Island Sound sediments: A measure of carbon flux and particle reworking. Journal of Marine Research 49, 379–401.

WOCE Data Products Committee, 2002. WOCE Global Data, Version 3.0. WOCE International Project Office.

Supplemental information to Chapter 3

B1. POWER LAW FIT TO DATA FROM A DEEP TRAP ARRAY

Honjo (1980) collected data from a sediment trap array moored at 13.5˚N 54.0˚W. The POC flux data was fit with a power law to calculate the attenuation coefficient with depth.

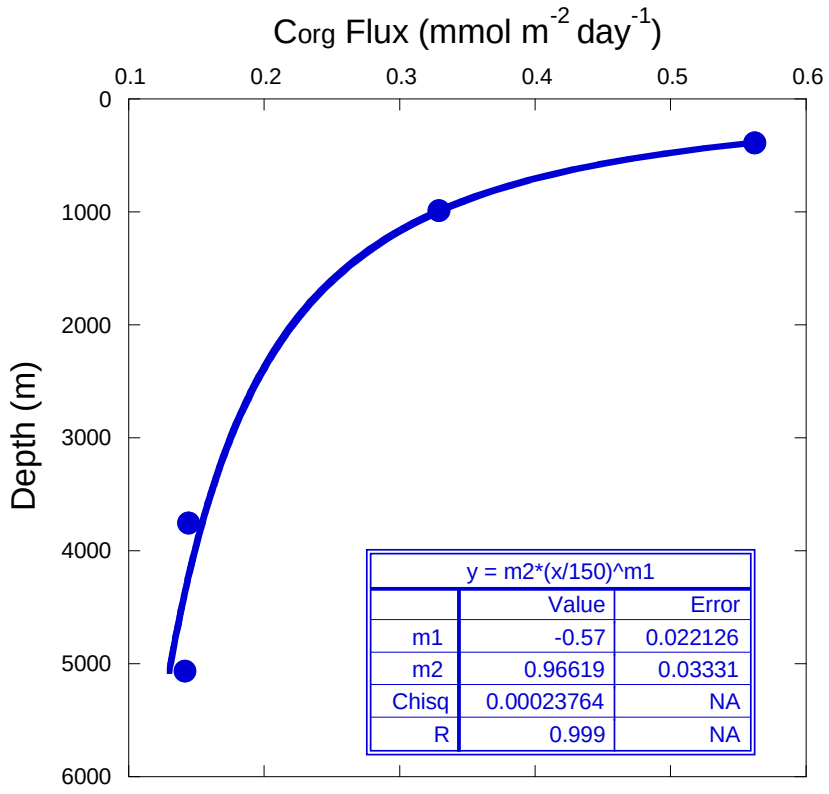

B.2 COMPARISON OF D_b TO SURFACE C_{org}

Assuming sediment C_{org} profile can be fit by $C = C_0 \exp(-ßz)$, where $ß = \sqrt{(k/D_b)}$, applying Fick's first law yields a relationship between the C_{org} flux and D_b

such that C_{org} flux = $C_0\sqrt{kD_b}$. A comparison of C_0 and $\sqrt{D_b}$ will determine the importance of the bioturbation rate to the surface C_{org} concentration.

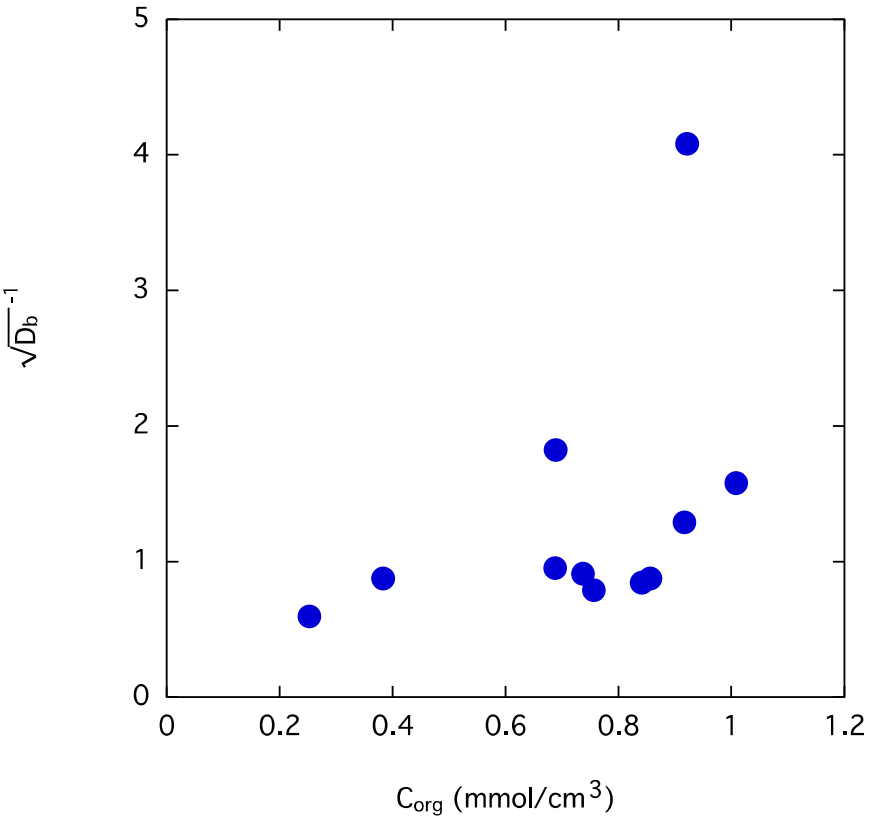

B.3 SEDIMENT MIXED LAYER BOX MODEL

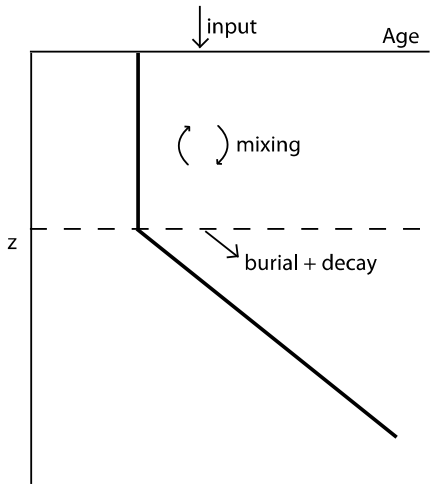

The ^{14}C activity of the sediment mixed layer is defined as:

$$A_0 s = A_m s + \lambda h A_m \qquad (1)$$

where A_0 is the ^{14}C activity of incoming material to the mixed zone, A_m is the ^{14}C activity of the mixed zone, s is the sedimentation rate, λ is the half-life of ^{14}C, and h is the depth of the mixed zone. The left side of Eq. 1 represents the input of material to the mixed zone, and the right side represents output via burial and decay. Eq. 1 can be simplified to

$$A_0 = A_m(\frac{s+\lambda h}{s}) \qquad (2)$$

^{14}C activity can be described as an exponential such that

$$A_i = e^{-\lambda t_i} \qquad (3)$$

where t is the calendar age. Eq. 3 can be substituted into Eq. 2 to obtain an equation in terms of the calendar age.

$$e^{-\lambda t_0} = e^{-\lambda t_m}(1 + \frac{\lambda h}{s}) \qquad (4)$$

Eq. 4 can be rewritten as

$$e^{\lambda(t_m - t_0)} = (1 + \frac{\lambda h}{s}) \qquad (5)$$

And solving for s, we obtain

$$s = \frac{\lambda h}{(e^{\lambda(t_m - t_0)} - 1)} \qquad (6)$$

Assuming the age of incoming material is equal to the deep water reservoir age of 800 years, and our measurements of the mixed layer calendar age and the depth of the sediment mixed layer, we calculated s for each station. At station 2010-27, we estimated the age of the mixed zone by extrapolating the sedimentation rate at depth to 10 cm. At station 2011-1, a mixed layer depth of 10 cm was assumed. The results of the model simulation are in the table below and in Chapter 3 Table 6.

B.3-1 Mixed Layer Box Model Results

Results of the box model simulation. (*) indicates stations where the ML depth was assumed rather than measured from excess ^{210}Pb profiles.

Station	ML depth (cm)	Age of ML kyr	ML Sed Rate (cm/kyr)

2010-19	16	1.407	25.4
2010-21	12	3.384	3.9
2010-27	10	4[a]	2.6
2011-1*	10	2.284	6.2
2011-9[b]	12	0.663	
2011-23	10	4.985	1.8
2011-31	12	3.573	3.2

[a] ML age estimated from extrapolation of the linear sedimentation rate to 10 cm.

[b] ML Sed. Rate not determined due to low ML age. The deep water reservoir age is likely younger here.

B.4 MULTI-CORE SOLID PHASE DATA

Year	Station	Depth (cm)	Porosity	$^{210}Pb_{excess}$ (Bq/kg)	bSi (wt%)	C_{org} (wt%)	$\delta^{13}C_{org}$ (‰)	CaCO3 (wt%)	$\delta^{13}C_{(TIC)}$ (‰)	$\delta^{15}N$ (‰)
2010	1	0.5				0.70	-18.73	28.7	0.93	5.20
2010	1	1.5	0.83							4.79
2010	1	2.5	0.82							
2010	1	3.5	0.82			0.64	-19.14	30.2	1.04	
2010	1	4.5	0.81			0.55	-19.22	28.6	1.04	
2010	1	6	0.78			0.50	-20.11	28.1	1.03	
2010	1	8				0.55	-16.83	27.7	1.03	
2010	1	10	0.74			0.38	-24.18	28.6	0.98	
2010	1	12	0.75							
2010	1	14	0.75			0.41	-19.48	28.9	0.96	
2010	1	16	0.75							
2010	1	18	0.75							
2010	1	20	0.74							
2010	1	22	0.74			0.35	-18.43	30.9	0.87	
2010	1	24	0.72							
2010	1	26	0.72			0.25	-24.18	28.7	0.78	
2010	1	28	0.71							
2010	1	30	0.69			0.19	-27.15	21.8	0.56	
2010	1	32	0.66							
2010	5	0.5	0.89		1.54	0.75	-21.64	15.0	0.89	5.04
2010	5	1.5	0.87	0.66						5.15
2010	5	2.5	0.85		1.26					
2010	5	3.5	0.81	0.17						

2010	5	4.5	0.82		1.19	0.59	-21.26	13.9	0.94	
2010	5	6	0.83	0.26						
2010	5	8	0.77		1.27	0.57	-19.76	20.6	1.07	
2010	5	10	0.76	0.12						
2010	5	12	0.73	0.05						
2010	5	14	0.73		1.02	0.54	-19.15	23.3	1.06	
2010	5	16	0.73	0.03						
2010	5	18	0.71			0.45	-22.42	24.4	0.99	
2010	5	20	0.70		0.83					
2010	5	22				0.25		29.9	0.97	
2010	5	24.5			0.69	0.38	-22.18	33.1	0.96	
2010	6	0.5	0.85		0.66	0.62	-18.86	19.6	0.91	4.88
2010	6	1.5	0.81							4.38
2010	6	2.5	0.79		1.07					
2010	6	3.5	0.80			0.58	-18.98	30.3	0.97	
2010	6	4.5	0.78		0.87					
2010	6	6	0.77			0.84	-19.07	31.7	0.90	
2010	6	8	0.78		0.81					
2010	6	10	0.75			0.49	-19.70	36.1	0.88	
2010	6	12	0.73							
2010	6	14	0.72		0.89	0.41	-18.84	37.1	0.74	
2010	6	16	0.72							
2010	6	18	0.71		0.61	0.46	-13.63	39.5	0.76	
2010	6	20	0.69							
2010	6	22	0.68					78.2	0.61	
2010	6	24	0.70							
2010	6	26	0.69		0.53	0.43	-12.24	39.7	0.52	
2010	6	28	0.69			0.42	-13.20	42.5	0.54	
2010	6	30	0.70			0.32	-17.89	37.9	0.41	
2010	6	32	0.66		0.49					
2010	7	0.5	0.84			0.45	-23.96	44.4	1.02	5.61
2010	7	1.5	0.81							4.58
2010	7	2.5	0.75							
2010	7	3.5	0.77			0.64	-12.18	46.1	1.10	
2010	7	4.5	0.76							
2010	7	6	0.73			0.44	-16.03	45.6	0.94	
2010	7	8	0.74							
2010	7	10	0.73					45.1	0.90	
2010	7	12	0.72							
2010	7	14	0.71			1.07		44.6	0.71	
2010	7	16	0.68							
2010	7	18	0.69			0.08		49.0	0.67	
2010	7	20	0.69							

2010	7	22	0.69		0.27	-18.59	44.4	0.56	
2010	7	24	0.70		0.27	-21.50	35.6	0.31	
2010	7	26	0.70		0.21	-27.37	31.7	0.28	
2010	7	28	0.71						
2010	7	30	0.71		0.28	-20.81	28.4	0.18	
2010	9	0.5	0.90						5.00
2010	9	1.5	0.87						5.15
2010	9	2.5	0.84						
2010	9	3.5	0.85						
2010	9	4.5	0.84						
2010	9	6	0.84						
2010	9	8	0.82						
2010	9	10	0.80						
2010	9	12	0.77						
2010	9	14	0.77						
2010	9	16	0.76						
2010	9	18	0.76						
2010	9	20	0.77						
2010	9	22	0.77						
2010	9	24	0.75						
2010	9	26	0.75						
2010	9	28	0.74						
2010	9	30	0.73						
2010	9	32	0.73						
2010	9	34	0.73						
2010	9	36	0.71						
2010	19	0.5	0.86		0.85	-20.08	8.4	0.92	5.22
2010	19	1.5	0.86	0.63					5.94
2010	19	2.5	0.84		0.73	-19.83	8.1	1.11	
2010	19	3.5	0.79	0.43					
2010	19	4.5	0.82						
2010	19	6	0.81	0.36	0.68	-20.30	8.4	1.06	
2010	19	8	0.79						
2010	19	10	0.78	0.19					
2010	19	12	0.75	0.11					
2010	19	14	0.75		0.61	-20.37	11.5	1.22	
2010	19	16	0.76	0.03					
2010	19	18	0.76		0.61	-20.31	14.1	1.19	
2010	19	20	0.76						
2010	19	22	0.74						
2010	19	24	0.76		0.67	-18.83	18.6	1.09	
2010	19	26	0.75						
2010	19	28	0.76						

2010	19	30	0.75			0.46	-18.79	22.0	1.13	
2010	19	32	0.74							
2010	19	34	0.75			0.40	-19.29	25.8	1.02	
2010	19	36	0.75							
2010	19	38	0.73			0.40	-18.73	28.6	0.89	
2010	20	0.5	0.89			0.95	-19.75	13.5	0.83	5.27
2010	20	1.5	0.84	0.30						5.05
2010	20	2.5	0.83							
2010	20	3.5	0.82	0.07		0.55	-20.52	15.0	1.21	
2010	20	4.5	0.81							
2010	20	6	0.79	0.01						
2010	20	8	0.79							
2010	20	10	0.78	0.04		0.55	-19.31	17.3	1.11	
2010	20	12	0.78	0.06						
2010	20	14	0.78							
2010	20	16	0.76	0.08		0.42	-19.99	23.2	1.18	
2010	20	18	0.75							
2010	20	20	0.77			0.37	-20.80	28.5	1.10	
2010	20	22	0.76							
2010	20	24	0.75			0.34	-17.57	33.1	0.91	
2010	20	26	0.74			0.45	-13.53	32.6	0.88	
2010	20	28	0.74			0.30	-19.27	35.0	0.81	
2010	20	30	0.74							
2010	20	32	0.74							
2010	20	34	0.74			0.23	-22.48	23.7	0.67	
2010	20	36	0.74							
2010	20	38	0.73							
2010	20	40	0.74			0.24	-19.96	12.9	0.53	
2010	20	42	0.75							
2010	20	44	0.75			0.24	-23.12	14.8	0.62	
2010	21	0.5	0.91		2.55	0.97	-20.51	5.8	0.71	5.00
2010	21	1.5	0.89	1.39						5.37
2010	21	2.5	0.88		1.61			5.6	0.72	
2010	21	3.5	0.87	0.71						
2010	21	4.5	0.86		1.60	0.88	-19.45	5.6	0.56	
2010	21	6	0.86	0.48						
2010	21	8	0.84		1.59	0.81	-20.46	5.7	0.87	
2010	21	10	0.83	0.33						
2010	21	12	0.83	0.03				5.9	0.74	
2010	21	14	0.81		1.38	0.68	-19.12	6.1	0.78	
2010	21	16	0.80	0.09						
2010	21	18	0.79			0.63	-19.29	7.1	0.95	
2010	21	20	0.79		1.54					

2010	21	22	0.78			0.58	-20.48	8.2	0.98	
2010	21	24	0.78			0.53	-18.86	10.8	1.09	
2010	21	26	0.78		1.46	0.59	-18.73	11.3	1.07	
2010	21	28	0.77			0.65	-17.99	13.4	1.18	
2010	21	30	0.77			0.61	-16.83	16.4	1.20	
2010	21	32	0.77		0.97	0.54	-15.91	18.7	1.22	
2010	21	34	0.77			0.52	-16.32	20.0	1.19	
2010	21	36	0.76			0.52	-15.26	21.7	1.16	
2010	21	38	0.76			0.52	-12.94	24.8	1.08	
2010	21	40	0.77			0.47	-13.23	27.1	1.12	
2010	21	42	0.76			0.47	-13.15	27.3	1.03	
2010	23	0.5	0.88		1.20	0.70	-19.07	17.5	1.10	
2010	23	1.5	0.85	0.21						
2010	23	2.5	0.83		1.28					
2010	23	3.5	0.83	0.33		0.67	-19.46	19.4	1.09	
2010	23	4.5			1.65	0.68	-19.67	19.7	1.11	
2010	23	6	0.81	0.26		0.61	-20.24	19.9	1.09	
2010	23	8	0.80		1.10	0.51	-20.80	20.1	1.10	
2010	23	10	0.77	0.05		0.49	-19.93	22.0	1.14	
2010	23	12	0.76	0.05		0.50	-20.62	20.4	1.07	
2010	23	14	0.75		1.23	0.46	-22.33	21.2	1.08	
2010	23	16	0.74	0.02		0.40	-21.82	23.8	1.07	
2010	23	18	0.74		0.73	0.36	-21.95	24.5	0.98	
2010	25	0.5	0.89		1.44	0.71	-20.72	26.0	0.95	4.58
2010	25	1.5	0.84	0.36						5.16
2010	25	2.5	0.81		0.91					
2010	25	3.5	0.82	0.17		0.51	-23.16	27.8	1.11	
2010	25	4.5	0.80		0.96					
2010	25	6	0.80	0.10		0.52	-21.01	27.2	1.08	
2010	25	8	0.80		1.03					
2010	25	10	0.77	0.04						
2010	25	12	0.77	0.03						
2010	25	14	0.75		0.87	0.39	-21.90	27.5	0.93	
2010	25	16	0.75	0.03						
2010	25	18	0.75			0.37	-20.46	30.1	0.89	
2010	25	20	0.75		0.80					
2010	25	22	0.74							
2010	25	24	0.74			0.30	-24.90	33.5	0.92	
2010	25	26	0.73		0.57					
2010	25	28	0.72			0.35	-17.60	25.4	0.66	
2010	25	30	0.72							
2010	25	32	0.71		0.54					
2010	25	34	0.71			0.25	-22.18	17.7	0.55	

2010	25	36	0.73							
2010	25	38	0.73			0.24	-23.67	15.4	0.48	
2010	26	0.5				0.76	-18.85	21.7	0.97	4.96
2010	26	1.5		0.27						5.13
2010	26	2.5								
2010	26	3.5		0.28		0.57	-17.97	23.5	1.02	
2010	26	4.5								
2010	26	6		0.14						
2010	26	8								
2010	26	10		0.07		0.59	-14.37	24.9	0.95	
2010	26	12		0.06						
2010	26	14								
2010	26	16		0.03		0.47	-11.77	31.5	0.83	
2010	26	18				0.40	-11.71	33.7	0.78	
2010	26	20				0.37	-16.72	34.5	0.76	
2010	26	22				0.27	-21.44	35.8	0.69	
2010	26	24				0.23	-23.44	34.2	0.58	
2010	26	26				0.24	-21.83	31.4	0.56	
2010	26	28								
2010	26	30				0.34	-15.93	27.9	0.62	
2010	26	32								
2010	26	34				0.27	-19.70	21.9	0.52	
2010	27	0.5	0.84		1.02	0.46	-21.90	17.4	0.96	4.46
2010	27	1.5	0.79	0.09						4.75
2010	27	2.5	0.79		0.68					
2010	27	3.5	0.79	0.14		0.32	-23.42	22.1	0.78	
2010	27	4.5	0.77		0.90					
2010	27	6	0.77	0.21		0.39	-20.44	20.3	0.86	
2010	27	8	0.76		1.06					
2010	27	10	0.76	0.07						
2010	27	12	0.74	0.10						
2010	27	14	0.74		0.73	0.25	-21.52	16.9	0.49	
2010	27	16	0.73	0.07						
2010	27	18	0.73			0.16		7.2	0.41	
2010	27	20	0.74		0.79					
2010	27	22	0.75							
2010	27	24	0.74			0.20		4.5		
2010	27	26	0.74		1.02					
2010	27	28	0.74							
2010	27	30	0.75			0.16		4.5		
2010	27	32	0.75		1.08					
2010	27	34	0.75			0.17		4.5		
2010	27	36	0.75							

2010	27	38	0.76						
2010	27	40	0.76		0.16		4.0		
2011	1	0.5	0.88	1.18	0.59		27.8	0.94	4.98
2011	1	1.5	0.79						4.42
2011	1	2.5	0.81	0.96					
2011	1	3.5	0.82						
2011	1	4.5	0.78	1.12					
2011	1	6	0.79						
2011	1	8	0.78	1.15	0.50		28.6	0.95	
2011	1	10	0.77						
2011	1	12	0.76						
2011	1	14	0.75	0.83					
2011	1	16	0.75						
2011	1	18	0.75	0.71					
2011	1	20	0.74						
2011	1	22	0.73						
2011	1	24	0.72						
2011	1	26	0.70	0.53	0.23		28.2	0.70	
2011	1	28	0.69						
2011	1	30	0.65						
2011	1	32	0.63	0.50					
2011	1	34	0.56						
2011	1	36	0.51						
2011	3	0.5	0.90				16.7	1.07	4.50
2011	3	1.5	0.86						4.84
2011	3	2.5	0.85						
2011	3	3.5	0.84						
2011	3	4.5	0.83		0.73	-19.00	18.6	1.22	
2011	3	6	0.82						
2011	3	8	0.80		0.65	-17.54	18.3	1.18	
2011	3	10	0.79						
2011	3	12	0.77						
2011	3	14	0.76		0.49	-20.80	19.3	1.20	
2011	3	16	0.75						
2011	3	18	0.75		0.43	-21.88	22.3	1.12	
2011	3	20	0.75						
2011	3	22	0.75		0.47	-17.39	25.7	1.12	
2011	3	24	0.75						
2011	3	26	0.75		0.37	-20.48	29.0	1.00	
2011	3	28	0.75		0.45	-9.22	30.5	1.02	
2011	3	30	0.75						
2011	3	32	0.75		0.35	-20.45	30.5	0.91	
2011	3	34	0.75						

2011	3	36	0.75			0.35	-17.82	26.0	0.75	
2011	3	38	0.74							
2011	6	0.5	0.90		2.46	0.78	-21.04	4.7	0.80	5.46
2011	6	1.5	0.87							5.29
2011	6	2.5	0.85		2.43					
2011	6	3.5	0.85		2.64	0.90	-20.33	3.0	0.56	
2011	6	4.5	0.83		2.55					
2011	6	5.5	0.81							
2011	6	6.5	0.80		2.52	0.92	-20.25	6.5	1.19	
2011	6	7.5	0.79		2.18	0.85	-20.14	6.9	1.23	
2011	8	0.5	0.91			0.78	-20.70	10.6	0.87	4.86
2011	8	1.5	0.87	0.65						5.29
2011	8	2.5	0.85							
2011	8	3.5	0.83	0.32		0.61	-21.40	8.6	0.76	
2011	8	4.5	0.83							
2011	8	6	0.81	0.34		0.63	-21.93	9.6	0.63	
2011	8	8	0.78							
2011	8	10	0.78	0.13		0.62	-22.71	18.5	0.52	
2011	8	12	0.78	0.06						
2011	8	14	0.77			0.59	-20.47	23.2	1.06	
2011	8	16	0.77	0.20						
2011	8	18	0.75			0.54	-19.84	24.5	1.15	
2011	8	20	0.74			0.46	-22.07	25.2	1.16	
2011	8	22	0.73			0.43	-22.01	26.5	1.15	
2011	8	24	0.73			0.49	-18.08	27.9	1.14	
2011	8	26	0.74			0.48	-20.07	27.1	1.09	
2011	9	0.5	0.88		1.17	0.60	-22.18	8.8	0.94	4.91
2011	9	1.5	0.86							5.06
2011	9	2.5	0.83		1.23					
2011	9	3.5	0.83			0.63	-21.46	9.8	0.86	
2011	9	4.5	0.83		1.19					
2011	9	6	0.79			0.58	-22.37	9.4	0.90	
2011	9	8	0.78		1.03					
2011	9	10	0.74			0.65	-20.80	20.2	0.93	
2011	9	12	0.76							
2011	9	14	0.76		0.86	0.52	-23.47	27.1	0.79	
2011	9	16	0.76							
2011	9	18	0.00		0.99	0.46	-22.92	33.4	0.94	
2011	9	20	0.74							
2011	9	22	0.73			0.53	-17.45	36.8	0.93	
2011	9	24	0.72							
2011	9	26			0.95					
2011	9	28	0.71			0.49	-15.86	39.5	0.81	

2011	9	30	0.71						
2011	9	32	0.71	0.61					
2011	9	34	0.71		0.35	-22.62	40.7	0.73	
2011	9	36	0.71						
2011	9	38	0.71		0.49	-14.20	38.9	0.60	
2011	13	0.5	0.87	2.50	0.80	-19.64	5.9	0.81	5.16
2011	13	1.5	0.86						4.93
2011	13	2.5	0.86	2.51					
2011	13	3.5	0.85		0.73	-20.01	5.4	0.82	
2011	13	4.5	0.85	2.51					
2011	13	6	0.84		0.71	-20.49	5.4	0.82	
2011	13	8	0.82	2.57					
2011	13	10	0.81		0.74	-20.66	6.0	1.25	
2011	13	12	0.80						
2011	13	14	0.79	2.54	0.71		6.0	0.76	
2011	13	16	0.78						
2011	13	18	0.78		0.68	-20.67	7.9	1.44	
2011	13	20	0.78	1.66	0.66	-19.65	9.1	1.12	
2011	13	22	0.79		0.71	-19.46	11.7	1.18	
2011	13	24	0.78		0.67	-26.79	14.2	1.11	
2011	13	26	0.78	1.11	0.52	-25.40	16.0	1.13	
2011	13	28	0.77		0.56	-22.07	16.1	1.46	
2011	13	30	0.76						
2011	13	32	0.76	0.90	0.49	-20.58	18.9	1.19	
2011	13	34	0.75						
2011	19	0.5	0.85		0.76	-15.55	44.8	0.94	4.65
2011	19	1.5	0.81						4.25
2011	19	2.5	0.78						
2011	19	3.5	0.77		0.69	-14.48	44.8	1.09	
2011	19	4.5	0.78						
2011	19	6	0.77		0.67	-21.04	45.0	0.97	
2011	19	8	0.75						
2011	19	10	0.74						
2011	19	12	0.72		0.29	-28.57	43.6	0.98	
2011	19	14	0.72						
2011	19	16	0.71		0.38	-16.68	41.9	0.68	
2011	19	18	0.71						
2011	19	20	0.71		0.33	-19.75	45.1	0.59	
2011	19	22	0.71						
2011	19	24	0.70		0.47	-14.19	42.2	0.51	
2011	19	26	0.71						
2011	19	28	0.72		0.37	-17.21	33.6	0.44	
2011	19	30	0.71		0.18		29.2	0.4	

2011	20	0.5	0.80		0.62	0.23		55.4	0.98	3.80
2011	20	1.5	0.79							3.84
2011	20	2.5	0.76		0.53					
2011	20	3.5	0.76			0.23		59.1	1.06	
2011	20	4.5	0.75		0.70					
2011	20	6	0.73			0.04		56.3	0.85	
2011	20	8	0.72		0.16					
2011	20	10	0.70			0.01		51.4	0.76	
2011	20	12	0.70							
2011	20	14	0.70		0.43					
2011	20	16	0.69			0.23		58.1	0.45	
2011	20	18	0.70							
2011	20	20	0.70		0.68	0.23		40.2	0.26	
2011	20	22	0.71			0.08		31.4	0.28	
2011	20	24	0.70			0.12		18.3	0.12	
2011	20	26	0.70		0.78	0.11		6.6	0.51	
2011	20	28	0.70			0.19		1.0	0.72	
2011	20	30	0.68							
2011	22	0.5	0.85			0.58	-20.00	44.3	0.98	4.13
2011	22	1.5	0.80							4.31
2011	22	2.5	0.78							
2011	22	3.5	0.77							
2011	22	4.5	0.76			0.57	-16.70	47.2	1.04	
2011	22	6	0.76			0.47	-19.67	46.8	1.05	
2011	22	8	0.75							
2011	22	10	0.74							
2011	22	12	0.73			0.39	-20.05	44.9	0.90	
2011	22	14	0.73							
2011	22	16	0.72			0.31	-22.09	45.5	0.65	
2011	22	18	0.72							
2011	22	20	0.72			0.32	-17.00	44.6	0.53	
2011	22	22	0.71							
2011	22	24	0.72							
2011	22	26	0.73							
2011	22	28	0.73			0.22	-28.66	31.9	0.32	
2011	22	30	0.73							
2011	22	32	0.74			0.25	-21.62	22.8	0.25	
2011	22	34	0.74							
2011	22	36	0.75							
2011	22	38	0.74			0.26	-22.28	2.6	0.11	
2011	23	0.5	0.86		1.33	0.25		34.9	1.07	5.08
2011	23	1.5	0.80	0.19						4.91
2011	23	2.5	0.77		0.90					

2011	23	3.5	0.76	0.11		0.25		40.7	1.02	
2011	23	4.5	0.76		1.07					
2011	23	6	0.76	0.17		0.23		40.8	0.98	
2011	23	8	0.74		0.98					
2011	23	10	0.74	0.03						
2011	23	12	0.73	0.02		0.32	-26.73	40.5	0.67	
2011	23	14	0.74		0.46					
2011	23	16	0.72	0.10		0.08		35.1	0.33	
2011	23	18	0.73							
2011	23	20	0.72		0.51			25.5	0.39	
2011	23	22	0.73			0.26	-20.46	7.5	0.16	
2011	23	24	0.73			0.23	-22.84	3.5	0.10	
2011	23	26	0.72		0.59	0.20	-26.95	1.5		
2011	23	28	0.65			0.25	-15.83	0.1		
2011	23	30	0.64							
2011	23	32	0.64		0.54					
2011	23	34	0.65			0.17	-23.75	0.8		
2011	23	36	0.72							
2011	23	38	0.73			0.27	-22.74	5.3	1.12	
2011	23	40	0.71							
2011	23	41.5	0.69			0.35	-21.16	9.4	1.00	
2011	24	0.5	0.89		0.79	0.74	-21.20	10.1	1.10	4.80
2011	24	1.5	0.87							5.48
2011	24	2.5	0.85		0.77					
2011	24	3.5	0.86							
2011	24	4.5	0.84		0.71	0.59	-23.90	11.0	1.32	
2011	24	6	0.83							
2011	24	8	0.80		0.96					
2011	24	10	0.81							
2011	24	12	0.78			0.52	-18.81	33.1	1.03	
2011	24	14	0.78							
2011	24	16	0.76		0.83					
2011	24	18	0.77			0.46	-19.08	37.9	1.03	
2011	24	20	0.76							
2011	24	22	0.74			0.39	-17.91	39.5	0.86	
2011	24	24	0.75							
2011	24	26	0.75		0.51	0.35	-19.14	41.0	0.68	
2011	24	28	0.75							
2011	24	30	0.74			0.35	-15.86	37.7	0.57	
2011	24	32	0.75		0.60					
2011	24	34	0.74			0.38	-14.19	27.9	0.41	
2011	24	36	0.76							
2011	24	38	0.77							

2011	24	40	0.77		0.75	0.31	-20.48	13.8	0.88	
2011	24	42	0.77							
2011	25	0.5	0.86		1.04	0.38	-31.07	26.4	1.07	
2011	25	1.5		0.26						
2011	25	2.5	0.82		1.06					
2011	25	3.5	0.81	0.29		0.55	-21.17	27.8	1.25	
2011	25	4.5	0.80		1.32					
2011	25	6	0.79	0.21		0.47	-23.68	31.8	1.22	
2011	25	8	0.79		1.33					
2011	25	10	0.78	0.04						
2011	25	12	0.77	0.02		0.51	-17.06	35.2	1.19	
2011	25	14	0.76		1.19					
2011	25	16	0.75	0.06		0.42	-19.22	34.7	1.00	
2011	25	18	0.75							
2011	25	20	0.74		1.00	0.33	-23.84	38.2	0.99	
2011	25	22	0.73			0.34	-19.56	40.5	0.83	
2011	25	24	0.72			0.41	-15.18	37.7	0.75	
2011	25	26	0.72		0.77	0.28	-18.95	37.0	0.66	
2011	25	28	0.72			0.27	-21.24	31.5	0.63	
2011	25	30	0.73							
2011	25	32	0.73		0.76	0.37	-15.80	26.7	0.53	
2011	25	34	0.73							
2011	25	36	0.73			0.18	-30.14	19.1	0.48	
2011	25	38	0.72							
2011	27	0.5	0.87			0.63	-19.69	19.7	1.10	4.99
2011	27	1.5	0.83							4.86
2011	27	2.5	0.80							
2011	27	3.5	0.81							
2011	27	4.5	0.80			0.74	-20.68	19.0	1.09	
2011	27	6	0.78							
2011	27	8	0.77			0.58	-21.50	20.9	1.12	
2011	27	10	0.76							
2011	27	12	0.79			1.00	-21.15	17.8	0.92	
2011	27	14	0.77							
2011	27	16	0.75							
2011	27	18	0.74							
2011	27	20	0.74							
2011	27	22	0.74							
2011	27	24	0.72							
2011	28	0.5	0.91							4.87
2011	28	1.5	0.87							4.98
2011	28	2.5	0.85							
2011	28	3.5	0.85							

2011	28	4.5	0.85							
2011	28	6	0.83							
2011	28	8	0.81							
2011	28	10	0.82							
2011	28	12	0.81							
2011	28	14	0.81							
2011	28	16	0.78							
2011	28	18	0.77							
2011	28	20	0.75							
2011	28	22	0.77							
2011	28	24	0.76							
2011	28	26	0.75							
2011	28	28	0.76							
2011	28	30	0.76							
2011	28	32	0.74							
2011	30	0.5	0.88							5.25
2011	30	1.5	0.86							5.42
2011	30	2.5	0.83							
2011	30	3.5	0.83							
2011	30	4.5	0.81							
2011	30	6	0.81							
2011	30	8	0.80							
2011	30	10	0.78							
2011	30	12	0.79							
2011	30	14	0.79							
2011	30	16	0.79							
2011	30	18	0.78							
2011	30	20	0.77							
2011	30	24	0.78							
2011	30	28	0.77							
2011	30	32	0.77							
2011	30	36	0.77							
2011	30	40	0.76							
2011	31	0.5	0.91		2.28	0.89	-20.64	9.3	0.67	5.09
2011	31	1.5	0.86	0.34						4.98
2011	31	2.5	0.85		1.34					
2011	31	3.5	0.83	0.22		0.65	-18.95	11.7	1.00	
2011	31	4.5	0.83		1.21					
2011	31	6	0.82	0.08		0.56	-19.63	13.2	0.99	
2011	31	8	0.80		1.09					
2011	31	10	0.79	0.12		0.60	-18.79	16.0	1.16	
2011	31	12	0.78	0.10						
2011	31	14	0.78		1.23	0.57	-17.22	18.3	1.09	

2011	31	16	0.78	0.08						
2011	31	18	0.77			0.44	-20.54	23.1	1.12	
2011	31	20	0.77		0.90	0.45	-18.23	26.2	0.97	
2011	31	24	0.77			0.42	-16.16	30.8	0.85	
2011	31	26	0.77		0.74	0.40	-16.73	31.7	0.83	
2011	31	30	0.76			0.38	-15.39	26.5	0.70	
2011	31	32			0.71					
2011	31	34	0.78			0.25	-26.09	26.5	0.81	
2011	31	38	0.76							
2011	31	40	0.77			0.32	-20.34	11.1	0.60	
2011	33	0.5	0.85			0.59	-22.28	22.6	1.04	4.42
2011	33	1.5	0.83							4.89
2011	33	2.5	0.82							
2011	33	3.5	0.80							
2011	33	4.5	0.81			0.56	-21.00	23.6	1.13	
2011	33	6	0.80							
2011	33	8	0.79			0.49	-21.39	24.7	1.09	
2011	33	10	0.78							
2011	33	12	0.77			0.45	-19.79	27.2	1.00	
2011	33	14	0.77							
2011	33	16	0.77							
2011	33	18	0.76			0.39	-20.50	31.0	0.87	
2011	33	20	0.79							
2011	33	22	0.76			0.41	-15.86	32.3	0.77	
2011	33	24	0.76							
2011	33	26	0.79			0.31	-21.07	29.7	0.75	
2011	33	30	0.76			0.32	-18.76	23.7	0.64	
2011	33	34	0.76			0.26	-22.74	17.2	0.58	
2012	2	0.5	0.90		2.24	0.91	-20.20	6.2	0.76	
2012	2	1.5	0.86							
2012	2	2.5	0.85		1.47					
2012	2	3.5	0.84			0.72	-19.91	6.4	0.99	
2012	2	4.5	0.84		1.55					
2012	2	6	0.83			0.71	-20.06	6.6	1.02	
2012	2	8	0.81		1.46					
2012	2	10	0.79			0.63	-21.15	6.9	1.03	
2012	2	12	0.77							
2012	2	14	0.78		1.26	0.70	-19.31	9.3	1.20	
2012	2	16	0.77							
2012	2	18	0.79			0.59	-19.12	10.9	1.17	
2012	2	20	0.77		1.02	0.59	-18.24	12.7	1.17	
2012	2	22	0.77							
2012	2	24	0.76			0.62	-19.08	17.0	1.25	

2012	2	26	0.76	0.80	0.36	-26.03	21.1	1.20
2012	2	28	0.76					
2012	2	30	0.77					
2012	2	32	0.77	0.49	0.57	-14.24	24.3	1.07
2012	2	34	0.76					

Supplemental information to Chapter 4

C.1 GRAVITY CORE PORE WATER DATA

Station	Depth (cm)	$Si(OH)_4$ (μM)	Si ±	Mn (μM)	Mn ±	Fe (μM)	Fe ±	NO_3^- (μM)	NO_3^- ±
3	20	111.9	3.0	8.77	0.1			17.2	0.1
3	25	215.7	5.7	33.5	0.5			8.4	0.0
3	30	205.7	5.4	39.0	0.5			4.6	0.1
3	35	203.2	5.4	51.7	0.5	0.59	0.19	3.5	0.0
3	40			60.4	0.6			3.2	0.1
3	50			85.4	0.7			3.3	0.1
3	60	151.9	4.0	69.8	0.6	1.39	0.19	5.7	0.1
3	70	153.2	4.1	73.6	2.1	17.58	0.22	2.1	0.1
3	80	155.7	4.1	77.8	0.8	32.44	0.22	3.2	0.0
3	100	168.2	4.5	75.8	0.5	50.96	0.28	3.3	0.1
3	120	178.2	4.7	66.2	2.1	60.6	1.3	1.2	0.1
3	140	176.9	4.7	62.6	0.6	68.2	1.5	2.7	0.2
3	170	205.7	5.4	48.8	0.7	84.4	1.0	0.8	0.0
3	200	221.9	5.9	47.5	0.7	83.5	1.2	0.8	0.0
3	230	229.4	6.1	47.6	0.7	81.1	1.2	2.3	2.3
3	260	246.9	6.5	49.4	0.8	84.1	1.1	1.0	0.1
3	290	256.9	6.8	51.1	0.7	86.4	1.2	0.8	0.0
3	320	254.4	6.7	55.7	0.7	96.2	1.1	1.1	0.1
3	350	255.7	6.8	56.7	0.7	90.9	1.0	1.2	0.0
3	380	253.2	6.7	60.6	0.7	96.0	1.1	1.3	0.0
3	410	249.4	6.6	66.3	0.7	121.5	1.2	0.8	0.0
3	430	228.2	6.0	64.5	0.7	105.4	1.0	1.4	0.1
9	40	162.5	6.8	65.7	0.6	0.36	0.05	1.0	0.0
9	45	157.5	6.6	49.6	0.6	1.30	0.05		
9	50	151.2	6.4	42.1	0.6	8.2	0.4	1.6	0.3
9	55	140.0	5.9	29.9	0.5	7.3	0.4	1.5	0.0
9	65	103.7	4.4	2.91	0.06	0.18	0.05	1.2	0.1
9	75	113.7	4.8	1.78	0.06	1.29	0.05	0.9	0.0
9	85	113.7	4.8	1.57	0.06	0.47	0.05	1.6	0.1
9	95	102.5	4.3	2.23	0.06			1.2	0.0
9	105	121.2	5.1	0.69	0.06	0.39	0.28	1.5	0.1
9	115	122.5	5.1	0.64	0.06	0.31	0.05	1.8	0.1
9	125	130.0	5.5	0.63	0.06	0.23	0.05	1.9	0.0
9	135	125.0	5.2	0.59	0.06	0.25	0.05	0.5	0.0

9	145	145.0	6.1	0.55	0.06	0.44	0.05	1.4	0.1
13	33	209.3	8.8	117.9	0.7	2.1	0.6	1.1	0.0
13	38	186.8	7.8	79.5	0.8			3.6	0.0
13	43	218.0	9.2	150.0	1.2			0.8	0.1
13	48	206.8	8.7	157.4	1.0			0.8	0.0
13	53	170.5	7.2	89.1	0.8			4.0	0.1
13	58	174.3	7.3	105.7	0.9			3.9	0.1
13	68	168.0	7.1	165.4	0.9			4.7	0.1
13	78	190.5	8.0	117.2	1.2	68.1	1.3	0.3	0.0
13	88	164.3	6.9	116.7	1.4	75.1	1.2	0.4	0.1
13	98	188.0	7.9					0.2	0.0
13	108	168.0	7.1	107.8	0.8	113.9	1.1	0.1	0.0
13	128	196.8	8.3					0.5	0.0
13	148	203.0	8.5	100.6	0.8	110.0	1.3	0.2	0.1
13	168	206.8	8.7	99.3	0.7	97.4	1.0	0.0	0.0
13	188	224.3	9.4					0.0	0.0
13	208							0.2	0.0
13	228	220.5	9.3					0.0	0.0
13	248	216.8	9.1	91.9	0.7	103.0	1.1	1.1	0.0
25	18	188.0	2.1	2.81	0.1	4.21	0.19	10.0	0.1
25	23	258.5	2.8	15.92	0.2	12.00	0.22	4.8	0.1
25	33	222.5	2.4	43.5	0.5	3.11	0.19	2.3	0.0
25	43	92.0	1.0	10.55	0.1	2.31	0.19	12.7	0.1
25	53	129.5	1.4	45.6	0.5	1.09	0.26	13.2	0.2
25	63	143.0	1.6	56.0	0.5	26.81	0.24	3.8	0.8
25	73	189.5	2.1	33.6	0.7	116.3	1.2	0.6	0.1
25	83	194.0	2.1	37.0	0.5	154.5	1.3	0.1	0.0
25	93	197.0	2.2	31.9	0.7	134.3	1.3	0.6	0.0
25	103	167.0	1.8	33.1	0.6	177.5	1.7	0.3	0.0
25	113	192.5	2.1	33.1	0.5	183.6	1.9	0.2	0.1
25	133	210.5	2.3	30.1	0.5	187.7	2.3	0.2	0.1
25	153	243.5	2.7	28.1	0.5	214.3	1.1	0.1	0.1
25	173	236.0	2.6	26.0	0.5	194.0	2.0	0.6	0.1
25	193		0.0	13.50	0.1	127.6	1.4		
25	213	251.0	2.7	13.81	0.1	124.1	9.1	1.5	0.0
25	233	237.5	2.6	22.16	0.2	181.6	2.2	0.1	0.1
25	253	288.5	3.2	22.21	0.2	240.1	1.3	0.2	0.1
25	273	287.0	3.1	22.86	0.1	272.2	1.8	0.0	0.1
25	293	258.5	2.8	20.68	0.1	142.6	1.8	0.3	0.1
25	313	245.0	2.7	19.25	0.1	142.4	9.6	0.1	0.1
27	15	221.2	1.5	33.4	0.5	10.8	0.7	2.8	0.1
27	25	252.4	1.7	64.0	0.6	3.82	0.16	1.2	0.1
27	35	222.4	1.5	85.9	0.7	3.27	0.40	0.7	0.1

27	45	162.4	1.1	90.1	0.7	3.27	0.31	4.5	0.0
27	65	167.4	1.1	124.4	1.2	9.5	0.4	0.6	0.0
27	85	128.7	0.9	95.4	0.7	125.4	1.1	0.4	0.0
27	105	154.9	1.1	60.6	0.9	89.6	1.5	1.2	0.0
27	125	156.2	1.1	87.3	0.7	132.2	1.0	0.3	0.0
27	145	164.9	1.1	92.9	0.7	152.7	1.2	0.1	0.0
27	165	177.4	1.2	93.0	0.7	154.5	1.1	0.1	0.0
27	185	173.7	1.2	88.0	0.7	128.8	1.1	0.3	0.0
27	205	172.4	1.2	69.9	0.7	107.3	1.0	0.0	0.0
27	225	174.9	1.2	89.8	0.7	118.6	1.0	0.2	0.0
27	245	199.9	1.4	96.6	0.7	113.6	1.1	0.1	0.0
27	265	194.9	1.3	54.8	0.7	78.0	1.1	0.3	0.0
29	20	180.6	7.6	108.7	1.1			5.0	0.1
29	30		0.0	119.5	1.2	4.1	0.7	2.4	0.0
29	40	189.4	8.0	142.7	0.7			2.6	0.1
29	50	171.9	7.2	74.8	0.9	3.4	0.7	6.6	0.0
29	60	170.6	7.2	130.8	0.7	49.3	1.0	2.0	0.0
29	80	176.9	7.4	118.3	1.1	89.2	1.2	1.0	0.0
29	100	169.4	7.1	115.7	0.8	105.4	1.1	0.7	0.0
29	120	165.6	7.0	114.3	1.0	117.5	1.2	0.5	0.0
29	140	150.6	6.3	114.2	0.8	135.6	1.3	2.1	0.0
29	160	158.1	6.6	110.8	1.0	126.7	1.3	0.3	0.0
29	180	168.1	7.1	113.4	0.8	133.3	1.7	2.0	0.0
29	200	180.6	7.6	110.3	0.9	133.1	1.3	0.9	0.1
29	220	191.9	8.1	112.7	1.0	133.0	1.5	1.0	0.0
29	240	160.6	6.7	114.1	1.0	145.7	1.0	2.4	0.0
29	260	170.6	7.2	115.2	0.9	169.8	1.2	2.2	0.1
31	13	275.5	8.5	1.58	0.1	15.93	0.20	19.8	0.0
31	23	263.2	8.1	0.49	0.1	1.91	0.19	16.6	0.1
31	33	242.7	7.5	5.18	0.1	4.40	0.19	11.0	0.1
31	43	240.0	7.4	17.32	0.1	7.65	0.20	5.7	0.0
31	53	219.5	6.8	28.2	0.5	23.51	0.26	3.2	0.1
31	73	114.5	3.5	31.0	0.6	2.85	0.19	10.1	0.1
31	93	144.5	4.5					2.2	0.1
31	113	145.9	4.5	48.0	0.7	93.9	1.0	2.2	0.0
31	133			46.5	0.8	93.2	1.4	0.7	0.0
31	153	195.0	6.0	35.1	0.5	51.9	1.3	0.9	0.1
31	173	210.0	6.5	45.9	0.7	108.2	1.1	0.7	0.1
31	193	230.5	7.1	50.3	0.8	128.7	1.5	0.0	0.0
31	213	229.1	7.1	52.0	0.7	127.0	1.1	0.0	0.0
31	233	248.2	7.7	58.3	0.9	132.1	1.5	0.0	0.0
31	253	238.6	7.4	64.9	0.9	145.8	1.9	0.0	0.0
31	273	241.4	7.5	66.3	0.7	148.7	1.4	0.2	0.0

31	293	264.5	8.2	69.3	0.8	144.9	1.5	0.0	0.0
31	313	250.9	7.7	74.5	0.8	160.2	1.4	0.1	0.0

C.2 GRAVITY CORE SOLID PHASE DATA

Station	Depth	$CaCO_3$	$\delta^{13}C_{(TIC)}$	C_{org}
13	18	11.1	1.39	
13	20	12.2	1.21	0.70
13	22	14.6	1.24	
13	24	15.1	1.11	
13	26	16.7	1.47	
13	27	17.1	1.53	
13	28	19.6	1.26	
13	30	21.3	1.25	
13	32	23.3	1.29	
13	34	24.8	1.25	
13	36	24.8	1.26	
13	37	27.4	1.28	
13	38	25.8	1.07	
13	40	25.8	1.06	0.40
13	42	28.8	0.99	
13	44	27.5	0.95	
13	46	30.8	1.13	
13	47	32.2	1.00	
13	48	30.4	0.89	
13	50	29.3	0.83	
13	52	27.9	0.75	0.62
13	53			0.71
13	54	28.0	0.68	0.51
13	55			0.49
13	56	26.6	0.84	0.72
13	57	26.6	0.76	0.50
13	58	26.3	0.65	0.41
13	59			0.35
13	60			0.18
13	62	20.8	0.86	0.52
13	63			0.51
13	64	18.8	0.55	0.53

13	65			0.47
13	66	15.5	0.66	
13	67	16.6	0.84	
13	68	10.9	0.84	
13	69	13.2	0.83	
13	70	7.3	0.84	
13	71	9.4	0.77	
13	72	3.2	0.87	
13	73	6.4	0.72	
13	74	2.8	0.22	
13	75	3.2		
13	76	3.5	0.15	
13	78	4.9	0.34	
13	80	8.7	0.53	
13	82	6.3	0.56	
13	84	4.8	0.71	
13	85			0.54
13	86	4.0	0.43	
13	92	3.2	0.06	
13	94	1.8	0.30	0.65
31	6	13.2	1.15	
31	8	14.9	1.22	
31	10	15.9	1.24	
31	12	17.4	1.31	
31	14	19.2	1.27	
31	16	21.7	1.31	
31	24	34.0	0.96	
31	26	32.8	0.89	
31	28	29.7	0.83	
31	30	32.5	0.79	
31	32	28.9	0.77	
31	34	30.4	0.75	
31	36	25.0	0.63	
31	38	21.4	0.72	
31	40	18.5	0.56	
31	42	16.3	0.63	
31	44	10.4	0.54	
31	46	9.3	0.60	
31	48	7.7		
31	50	5.2		
31	51	0.5		
31	52	1.5		
31	53	4.9		

31	54	0.9
31	55	0.4
31	57	0.4
31	59	2.4
31	61	3.2
31	63	0.2
31	65	2.1
31	67	0.2
31	69	0.2

C.3 ANACONDAS GRAVITY CORE POROSITY DATA

Station	Depth (cm)	Porosity
25	18	0.75
	23	0.72
	33	0.73
	43	0.73
	73	0.77
	113	0.80
	153	0.71
	213	0.66
	273	0.64
27	15	0.76
	25	0.73
	35	0.74
	65	0.75
	105	0.82
	145	0.82
	205	0.81
	245	0.81
29	30	0.76
	60	0.82
	100	0.85
	160	0.82
	200	0.81
	240	0.64

31	13	0.78
	33	0.78
	73	0.79
	93	0.84
	173	0.81
	213	0.821
	253	0.832

Supplemental Information to Chapter 5

D.1 COMPARISON OF THE EFFECT OF O_2 ON MEASUREMENTS OF N_2/AR

50 ppt Na Cl solutions were equilibrated at 6.4 ˚C with atmosphere and amended with variable amounts of sodium sulfite. Here we plot the 32.40 ion current (O2/Ar ratio) vs. the deviation from the expected equilibrium N2/Ar ratio at 50 ppt and 6.4 ˚C. The triangle represents the O2/Ar ratio at 100% saturation.

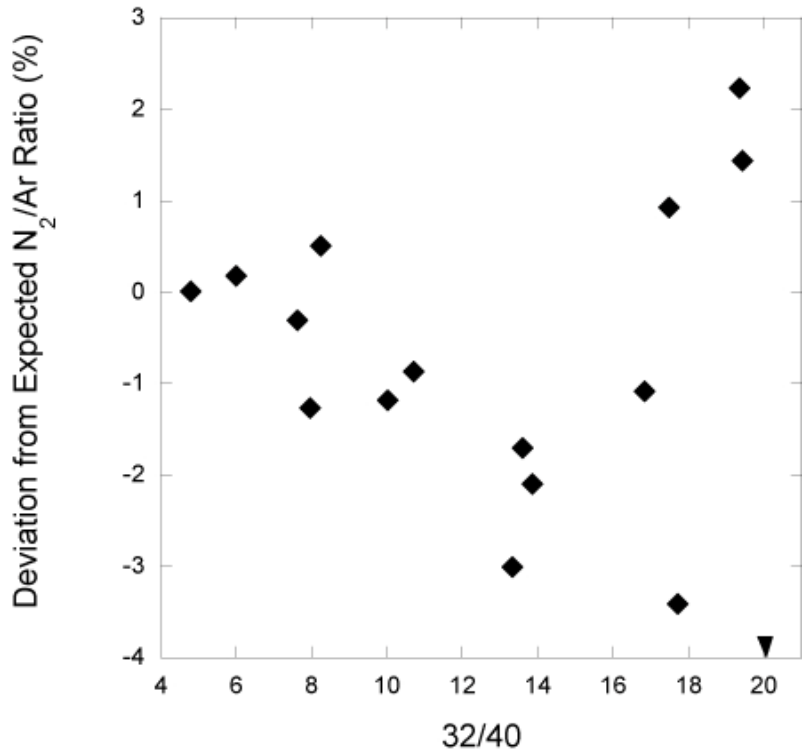

D.2 PORE WATER DATA

Station-wise listing of individual pore water measurements sorted by station and core type (WCS or Rhizon).

Station	Core Type	Depth cm	NO_3 µM	NO_3 ±	NO_2 µM	NO_2 ±	N_2 µM	N_2 ±	N_2O nM	N_2O ±	HS^- µM	HS^- ±	Fe µM	Fe ±
Pescadero	WCS-PA1	0	36.6	0.3										
Pescadero	WCS-PA1	0.02	5.1	0.2										
Pescadero	WCS-PA1	0.11	3.4	0.2	3.4	0.1								
Pescadero	WCS-PA1	0.67	3.1	2.0	0.9	0.0		0.62	36.9	1.8				
Pescadero	WCS-PA1	1.20	22.6	0.6	1.3	0.0		1.15	62.8	3.1				
Pescadero	WCS-PA1	1.76	10.3	0.3				1.70	203.1	10.2				
Pescadero	WCS-PA1	2.43	5.5	0.2	1.5	0.0		2.38	195.1	9.8				
Pescadero	WCS-PA1	2.94	3.5	0.0	1.4	0.0		2.89	272.6	13.6				
Pescadero	WCS-PA1	3.48	3.3	0.1	1.3	0.0		3.43	346.5	17.3				
Pescadero	WCS-PA1	3.88	2.7	0.1				3.81	63.9	3.2				
Pescadero	WCS-PB1	3.09	24.3	0.0										
Pescadero	WCS-PB1	3.33	14.2	0.1										
Pescadero	WCS-PB1	3.46	14.9	0.3										
Pescadero	WCS-PB1	3.92	3.7	0.1	1.3	0.0		3.81	38.4	1.9				
Pescadero	WCS-PB1	4.16							31.0	1.5				
Pescadero	WCS-PB1	4.46	3.0	0.1	1.7	0.1								
Pescadero	WCS-PB1	4.34							50.6	2.5				
Pescadero	WCS-PB1	4.89							49.9	2.5				
Pescadero	WCS-PB1	4.99	2.6	0.1	1.2	0.0								
Pescadero	WCS-PB2	3.05	10.3	0.0										
Pescadero	WCS-PB2	3.21	7.8	0.0										
Pescadero	WCS-PB2	3.31	6.5	0.1	1.0	0.0								
Pescadero	WCS-PB2	3.86	10.3	0.3	1.3	0.0								
Pescadero	WCS-PB2	4.38	5.7	0.3	1.4	0.0								

Pescadero	WCS-PB2	4.88							55.8	2.8				
Pescadero	WCS-PB2	4.93	9.9	0.0	1.9	0.1								
Pescadero	WCS-PB2	5.40							81.9	4.1				
Pescadero	WCS-PB2	5.42							112.2	5.6				
Pescadero	WCS-PB2	5.45	3.9	0.2	1.5	0.0								
Pescadero	WCS-PB2	5.84							118.8	5.9				
Pescadero	WCS-PB2	5.95							55.5	2.8				
Pescadero	WCS-PB2	6.00	1.8	0.1	1.2	0.0								
Pescadero	WCS-PB2	6.19							59.6	3.0				
Pescadero	WCS-PB2	6.36							38.9	1.9				
Pescadero	WCS-PB2	6.46							49.0	2.5				
Pescadero	Rhizon	0									0.5	2.5	3.83	0.01
Pescadero	Rhizon	2									0.7	2.5	262.60	2.11
Pescadero	Rhizon	4									0.7	2.5	315.10	2.69
Pescadero	Rhizon	6											309.42	0.72
Pescadero	Rhizon	8									0.9	2.5	295.85	0.84
Pescadero	Rhizon	10											267.47	1.20
Pescadero	Rhizon	12											234.17	14.23
Pescadero	Rhizon	16											165.63	10.32
Pescadero	Rhizon	26									0.8	2.5	60.81	0.18
Pescadero	Rhizon	30											38.01	1.36
Pescadero	Rhizon	34											17.51	0.14
Pescadero	Rhizon	38									1.2	2.5	7.20	0.02
Pescadero	Rhizon	42											2.72	0.01
Pescadero	Rhizon	46									1.4	2.5	1.54	0.09
Pescadero	Rhizon	52											1.81	0.19
Magdalena	WCS-MA1	0	36.4	0.1			555.90	11.12						
Magdalena	WCS-MA1	0.02	2.9	0.1										
Magdalena	WCS-MA1	0.06	0.9	0.1	0.2	0.0								
Magdalena	WCS-MA1	0.23					605.54	12.11						
Magdalena	WCS-MA1	0.48	0.5	0.0	0.1	0.0			7.3	0.4				
Magdalena	WCS-MA1	0.66					599.64	11.99						
Magdalena	WCS-MA1	0.91	1.1	0.0	0.1	0.0			7.5	0.4				

Magdalena	WCS-MA1	1.07					597.35	11.95						
Magdalena	WCS-MA1	1.34	1.6	0.0	0.4	0.0			6.7	0.3				
Magdalena	WCS-MA1	1.50					611.65	12.23						
Magdalena	WCS-MA1	1.76	1.6	0.9	0.2	0.0			8.4	0.4				
Magdalena	WCS-MA1	1.92					610.34	12.21						
Magdalena	WCS-MA1	2.21	4.1	0.1	0.5	0.0			9.4	0.5				
Magdalena	WCS-MA1	2.38					621.24	12.42						
Magdalena	WCS-MA1	2.65	5.2	0.2	2.0	0.1			12.2	0.6				
Magdalena	WCS-MA1	2.82					682.32	13.65						
Magdalena	WCS-MA1	3.10	10.7	0.2	3.0	0.1			25.7	1.3				
Magdalena	WCS-MA1	3.28					676.52	13.53						
Magdalena	WCS-MA1	3.56	5.6	0.0	2.4	0.1			40.2	2.0				
Magdalena	WCS-MA1	3.73					625.28	12.51						
Magdalena	WCS-MA1	4.02	5.2	0.0	3.0	0.1			60.0	3.0				
Magdalena	WCS-MA1	4.21					637.77	12.76						
Magdalena	WCS-MB1	4.05	28.7	0.3										
Magdalena	WCS-MB1	4.19	23.2	0.0	4.9	0.1								
Magdalena	WCS-MB1	4.21					629.26	12.59						
Magdalena	WCS-MB1	4.72	4.0	0.0	3.0	0.1			23.3	1.2				
Magdalena	WCS-MB1	5.02	3.7	0.1	2.0	0.1	631.86	12.64	16.3	0.8				
Magdalena	WCS-MB1	5.42												
Magdalena	WCS-MB1	5.48	4.0	0.1	0.8	0.0			12.4	0.6				
Magdalena	WCS-MB1	5.76	0.3	0.0	0.1	0.0			7.5	0.4				
Magdalena	WCS-MB1	5.93					627.31	12.55						
Magdalena	WCS-MB1	6.22	0.2	0.0	0.0	0.0			7.5	0.4				
Magdalena	WCS-MB1	6.52	0.3	0.0	0.0	0.0			7.2	0.4				
Magdalena	WCS-MB1	6.7					628.07	12.56	12.1	0.6				
Magdalena	WCS-MB1	7.01	0.3	0.1	0.1	0.0								
Magdalena	WCS-MB1	7.31	1.3	0.0	0.1	0.0			10.3	0.5				
Magdalena	WCS-MB1	7.5					631.25	12.63	13.2	0.7				
Magdalena	WCS-MB1	7.79	0.3	0.0										
Magdalena	WCS-MB1	8.10	0.3	0.0	0.0	0.0			10.4	0.5				
Magdalena	WCS-MB2	6.03	17.8	0.2										

Magdalena	WCS-MB2	6.15	11.5	0.1										
Magdalena	WCS-MB2	6.28	6.2	0.1										
Magdalena	WCS-MB2	6.43					619.01	12.38						
Magdalena	WCS-MB2	6.77	1.5	0.0	0.3									
Magdalena	WCS-MB2	6.96					627.26	12.55	9.1	0.5				
Magdalena	WCS-MB2	7.26	1.3	0.0	0.2				12.2	0.6				
Magdalena	WCS-MB2	7.58	1.8	0.1	0.2									
Magdalena	WCS-MB2	7.77					628.45	12.57	8.9	0.4				
Magdalena	WCS-MB2	8.11	0.5	0.0	0.1				7.3	0.4				
Magdalena	WCS-MB2	8.41	0.7	0.1	0.1				8.7	0.4				
Magdalena	WCS-MB2	8.62					620.75	12.42						
Magdalena	WCS-MB2	8.95	0.4	0.0	0.1				7.6	0.4				
Magdalena	WCS-MB2	9.25	0.3	0.0	0.0				8.4	0.4				
Magdalena	WCS-MB2	9.54	0.5	0.0	0.0				6.0	0.3				
Magdalena	WCS-MB2	9.74					614.24	12.28						
Magdalena	WCS-MB2	9.92	0.3	0.1	0.0				7.6	0.4				
Magdalena	WCS-MB2	10.21					614.32	12.29						
Magdalena	WCS-MB2	10.58					612.12	12.24	6.0	0.3				
Magdalena	Rhizon	0									0.6	2.5	<0.05	
Magdalena	Rhizon	1									2.1	2.5	4.58	0.03
Magdalena	Rhizon	3									0.8	2.5	12.13	0.08
Magdalena	Rhizon	11									0.9	2.5	14.23	0.02
Magdalena	Rhizon	13									1.4	2.5	14.72	0.13
Magdalena	Rhizon	15									1.8	2.5	13.28	0.07
Magdalena	Rhizon	17											11.19	0.10
Magdalena	Rhizon	19									4.5	2.5	6.71	0.05
Magdalena	Rhizon	21									1.9	2.5	4.02	0.04
Magdalena	Rhizon	23									2.9	2.5	3.81	0.05
Magdalena	Rhizon	25									4.5	2.5	0.62	0.02
Magdalena	Rhizon	29									21.9	2.7	<0.05	
Magdalena	Rhizon	33									94.6	5.4	<0.05	
Magdalena	Rhizon	37									56.0	3.8	<0.05	
Soledad	WCS-SA1	0	17.4	0.2			522.14	7.75						

Soledad	WCS-SA1	0.03	10.0	0.0	0.5	0.0								
Soledad	WCS-SA1	0.46	3.9	0.1	0.8	0.0			18.6	0.9				
Soledad	WCS-SA1	0.76							17.2	0.9				
Soledad	WCS-SA1	0.93					598.95	8.98						
Soledad	WCS-SA1	1.14	5.3	0.1	0.4	0.0								
Soledad	WCS-SA1	1.44							44.1	2.2				
Soledad	WCS-SA1	1.62					674.88	10.12						
Soledad	WCS-SA1	1.83	271.9	2.1	5.5	0.1								
Soledad	WCS-SA1	2.11							319.9	16.0				
Soledad	WCS-SA1	2.27					672.43	10.09						
Soledad	WCS-SA1	2.48	118.2	0.9	7.0	0.1								
Soledad	WCS-SA1	2.72							484.5	24.2				
Soledad	WCS-SA1	2.85					665.93	9.99						
Soledad	WCS-SA1	3.09	8.3	0.2	1.3	0.0								
Soledad	WCS-SA1	3.37							164.5	8.2				
Soledad	WCS-SA1	3.52	3.9	0.2	0.7	0.0								
Soledad	WCS-SA1	3.76					658.31	9.87						
Soledad	WCS-SA1	3.88							26.9	1.3				
Soledad	WCS-SA1	4.31	3.6	0.1	0.5	0.0								
Soledad	WCS-SA1	4.57					644.12	9.66						
Soledad	WCS-SA1	4.89							49.0	2.5				
Soledad	WCS-SA1	5.05	1.8	0.0	0.5	0.0								
Soledad	WCS-SA1	5.26					657.83	9.87						
Soledad	WCS-SA1	5.47	39.5	0.4	1.9	0.0								
Soledad	WCS-SA1	5.70					668.78	10.03						
Soledad	WCS-SA1	5.89	7.7	0.1										
Soledad	WCS-SB1	3.08	5.4	0.1	2.1	0.0								
Soledad	WCS-SB1	3.39							32.9	1.6				
Soledad	WCS-SB1	3.48					644.71							
Soledad	WCS-SB1	3.64	3.6	0.1	1.0	0.0								
Soledad	WCS-SB1	4.00					642.74							
Soledad	WCS-SB1	4.11							28.7	1.4				
Soledad	WCS-SB1	4.17	5.7	0.1	1.4	0.0								

Soledad	WCS-SB1	4.47							45.0	2.3				
Soledad	WCS-SB1	4.58					678.24							
Soledad	WCS-SB1	4.75	1.6	0.1	0.9	0.0								
Soledad	WCS-SB1	5.00							73.5	3.7				
Soledad	WCS-SB1	5.18					661.26							
Soledad	WCS-SB1	5.34	0.9	0.0										
Soledad	WCS-SB1	5.58							62.7	3.1				
Soledad	WCS-SB1	5.77					665.40							
Soledad	WCS-SB1	6.04	0.8	0.0					61.6	3.1				
Soledad	WCS-SB1	6.21					672.05							
Soledad	Rhizon	0									5.6	2.6	0.66	0.02
Soledad	Rhizon	1.2									2.5	2.6	65.96	0.46
Soledad	Rhizon	3.5									15.2	2.7	51.93	0.43
Soledad	Rhizon	5.5									2.5	2.6	20.03	0.67
Soledad	Rhizon	7.5									3.7	2.6	0.68	0.03
Soledad	Rhizon	9.5									41.5	3.3	<0.05	
Soledad	Rhizon	11.5									100.0	5.6	<0.05	
Soledad	Rhizon	13.5									122.7	6.6	<0.05	
Soledad	Rhizon	21.5									289.1	14.7	<0.05	
Soledad	Rhizon	25.5									260.8	13.3	<0.05	
Soledad	Rhizon	29.5									273.4	13.7	<0.05	
Soledad	Rhizon	33.5									175.3	8.8	<0.05	
Soledad	Rhizon	37.5									52.0	2.7	<0.05	
Soledad	Rhizon	41.5											<0.05	
Soledad	Rhizon	45.5											<0.05	
Santa Monica	WCS-SMA1	0	28.4	0.2			582.70	8.74						
Santa Monica	WCS-SMA1	0.02	26.2	0.2										
Santa Monica	WCS-SMA1	0.30					588.35	8.83	34.4	1.7				
Santa Monica	WCS-SMA1	0.44	16.5	0.1	1.8	0.0								
Santa Monica	WCS-SMA1	0.79					603.94	9.06	18.7	0.9				
Santa Monica	WCS-SMA1	1.18	77.2	0.8	1.5	0.0			12.8	0.6				
Santa Monica	WCS-SMA1	1.37					610.27	9.15						
Santa Monica	WCS-SMA1	1.73	87.5	0.1	15.6	0.3			98.5	4.9				

Santa Monica	WCS-SMA1	1.90					618.09	9.27						
Santa Monica	WCS-SMA1	2.24	235.1	5.2	27.2	0.5			207.5	10.4				
Santa Monica	WCS-SMA1	2.45					628.78	9.43						
Santa Monica	WCS-SMA1	2.81	8.5	0.1	5.6	0.1			191.0	9.6				
Santa Monica	WCS-SMA1	3.01					625.87	9.39						
Santa Monica	WCS-SMA1	3.34	1.2	0.0	1.7	0.0			49.5	2.5				
Santa Monica	WCS-SMA1	3.54					626.68	9.40						
Santa Monica	WCS-SMA1	3.87	4.5	0.0	4.4	0.1								
Santa Monica	WCS-SMA1	3.92							20.7	1.0				
Santa Monica	WCS-SMA1	4.08					630.05	9.45						
Santa Monica	WCS-SMA1	4.41	42.2	0.3	15.8	0.3								
Santa Monica	WCS-SMA1	4.62					641.70	9.63						
Santa Monica	WCS-SMB1	3.05	18.4	0.1										
Santa Monica	WCS-SMB1	3.14			5.5				24.3	1.2				
Santa Monica	WCS-SMB1	3.34												
Santa Monica	WCS-SMB1	3.46					608.81	9.13						
Santa Monica	WCS-SMB1	3.66	8.5	0.1										
Santa Monica	WCS-SMB1	3.73			1.5									
Santa Monica	WCS-SMB1	3.81							55.9	2.8				
Santa Monica	WCS-SMB1	4.05					615.20	9.23						
Santa Monica	WCS-SMB1	4.26	1.2	0.0										
Santa Monica	WCS-SMB1	4.36			0.8				59.5	3.0				
Santa Monica	WCS-SMB1	4.55							32.2	1.6				
Santa Monica	WCS-SMB1	4.69					618.36	9.28						
Santa Monica	WCS-SMB1	4.89							31.9	1.6				
Santa Monica	WCS-SMB1	4.92	0.4	0.0										
Santa Monica	WCS-SMB1	5.06			0.4									
Santa Monica	WCS-SMB1	5.24							17.1	0.9				
Santa Monica	WCS-SMB1	5.40					620.11	9.30						
Santa Monica	WCS-SMB1	5.59	0.6	0.0										
Santa Monica	WCS-SMB1	5.69			0.3									
Santa Monica	WCS-SMB1	5.77	0.3	0.0										
Santa Monica	WCS-SMB1	5.87			0.2									

Santa Monica	WCS-SMB1	6.06							9.9	0.5				
Santa Monica	WCS-SMB1	6.25					619.56	9.29						
Santa Monica	WCS-SMB1	6.47	0.6	0.0										
Santa Monica	WCS-SMB1	6.57			0.1									
Santa Monica	WCS-SMB1	6.78							8.5	0.4				
Santa Monica	WCS-SMB1	6.92					619.69	9.30						
Santa Monica	WCS-SMB1	7.26							9.2	0.5				
Santa Monica	WCS-SMB1	7.44	0.3	0.0										
Santa Monica	WCS-SMB1	7.71					620.08	9.30						
Santa Monica	WCS-SMB1	7.99							9.0	0.4				
Santa Monica	Rhizon	0											<0.05	
Santa Monica	Rhizon	2											228.44	1.43
Santa Monica	Rhizon	4											231.90	1.17
Santa Monica	Rhizon	6											249.08	1.18
Santa Monica	Rhizon	8											252.47	1.25
Santa Monica	Rhizon	10											245.96	1.10
Santa Monica	Rhizon	14											234.14	1.18
Santa Monica	Rhizon	18											209.94	0.94
Santa Monica	Rhizon	22											198.78	1.27
Santa Monica	Rhizon	26											170.24	1.28
San Clemente	WCS-STA1	0	38.3	0.0			571.72	8.58						
San Clemente	WCS-STA1	0.06					565.76	8.49						
San Clemente	WCS-STA1	0.36							22.5					
San Clemente	WCS-STA1	0.42	37.6	0.3										
San Clemente	WCS-STA1	0.60					567.86	8.52						
San Clemente	WCS-STA1	0.87							14.7					
San Clemente	WCS-STA1	0.92	16.9	0.1										
San Clemente	WCS-STA1	1.12					582.41	8.74						
San Clemente	WCS-STA1	1.38							14.4					
San Clemente	WCS-STA1	1.44	8.5	0.1										
San Clemente	WCS-STA1	1.65					587.89	8.82						
San Clemente	WCS-STA1	1.91							14.3					
San Clemente	WCS-STA1	1.95	4.9	0.0										

San Clemente	WCS-STA1	2.16					570.54	8.56						
San Clemente	WCS-STA1	2.43							14.5					
San Clemente	WCS-STA1	2.48	2.3	0.2										
San Clemente	WCS-STA1	2.69					588.17	8.82						
San Clemente	WCS-STA1	2.96							13.6					
San Clemente	WCS-STA1	3.05	1.0	0.0										
San Clemente	WCS-STA1	3.30					597.54	8.96						
San Clemente	WCS-STA1	3.56							14.5					
San Clemente	WCS-STA1	3.65	0.5	0.0										
San Clemente	WCS-STA1	3.84					591.14	8.87						
San Clemente	WCS-STA1	4.12							12.3					
San Clemente	WCS-STA1	4.17	0.4	0.0										
San Clemente	WCS-STA1	4.40					596.51	8.95						
San Clemente	WCS-STA1	4.68							9.2					
San Clemente	WCS-STA1	4.75	0.4	0.1										
San Clemente	WCS-STA1	4.97					596.19	8.94						
San Clemente	WCS-STA1	5.24							7.0					
San Clemente	WCS-STA1	5.30	0.3	0.0										
San Clemente	WCS-STA1	5.53					598.15	8.97						
San Clemente	WCS-STA1	5.80							6.2					
San Clemente	Rhizon	1											<0.05	
San Clemente	Rhizon	3											<0.05	
San Clemente	Rhizon	7											19.98	0.82
San Clemente	Rhizon	9											15.23	0.76
San Clemente	Rhizon	11											15.47	0.71
San Clemente	Rhizon	13											16.43	0.23
San Clemente	Rhizon	17											12.97	0.54
San Clemente	Rhizon	21											12.90	0.52
San Clemente	Rhizon	25											12.14	0.51
San Clemente	Rhizon	29											10.56	0.08
San Clemente	Rhizon	33											5.94	0.03

D.3 CORE INCUBATION DATA

Station-wise listing of core incubation results. For Soledad and Santa Monica, 'W' refers to incubations in the temperature-controlled van, 'C' refers to incubations in the cold room (see text).

Station	Core#	Time (hrs)	NO_3 (µM)	NO_3 ±	N_2 (µM)	N_2 ±	NH_4 (µM)	NH_4 ±
Pescadero	INC-P1	0	30.7	0.3				
Pescadero	INC-P1	6	20.2	0.1				
Pescadero	INC-P1	15.5	12.7	0.1				
Pescadero	INC-P1	24.25	4.8	0.1				
Pescadero	INC-P1	31.5	0.6	0.1				
Pescadero	INC-P2	0	30.5	0.1				
Pescadero	INC-P2	6	24.4	0.1				
Pescadero	INC-P2	15.5	15.0	0.2				
Pescadero	INC-P2	24.25	6.4	0.1				
Pescadero	INC-P2	31.5	1.3	0.1				
Pescadero	INC-P3	0	30.9	0.3				
Pescadero	INC-P3	6	21.5	0.3				
Pescadero	INC-P3	15.5	12.5	0.1				
Pescadero	INC-P3	24.25	4.8	0.1				
Pescadero	INC-P3	31.5	2.2	0.1				
Magdalena	INC-M1	0	36.6	2.7	550.05	15.08	8.1	0.1
Magdalena	INC-M1	8	33.6	2.2	575.67	11.39	9.7	0.0
Magdalena	INC-M1	16.5	37.6	0.2	552.15	10.07	7.6	0.0
Magdalena	INC-M1	27	35.2	0.3	558.05	14.76	9.0	0.2
Magdalena	INC-M1	32.5	33.9	0.2	563.00	7.18	9.3	0.3
Magdalena	INC-M2	0	37.4	0.5	551.25	14.41	6.3	0.2
Magdalena	INC-M2	8	24.1	0.4	557.17	8.66	7.6	0.0
Magdalena	INC-M2	16.5	33.1	0.3	557.69	7.90	6.9	0.0
Magdalena	INC-M2	27	31.2	0.0	557.19	13.65	7.2	0.2
Magdalena	INC-M2	32.5	29.7	0.0	560.27	7.59	6.9	0.0
Magdalena	INC-M2	40.75	26.6	0.2	563.17	7.85	6.9	0.0
Magdalena	INC-M3	0	37.0	0.2	548.60	14.27	7.2	0.0
Magdalena	INC-M3	8	33.8	0.1	577.09	8.62	7.2	0.0
Magdalena	INC-M3	16.5	34.1	0.5	553.09	4.99	7.9	0.0
Magdalena	INC-M3	27	33.1	0.7	549.71	13.09	11.6	1.9
Magdalena	INC-M3	32.5	31.8	0.4	585.17	6.99	7.7	0.1
Magdalena	INC-M3	40.75	30.1	0.1	560.11	7.68	7.7	0.1
Soledad	INC-SW1	0	14.0	0.8	551.98	27.60	24.1	0.3
Soledad	INC-SW1	9	9.4	0.9	560.91	49.97	54.7	4.3
Soledad	INC-SW1	18.25	6.4	0.2	571.36	35.67	79.1	21.8
Soledad	INC-SW1	25.25	5.4	0.0	579.69	52.61	75.5	1.1
Soledad	INC-SW1	34.75	3.3	0.0	594.92	75.38	89.2	0.5

Soledad	INC-SW1	42.25	2.2	0.0	621.33	139.03	107.1	2.7
Soledad	INC-SW2	0	13.9	0.0	551.53	74.07	15.4	4.0
Soledad	INC-SW2	9	10.0	0.1	551.56	74.07	19.1	3.0
Soledad	INC-SW2	18.25	6.9	0.1	572.28	76.86	25.2	3.0
Soledad	INC-SW2	25.25	4.7	0.0	562.93	75.60	28.6	0.3
Soledad	INC-SW2	34.75	2.6	0.0	561.76	75.44	37.2	1.6
Soledad	INC-SW2	42.25	1.8	0.1	568.22	76.31	46.3	0.5
Soledad	INC-SW3	0	11.8	0.1	560.49	75.27	47.8	0.0
Soledad	INC-SW3	9	8.5	0.2	561.84	75.45	48.0	0.8
Soledad	INC-SW3	18.25	6.3	0.2	573.41	77.01	70.0	1.9
Soledad	INC-SW3	25.25	4.7	0.0	577.76	77.59	86.0	0.8
Soledad	INC-SW3	34.75	3.5	0.0	588.34	79.01	92.8	0.3
Soledad	INC-SW3	42.25	2.8	0.1	583.49	78.36	91.5	1.1
Soledad	INC-SC1	0	12.5	0.4	554.42	74.46		
Soledad	INC-SC1	9	7.7	0.1	558.13	74.95		
Soledad	INC-SC1	18.5	7.1	0.1	563.65	75.70		
Soledad	INC-SC1	25	8.4	0.3	568.39	76.33		
Soledad	INC-SC1	34.5	2.0	0.0	572.60	76.90		
Soledad	INC-SC1	42	2.5	0.4	575.08	77.23		
Soledad	INC-SC2	0	13.0	1.3	552.28	74.17		
Soledad	INC-SC2	9	7.8	0.2	578.35	77.67		
Soledad	INC-SC2	18.5	3.9	0.3	577.78	77.59		
Soledad	INC-SC2	25	2.7	0.0	578.58	77.70		
Soledad	INC-SC2	34.5	2.7	0.0	580.67	77.98		
Soledad	INC-SC2	42	0.7	0.1	589.38	79.15		
Santa Monica	INC-SMW1	0	26.1	0.2	586.67	9.50	0.4	0.6
Santa Monica	INC-SMW1	9	22.6	0.1	589.34	4.33	0.3	0.3
Santa Monica	INC-SMW1	21	19.5	0.1	590.61	5.18	0.5	0.3
Santa Monica	INC-SMW1	26.5	20.2	0.1	592.41	6.50	1.5	2.5
Santa Monica	INC-SMW1	31	15.2	0.0	592.29	7.32	1.0	0.0
Santa Monica	INC-SMW2	0	25.8	0.1			0.7	0.3
Santa Monica	INC-SMW2	9	22.5	0.1	589.91	3.81	0.7	0.3
Santa Monica	INC-SMW2	21	19.3	0.2	591.79	4.89	0.8	0.0
Santa Monica	INC-SMW2	26.5	16.2	0.3	592.59	4.90	0.9	0.3
Santa Monica	INC-SMW2	31	14.5	0.0	593.28	4.76	0.8	1.1
Santa Monica	INC-SMW3	0	27.8	2.5	588.84	5.71		
Santa Monica	INC-SMW3	9	22.3	0.0	588.73	3.74	0.5	0.3
Santa	INC-	21	17.0	0.9	589.08	4.50	1.0	0.0

Monica	SMW3							
Santa Monica	INC-SMW3	26.5	16.1	0.0	590.52	4.75	1.1	0.3
Santa Monica	INC-SMW3	31	16.2	0.2	590.64	3.89	1.4	0.0
Santa Monica	INC-SMC1	0	26.1	0.5	587.77	10.13	0.1	0.8
Santa Monica	INC-SMC1	8.5	21.2	0.2	591.51	3.72	0.2	1.0
Santa Monica	INC-SMC1	19.5	18.3	0.1	593.31	3.81	0.2	0.5
Santa Monica	INC-SMC1	25.5	16.3	0.1	594.43	3.81	2.8	0.3
Santa Monica	INC-SMC1	32	13.6	2.0	594.93	4.18	3.3	1.0
Santa Monica	INC-SMC2	0	25.7	0.1	587.07	10.22	1.4	0.5
Santa Monica	INC-SMC2	8.5	23.2	1.0	590.28	3.72	2.3	0.0
Santa Monica	INC-SMC2	19.5	18.1	0.6	593.73	3.72	1.8	0.0
Santa Monica	INC-SMC2	25.5	16.3	0.0	595.09	3.81	2.8	2.3
Santa Monica	INC-SMC2	32	15.2	0.1	593.32	4.18	2.4	0.3
San Clemente	INC-ST1	0	38.3	0.0	563.84	8.71	6.9	0.1
San Clemente	INC-ST1	5	38.2	0.3	568.77	6.15	5.8	0.1
San Clemente	INC-ST1	7.25	38.3	0.1	566.64	6.13	5.8	0.1
San Clemente	INC-ST1	12.25	39.3	1.9	560.46	3.87	5.8	0.1
San Clemente	INC-ST1	20.25	37.9	1.3	572.59	3.91	5.8	0.1
San Clemente	INC-ST1	23.75	37.2	0.1	572.08	4.60	5.8	0.1
San Clemente	INC-ST2	0	36.9	0.6	561.26	4.19	6.9	0.1
San Clemente	INC-ST2	5	30.9	0.3	569.25	5.82	6.9	0.1
San Clemente	INC-ST2	7.25	37.7	0.1	570.96	6.24	6.5	0.1
San Clemente	INC-ST2	12.25	37.5	0.0	567.61	3.91	6.9	0.1
San Clemente	INC-ST2	20.25	37.8	0.1	570.41	3.73	6.5	0.1
San Clemente	INC-ST2	23.75	36.7	0.4	571.50	4.31	6.2	0.1
San Clemente	INC-ST3	0	37.2	0.0	569.21	8.88	6.9	0.1
San Clemente	INC-ST3	5	37.1	0.0	566.71	5.19	7.2	0.1

San Clemente	INC-ST3	7.25	37.0	0.8	568.31	5.27	6.9	0.1
San Clemente	INC-ST3	12.25	36.5	0.1	563.93	3.77	7.2	0.1
San Clemente	INC-ST3	20.25	36.6	0.6	566.87	3.98	8.3	0.1
San Clemente	INC-ST3	23.75	36.8	1.1	569.99	4.60	7.2	0.1